

# Material bond, formation, and growth, in Al/Mg compound castings



A thesis submitted for the degree of Doctor of Philosophy

By

Kilian Tobin Schneider

Institute of Materials and Manufacturing, Department of Mechanical and  
Aerospace Engineering, Brunel University London.

## **Acknowledgements**

I would like to thank everyone for supporting me during the creation of this thesis. I am very grateful to Dr Brian McKay and Dr Hari Nadendla for accepting me as a PhD student and providing guidance and important input over the past four years.

Furthermore, I would like to thank my family for supporting and encouraging me throughout my life. I want to especially express my gratitude to my father, who showed me the way and made all of it possible.

Additional thanks to Cara, for being always there for me, and to Alberto, Jaime and Susanna, for the good times together.

## Abstract

Al/Mg compound castings possess a number of benefits compared to conventional single material castings. High specific strength, low weight, economic viability and the possibility for a “tailored-to-need” design have been cited. In compound castings, the material bond is of great importance to the mechanical stability and soundness of the compound casting and thus ultimately their economic and practical viability. Whilst aluminium and magnesium have been successfully joined by a number of processes, little is known about the formation of the material bond in the compound casting process and how to influence it.

Consequently, in this study a methodology was devised to assess the factors influencing the formation of this material bond. The results of the experimentation were characterised using SEM, EDS, XRD, DSC measurements and mechanical testing. As similar to the solid state joining of the two metals, the primary constituents of the material bond were found to be the intermetallic phases  $\beta(\text{Al}_3\text{Mg}_2)$  and  $\gamma(\text{Al}_{12}\text{Mg}_{17})$ . Aluminium’s intrinsic oxide layer did not inhibit the formation of a bond at the interface between the two metals. In fact, the oxide layer was found to be reduced by the magnesium melt upon contact, forming MgO. The resultant MgO is then dispersed in the surrounding melt. Dissolution of the solid aluminium into the magnesium melt and the subsequent precipitation of the material bond from the liquid phase was identified to be the main mechanism behind the formation of the material bond. A direct correlation between the amount of aluminium and thickness of the material bond exists. Based on the results from experimentation, a step-by-step model was developed to explain and understand the underlying mechanism and processes that contribute to the formation and growth of the material bond in Al/Mg compound castings. The different steps were identified as:

1. Initial contact of melt and solid metal
2. Dissolution of the solid metal and solidification of the melt
3. Growth of the material bond due to solid state diffusion

The addition of silicon and zinc resulted in the formation of phases according to the corresponding ternary phase diagrams. The addition of silicon resulted in the formation of an  $\text{Mg}_2\text{Si}$  phase. The formation of this phase was found to be an exception, resulting from a diffusion reaction process rather than precipitation from the liquid phase. Unlike silicon, zinc was dissolved by the magnesium and crystallised during solidification on the crystal lattice of the intermetallic phases  $\beta$  and  $\gamma$ . The zinc-rich phases  $\tau_1$  and  $\phi$  were only formed in the presence of an abundance of zinc and displayed a very low solidification range of 367-433°C. The low melting temperature and rapid and imbalanced diffusion of zinc caused the formation of evenly shaped voids (similar to the Kirkendall effect). This was only observed with zinc concentrations greater than 15wt%. Based on the observations made during

experimentation and assessment of the compound castings, a model was developed to explain the formation of these aforementioned voids.

The temperature distributions during casting, solidification and cooling at the solid/liquid interface were measured and simulated with the CAE software package Magmasoft 5.31. As the formation of the interface is a complex interaction of temperature, dissolution, diffusion and solidification it cannot be precisely simulated. Despite a number of discrepancies between simulation and reality, a simulated and measured distribution was determined, that was in relatively good accordance, especially at higher temperatures. The melt composition near the solid/liquid interface was changed by the dissolution of aluminium into the magnesium melt. As a result, the melt near the solid/liquid interface solidified last, thus causing shrinkage, which negatively affected the soundness of the bond. Furthermore, soundness was impaired by fractures and cracks, thought to originate during cooling or handling of the castings.

Mechanical strength of the material bond was approximated with Vickers micro-hardness measurements and push-out testing. Regardless of the used alloys and parameters, the bond displayed high brittleness with the push-out tests revealing that the material bond always fails in the aluminium-rich region. The magnesium-rich phases  $\gamma$  and  $\phi$  (in the presence of zinc) showed signs of increased ductility (compared to the aluminium-rich phases  $\beta$  and  $\tau_1$ ). Overall push-out resistance of the bond varied between 5-25MPa. Although no correlation between the thickness of the material bond and push-out resistance was evident, push-out resistance was found to be greatly affected by the soundness of the castings. Micro-hardness of the intermetallic phases in the material bond was up to 300Hv higher than that of the used aluminium and magnesium alloys. The magnesium-rich phases  $\beta$  and  $\phi$  were found to exhibit a slightly lower hardness than the aluminium-rich phases  $\beta$  and  $\tau_1$ , whilst retaining some ductility.

Several problems/drawbacks of compound castings have been identified in this study. Especially the low mechanical strength of less than 25MPa, which is considerably below than that of other joining techniques, is to be seen as problematic. Moreover, the material bond was found to be highly susceptible to galvanic corrosion, with signs of corrosion already being present on the samples after preparation. Lastly, fractures and pores were commonly found within in the bond of the compound castings, reducing the soundness of it. These problems/drawbacks will need to be overcome if Al/Mg compound castings are ever to become a viable alternative to already established and proven joining techniques.

# Table of contents

	<b>Page</b>
<b>Chapter 1: Introduction</b>	1
<b>1.1: Background</b>	1
<b>1.2: Objectives</b>	2
<b>1.3: Thesis outline</b>	3
<b>1.4: References</b>	4
<b>Chapter 2: Literature review</b>	6
<b>2.1: Types of compound castings</b>	6
2.1.1: Similar metals	6
2.1.1.1: Aluminium/Aluminium compound casting	6
2.1.1.2: Magnesium/Magnesium compound casting	8
2.1.2: Dissimilar metals	11
2.1.2.1: Iron/Aluminium compound casting	11
2.1.2.2: Aluminium/Copper compound casting	17
2.1.2.3: Iron/Magnesium compound casting	18
2.1.3: Aluminium/Magnesium compound casting	21
2.1.4: Alternative Aluminium/Magnesium joining methods	25
<b>2.2: Metallurgy of the Al-Mg system</b>	27
2.2.1: Aluminium-Magnesium phase diagram	27
2.2.2: Intermetallic compounds in the Al-Mg system	29
2.2.3: Mechanical properties of Al-Mg intermetallic compounds	31
2.2.4: Coatings	31
2.2.4.1: Zinc-based coatings	32
2.2.4.2: Manganese-based coatings	33
2.2.5: Diffusion in compound castings	34
2.2.5.1: Fundamentals of diffusion	34
2.2.5.2: Lattice and grain boundary diffusion	36
2.2.6: Metallurgy of the interfacial reaction in the Al-Mg system	39
2.2.7: Diffusion controlled growth of the material bond in the Al/Mg system	42

<b>2.3:</b>	<b>Summary</b>	46
<b>2.4:</b>	<b>References</b>	47
<b>Chapter 3:</b>	<b>Experimental methodology</b>	55
<b>3.1:</b>	<b>Outline</b>	55
<b>3.2:</b>	<b>Equipment Used</b>	56
3.2.1:	Moulds and furnaces	56
3.2.1.1:	Moulds	56
3.2.1.2:	Furnaces	58
3.2.1.3:	Additional Equipment	58
3.2.2:	Alloys	58
3.2.3:	Characterisation equipment	58
3.2.3.1:	Optical Microscopy (OM)	58
3.2.3.2:	Scanning Electron Microscopy (SEM)	59
3.2.3.3:	X-ray Diffraction (XRD)	59
3.2.3.4:	Optical Emission Spectroscopy (OES)	60
3.2.3.5:	Thermal Analysis	60
3.2.3.6:	Micro-Hardness Indenter	61
3.2.3.7:	Three-point Bending Machine	61
3.2.3.8:	Numerical Simulation	61
<b>3.3:</b>	<b>Material Selection in Al/Mg Compound Castings</b>	62
3.3.1:	Selection of a Magnesium Alloy	62
3.3.2:	Influence of Silicon & Zinc on the Formation of the Material Bond	63
<b>3.4:</b>	<b>Interfacial Phenomena in Al/Mg Compound Castings</b>	66
3.4.1:	Chemical Reaction of Alumina with Magnesium	66
3.4.2:	AlMgZn Phases	66
3.4.3:	Thermophysical Description of Interfacial Reaction Using Numerical Simulation	68
3.4.4:	Growth of the Material Bond via Solid State Diffusion in Diffusion Couples	71
<b>3.5:</b>	<b>Mechanical Properties of the Material Bond of Al/Mg Compound Castings</b>	72
3.5.1:	Mechanical Strength of the Material Bond	72

<b>3.6:</b>	<b>References</b>	75
<b>Chapter 4:</b>	<b>Material Selection in Al/Mg Compound Castings</b>	77
<b>4.1:</b>	<b>Selection of a Magnesium Alloy</b>	77
<b>4.2:</b>	<b>Influence of Silicon and Zinc on the Formation of the Material Bond</b>	79
4.2.1:	The Material Bond of AlSi/AZ31 Compound Castings	82
4.2.2:	The Material Bond of AlZn/AZ31 Compound Castings	90
<b>4.3:</b>	<b>Micro-hardness of the Material Bond in AlZn/AZ31 and AlSi/AZ31 Compound Castings</b>	103
<b>4.4:</b>	<b>Conclusion</b>	109
<b>4.5:</b>	<b>References</b>	110
<b>Chapter 5:</b>	<b>Interfacial Phenomena in Al/Mg Compound Castings</b>	111
<b>5.1:</b>	<b>Outline</b>	111
<b>5.2:</b>	<b>Chemical Reaction of Alumina with Magnesium</b>	112
<b>5.3:</b>	<b>AlMgZn Phases</b>	116
<b>5.4:</b>	<b>Thermophysical Description of Interfacial Reaction using Numerical Simulation</b>	120
<b>5.5:</b>	<b>Growth of the Material Bond via Solid State Diffusion in Diffusion Couples</b>	124
<b>5.6:</b>	<b>Conclusion</b>	128
<b>5.7:</b>	<b>References</b>	128
<b>Chapter 6:</b>	<b>Mechanical Properties of the Material Bond of Al/Mg Compound Castings</b>	129
<b>6.1:</b>	<b>Mechanical Strength of the Material Bond</b>	129
<b>6.2:</b>	<b>Conclusion</b>	137
<b>6.3:</b>	<b>References</b>	141
<b>Chapter 7:</b>	<b>Discussion</b>	142
<b>7.1:</b>	<b>Introduction</b>	142
<b>7.2:</b>	<b>Reactions at the Solid/liquid Interface in Al/Mg Compound Castings</b>	145

7.2.1:	Wetting of the Aluminium Alloy by the Melt	145
7.2.2:	Chemical Interaction with the Alumina Layer	148
<b>7.3:</b>	<b>Dissolution of the Solid Metal and Solidification of the Melt</b>	151
<b>7.4:</b>	<b>Growth of the Material Bond due to Diffusion in the Solid State</b>	160
<b>7.5:</b>	<b>Formation of the Material Bond in Al/Mg Compound Casting – Summary</b>	164
<b>7.6:</b>	<b>Impact of Alloying Elements on the Formation of the Material Bond</b>	165
7.6.1:	Silicon	165
7.6.2:	Zinc	169
<b>7.7:</b>	<b>Soundness and Mechanical Strength of the Material Bond in Al/Mg Compound Castings</b>	178
7.7.1:	Soundness of the Material Bond of Al/Mg Compound Castings	178
7.7.2:	Mechanical Strength of the Material Bond of Al/Mg Compound Castings	179
<b>7.8:</b>	<b>Discussion Remarks - An Assessment of the Viability of Al/Mg Compound Castings</b>	182
<b>7.9:</b>	<b>References</b>	184
<b>Chapter 8:</b>	<b>Conclusion and Future Work</b>	190



# Chapter 1: Introduction

## 1.1: Background

To meet increasing environmental standards and customer demands, lightweight construction has developed into a major driving force within the automotive and aerospace industries. In order to meet these requirements, single-material components may not always be the best choice with regard to cost and performance. Preliminary studies indicate that the metal/metal compound casting is a promising approach (Bührig-Polaczek et al., 2006; Oberschelp, 2012; Lao, 2013). J. P. Volders defined compound casting as a process in which a metallic melt is cast onto or around a solid metal shape, forming a diffusion and reaction zone and thus a continuous metallic transition. According to research, the benefits of compound castings are:

- low specific weight and high specific strength. For an automotive Body-in-white structure Bührig-Polaczek et al. identified possible weight saving of up 45% compared to a conventional steel structure and an increase of more than 100% in the specific strength in regards to a steel structure of the same weight (Tayal et al., 2012; Bührig-Polaczek et al., 2006)
- meeting a wide range of requirements with one component (i.e. a single component can fulfil several requirements) (Tayal et al., 2012);
- reduced machining costs, due to high function integration (Tayal et al., 2012; Bührig-Polaczek et al., 2006).

Depending on the metals used in the compound casting, the process can be classified into the compound casting of similar metals and dissimilar metals. Similar metals are identical metals but may contain differing alloy elements. As such, the thermo-physical properties are identical or similar (e.g. an aluminium sheet is overcast with pure aluminium or vice versa). Dissimilar metals are different metals with, therefore, dissimilar thermo-physical properties (e.g. a steel insert is overcast with a magnesium alloy).

The main focus of existing research has been the metallurgical characterisation of compound castings. So far researchers have successfully joined the following materials using compound casting:

- Aluminium/Aluminium (Papis, Löffler, and Uggowitzer, 2009; Papis et al., 2008);
- Aluminium/Steel (Bührig-Polaczek et al., 2006);
- Aluminium/Cast iron (Bouché, Barbier, and Coulet, 1998);
- Aluminium/Copper (Tanaka, Kajihara, and Watanabe, 2007);
- Magnesium/Magnesium (Papis, Löffler, and Uggowitzer, 2010);

- Magnesium/Steel (Pierre et al., 2003);
- Magnesium/Aluminium (Lao, 2013; Papis, Löffler, and Uggowitz, 2009; Hajjari et al., 2011; Liu, Chen, and Yang, 2015).

It was concluded that for the stability of a hybrid structure it is imperative that both metals form a sound connection via form closure, force closure, or material bonding (Lao, 2013; Oberschelp, 2012). A continuous material bond between the two metals is also highly desirable, as a crevice between the metals could lead to galvanic corrosion, particular in a humid environment (Rübner et al., 2011; Lao, 2013). However, compound casting itself is not entirely new and has already been used to produce a number of products, such as BMW's N52 engine block (Lichy et al., 2004). The N52 engine block was cast in magnesium with an aluminium insert. As magnesium is susceptible to corrosion from the cooling water and lacks sufficient creep resistance under high temperatures, aluminium was used for the crankcase. However, the N52 engine block was discontinued in 2015, with its successor models not utilizing compound casting. The reason for the discontinuation of the compound casting process was not given by BMW. Other examples for the mass production of compound castings include aluminium cylinder blocks with cast-in grey iron liners, or liners made of ductile iron and grey iron (Jürgensen, 2021). In recent years a steel/aluminium compound casting technology called Variostruct<sup>®</sup> has been developed in Germany (Von Kulmiz, 2012). Variostruct<sup>®</sup> castings consist of a cold-formed steel sheet on which a supporting aluminium structure is cast via High Pressure Die Casting (HPDC). Conventional metals and alloys such as TRIP 780 (transformation induced plasticity steel where the austenite is embedded within a primary matrix of ferrite) and Castasil 37<sup>®</sup> (AlSi alloy with 8.5-10.5wt% silicon and 0.06wt% magnesium) are used (Imperia GmbH, 2016; Von Kulmiz, 2012). To the best of the author's knowledge, this technology has not been used in any actual application to date, despite its potential benefits.

## 1.2: Objectives

So far, no detailed knowledge about the formation and properties of the material bond in Al/Mg compound castings exists in the literature. Therefore, the object of this thesis is to acquire a more in-depth understanding of the metallurgical principles and processes occurring during the production of Al/Mg compound castings, and how these affect the resultant casting. More specifically, this thesis focuses on the following.

1. **Phase selection in the material bond.** So far it is unknown if the phase selection of the material bond in compound castings can be altered or manipulated. This thesis aims to provide a better understanding of the underlying mechanics that affect the phase formation, and to understand the impact of ternary alloying elements on the bond in compound castings.

2. **Formation and growth of the material bond.** It is known that the formation and growth of the bond is the result of a number of physical (dissolution of the solid phase, diffusion) and chemical (reduction of the aluminium's oxide layer, forming of intermetallic phases) reactions. However, it is unknown to what extent each reaction contributes to the material bonds final appearance.
3. **Mechanical strength of the material bond.** Mechanical strength of the bond is considered of great importance for any potential industrial application. There is little information in the literature about the mechanical properties of Al-Mg intermetallics, found in the material bond. Consequently, this thesis will investigate the mechanical strength of the material bond.

### 1.3: Thesis outline

Chapter 2 aims to provide an overview of the existing research in the area of compound castings and the joining of aluminium and magnesium. It begins by discussing the compound casting of similar metals and dissimilar metals (other than aluminium and magnesium). A description of the materials and techniques used, as well as the results and their interpretation, is given. This is followed by a detailed discussion about the compound casting of aluminium and magnesium, after which other joining methods for the two metals are discussed. The literature review is concluded by detailing important metallurgical processes during compound casting, such as diffusion, phase growth and the role and formation of intermetallic phases and phase growth. Based on the existing research, a number of experiments were designed and conducted. The results are divided into three distinct chapters:

1. Chapter 4: Material selection in Al/Mg compound castings;
2. Chapter 5: Interfacial phenomena in Al/Mg compound castings;
3. Chapter 6: Mechanical properties of the material bond of Al/Mg compound castings.

A detailed description of all experiments and the materials and equipment used therein is given in chapter 3, with the results from the experimentation presented in the aforementioned chapters 4-6. These chapters are followed by the discussion of the results and their significance to the compound casting process, in chapter 7. As part of the discussion, a model of the formation and growth of the material bond has been developed, based on the experimental results from this study and reports from the literature. Using this model, the sequence of metallurgical reactions and the influence of factors – such as alloying elements contributing to the formation of the bond – are described. The discussion is then concluded by the assessment of the mechanical properties of Al/Mg compound casting. Using the acquired data and developed model, the disadvantages and shortcomings of compound castings, in comparison to other established joining methods, are argued as a concluding point of this thesis.

When discussing the different metal combinations produced with compound castings, the following nomenclatures will be used: the solid metal is stated first, separated by a slash from the liquid metal

used for overcasting, e.g. Al/Mg compound casting refers to a solid aluminium alloy overcast with a magnesium melt. Furthermore, in the literature, the terms *interface* and *material bond* are used interchangeably to describe the reaction zone in compound castings. For clarity, in this study the term *material bond* is used when referring to the reaction zone, while *interface* is used to describe a boundary between two phases or states (e.g. solid/liquid interface).

## 1.4: References

BOUCHÉ, K., BARBIER, F. and COULET, A. (1998) Intermetallic compound layer growth between solid iron and molten aluminium. *Materials Science & Engineering A*, **249**(1), pp. 167-175.

BÜHRIG-POLACZEK, A., RÖTH, T., BAUMEISTER, E., NOWACK, N. and SUSSMANN, T. (2006). Hybride Leichtbaustrukturen in Stahlblech-Leichtmetall Verbundguss. *Internationaler Expertenkreis Automobil-Leichtbau 15. Europäische Automobil-Leichtbaukonferenz*, 9-10 May, 2006.

HAJJARI, E., DIVANDARI, M., RAZAVI, S.H., EMAMI, S.M., HOMMA, T. and KAMADO, S. (2011) Dissimilar joining of Al/Mg light metals by compound casting process. *Journal of Materials Science*, **46**(20), pp. 6491-6499.

IMPERIA GMBH (2016) *Leistung wird leichter*. Available: <http://www.variostruct.de/> [27 April 2016].

JÜRGENSEN, M. (2016) *Verbundguss*. Available: <http://www.m-juergensen.de/de/technologie/werkstoffe/verbundguss.html> [5 May 2016].

LAO, B. (2013) *Druckgegossene Metallhybridstrukturen für den Leichtbau- Prozess, Werkstoffe und Gefüge der Metallhybriden*. Aachen: Foundry institute RWTH.

LICHY, A., HOFFMANN, T., KINNINGER, P. and BORGMANN, K. (2004) *Der neue BMW Reihensechszylinder Ottomotor*. München: BMW AG.

LIU, Y., CHEN, Y. and YANG, C. (2015) A study on atomic diffusion behaviours in an Al-Mg compound casting process. *AIP ADVANCES*, **5**(8), pp. 087147-087147-13.

OBERSCHELP, C. (2012) *Hybride Leichtbaustrukturen für den Karosseriebau – Gusswerkstofforientierte Anwendungsuntersuchungen für das Druckgießen*. Aachen: Foundry Institute RWTH.

PAPIS, K. J. M., HALLSTEDT, B., LÖFFLER, J. F., and UGGOWITZER, P. J. (2008) Interface formation in aluminium–aluminium compound casting. *Acta Materialia*, **56**(13), pp. 3036-3043.

PAPIS, K. J. M., LÖFFLER, J. F., and UGGOWITZER, P. J. (2009) Light metal compound casting. *Science in China, Series E: Technological Sciences*, **52**(1), pp. 46-51.

PAPIS, K. J. M., LÖFFLER, J. F., and UGGOWITZER, P. J. (2010) Interface formation between liquid and solid Mg alloys—An approach to continuously metallurgic joining of magnesium parts. *Materials Science & Engineering A*, **527**(9), pp. 2274-2279.

PIERRE, D., VIALA, J.C., PERONNET, M., BOSSELET, F. and BOUIX, J. (2003) Interface reactions between mild steel and liquid Mg–Mn alloys. *Materials Science & Engineering A*, **349**(1), pp. 256-264.

RÜBNER, M., GÜNZL, M., KÖRNER, C. and SINGER, R. F. (2011) Aluminium–aluminium compound fabrication by high pressure die casting. *Materials Science & Engineering A*, **528**(22), pp. 7024-7029.

TANAKA, Y., KAJIHARA, M. and WATANABE, Y. (2007) Growth behavior of compound layers during reactive diffusion between solid Cu and liquid Al. *Materials Science & Engineering A*, **445**, pp. 355-363.

TAYAL, R., SINGH, V., KUMAR, S. and GARG, R. (2012) Compound Casting - A literature Review. *National Conference on Trends and Advances in Mechanical Engineering*, Oct 19-20, 2012.

VON KULMIZ, G. (2012) VarioStruct - Light Weight Structures. *ROADSHOW 2012 - LIGHTWEIGHT TECHNOLOGY*, October 2012.

## Chapter 2: Literature Review

### 2.1: Types of Compound Castings

#### 2.1.1: Similar metals

##### 2.1.1.1: Aluminium/Aluminium compound casting

Al/Al compound castings have been successfully produced by several researchers. Rübner et al. used high pressure die-casting (HPDC) to join an Al99.5 insert with AlSi9Cu3. Unless otherwise stated hereafter, all alloy composition are given in wt%. To promote adhesive bonding, the oxide layer of the Al99.5 insert was removed and replaced with a zinc layer. A zincate treatment and zinc electroplating were used for this. Zincate treatment is an electroless immersion process to plate aluminium with zinc (Mallory and Hajdu, 1990). A definition and detailed description of the zincate treatment can be found in section 2.2.4. As zinc is highly soluble in aluminium it forms a chemical bond and has a relatively low melting point. Therefore, it seems to be an ideal candidate to be used as a connecting layer. To prevent gas porosity in the casting a vacuum was applied. It was discovered that a zincate treatment alone is not sufficient to create an adhesive bond between the two alloys. The scanning electron microscope (SEM) image of the insert-melt interface is shown in figure 2.1. When using only a zincate treatment, a gap between the two alloys is clearly visible (see figure 2.1(a)). Adhesive bonding is only achieved by combining the zincate treatment with zinc electroplating. The thickness of the zinc layer ranges from 100nm (zincate treatment) to 22 $\mu$ m (zincate treatment + zinc electroplating). However, a thick zinc layer leads to the formation of brittle intermetallic phases at the interface, possibly weakening

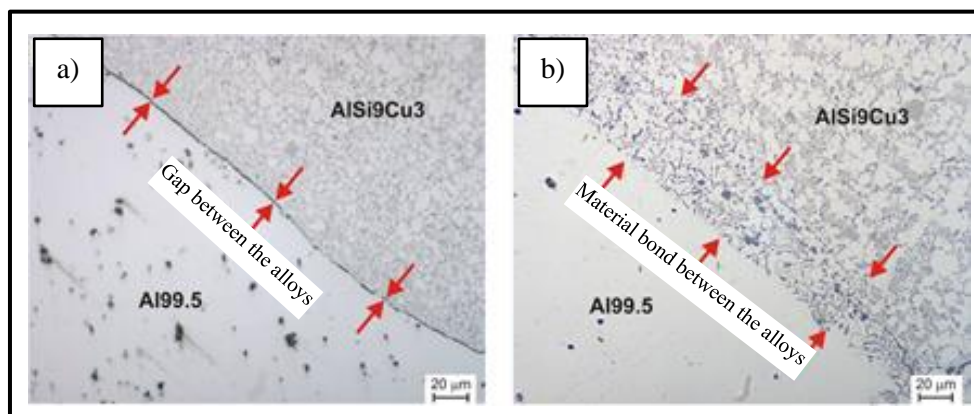


Figure 2.1. (a) Insert-melt interface of an Al/AlSi9Cu3 compound casting after a zincate treatment. A gap, indicated by the arrows, between the two aluminium alloys is visible. (b) Insert-melt interface of an Al/AlSi9Cu3 compound casting after a zincate treatment + zinc electroplating. No gap is present between the two aluminium alloys. The arrows are indicating the thickness of the material bond (Rübner et al., 2011).

the whole compound casting. Electron microprobe analysis revealed that the material bond depicted in figure 2.1(b) consists of three distinct layers:

1. Diffusion zone into Al99.5, which consists of aluminium and zinc;
2. Zn-rich interlayer, which consists of aluminium, silica and zinc;
3. Diffusion zone into AlSi9Cu3, which consists of AlSi9Cu3 and zinc (Rübner et al., 2011).

The experimental work undertaken showed that an optimal thickness of the zinc layer exists. The best adhesive bonding was achieved if the zinc layer is just thick enough to promote sufficient adhesive bonding, but thin enough to prevent the formation of intermetallic phases. To this end, Schwankl et al. (2013) optimised the zincate treatment process. Using these results, Koerner, Schwankl, and Himmler (2014) successfully joined Al99.5 with AlSi9Cu3 with high pressure die-casting; the zinc layer resulting from the optimised zincate treatment was less than 1µm thick with no embrittlement of the interface detected.

Papis et al. joined an AlMg1 substrate with several different aluminium alloys using a horizontal furnace, pictured in figure 2.2. Before casting, the oxide layer was removed and a zincate and zinc electroplating treatment were used to coat the substrate's surface. During casting, the normal atmosphere was replaced with a 99.99% argon atmosphere, and a processing temperature of 700°C was used. It was determined that a zincate treatment alone was not sufficient as the thin zinc layer vaporised during casting. Nevertheless, the AlMg1 substrate was successfully joined with AlCu7, AlSi7, AlZn7 and Al99.99 alloys. The interface of these couples can be seen in figure 2.2. The AlMg1-AlCu7 and AlMg1-AlSi7 show a continuous transition across the interface. The AlMg1-AlZn7 couple shows only a small transition while the AlMg1-Al99.99 couple displays a 150µm wide reaction layer. The couples were solution annealed at 500°C for 30min and then aged at temperatures ranging from 120-190°C for

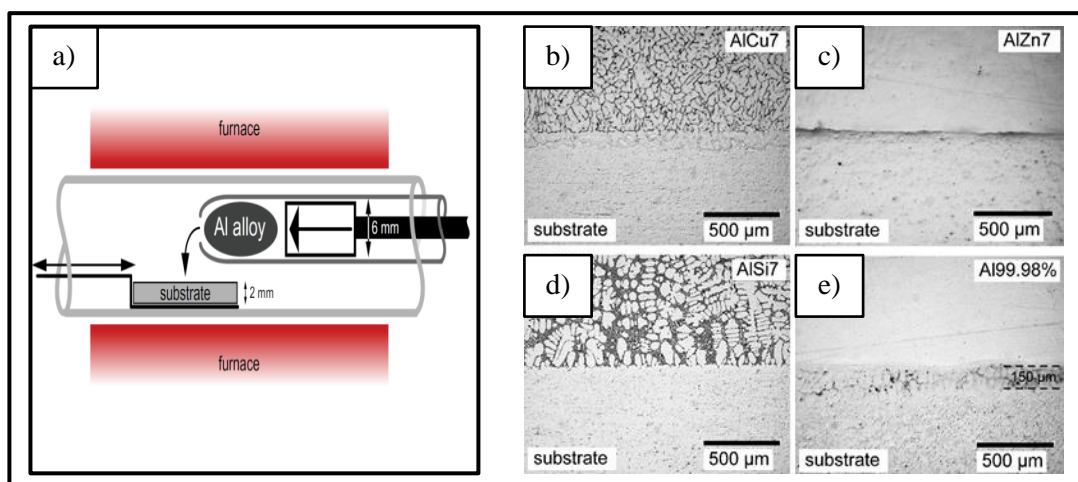


Figure 2.2. (a) Schematic of the experimental setup used by Papis et al. Optical microscope images of the interfaces between: (b) AlMg1/AlCu7; (c) AlMg1/AlZn7; (d) AlMg1/AlSi7; and (e) AlMg1/Al99.99

(Papis et al., 2008).

up to 24h. After this heat treatment a sharp increase in hardness near the interface (up to 200µm from

both sides) was measured. This increase in hardness was particularly distinct for the AlMg1-AlCu7 and AlMg1-AlSi7 couples. This was linked to the precipitation of hardness-increasing phases ( $Mg_2Si$ ,  $Al_2CuMg$  and  $Zn_2Mg$ ) (Papis et al., 2008).

### 2.1.1.2: Magnesium/Magnesium compound casting

Similarly to aluminium alloys, magnesium's intrinsic oxide layer was thought to impede any adhesive bonding in Mg/Mg compound castings. However, Papis, Löffler, and Uggowitzer managed to successfully produce an adhesive bond between an AZ31 (magnesium alloy with 3wt% aluminium and 1wt% zinc) substrate and pure magnesium as well as AJ62 (magnesium alloy with 6wt% aluminium and 2wt% strontium). The oxide layer was removed and replaced by a zinc coating through a combination of several surface treatments. Zinc displays a similar chemical affinity to magnesium as to aluminium and is thus an ideal candidate to be used as a connecting layer. After grinding, cleaning and pickling, the substrate was immersed in a zinc sulphate solution, which yielded a 200nm thick zinc layer. Subsequent zinc- galvanising increased the thickness of the layer to about 2-3 $\mu m$ . Before casting, the coated substrate was heated to 285°C for 2h to increase adhesion between the zinc and magnesium. SEM images of the zinc coating before and after the heat treatment can be seen in figure 2.3. It was found that zinc and magnesium form the compound  $MgZn_2$ .

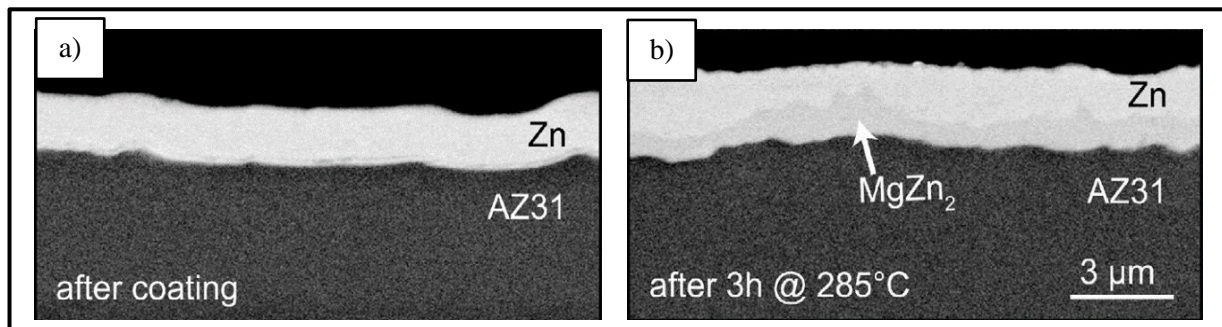


Figure 2.3. SEM Micrographs of the zinc coating of an AZ31 alloy: (a) before heat treatment; and (b) after heat treatment (Papis, Löffler, and Uggowitzer, 2010).

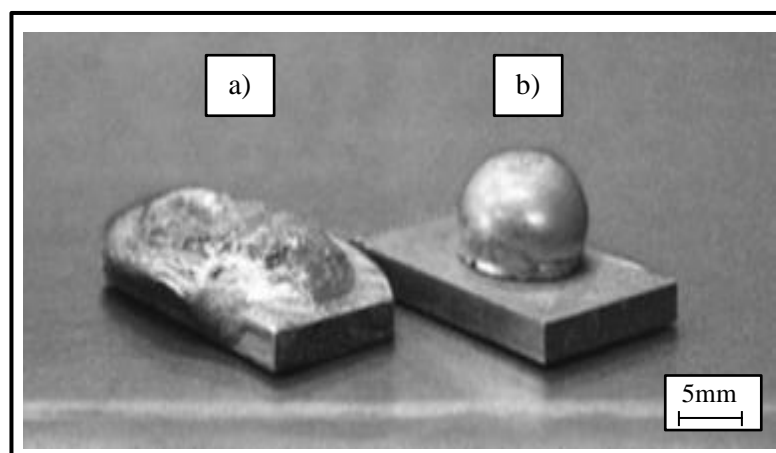


Figure 2.4. Impact of a zinc coating on wettability of an AZ31 alloy. (a) Wettability with a coating. (b) Wettability without a coating. (Papis, Löffler, and Uggowitzer, 2010).



The experimental setup was identical to the one displayed in figure 2.2. An inert argon atmosphere was used and the furnace temperature ranged between 700-750°C. Due to the almost identical properties of the magnesium alloys used, characterisation of the interface using SEM proved to be insufficient. EDX measurements revealed that the Zn/Mg<sub>2</sub>Zn coating was completely dissolved into the liquid melt. This resulted in an increased wettability on the substrate. The effect of a Zn-coating on the substrate can be seen in figures 2.3 and 2.4. Micro-hardness measurements reveal that the coating, as it is completely dissolved, has no significant influence on the microstructure or mechanical properties of the compound. The reaction layer in both couples is about 100-200µm thick (Papis, Löffler, and Uggowitzer, 2010).

Another casting process to create compound castings is the insert moulding method (Zhao et al., 2016). This method consists of inserting and keeping a machined rod (diameter: 30mm, height: 100mm) in a melt for a specified amount of time before removing the whole assembly from the furnace and cooling it down to room temperature. Zhao et al. used this method to study the effect of cooling and solidification rate on the interface of an AZ31/AZ91 couple. After the AZ91 was heated up to different temperatures (650°C, 675°C & 700°C), the machined AZ31 rod was immersed into the melt for 2 minutes before the whole assembly was removed from the furnace. The temperature of the AZ31 rod at the point of immersion is unclear. Before immersing the AZ31 rod into the melt it was thoroughly cleaned with alkaline and acid pickling, and ultrasonically degreased. The surface roughness was set to grit 1500 with carbide papers but no coating was applied. Besides melt temperature, differing solid-liquid volume ratios ( $V_{AZ91}:V_{AZ31} = 1:1$  or  $2:1$ ) were tested with this setup (Zhao et al., 2016).

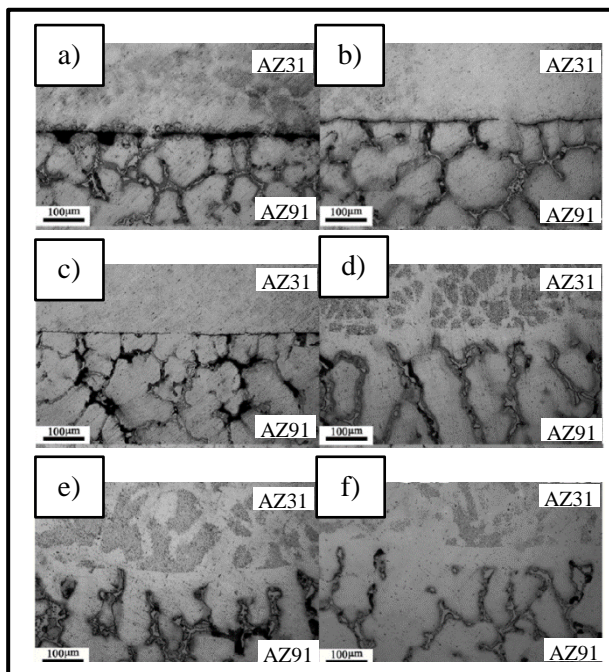


Figure 2.5. (a-f) Optical micrographs of the interface of an AZ31/AZ91 compound casting with different process parameters. Parameters are listed in table 2.1 (Zhao et al., 2016)

Index	Melt temperature [°C]	Volume ratio ( $V_{AZ91}:V_{AZ31}$ )	Bonding
a)	650	1:1	No
b)	650	2:1	No
c)	675	1:1	Partial
d)	675	2:1	Yes
e)	700	1:1	Yes
f)	700	2:1	Yes

Table 2.1: Parameters of the compound castings displayed in figure 2.5

The results of these experiments are displayed in figure 2.5 and table 2.1. These results clearly show that temperature and thus solidification and cooling rate play a major role in the formation of a material bond. If the temperature is too low the melt immediately solidifies, hindering any diffusion and thus material bonding. EDS (energy-dispersive X-ray spectroscopy) and EPMA (electron probe micro-analyser) scans of experiment *d* identified three phases at the interface:  $\beta$ -Mg<sub>17</sub>Al<sub>12</sub>,  $\alpha$ -Mg and an Mn-rich phase. However, there was no continuous intermetallic phase present in the interface and therefore no sharp increase in micro-hardness. The reaction layer of an AZ31/AZ91 compound is about 100 $\mu$ m thick. Even though the AZ31 intrinsic oxide layer was not removed before immersion, no evidence of the oxygen has been found, using SEM techniques, at or near the interface. This indicates that the oxide layer completely melted and then dispersed into the melt. Shear strength tests of the interface revealed that the samples with a liquid/solid volume ratio of 2:1 and a melt temperature of 675°C displayed, with 98MPa, the highest shear resistance. Shear resistance of the AZ91 alloy (which displays a lower shear resistance, compared to AZ31 with 202MPa) was with 101MPa only slightly higher. This indicates that the mechanical strength of the material bond is not the limiting factor for AZ31/AZ91 compound casting.

## 2.1.2: Dissimilar metals

### 2.1.2.1: Iron/Aluminium compound casting

As aluminium and iron are probably the two most commonly used metals in industry, aluminium-iron couples are of significant technical relevance (e.g. aluminised steel). The first research into the characterisation of the interface of an Al/Fe compound casting dates back to as early as 1953. Gebhardt and Obrowski detected an  $\text{Fe}_2\text{Al}_5$  phase at the interface but were unable to specify the growth kinetics of this phase – which, when later researched further by Heumann and Dittrich, was revealed to be a parabolic time dependence (Gebhardt and Obrowski, 1953; Heumann and Dittrich, 1959). Subsequent research by Eremenko et al. (Natanzon, Gorb, and Dybkov, 1980), Dybkov (1990) and Eggeler (Eggeler, Auer, and Kaesche, 1986) also found an  $\text{FeAl}_3$  phase at the interface but came to deviating conclusions concerning the growth kinetics of this phase.

In 1998, in an attempt to clarify these discrepancies, Bouché, Barbier, and Coulet studied the formation and growth kinetics of the interface of commercially pure iron and aluminium. The experimental approach used was similar to the insert moulding method, described in section 2.1.1.2. The iron specimen was immersed into the aluminium melt once the melt reached the required temperatures (700, 800 & 900°C) and was kept immersed for a specific amount of time (30s-45min). After turning off the heating, the whole assembly was cooled down under a cover gas. Optical microscopy and SEM revealed the typical morphology and composition of the interface, as can be seen in figure 2.6. Consistent with the previous research,  $\text{Fe}_2\text{Al}_5$  and  $\text{FeAl}_3$  phases were found, with the  $\text{Fe}_2\text{Al}_5$  phase being the major constituent of the interface. The transition between pure iron and  $\text{Fe}_2\text{Al}_5$  was found to be highly irregular, with increasing reaction times amplifying this effect. It was concluded that the growth of the

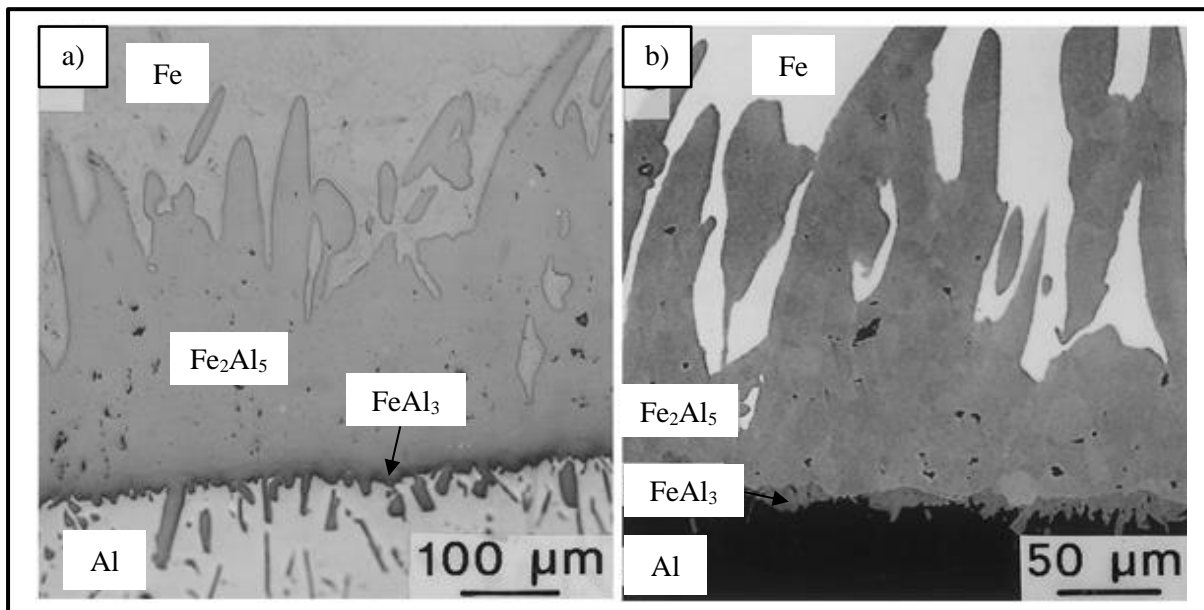


Figure 2.6. (a) Interface of an Fe/Al compound casting as seen with an optical microscope. (b) Interface of an Fe/Al compound casting as seen with a Scanning Electron Microscope (Bouché, Barbier, and Coulet, 1998).

phases is controlled by interdiffusion after a non-parabolic initial transient period. Based on the experimental results, a theoretical approach to determine phase growth was developed. According to the researchers, the absence of FeAl and FeAl<sub>2</sub> phases at the interface is due to their very low growth rates (Bouché, Barbier, and Coulet, 1998).

As the Fe<sub>2</sub>Al<sub>5</sub> phase was the dominant phase in the material bond, most focus was directed towards this phase, and little attention was paid to the FeAl<sub>3</sub> phase and how longer reaction times would influence this particular phase. Thus Shahverdi et al. used an identical experimental setup as Bouché to study the FeAl<sub>3</sub> phase in more detail. The pure iron samples were immersed into the pure liquid aluminium at 800°C for different amounts of time (90-3000s) and then studied. The interface observed was identical to the one pictured in figure 2.6. Measurements of the thickness of the interface showed that even after 3000s of immersion the FeAl<sub>3</sub> phase does not exceed a thickness of 10µm (thickness of the Fe<sub>2</sub>Al<sub>5</sub> phase was, with >100µm, several times higher). As Fe<sub>2</sub>Al<sub>5</sub> is steadily growing with the reaction time it was assumed that the Fe<sub>2</sub>Al<sub>5</sub> has a faster growth rate. Furthermore, it seems that the formation of the material bond does not follow the conventional diffusion and dissolution of iron atoms into the aluminium melt. Rather, after the initial reaction of aluminium and iron to FeAl<sub>3</sub>, this phase starts to crack and dissolve into the aluminium melt providing the iron to form the intermetallic (Fe<sub>2</sub>Al<sub>5</sub>) needles. FeAl<sub>3</sub> is harder

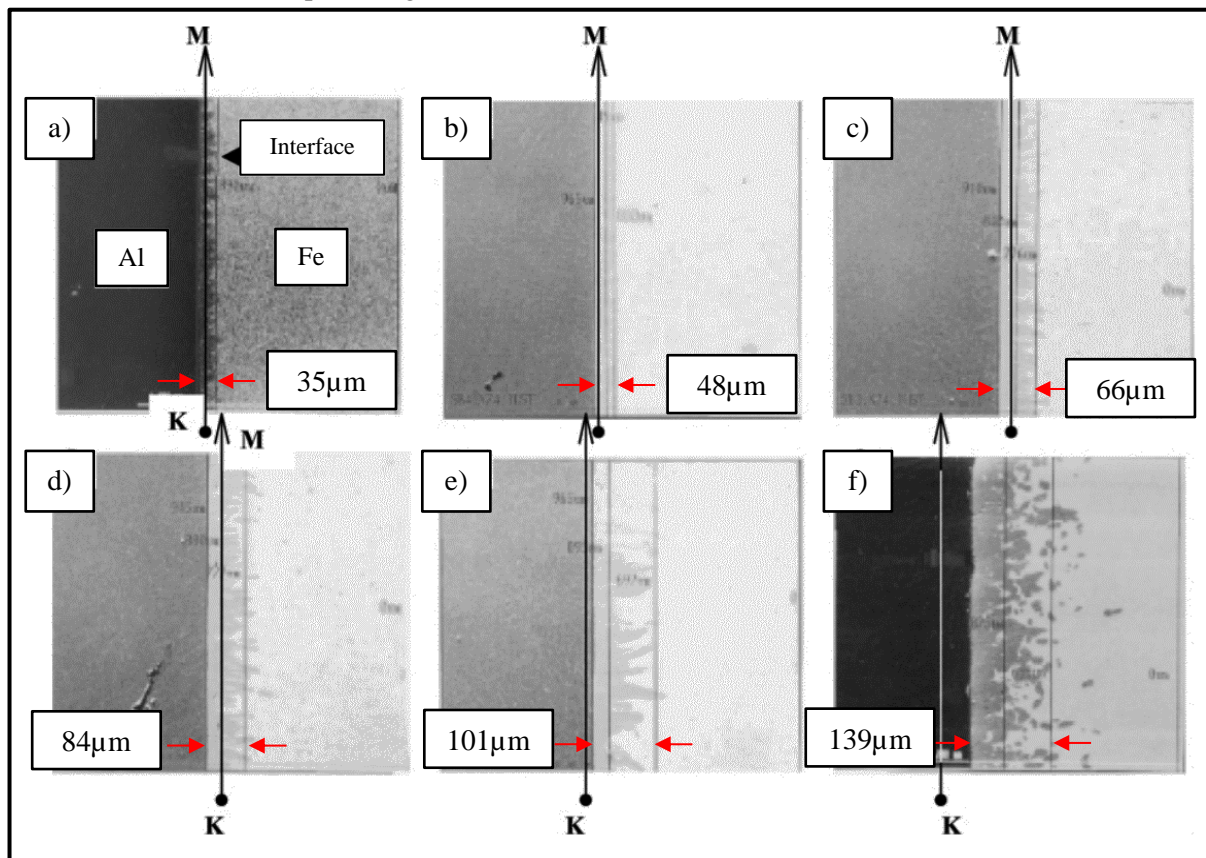


Figure 2.7. SEM micrographs of the material bond of an Fe/Al compound casting at 800°C after: (a) 95s; (b) 185s; (c) 375s; (d) 750s; (e) 1500s; and (f) 3000s. Approximate thicknesses of the material bond at each time step are indicated by the red arrows. The M-K line represents the position of Fe-Al interface before reaction. No scale bars were given by Shahverdi et al. (Shahverdi et al., 2002a).

than  $\text{Fe}_2\text{Al}_5$  and thus more likely to crack due to the stress arising from cooling and interfacial reactions. Shahverdi's work suggested that kinetics play a major role in the formation of a material bond in Fe/Al compound castings (Shahverdi et al., 2002b).

To further understand the kinetics in the Fe-Al system, Shahverdi's team explicitly studied the growth of the material bond. A similar experimental setup as used in their previous work was utilised (Shahverdi et al., 2002a). The melt temperature was varied (700, 800 & 900°C) as were the immersion times (90, 185, 375, 750, 1500 & 3000s). Differing from the previous experiments, the whole assembly was quenched in water and not cooled down under a cover gas. Examinations of the samples then showed the growth of the interface after different immersion times, as seen in figure 2.7. On the basis of these observations the growth rate with respect to immersion temperature was calculated. For an immersion temperature of 700 or 800°C a parabolic relation of interface thickness and immersion time was identified. However, for an immersion temperature of 900°C this relation was not seen. Further studies revealed that the main mechanisms of the interface growth are diffusion, dissolution and recrystallisation. At lower temperatures (700°C & 800°C), diffusion is the main driving force, which is associated with the identified parabolic relation of interface thickness and immersion time. However,

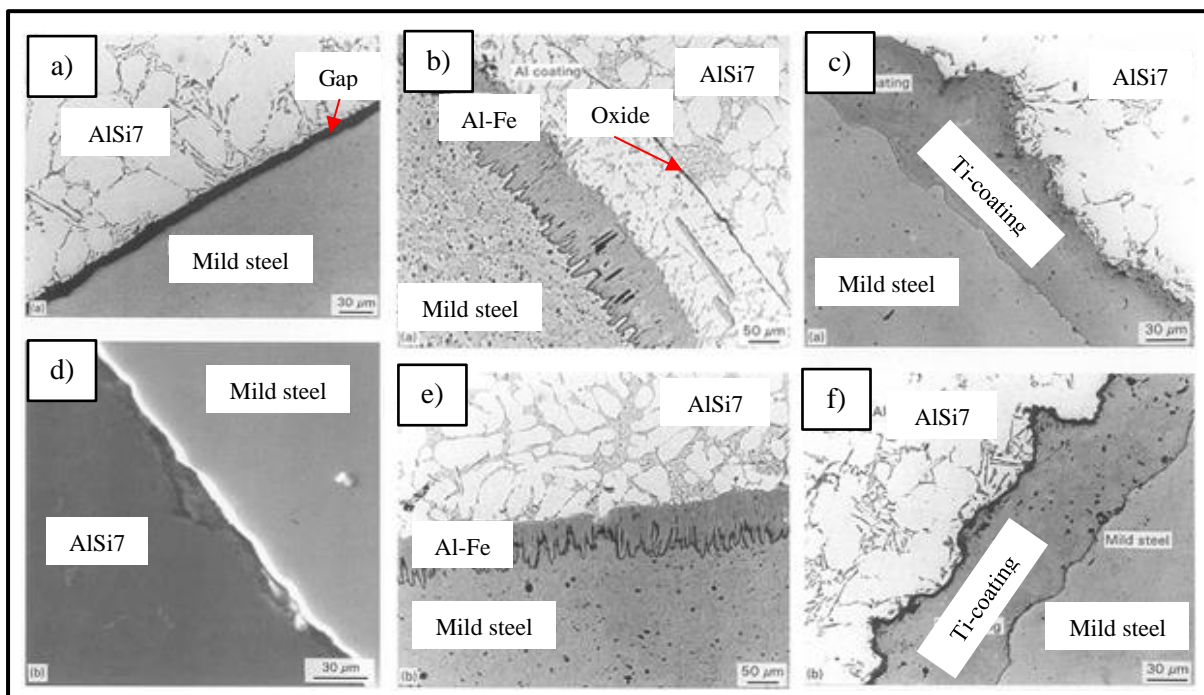


Figure 2.8. Interface between a mild steel insert and an AlSi7 alloy: (a) optical microscope image from an uncoated steel insert where a gap (indicated by the arrow) between the AlSi7 and steel insert is clearly visible; (b) in AlFe10 hot dipped steel insert, some oxides are visible (indicated by the arrow); (c) optical micrograph of a titanium sprayed steel insert after preheating to 300°C; (d) SEM micrograph of mild steel/AlSi7 compound casting without coating; (e) oxide-free region after hot dipping in AlFe10; and (f) optical micrograph of the titanium coating after preheating to 900°C (Durrant, Gallerneault, and Cantor, 1996).

at higher temperatures ( $>900^{\circ}\text{C}$ ) dissolution and recrystallisation replaces diffusion as the main driving force and does not follow the described parabolic relation (Shahverdi et al., 2002a).

Further research into the diffusion of iron and aluminium was undertaken by Kobayashi and Yakou. Structural carbon steel (0.45% carbon) specimens were immersed into pure aluminium for 300s at a variety of melt temperatures (700, 750, 800, 850 &  $900^{\circ}\text{C}$ ). After immersion, the specimens were cooled down in air, before being subjected to a heat treatment ( $600, 800, 1000$  &  $1100^{\circ}\text{C}$  for 1200 & 3600s). Afterwards, the specimens were cut and analysed. Before any heat treatment the coating mainly consisted of aluminium and  $\text{Fe}_2\text{Al}_5$ ; at this stage it remains unclear if any  $\text{FeAl}_3$  phases were present in the examined samples. Conducting a heat treatment below  $1000^{\circ}\text{C}$  resulted in a single grown phase of  $\text{Fe}_2\text{Al}_5$  in the coating. Increasing the temperature during heat treatment above  $1000^{\circ}\text{C}$  promotes the formation of intermetallic  $\text{FeAl}$  and  $\text{Fe}_3\text{Al}$  phases. As the fracture resistance of  $\text{FeAl}$  and  $\text{Fe}_3\text{Al}$  is higher than that of  $\text{Fe}_2\text{Al}_5$  it was concluded that a customised heat treatment might be a promising approach to increase the aluminised steel's mechanical properties (Kobayashi and Yakou, 2002).

With the rise in importance of aluminium in the transport industry, researchers started to investigate material bonding in more complex Al/Fe compound castings. Durrant, Gallerneault, and Cantor (1996) studied the bonding of a mild steel insert with an AlSi7 alloy using the squeeze casting process. The applied pressure, during solidification of the squeeze cast parts, shows less porosity and shrinkage compared to those that were sand- or die-cast. Mild steel inserts (0.16% Carbon) were cut, bead blasted, immersed in nitric acid to remove any iron hydroxide on the surface and washed with acetone. To study the effect of a coating on the metallurgical reaction at the interface, some of the mild steel samples were hot dipped in aluminium or spray-coated with titanium. The hot dipping was performed with an AlFe10 alloy at  $900^{\circ}\text{C}$ , which resulted in a  $140\mu\text{m}$  thick reaction layer. Consistent with previous work the reaction layer was reported to consist mainly of  $\text{Fe}_2\text{Al}_5$  and some  $\text{FeAl}_3$ . The titanium coating of the insert was achieved by vacuum plasma spraying. After ten spraying passes the insert was coated with an  $80\mu\text{m}$  thick pure titanium coating. The prepared steel inserts were heated to  $300^{\circ}\text{C}$  and  $900^{\circ}\text{C}$  before being inserted into the mould, which was also preheated to  $300^{\circ}\text{C}$ . The pouring temperature of the AlSi7 alloy was  $750^{\circ}\text{C}$  and immediately after filling of the mould a pressure of 100MPa was applied. To assess the strength of the material bond between the steel insert and AlSi7 alloy, push-out tests were performed in addition to an examination of the interface. Figure 2.8 shows the interface for all three variants. The push-out test confirmed that the steel inserts that were uncoated and preheated to  $300^{\circ}\text{C}$  do not show any significant reaction between the steel insert and the aluminium. Increasing the preheat temperature to  $900^{\circ}\text{C}$  marginally improved the interface reaction as the interface shear strength increased. At this temperature, the formation of an  $\text{Fe}_3\text{O}_4$  magnetite layer at the surface of the mild steel inserts prevents further interaction and thus increase in shear strength. The authors attributed the formation of this magnetite layer to the exposure to oxygen in the atmosphere during transport and handling of the mild steel insert. Hot dipping the steel insert in an AlFe10 alloy, before being overcast

with an AlSi7 alloy, greatly increased the shear strength, from ~45MPa to ~110MPa. These samples failed in the AlSi7 cast matrix rather than at the interface. The titanium spray-coated sample displayed the highest shear strength with ~150MPa. This high shear strength, however, was achieved without any direct reaction between the steel insert and the AlSi7 alloy. Instead, it was caused by high residual stresses in the AlSi7 combined with mechanical interlocking on the rough titanium surface. Reducing the height amplitude on the titanium's surface to 1  $\mu\text{m}$  (from 40 $\mu\text{m}$ ) lowers the shear strength to 5MPa (Durrant, Gallerneault, and Cantor, 1996).

With similar intentions, Viala et al. (2002) manufactured a suspension part using an Al/Fe compound casting. Using conventional die-casting a cogwheel-shaped spheroidal cast iron insert was overcast with an AlSi7Mg0.3Sb alloy. Before the casting, the cast iron insert was degreased, sandblasted, heated to 220°C and then hot dipped into AlSi7Mg0.3Sb superheated to 780°C. The resultant coating was 30-100 $\mu\text{m}$  thick and the coated insert was placed in a mould and heated to 400°C before being overcast with AlSi7Mg0.3Sb. These couples were cooled down to room temperature in air, with some couples receiving an additional heat treatment for 12h at 520°C before being water-quenched. Inspection of the air-cooled samples revealed a material bond 12 $\mu\text{m}$  thick, with three consecutive layers. These layers were identified as  $\text{Al}_5\text{Fe}_2$  ( $\eta$ ),  $\text{Al}_{7.4}\text{Fe}_2\text{Si}$  ( $\tau_5$ ) and  $\text{Al}_{4.5}\text{FeSi}$  ( $\tau_6$ ). The  $\tau_{1-9}$  phases are triclinic and silicon-rich. Based on the observations of Viala et al., Li et al., and Eggeler et al., the chemical changes at the interface can be divided into three distinct stages (Eggeler, Auer, and Kaesche, 1986; Li et al., 1998).

1. **Wetting reactions during hot dip aluminising.** If bubbles and thus surface turbulences can be avoided, by carefully submerging the insert, oxidisation of the melt or the insert at the interface can be completely prevented. The wetting reaction spreads from areas where a direct metal to metal contact has been established. This spreading, however, is relatively slow as increasing the immersion time from 1 to 2 or 4 minutes still resulted in only partial wetting. According to conducted simulations four intermediate phases are formed: a ternary  $\alpha$  Fe(Al,Si) solid solution and three intermetallic compounds  $\eta$  ( $\text{Al}_5\text{Fe}_2$ ),  $\tau_1$  ( $\text{Al}_3\text{Fe}_3\text{Si}_2$ ) and  $\theta$  ( $\text{Al}_{13}\text{Fe}_4$ ). The thickness of the reaction layer is closely linked to the iron content of aluminium melt. In iron under-saturated aluminium melts, the reaction layer grows approximately as fast as it is dissolved, thus resulting in a 2-3 $\mu\text{m}$  thick layer. In iron saturated melts (6-8wt% Fe) the reaction layer can reach thicknesses of up to 40 $\mu\text{m}$  after an immersion time of four minutes.
2. **Transfer to the mould and casting.** During transfer, the surface of the aluminium coating is exposed to the atmosphere and thus oxidises very quickly to  $\text{Al}_2\text{O}_3$ . This thin layer of  $\text{Al}_2\text{O}_3$ , however, is not very stable and is therefore broken up and washed away during casting. Growth of the interface and dissolution into the liquid melt are in balance during casting and therefore the interface does not change in thickness.
3. **After casting.** As the temperature starts to decrease, both growth and dissolution processes proceed at a slower rate. As the iron content in the aluminium melt near the interface draws

near to the saturation level, dissolution processes slow down at a higher rate than the growth of the interface. This results in the rapidly growing thickness of the reaction layer.

The heat treatment described above has a major influence on the morphology of the interface. The thickness of the reaction zone increases from  $\sim 12$  to  $\sim 22\mu\text{m}$ . Specifically, the  $\eta$  layer appears to thicken while the  $\tau_6$  layer (partially) and the  $\tau_5$  layer (completely) disappear. In addition, two new phases were discovered:  $\tau_2$  ( $\text{Al}_5\text{Fe}_2\text{Si}_2$ ) and  $\tau_{10}$  ( $\text{Al}_{12}\text{Fe}_5\text{Si}_3$ ) (Viala et al., 2002). These two new phases, as well as the  $\eta$  layer, grow during the heat treatment, consuming the  $\tau_5$  and  $\tau_6$  layers. Also, the heat treatment resulted in the formation of Kirkendall voids (referred to as K voids in figure 2.9) due to the unbalanced solid state diffusion of aluminium atoms to the Fe/ $\eta$  reaction front (Viala et al., 2002). These Kirkendall voids are the result of an imbalanced diffusion process, generally referred to as the Kirkendall effect (Aloke, 2004). The interface before and after casting is displayed in figure 2.9, in which the Kirkendall voids are clearly visible at the interface. It is likely that the Kirkendall voids reduce the strength of the interface and thus weaken the whole compound casting (Viala et al., 2002).

Further characterisation of the chemical changes at the interface of a low carbon steel/AlSi7Mg0.3 compound casting during heat treatment was undertaken by Zhe et al. (2011). Galvanised low carbon steel plates were immersed in AlSi7Mg0.3 at  $680^\circ\text{C}$  for 40s. Zinc is highly soluble in aluminium and thus the thin zinc layer on the steel's surface was dissolved during the immersion. Heat treatment of the obtained samples was conducted at  $535^\circ\text{C}$  with holding times from 3-160h. SEM was used to characterise the interface. The change of the interface with increasing holding time is displayed in figure 2.10. Before heat treatment a continuous reaction layer about  $2\mu\text{m}$  thick was present throughout the samples. This layer mainly consisted of  $\text{Al}_{7.4}\text{Fe}_2\text{Si}$  ( $\tau_5$ ), which is in good accordance with the earlier described work (Viala et al., 2002; Pierre et al., 2002).

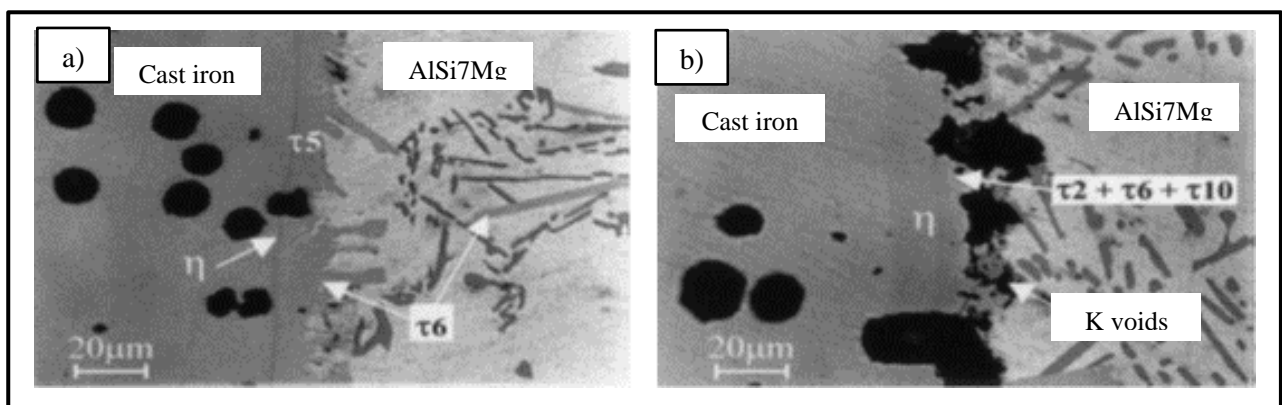


Figure 2.9. Kirkendall voids in a Fe/Al compound casting: (a) morphology of the interface in as-cast condition; and (b) morphology of the interface after receiving additional heat treatment. The heat treatment increases the size and number of the Kirkendall voids (Viala et al., 2002).

Heat treating the sample for the relative short time of 3h resulted in a two-layer appearance. The two layers were identified as  $\tau_6$  and  $\eta$  ( $\text{Al}_5\text{Fe}_2$ ). A closer inspection of the  $\eta$  ( $\text{Al}_5\text{Fe}_2$ ) phase detected numerous



silicon-rich inclusions within. These inclusions were believed to be the  $\tau_{1-9}$  phases. Increasing the holding time to 15h also increased the number of reaction layers to three. In addition to the already found  $\eta\text{Al}_5\text{Fe}_2 + \tau_{1-9}$  and  $\tau_6$  phases, a multiphase transition layer (consisting of  $\tau_{10} + \tau_2$  phases) was clearly visible between the former two. A further increase of the holding time to 40h lead to more homogenized reaction layers in term of Al, Fe and Si content. Also the  $\tau_{1-9}$  phases found within the  $\eta$  ( $\text{Al}_5\text{Fe}_2$ ) were observed to gather at the outer part and form a new, fourth, reaction layer. As in the work described earlier, Kirkendall voids were present at the interface after an extended heat treatment (Zhe et al., 2011).

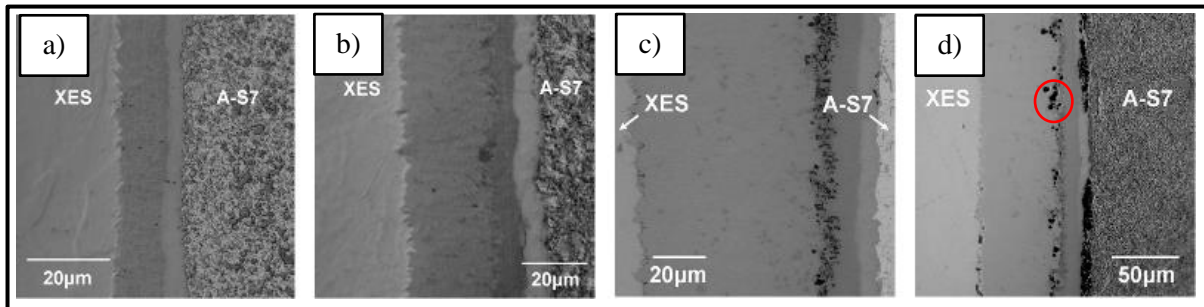


Figure 2.10. Scanning electron microscope image of the interface of XES (cold rolled low carbon steel) and an AS7 ( $\text{AlSi7Mg0.3}$ ) alloy after: (a) 3h; (b) 15h; (c) 72h; and (d) 160h. Kirkendall voids (circled) are present after the long term heat treatment (Zhe et al., 2011)

### 2.1.2.2: Aluminium/Copper compound casting

To investigate the diffusion behaviour at the interface of an Al/Cu couple, Tanaka, Kajihara, and Watanabe (2007) fabricated a couple out of commercially pure metals. The copper was separately annealed in a vacuum at  $900^\circ\text{C}$  for 2h and mechanically polished with grit 4000. Both metals were then encapsulated together in a vacuum and exothermically heated for 30mins at temperatures between  $700$  and  $800^\circ\text{C}$ . This temperature range is above the liquidus temperature of aluminium but below that of copper. Observing the microstructure under an SEM revealed three diffusion layers within the interface of the couple, as seen in figure 2.11(a). It was established that the growth rate of each diffusion layer is governed by different diffusion mechanisms. Hence the thickness of each layer is a differing function of annealing time and temperature (Tanaka, Kajihara, and Watanabe, 2007). Divandari and Vahid Golpayegani (2009) investigated the interface of an A356 alloy and pure copper using lost foam casting. For this purpose, copper wires were cleaned with alcohol and inserted into a polystyrene structure. The copper wires used had diameters of 0.4, 0.8 and 1.2 mm and the pouring temperature of the aluminium melt was  $730^\circ\text{C}$ . SEM and optical microscope (OM) were used for characterisation of the microstructure of the interface. Copper-rich phases were discovered along with a number of other phases such as the  $\delta$  phase,  $\text{AlCu}$  and  $\text{Al}_2\text{Cu}$ . Also silicon particles and intermetallic phases containing iron were found in the material bond. It was discovered that the material bond consists of two different

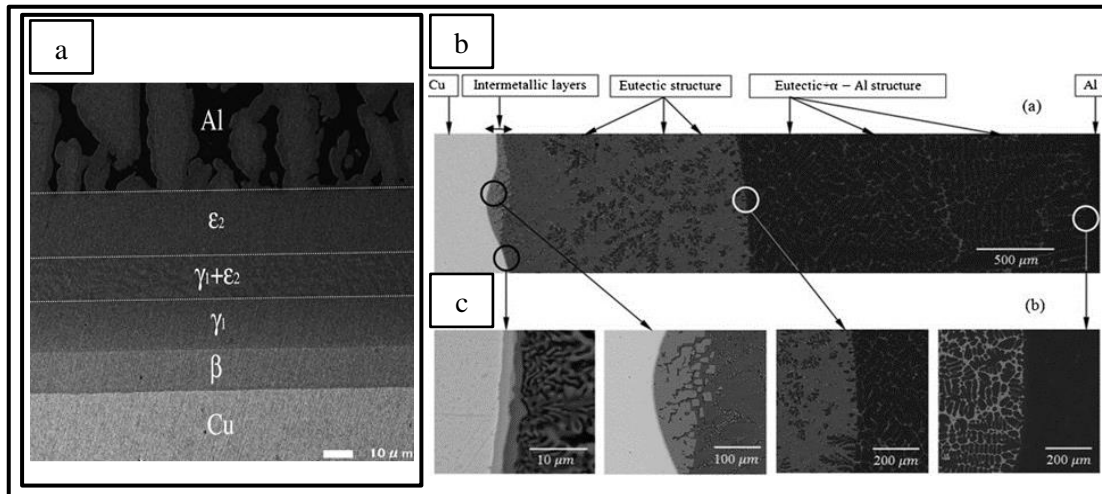


Figure 2.11. Micrographs of the material bond in Al/Cu compound castings: (a) interface of a pure Al/Cu couple after heat treatment according to Tanaka, Kajihara, and Watanabe; (b) interface of a pure Al/Cu couple after casting according to Zare, Divandari, and Arabi; and (c) interface of an Al/Cu couple in greater detail according to Zare, Divandari, and Arabi

(Tanaka, Kajihara, and Watanabe, 2007; Zare, Divandari, and Arabi, 2013).

zones; the cooling affected zone and the composition affected zone. The cooling affected zone consists of precipitated silicon particles due to the cooling effect of the wire. Areas where the melt partially or completely melted the wire and subsequently formed a number of phases are classified as composition affected zones (Divandari and Vahid Golpayegani, 2009). Following up on this research, Zare, Divandari, and Arabi (2013) manufactured an Al/Cu compound using pure alloys that were sand-cast. The copper specimens were ground to grit 1500 and cleaned with acetic acid before being placed in the sand mould and overcast with aluminium at 700°C. The microstructure was observed using SEM and energy-dispersive X-ray spectroscopy (EDS). The resulting interface, as shown in figure 2.11, contained different phases and numbers of reaction layers in the material bond compared with those observed by Tanaka, Kajihara, and Watanabe. The differing composition of the interface can be attributed to the different production process of each couple. Due to the intermetallic phases, a strong increase in microhardness was detected directly at the interface (Zare, Divandari, and Arabi, 2013).

### 2.1.2.3. Iron/Magnesium compound casting

Iron and pure magnesium cannot form a chemical compound and their solubility in each other is very low (Von Goldbeck, 1982). Therefore iron-based substrates display significant chemical inertness to pure liquid magnesium (Roberts, 1960). However, researchers such as Pierre have shown that the chemical inertness can be altered by adding trace amounts (as low as 0.02at% depending on the element) of alloying metals to the magnesium. So far this has been observed for aluminium (Viala et al., 1999), silicon (Pierre et al., 2002), manganese (Pierre et al., 2003) and zirconium (Pierre et al., 2001). The experiments were conducted using an experimental horizontal tubular furnace pictured in figure 2.12. The magnesium alloy was deposited around the iron-based substrate and then heated in an argon

atmosphere at 727°C (1000K) for up to 65h. To prevent excessive evaporation of the magnesium, additional magnesium powder was placed in the furnace. X-ray powder diffraction (XRD), electron probe microanalysis (EPMA), OM and SEM were used to characterise the samples. The same experimental setup was used to investigate the influence of adding zinc to the magnesium. Despite the fact that zinc can form an  $\alpha$ -Fe solid solution with iron at 727°C (1000K), no traces of zinc were found in the material bond. Instead, the interface was identical to the one created with a zinc-free melt, and consisted of an Fe-rich  $\alpha$ -Fe (Al, Si) solid solution. Aluminium and silicon are common impurities in magnesium melts. Table 2.2 gives an overview of the conducted research, the phases found and morphology of the interface (Viala et al., 1999). Characterisation of the interface in any compound casting is a time-consuming and extensive process. To reduce the time and resources needed for such a characterisation, Sacerdote-Peronnet et al. (2007) tried to relate the load-displacement curve obtained from push-out testing with the quality (i.e. soundness and mechanical strength) of the reaction zone at the interface. For this purpose, a number of cylindrical Fe/Mg compound castings were produced via hot dipping mild steel (0.2% carbon) rods in liquid magnesium melts (AZ61 & AZ101) for varying times. The steel rods were ground to a 3 $\mu$ m surface finish to remove the oxide layer. Once the melt was heated up to the designated temperature (650-750°C) the steel rods were immersed for 1-5min. Short immersion times (30-100s) and low temperatures (630-650°C) resulted in no interfacial reaction. A 0.5-2 $\mu$ m thick oxide layer was found to prevent any contact between the steel and magnesium. It was deemed unlikely that the found oxide layer was a result of a surface reaction between the magnesium and iron oxide, as the steel rod's oxide layer was removed shortly before immersion. Even though argon was used as a cover gas, the remaining atmospheric oxygen (estimated to be around 0.1ppm), was established to be the most likely source. In addition to the oxide layer, large repeating cracks and gaps were present at the interface. These were attributed to typical shrinkage upon solidification and the highly differing thermal expansion coefficients of magnesium ( $78 \times 10^{-6} / \text{K}$ ) and steel ( $\sim 33-39 \times 10^{-6} / \text{K}$ ).

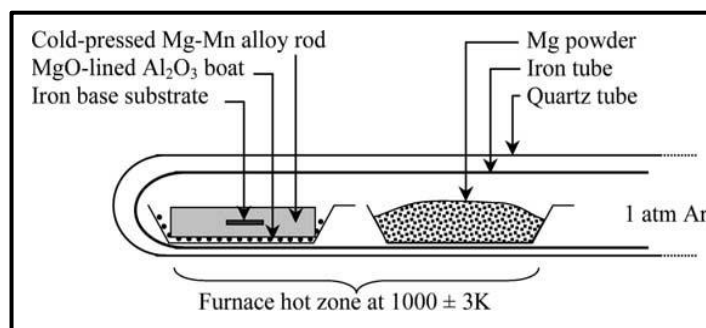


Figure 2.12. Schematic of a horizontal tubular furnace used by Pierre et al. (2003).

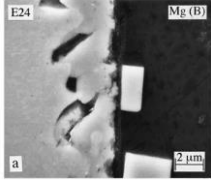
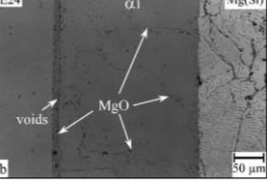
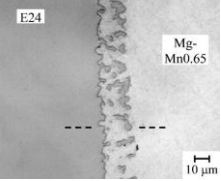
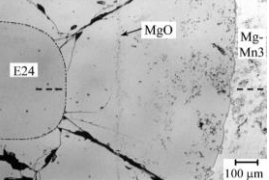
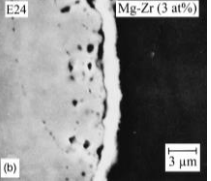
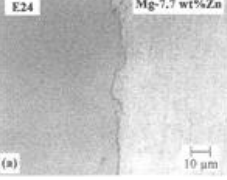
Added element	Amount [at. %]	Phases in the material bond	Growth mechanisms	Appearance of the material bond
<b>Aluminium</b> (Viala et al., 1999)	0.02	$\alpha$ -Fe(Al) Fe <sub>2</sub> (Al,Mg)C	<ul style="list-style-type: none"> <li>• Solid state diffusion</li> <li>• Dissolution-precipitation processes</li> </ul>	
<b>Silicon</b> (Pierre et al., 2002)	0.025	$\alpha$ -Fe(Si)	<ul style="list-style-type: none"> <li>• Solid state diffusion</li> </ul>	
	>0.045	$\alpha$ 1-Fe <sub>3</sub> Si	<ul style="list-style-type: none"> <li>• Solid state diffusion</li> </ul>	
<b>Manganese</b> (Pierre et al., 2003)	0.65 (half saturated)	$\alpha$ -Fe(Mn) $\gamma$ (Fe, Mn)	<ul style="list-style-type: none"> <li>• Solid state diffusion</li> </ul>	
	3 (oversaturated)	$\beta$ -Mn(Fe)		
<b>Zirconium</b> (Pierre et al., 2001)	0.10-3	ZrC <sub>x</sub> Fe <sub>2</sub> Zr	<ul style="list-style-type: none"> <li>• Dissolution-precipitation</li> <li>• Solid state diffusion</li> </ul>	
<b>Zinc</b> (Pierre, 1999)	7.7	$\alpha$ -Fe(Al, Si) Fe <sub>2</sub> (Al, Mg)C	<ul style="list-style-type: none"> <li>• Solid state diffusion</li> <li>• Dissolution-precipitation processes</li> </ul>	

Table 2.2: Phases and microstructure of the material bond of Fe/Mg compound castings in dependence of an added ternary element.

### 2.1.3: Aluminium/Magnesium compound casting

Al/Mg compound castings offer, in comparison to conventional all-steel structures, the greatest possible weight savings. Despite these potential benefits, however, Al/Mg compound castings have only received interest from researchers in recent years. So far, research has focused mainly on the characterisation of the compound casting of pure metals using lab-scale equipment (Hajjari et al., 2011; Xu et al., 2014; Emami et al., 2013a; Papis, Löffler, and Uggowitzer, 2009). As such, only limited knowledge about Al/Mg compound castings with regard to any industrial application exists. Without any alloying elements, both magnesium and aluminium display a similar melting point (660.3°C for aluminium and 650.0°C for magnesium), thus making it theoretically possible for both metals to be either the molten or solid part in the compound casting process. However, experimental trials with pure metals revealed that when the aluminium melt is cast around a magnesium insert a gap forms at the interface of the two metals (Hajjari et al., 2011). This gap was not observed when casting magnesium around an aluminium insert. Figure 2.13 displays the interfaces for both setups. According to the authors, the gap is due to a difference in the thermal expansion coefficients for aluminium ( $24 \times 10^{-6} \text{K}^{-1}$ ) and magnesium ( $25.5 \times 10^{-6} \text{K}^{-1}$ ), as well as aluminium's more stable oxide skin. As can be seen in figure 2.13(a) the gap was present in all specimens where aluminium was cast around a magnesium insert; further research into (liquid) aluminium/(solid) magnesium compound castings was not conducted (Hajjari et al., 2011).

Similarly to Al/Al compound castings, the aluminium's intrinsic oxide layer was thought to impede any interfacial reaction between the aluminium and the magnesium. Accordingly, researchers have used similar means (e.g. zincate process, zinc-galvanising) to remove aluminium's oxide layer and prevent a new one from forming (Xu et al., 2014). Besides zinc-based coatings, researchers have also investigated manganese as a possible coating, as it was thought, due to the chemical inertness of

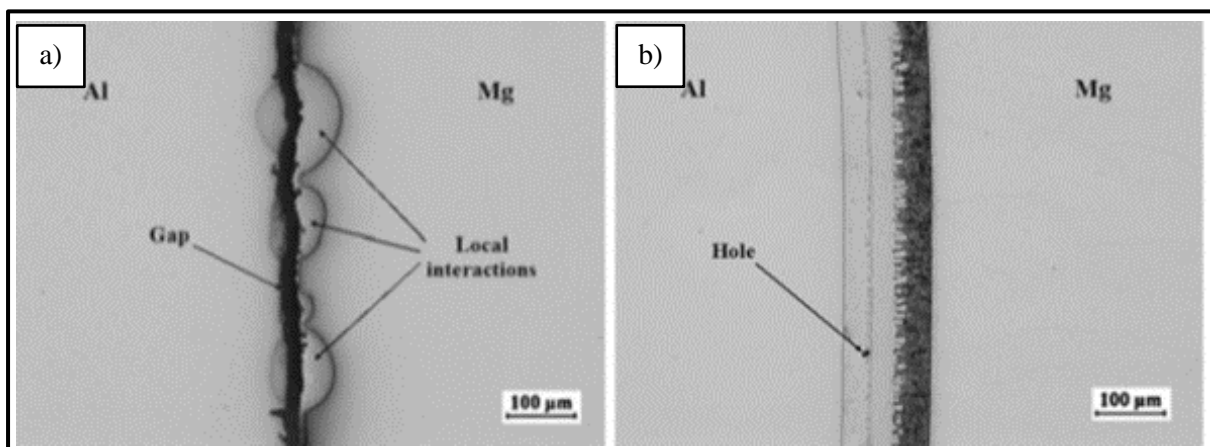


Figure 2.13. (a) Interface of an Al/Mg compound casting with a magnesium insert. (b) Material bond of an Al/Mg compound casting with an aluminium insert. The gap was reported to be always present when using magnesium inserts (Hajjari et al., 2011).

manganese and magnesium, to prevent the forming of brittle intermetallic phases (Papis, Löffler, and Uggowitzer, 2009). Using a horizontal furnace, researchers successfully created pure Al/Mg as well as A390/AM60 compound castings (A390 is a hypereutectic AlSiCu alloy) (Xu et al., 2014; Zhang, Chen, and Luo, 2014a, 2014b). As with Al/Al compound castings a zinc coating improved the material bonding between the aluminium and magnesium, leading to improved wettability and bonding strength. The impact of a zinc coating on wettability can be seen in figure 2.14. An alternative, coating free, surface treatment to promote material bonding and wettability was developed for AlSn1 alloys and aluminium alloys containing low amounts of gallium (0.08wt%) (Zhang, Chen, and Luo, 2014a). It includes electropolishing and subsequent anodising of the aluminium insert and was termed ‘electropolishing+anodising’. This surface treatment results in the partial puncturing of the aluminium’s oxide film, thereby increasing wettability with the molten magnesium. It is mainly caused by the fact that aluminium oxides are preferably formed over selenium or gallium oxides (due to the lower Gibbs free energy of the formation of  $\text{Al}_2\text{O}_3$  compared to  $\text{SnO}_2$  or  $\text{Ga}_2\text{O}_3$ ). Eventually this leads to an enrichment of selenium or gallium adjacent to the  $\text{Al}_2\text{O}_3$  layer. Upon further oxidisation the selenium or gallium will oxidise, forming honeycomb-like voids in the process (Xu et al., 2014; Zhang, Chen, and Luo, 2014a, 2014b). These voids are caused by the differing Pilling-Bedworth ratios (PBR: the ratio of the volume of the elementary cell of a metal and its oxide) between  $\text{Al}_2\text{O}_3$  and  $\text{SnO}_2$  or  $\text{Ga}_2\text{O}_3$ . The PBR of  $\text{SnO}_2$  is 24% and that of  $\text{Ga}_2\text{O}_3$  26% smaller than that of  $\text{Al}_2\text{O}_3$ . The smaller volume of  $\text{SnO}_2$  or  $\text{Ga}_2\text{O}_3$  causes the voids to form. During the anodising these voids will eventually create the punctures in the oxide layer. A schematic of the processes responsible for the forming of the punctures in the oxide layer is displayed in figure 2.14. Considering gallium’s detrimental effect on the mechanical properties of aluminium, it is questionable if Al/Mg compound castings containing gallium are viable for any industrial applications. Researchers using larger experimental setups successfully produced an Al/Mg compound casting couple without the use of a coating (Emami et al., 2013b; Hajjari et al., 2011; Emami et al., 2013a). Provided the melt possesses sufficient thermal energy, the aluminium underneath the oxide layer will start melting, washing out the oxide layer into the melt and thus allowing a chemical reaction between the aluminium insert and magnesium melt to occur. This however also means that the oxide layer is still present in some form in the compound casting. Characterisation of the interface of the compound castings via SEM revealed its typical three-layered appearance (Emami et al., 2013b; Hajjari et al., 2011; Emami et al., 2013a):

1. Aluminium-rich layer of  $\text{Al}_3\text{Mg}_2$  ( $\beta$ );
2. Magnesium-rich layer of  $\text{Al}_{12}\text{Mg}_{17}$  ( $\gamma$ );
3. Magnesium-rich layer of  $\text{Al}_{12}\text{Mg}_{17}$  ( $\gamma$ ) plus eutectic magnesium ( $\delta$ ).

Table 2.3 in section 2.2.1 lists the composition ranges for the two compounds  $\beta$  and  $\gamma$ . A typical interface of an Al/Mg compound casting can be seen in figure 2.13(b). The appearance remains very similar, independent of the alloys used or casting process, with the main difference being the thickness of each

layer. This has been verified so far for: pure aluminium and magnesium (Hajjari et al., 2011); AlGa (Zhang, Chen, and Luo, 2014a); AlSn (Zhang, Chen, and Luo, 2014b); Al413 (Hajjari et al., 2012); A390 (Xu et al., 2014); and AM60 (Xu et al., 2014); as well as sand-casting (Emami et al., 2013a) and lost foam casting (Emami et al., 2013b). When using silicon containing aluminium alloys, the formation of  $Mg_2Si$  particles has been observed (Dietrich et al., 2011). These particles are formed upon contact of the magnesium melt and the silicon phase within the aluminium alloy and then dispersed throughout the interface. Additionally, when casting under atmosphere rather than vacuum, an accumulation of magnesium oxide films within the  $\gamma+\delta$  layer has been reported. These oxides weaken the strength of the interface and are a possible spot for crack initiation (Hajjari et al., 2012). Depending on the casting process used, solidification related shrinkage and pores may be present in the interface as well.

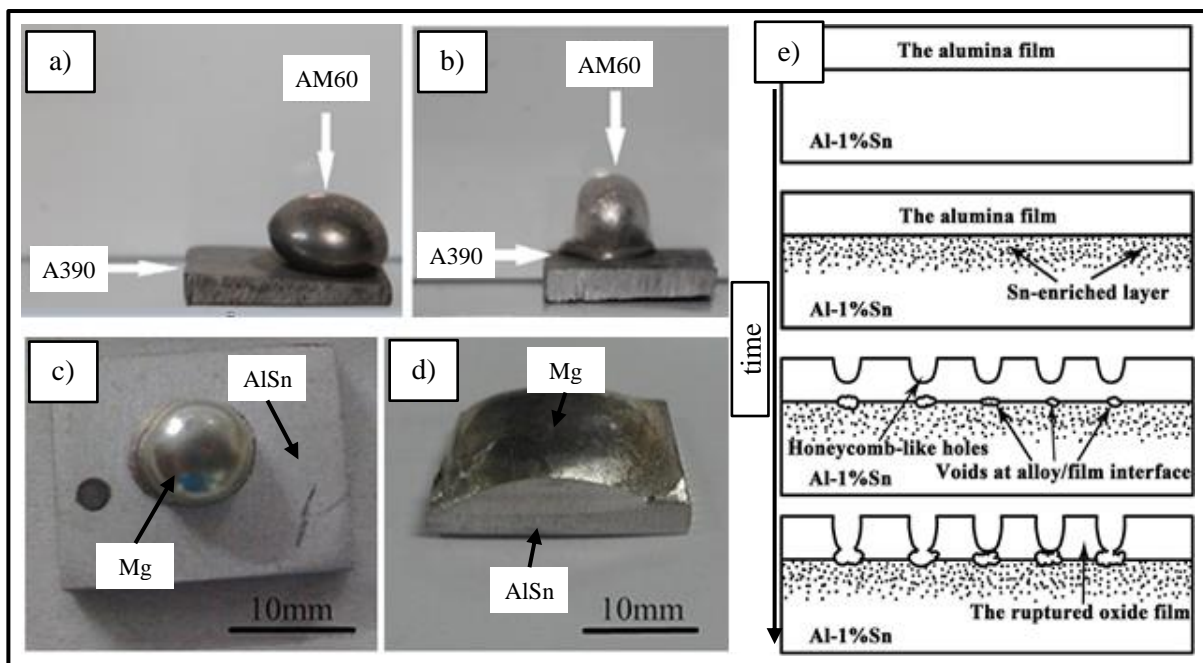


Figure 2.14. (a) Wetting behaviours of an A390 and AM60 alloy without surface treatment (b) wetting behaviours of an A390 and AM60 alloy with a 'zincate + galvanising' treatment (c) wetting behaviour of an AlSn alloy with pure magnesium without surface treatment (d) wetting behaviour of an AlSn alloy with pure magnesium with 'electropolishing + anodising' treatment (e) schematic display of the formation of the punctured oxide layer during 'electropolishing + anodising' (Xu et al., 2014; Zhang, Chen, and Luo, 2014a, 2014b).

As the interface predominantly consists of the intermetallic compounds, its thickness and morphology is therefore controlled by the growth kinetics of the  $\beta$  and  $\gamma$  intermetallic compounds. Researchers concluded that a dependency between the strength of the interface and the heat balance, and thus solidification and cooling rate of the casting, exists. Accordingly, it was reported that preheating and varying the melt-insert volume ratio enabled the interfacial strength to be manipulated and controlled (Emami et al., 2013a; Xu et al., 2014). This is not surprising, as growth of the intermetallic compounds is mainly temperature controlled (Liu, Chen, and Yang, 2015). A detailed description of growth kinetics

and mechanisms for these intermetallic compounds can be found later in section 2.2.7. Moreover, shear strength was identified as a suitable parameter to characterise the interface of compound castings, as a microscopical inspection does not reveal its mechanical properties (Sacerdote-Peronnet et al., 2007). A relationship between interfacial strength and interface thickness is described in the literature (Hajjari et al., 2011; Emami et al., 2013b). According to these data, a thicker interface causes a decline in interfacial strength. This relationship is displayed in figure 2.15. It is known that in a thicker material bond, the  $\beta(\text{Al}_3\text{Mg}_2)$  intermetallic compound is the dominating phase within the material bond. There is an indication that the  $\beta$  phase, as will be detailed in section 2.2.3, displays unfavourable mechanical properties (compared to the  $\gamma$  phase), resulting in the mechanical weakening of the bond.

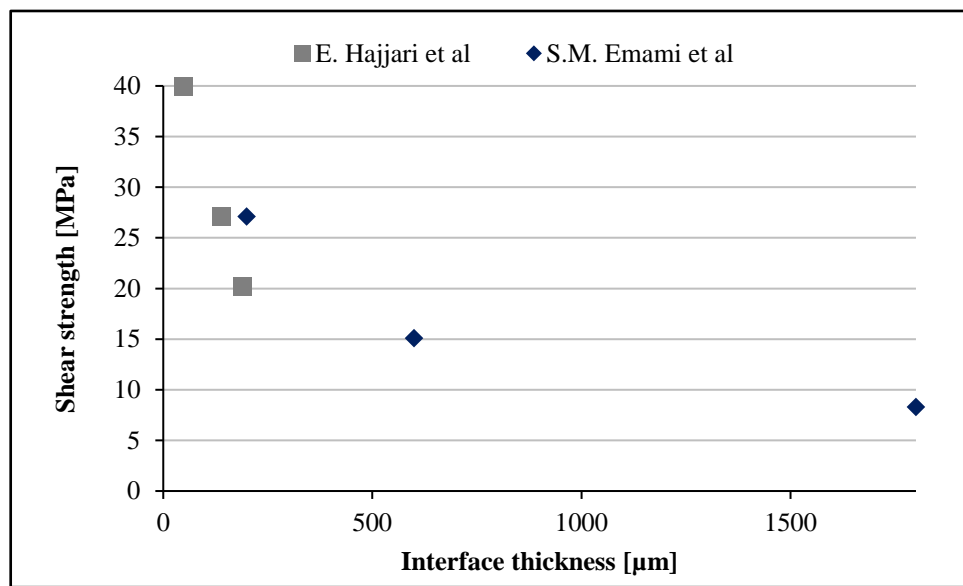


Figure 2.15. Relation between interface thickness and shear strength of commercially pure Al/Mg compound castings. Data from two different publications are displayed. Each data point represents one measurement (Emami et al., 2013b; Hajjari et al., 2011).



#### 2.1.4: Alternative Aluminium/Magnesium joining methods

Due to the technical relevance of both aluminium and magnesium, other joining methods besides compound castings were covered by researchers. In the following section a small overview of recent research, concerning the joining of aluminium and magnesium, is given. The main joining methods for aluminium and magnesium, besides compound casting, covered by the literature, are: roll-bonding (Hsieh, Chen, and Wu, 2013; Ruppert et al., 2015); welding (Benfer et al., 2016); and forging (Kittner et al., 2015). As these processes and techniques differ significantly from casting; only information relevant to Al/Mg compound castings is given.

Accumulative roll bonding of a commercial AZ31 alloy and 5052 aluminium alloy sheets at 400°C resulted in the formation of two intermetallic compounds  $\beta$  and  $\gamma$ . Under the experimental conditions used, the  $\beta$  phase was reported to be thicker. Deep drawing of the roll bonded sheets at 150°C resulted in the fracture of the material bond adjacent to the aluminium. The fracture was attributed to the brittle  $\beta$  phase. Fewer fractures in the sheets were observed after increasing the temperature to 200°C during deep drawing. At this elevated temperature the  $\gamma$  phase shows increased deformability and softness (Li et al., 2015). The presence of the two intermetallic compounds  $\beta$  and  $\gamma$  was reported after cold rolling and annealing at temperatures ranging from 200-400°C of a commercially pure Al and Mg<sub>0.2</sub>Al<sub>1.75</sub>Mn<sub>0.75</sub>Ce alloy. Yield strength of the roll bonded sheets was found to decrease with annealing temperature while breaking elongation was observed to increase. The thickness of the interface was observed to increase linearly with the square root of the annealing time. However, no distinction in the thicknesses of the two phases  $\beta$  and  $\gamma$  was made (Macwan et al., 2013). Chen et al. (2018) hot rolled explosion-welded AZ31/AA6061 alloy sheets. After rolling, the bonded sheets were annealed for varying amounts of time. The mechanical properties of the bond between the two alloys were identified to be dependent on annealing temperature, and degraded when temperatures above 200°C were used. Similarly, the thickness of the material bond increased with annealing temperature and time, but no information about phases present in the bond were given (Chen et al., 2018). Increasing the reduction ratio during roll bonding of Al/Mg alloys resulted in an increase of the material bond. Growth of the interface was reported to be in the direction of the magnesium alloy (Zhang et al., 2011).

Joining aluminium and magnesium at room temperature using high pressure torsion (HPT) (Qiao et al., 2016) showed that only the magnesium rich compound  $\gamma$  is formed. Diffusional mobility of both elements is inhibited and thus only a thin layer of  $\gamma$  was found at the interface. Considerations of the interfacial energies of the intermetallic revealed that below a critical thickness of the intermetallic layer only one phase is thermodynamically stable (Qiao et al., 2016). These findings were confirmed by research conducted by Han et al. (2017). A commercially pure aluminium alloy was joined with an ZK60 magnesium alloy using HPT. The joined specimens were then annealed. Before annealing, only a negligible amount of the  $\beta$  phase was detected within the specimens. Specimens that were annealed

at 300°C for 1h contained a significant amount of the  $\beta$  phase. The annealing was also found to decrease the hardness of the intermetallic phases (Han et al., 2017).

Benfer et al. (2016) confirmed the existence of the two intermetallic compounds  $\beta$  and  $\gamma$  at the interface of a friction stir welded AZ80 magnesium/AC-48000 aluminium couple. Using ultrasound during welding resulted in the suppression of the growth of the  $\beta$  phase. Moreover, the use of ultrasound promoted growth of the  $\gamma$  phase. Its thickness increased from 2 $\mu$ m (when no ultrasound was applied) to 50 $\mu$ m (when ultrasound was applied). It was shown that an increase in tensile strength of 25% was possible when applying ultrasound during friction stir welding. While no details about the suppression of the  $\beta$  phase were given, the authors stated that the phase was mechanically shattered by using ultrasound (Benfer et al., 2016). However, the mechanical strength of the interface in ultrasonic spot welded Al/Mg was found to be lower than in Al/Al sheets procured under the same conditions (Macwan et al., 2014).

Another joining method used to successfully join aluminium and magnesium was electromagnetic impact welding. Kore et al. (2009) joined an AZ31 magnesium alloy with a 3003 aluminium alloy sheet using this technique. The joined couples showed complete continuity at the interface; however, no distinct material bond was detected. Analysis of the interface revealed no sign of intermetallic phases. The exact bonding mechanism between the two sheets remains unclear. The lack of chemical reaction on a macroscopic level indicates that the two sheets were bonded mechanically. However, the possibility of reaction on a smaller scale was not ruled out by the researchers (Kore et al., 2009).

The hydro-static extrusion and subsequent forging of Al/Mg compounds has been studied by Kittner et al. (2015). The interface of the forged Al/Mg part consisted, in agreement with the compound casting process, of the two intermetallic phases  $\beta$  and  $\gamma$ . Total thickness ranged between 25 and 35 $\mu$ m, with the  $\beta$  phase being visible thicker. However, exact thicknesses of the two phases were not reported. Thinner interfaces showed a higher resistance to load before failing. Fractures at the interface were observed to start at the border between the aluminium and the  $\beta$  phase, and then from there to propagate perpendicularly across the whole interface. As the extrusion and forging process causes continuous material flow at the interface, a cohesive bond was achieved despite the fractures (Kittner et al., 2015). A similar thickness and make-up of the interface of an 6082 aluminium alloy and an AZ31 magnesium alloy was reported by Förster et al. (2017). Mróz et al. (2018) investigated the forging of an explosion welded AZ31/1050 aluminium alloy couple. They reported the formation of an intermetallic layer at the interface, but did not provide a detailed description of it. It was concluded that such produced parts are able to meet the requirements in terms of mechanical properties and forgeability. Temperature distribution and control was judged vital for the production of sound parts (Mróz et al., 2018).

## 2.2: Metallurgy of the Al-Mg system

### 2.2.1: Aluminium-Magnesium phase diagram

The Al-Mg binary phase diagram is of great importance, as aluminium is added to many magnesium alloys with technical relevance, and vice versa. As a consequence, the Al-Mg phase diagram is well researched, with the classical Al-Mg phase diagram displayed in figure 2.16(a) below. Thermodynamic calculations were used to obtain the phase boundaries, with the exception of the  $\beta$  phase. Even though  $\beta$  phase is known to exist over a wide range of compositions, a line compound was used in its calculation. More recently Aljarrah (2008) calculated an optimised Al-Mg phase diagram using experimental data from the literature. This optimised phase diagram is shown in figure 2.16(b).

Most notably, this diagram is missing  $\beta$  phase, which was attributed to the lack of experimental data existing in the literature about the phase boundaries, as well as the assumption that the  $\beta$  phase is not actually limited to a single phase field (Aljarrah, 2008). However, this phase diagram is congruent with experimental data and is thus considered to be accurate (Mezbahul-Islam, Mostafa, and Medraj, 2014).

In the Al-Mg system the following five equilibrium phases exist:

1. Mg solid solution;
2. Al solid solution;
3.  $\beta$  ( $\text{Al}_3\text{Mg}_2$ );
4.  $\gamma$  ( $\text{Al}_{12}\text{Mg}_{17}$ );
5.  $\epsilon$  or R ( $\text{Al}_{30}\text{Mg}_{23}$ ).

Table 2.3 lists all equilibrium phases and their corresponding crystal structures, while table 2.4 lists all special points of the Al-Mg system. In our study, data from Massalski regarding temperatures and

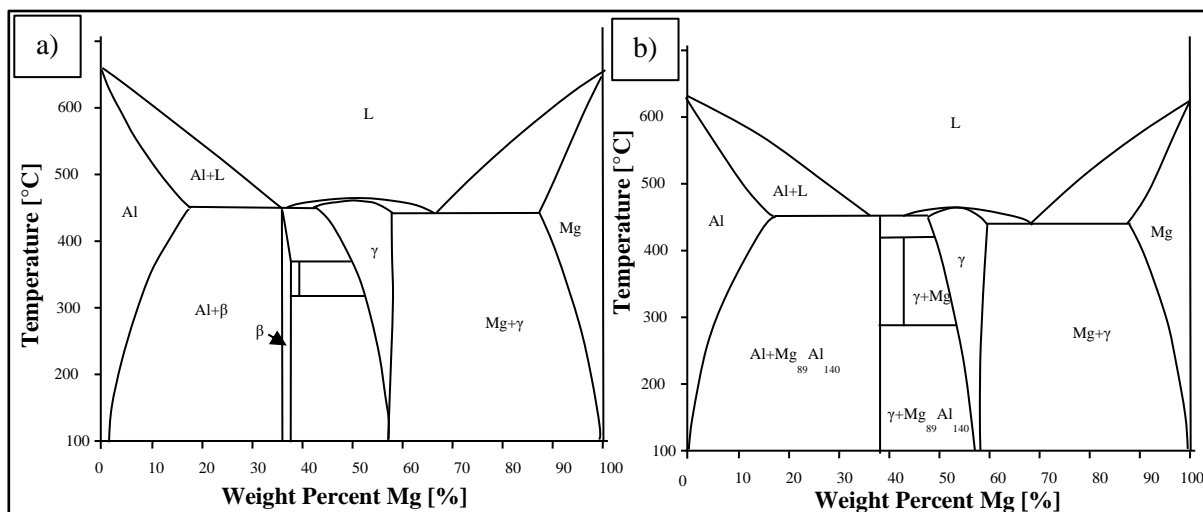


Figure 2.16. (a) Al-Mg phase diagram according to Massalski (b) Optimised Al-Mg phase diagram according to Aljarrah (Aljarrah, 2008; Massalski, 1990).

chemical compositions are used. Massalski's data were chosen as they are commonly used and considered accurate enough for the scope of this work. The potentially higher accuracy of Aljarrah's data is considered not to be relevant in the context of this study. High quenching rates may lead to the formation of additional metastable phases. A new phase, denoted  $\phi$ , was found after quenching Al-Mg alloys containing 25-55at% Mg. Similarly, Suryanarayana, Tiwari, and Anantharaman (1978) discovered a metastable solid solution in a 30at% Mg alloy after rapid cooling. This phase had the approximate stoichiometry of  $\text{Al}_2\text{Mg}$ . Murray (1982) gives the maximum solubility of aluminium in the Mg solid solution as 11.8at% Al at 437°C (710K), and for magnesium in the Al solid solution as 18.9at% Mg at 723 K. Both metals possess similar atomic radii (125pm for aluminium and 150pm for magnesium (Slater, 1964)), which suggests good solubility in the solid phase (Mezbahul-Islam, Mostafa, and Medraj, 2014).

Phase	Approximate chemical composition (at% Al)	Crystal structure	Pearson symbol
Al solid solution	81.4-100	FCC	cF4
Mg solid solution	0-12.9	HCP	hp2
$\beta$ ( $\text{Al}_3\text{Mg}_2$ )	59.7-61.5	Complex FCC	cF1168
$\gamma$ ( $\text{Al}_{12}\text{Mg}_{17}$ )	39.5-55.0	$\alpha\text{Mn}$	cI58
$\epsilon$ or R ( $\text{Al}_{30}\text{Mg}_{23}$ )	58.0		hR53

Table 2.3: Equilibrium phases, their corresponding chemical compositions and crystal structures (Massalski, 1990; Singh et al., 2003).

Reaction	Composition (at% Mg)	Temperature [°C]	Reaction type
$\text{L} \leftrightarrow \text{Al} + \beta$	38	450	Eutectoid
$\text{L} \leftrightarrow \gamma + \text{Mg}$	69	437	Eutectoid
$\text{L} \leftrightarrow \beta + \gamma$	41.2	450	Eutectoid
$\beta + \gamma \leftrightarrow \text{R}$	40,3	370	Peritectoid
$\text{R} \leftrightarrow \beta + \gamma$	42	320	Eutectoid
$\text{L} \leftrightarrow \gamma$	42.8-43.4	455	Congruent
$\text{L} \leftrightarrow \beta$	38.5	451	Congruent
$\text{L} \leftrightarrow \text{Al}$	0	660	Melting
$\text{L} \leftrightarrow \text{Mg}$	100	650	Melting

Table 2.4: Special points of the Al-Mg system according to Massalski (1990).

### 2.2.2: Intermetallic compounds in the Al-Mg system

Usually intermetallic compounds are defined as ‘solid phases containing two or more metallic elements, with optionally one or more non-metallic elements, whose crystal structure differs from that of the other constituents’ (Schulze, 1967). They are a unique class of materials as they display properties associated with metals (generally softer and more ductile) and ceramics (generally harder and more brittle). These properties are due to the presence of metallic as well as covalent bonds, dependent on the constituent metals, as opposed to only metallic bonds (as in metals) or only covalent and ionic bonds (as in ceramics) (National Research Council, 1997). However, it is known that intermetallic compound layers in a metal matrix tend to fail before the metal, and are thus the place of origin for crack initiation, propagation and eventual complete failure of the component (Rawers and Perry, 1996; Zhou et al., 2016). For this reason, intermetallic compounds are generally unwanted in any structure in the transportation industry. In fact, brittle intermetallic Al-Mg phases are a reason why joined aluminium-magnesium parts, despite their weight-saving potential, have not seen extensive use in industry. As mentioned earlier, there are three intermetallic phases in the binary Al-Mg system; the magnesium-rich  $\gamma$ (Al<sub>12</sub>Mg<sub>17</sub>), the aluminium-rich  $\beta$ (Al<sub>3</sub>Mg<sub>2</sub>) and the  $\epsilon$ (Al<sub>30</sub>Mg<sub>23</sub>) phase. While the  $\epsilon$ (Al<sub>30</sub>Mg<sub>23</sub>) phase was detected experimentally (Su et al., 1997), several researchers working on Al-Mg compounds did not observe the  $\epsilon$  phase in their experiments (Xiao and Wang, 2015; Hajjari et al., 2012; Cao et al., 2013; Brennan et al., 2012). Therefore, it is assumed that the  $\epsilon$  phase does not play any significant role in the bonding of Al-Mg, even though the exact reason for its absence remains unknown. To better understand the growth and formation of Al-Mg intermetallic phases it is important first to understand the growth kinetics of the involved  $\beta$  &  $\gamma$  phases. In Al/Mg compound castings intermetallic compounds are formed through two possible routes:

1. Localised melting of the surface of the aluminium and subsequent reaction of both metals upon solidification (Cao et al., 2013);
2. Solid state diffusion (Brennan et al., 2012).

A direct link between temperature and the formation of Al-Mg intermetallic compounds is described in the literature, where researchers are in good accordance with each other. Researchers have reported an interface consisting of the  $\beta$ -Al<sub>3</sub>Mg<sub>2</sub> and  $\gamma$ -Al<sub>12</sub>Mg<sub>17</sub> phases. While the chemical composition of these phases were quite similar for a range of different Al and Mg alloys and experimental setups, the morphology and thickness of the interface varied with each experimental setup used. Welded (Dietrich et al., 2011) and heat treated (Brennan et al., 2012) specimens displayed a two-layered interface, while specimens produced with compound casting had a third  $\beta$ (Al<sub>3</sub>Mg<sub>2</sub>)+ $\delta$  phase layer (Hajjari et al., 2011). It is also noteworthy that in the presence of silicon, precipitations consisting of Mg<sub>2</sub>Si can form between the  $\alpha$ (Al) and  $\beta$ (Al<sub>3</sub>Mg<sub>2</sub>) layer (Dietrich et al., 2011). An overview of the interfaces acquired through different experiments can be seen in figure 2.17.

Considering the importance of (the absence of) intermetallic phases, in advanced structures for the transportation industry, there is little research existing on how to influence these phases actively. Two main things are known so far.

1. Common alloying of magnesium and aluminium do not significantly alter the formation or morphology of intermetallic phases. This has been observed for the following alloys:
  - AlSi1MgMn (Dietrich et al., 2011);
  - AZ31 (Dietrich et al., 2011);
  - AlZn5.5MgCu (Cao et al., 2013).
2. In the presence of silicon,  $Mg_2Si$  is formed within the material bond (Dietrich et al., 2011).

Moreover, it seems that the formation of  $\beta$  &  $\gamma$  Al-Mg intermetallic compounds is inherent in all types of joining, provided aluminium and magnesium come into direct contact with each other. Coating one of the constituents with a material which has a higher melting point, such as manganese, may prevent direct contact of the aluminium and magnesium during casting. However, it is unclear if this approach yields any advantages, as the Al-Mg intermetallic compounds are simply replaced by Al-Mn compounds (Papis, Löffler, and Uggowitzer, 2009). Magnesium and manganese do not form any intermetallic compounds and display only a very limited solubility in each other (Gröbner et al., 2005). Thus, it is questionable if an Mg-Mn layer will display sufficient beneficial mechanical properties. A zinc coating, on the other hand, does not alter the interfacial reaction significantly, as zinc has a relatively low melting point and is therefore usually completely dissolved during casting. Coatings may be a suitable method to alter the interfacial reaction and prevent the formation of the Al-Mg intermetallic compounds. In compound castings without a coating, the formation of intermetallic phases is synonymous with interfacial reaction and it is thus analysed with respect to the mechanisms (dissolution, crystallisation and solid state diffusion) governing interfacial reaction.

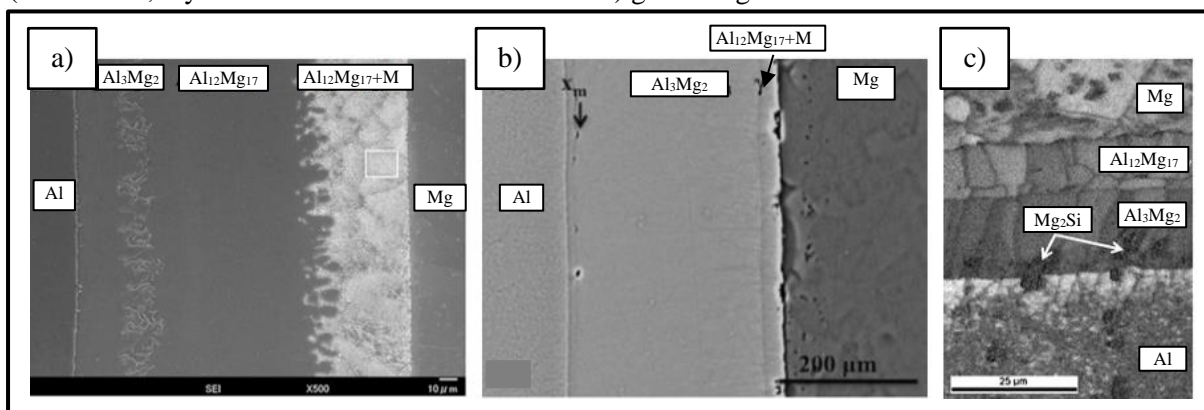


Figure 2.17. The material bonds of Al/Mg compounds: (a) pure Al/Mg compound casting (Hajjari et al., 2011); (b) pure Al/Mg diffusion couple after 720h at 300°C (Brennan et al., 2012); and (c) diffusion welded AlSi1MgMn/AZ31 couple (Dietrich et al., 2011).

### 2.2.3: Mechanical properties of Al-Mg intermetallic compounds

Besides studies of the growth rate of the  $\beta(\text{Al}_3\text{Mg}_2)$  and  $\gamma(\text{Al}_{12}\text{Mg}_{17})$  phases, existing research revealed discrepancies concerning the roles of the two phases with respect to mechanical properties at the interface. Dietrich et al. (2011) reported that cracks primarily occur in the  $\text{Al}_3\text{Mg}_2$  phase and adjacent Al, while Cao et al. (2013) observed that cracks originate in the  $\text{Al}_{12}\text{Mg}_{17}$  phase. These conflicting findings can have various reasons, as the research teams did not use the same experimental setup. This might be an indicator that despite the reaction layers' similar appearance and morphology, alloying elements and processing route might have a significant impact on the intermetallic phases. Theoretical calculations of the mechanical properties of the  $\text{Al}_{12}\text{Mg}_{17}$  phase, using first-principle calculations, identified this phase as a non-brittle phase (Wang et al., 2008). It is known that with increasing interface thickness the interfacial strength decreases. As an increase in interface thickness is associated with the growth of the  $\beta(\text{Al}_3\text{Mg}_2)$  intermetallic compound, the  $\gamma(\text{Al}_{12}\text{Mg}_{17})$  intermetallic compound may be more favourable to the interfacial strength.

### 2.2.4: Coatings

The connection of the aluminium and magnesium is, as explained in section 1.1, of vital importance to the functionality of a compound casting. Hence it is not surprising that many studies have investigated how to improve the reactivity of the aluminium's surface. The application of a coating was considered by many researchers to be the most promising approach as it:

1. protects the surface of the aluminium from re-oxidation after removal of the oxide layer (Papis et al., 2008);
2. facilitates the presence of a material/chemical bond under conditions normally not allowing for such a bond (Rübner et al., 2011);
3. increases wettability (Papis, Löffler, and Uggowitzer, 2009).

Wettability only becomes important when using very small amounts of magnesium melt. Increasing the amount of magnesium results in the partial melting of the aluminium surface and thus nullifying the impact of the aluminium's wettability (Hajjari et al., 2011). So far researchers have investigated both zinc and manganese as coatings (Papis et al., 2008; Rübner et al., 2011; Koerner, Schwankl, and Himmler, 2014; Papis, Löffler, and Uggowitzer, 2010; Zyska et al., 2010). It should also be noted that the overwhelming majority of research concerning coatings has been undertaken using similar metals in compound castings (e.g. Al/Al and Mg/Mg). Research indicates that, besides melt temperature, the thickness of the coating plays an important role in the bonding process. The optimal thickness seems to be dependent on the casting process used. High melt velocities (as present during HPDC) might wash away the coating during casting, while extended exposure to the casting heat causes the evaporation of the coating.

### 2.2.4.1: Zinc-based coatings

Zinc has a melting temperature of  $\sim 420^{\circ}\text{C}$  and its high solubility in aluminium and magnesium makes it well suited to be used as a coating in compound castings (Rübner et al., 2011). There are two main processes, described in the literature, with which aluminium can be coated with a zinc layer.

1. The zincate process or ‘zincating’. The zincate process is based on the nickel plating of aluminium surfaces for electrical applications (Saito, Maegawa, and Homma, 2005; Qi, Chen, and Shao, 2002; Tang and Davenport, 2001; Robertson, Ritchie, and Druskovich, 1995). It can include a pre-treatment (Monteiro et al., 1991). The primary process consists of two parallel chemical reactions; an etching reaction which removes the  $\text{Al}_2\text{O}_3$  layer at the surface, and a redox reaction which deposits a dense zinc layer on the aluminium. The resulting metallic zinc layer was 300-500 nm thick (Papis et al., 2008).
2. Galvanisation. Galvanising is a commonly used industrial process to coat a component surface with a protective zinc layer. A relatively thick ( $>85\mu\text{m}$ ) zinc layer can be obtained via hot dip galvanising, while electrogalvanising is used if a thinner ( $5\text{--}10\mu\text{m}$ ) layer of zinc is needed (Papis et al., 2008; Galvanisers Association, 2016).

It was observed that the zinc layer resulting from the zincate process would, if the coated aluminium part was preheated, evaporate (Papis et al., 2008). To compensate for this, a combination of the zincate process and galvanisation was proposed. A  $<10\mu\text{m}$  thick zinc layer was created, which eventually led to the production of defect-free Al/Al compound castings (Papis et al., 2008). This combination, however, was found to be insufficient to achieve sound material bonding in Al-Al compound castings using HPDC. In some areas the zinc layer was completely washed away during casting, while in areas

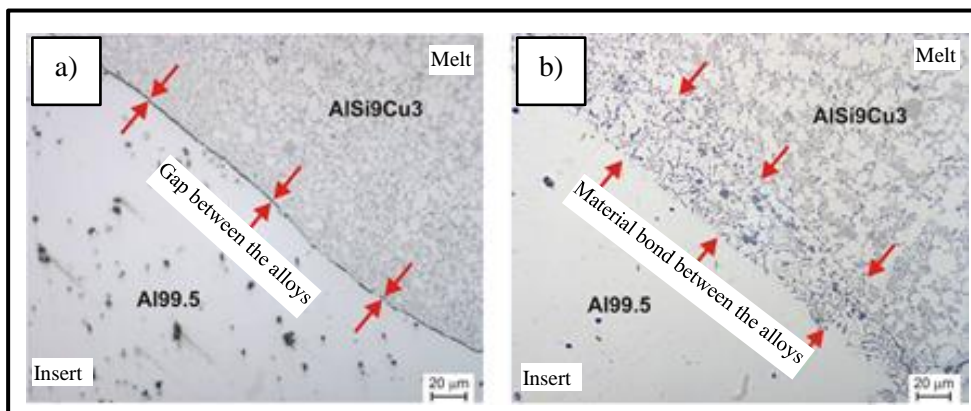


Figure 2.18. Insert-melt interface of Al/Al compound casting after:  
(a) zincate treatment; and (b) zincate treatment and electroplating (Rübner et al., 2011).

with material bonding the thick zinc layer caused an embrittlement of the interface. Experiments using only the zincate process were also not successful, as the zinc layers, while not being washed away or



evaporated, were too thin to promote any material bonding; these observations are displayed in figure 2.18 (Rübner et al., 2011). As a consequence, an optimised zincate process was developed that resulted in a zinc layer less than 1µm thick (Schwankl, Kellner et al. 2013). Using this new optimised zincate process Koerner, Schwankl, and Himmler (2014) successfully produced Al/Al compound castings using HPDC. No embrittlement of the interface was detected as the thin zinc layer was completely dissolved and diffused into the aluminium (Koerner, Schwankl, and Himmler, 2014).

#### 2.2.4.2: Manganese-based coatings

In contrast to zinc, manganese coatings have to date received little interest from researchers. Manganese's high melting temperature prevents melting and diffusion of the layer into the surrounding metals. Thus the manganese layer is still present in the casting after solidification and its mechanical properties are dependent on the bonding between the aluminium/magnesium and manganese. However, it is questionable whether sufficient bonding between the magnesium and manganese takes place. According to the Mg-Mn phase diagram, pictured in figure 2.19(a) (Asgar-Khan and Medraj, 2009), neither element forms any intermediate compounds, and they display a large miscibility gap in the liquid and solid phases (Nayeb-Hashemi and Clark, 1985; Asgar-Khan and Medraj, 2009). The solubility for manganese in magnesium is stated in the literature to range between from 1.03at% (2.298wt%) Mn (Petrov et al., 1958) to 2.0at% (4.410wt%) Mn in Mg (Tiner, 1945). Figure 2.19(b) shows the SEM image of an Al/Mg compound casting. The aluminium substrate was coated with a manganese layer before casting. This resulted in the formation of  $Al_8Mn$  and  $\mu+Al_{11}Mn_4$  layers. As expected, no extensive reaction between the magnesium and manganese can be observed.

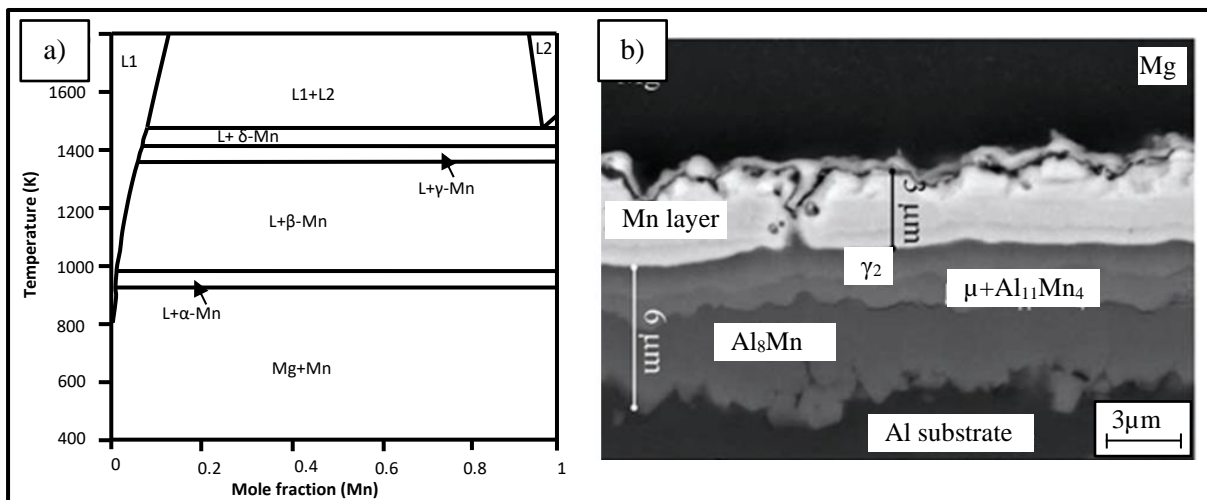


Figure 2.19. (a) Mg-Mn phase diagram (Asgar-Khan and Medraj, 2009). (b) Morphology of the interface in an Al/Mg compound casting. The Al substrate was coated before casting with a layer of Mn ( Papis, Löffler, and Uggowitzer, 2009).

## 2.2.5: Diffusion in compound castings

### 2.2.5.1: Fundamentals of diffusion

Gottstein (2007) defines (solid state) diffusion as the random movement of atoms in the crystal structure in the absence of any outside force. In metals where diffusion takes place within the crystalline lattice, the term lattice or volume diffusion is commonly used. Diffusion along an outer and inner surface (e.g. grain boundary) is referred to as surface and grain boundary diffusion. As detailed later on, in section 2.2.7, in Al/Mg compound castings the dominating diffusion mechanisms are lattice and grain boundary diffusion (Brennan et al., 2012; Liu et al., 2015). For a mathematical description of diffusion, Fick's laws of diffusion are used (Gottstein, 2007). According to Fick's first law, a diffusive flux always follows the concentration gradient:

$$J = -D\nabla\varphi \quad (\text{Eq.2.1})$$

where

$$J = \text{Diffusion flux } \left[\frac{1}{\text{cm}^2\text{s}}\right]$$

$$D = \text{Diffusion coefficient } \left[\frac{\text{cm}^2}{\text{s}}\right]$$

$\nabla\varphi$  = Three-dimensional vector of the concentration gradient

$$\varphi = \left(\frac{\delta\varphi}{\delta x}, \frac{\delta\varphi}{\delta y}, \frac{\delta\varphi}{\delta z}\right) \quad (\text{Eq.2.2}).$$

Thus the one-dimensional first law of Fick is:

$$J = -D \frac{\delta\varphi}{\delta x} \quad (\text{Eq.2.3})$$

where

$\varphi$  = Concentration

$x$  = Position.

Fick's second law describes the overall change of the concentration in a specified volume:

$$\frac{\delta\varphi}{\delta t} = \nabla(D\nabla\varphi) \quad (\text{Eq.2.4})$$

where

$t$  = Time [s].

The respective diffusion coefficient determines the diffusive flux at a given concentration gradient and is thus an important material parameter. Technically, the diffusion constant is a directional tensor and as such influenced by the crystal structure. Highly symmetrical crystals such as cubic aluminium show only little directional dependence; while magnesium, with its lower symmetry hexagonal crystal structure, shows a much more profound directional dependency. The tensor representations for the diffusion coefficient in cubic and hexagonal systems are:

$$D_{cub} = \begin{pmatrix} D_1 & 0 & 0 \\ 0 & D_1 & 0 \\ 0 & 0 & D_1 \end{pmatrix} \quad (\text{Eq.2.5})$$

$$D_{hex} = \begin{pmatrix} D_{11} & 0 & 0 \\ 0 & D_{11} & 0 \\ 0 & 0 & D_{33} \end{pmatrix} \quad (\text{Eq.2.6})$$

where

$D_{ij}$  = Directional diffusion coefficient.

Diffusion is a thermally activated process and as such the diffusion coefficient is highly dependent on the system's temperature (Gottstein, 2007). The literature gives the temperature dependence as follows:

$$D = D_0 * e^{-\frac{Q}{kT}} \quad (\text{Eq.2.7})$$

$[-\frac{Q}{kT}$  is also referred to as the Boltzmann factor]

where

$D$  = Diffusion coefficient at a given temperature

$D_0$  = Diffusion coefficient at 0K

$k$  = Boltzmann constant

$T$  = Temperature in [K]

$Q$  = Activation energy [ $\frac{kJ}{mol}$ ].

This relation was experimentally observed in a number of systems and is valid for substitutional diffusion and interstitial diffusion (Gottstein, 2007). The activation energy itself depends on a number of parameters (crystal structure, material) and is significantly lower for smaller atoms and thus interstitial diffusion. Furthermore, the activation energy is closely linked to the material's melting

temperature, meaning that with increasing melting temperature the activation energy increases as well. As the activation energy follows the solidus line of an alloy, the diffusion coefficient is the greatest at the composition with the lowest melting point. Table 2.5 gives the self-diffusion coefficient  $D$  and activation energy  $Q$  for cubic aluminium and hexagonal magnesium in a direction parallel and vertical to the base plane.

	Self-diffusion coefficient $D$ [ $\frac{cm^2}{s}$ ]		Activation energy $Q$ [ $\frac{kJ}{mol}$ ]	
	$D_{0,parallel}$ [ $\frac{cm^2}{s}$ ]	$D_{0,vertical}$ [ $\frac{cm^2}{s}$ ]	$Q_{parallel}$ [ $\frac{kJ}{mol}$ ]	$Q_{vertical}$ [ $\frac{kJ}{mol}$ ]
<b>Al</b>	2.25		144.4	
<b>Mg</b>	1.5	1.0	136	135

Table 2.5: Self-diffusion coefficients for cubic aluminium and hexagonal magnesium  
(Gottstein, 2007; Smithells, Brandes, and Brooke, 1992).

### 2.2.5.2: Lattice and grain boundary diffusion

Six atomic mechanisms for diffusion are described in the literature (Gottstein, 2007):

1. Neighbouring atom exchange mechanism;
2. Ring mechanism;
3. Vacancy diffusion;
4. Direct interstitial diffusion;
5. Indirect interstitial diffusion;
6. Crowdion.

Figure 2.20 displays the possible diffusion mechanisms. As aluminium and magnesium atoms possess similar atomic radii, interstitial diffusion is likely not to occur. Vacancy diffusion has the lowest activation energy and is thus the most likely diffusion mechanism to take place. However, most atoms do not have an adjacent vacancy and therefore it is probable that the bulk of the atom diffusion takes place via substitutional diffusion (Gottstein, 2007). The activation energy for interstitial and substitutional diffusion is displayed in table 2.6. It is easy to see that the activation energy is the lowest for vacancy diffusion and highest for substitutional diffusion.

Less restrictive structural regions such as surfaces and grain boundaries offer less resistance to any diffusion process. Therefore, grain boundary diffusion, in comparison to lattice diffusion, displays significantly lower required activation energy and as such can take place at temperatures too low for lattice diffusion. The diffusion coefficients for lattice, surface and grain boundary diffusion of thorium in tungsten are shown in figure 2.21 (Gottstein, 2007). As discussed in more depth in the next section,

the growth of intermetallic compounds in Al/Mg compound castings is linked to lattice and grain boundary diffusion.

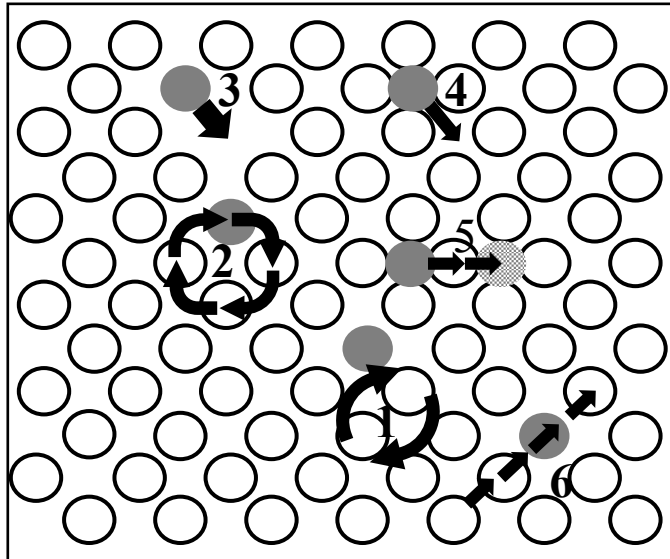


Figure 2.20. Illustration of diffusion mechanisms: (1) Neighbouring atoms exchange mechanism; (2) Ring mechanism; (3) Vacancy diffusion; (4) Direct interstitial diffusion; (5) Indirect interstitial diffusion; and (6) Crowdion (Gottstein, 2007).

Diffusion mechanism	Activation energy [eV]		
	Migration	Formation	Total
Neighbouring atoms exchange mechanism	8		8
Ring mechanism	Lower, but less probable		
Vacancy diffusion	1	1	2
Direct interstitial diffusion	0.6	3.4	4
Crowdion	0.2	3.4	3.6

Table 2.6: Activation energies in [eV] for the migration and formation of the different diffusion mechanisms (Gottstein, 2007).

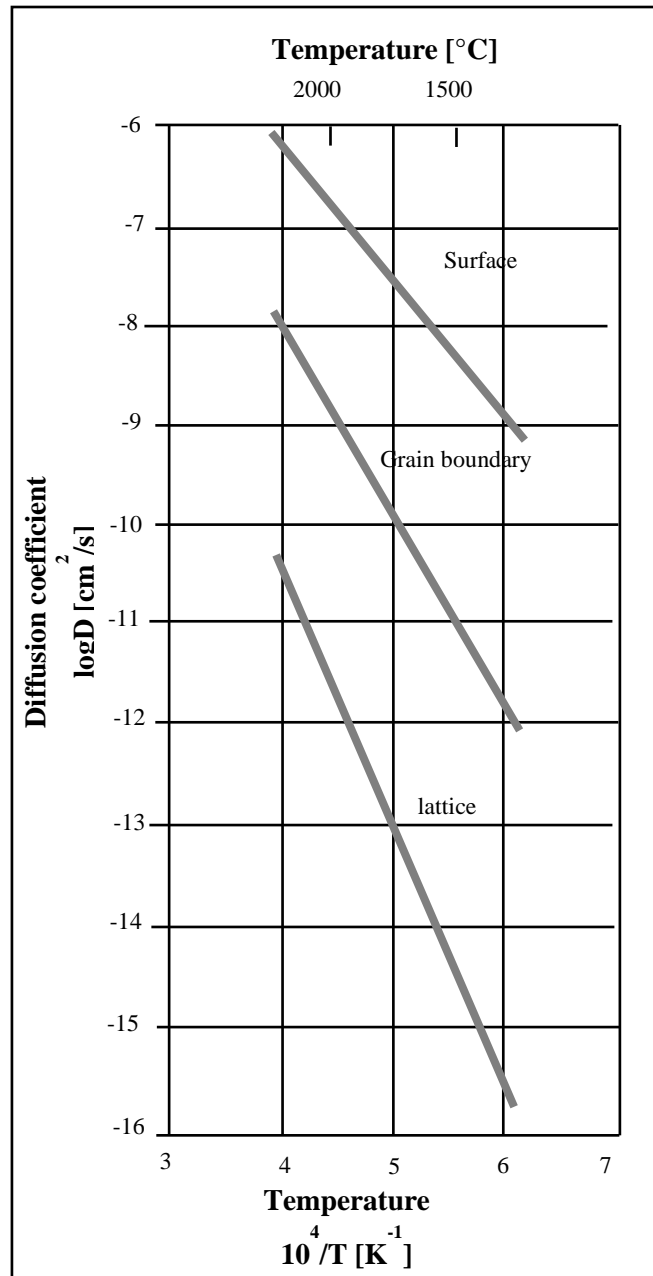


Figure 2.21. Arrhenius plot of the lattice (volume), surface and grain boundary diffusion of thorium in tungsten under the assumption of identical  $D_0$  (Gottstein, 2007).

### 2.2.6: Metallurgy of the interfacial reaction in the Al-Mg system

As identified by previous research (Viala et al., 1999; Pierre et al., 2001, 2002, 2003), the formation of the interface is mainly due to two mechanisms:

1. Dissolution & crystallisation;
2. Solid state diffusion.

However, it remains unclear to what extent each of the two mechanisms contributes to the final thickness and morphology of the interface. To increase understanding of the processes of both mechanisms, Dybkov (Dybkov and Dybkov, 2004; Dybkov, 2007; Dybkov, 2009) established a mathematical model for the liquid-solid interaction in metal solders as well as compound castings. Upon contact of the liquid magnesium with the solid aluminium, part of the melt immediately solidifies forming an intermetallic compound layer in the process via a chemical reaction. The direct chemical reaction stops after the intermetallic compound layer in the material bond reaches a thickness of a few crystal-lattice units (Dybkov, 2007). Depending on the heat balance the intermetallic compound layer, as well as part of the aluminium, may remelt. Assuming sufficient heat extraction, the mechanisms of further growth of the interface are displayed in figure 2.22. Accordingly, the net growth of the interface is the sum of the growth at the interfaces and the rate at which the layer is dissolved into the liquid melt. As such the net growth  $dx_{net}$  is given by:

$$\frac{dx_{net}}{dt} = \frac{dx_{growth}}{dt} - \frac{dx_{dissolved}}{dt} \quad (\text{Eq.2.8}).$$

It has to be taken into account that the material bond grows in the direction of the solid aluminium at the rate  $dx_{B1}$  and in the direction of the liquid magnesium at the rate  $dx_{A2}$ :

$$\frac{dx_{growth}}{dt} = dx_{B1} + dx_{A2} \quad (\text{Eq.2.9}).$$

The growth of the layer is controlled by the diffusion of both metals across the interface and the subsequent chemical reaction between diffusion and surface atoms. The literature (Dybkov, 2007) provides the following equation:

$$\frac{dx_{growth}}{dt} = \frac{k_{0B1}}{1 + \frac{k_{0B1}x}{k_{1B1}}} + \frac{k_{0A2}}{1 + \frac{k_{0A2}x}{k_{1A2}}} \quad (\text{Eq.2.10})$$

where

$k_{1B1}$  &  $k_{1A2}$  = Reaction–diffusion coefficients

$k_{0B1}$  &  $k_{0A2}$  = Chemical constants.

Thus the growth kinetics of the interface are initially, up to an interface thickness of approximately 600nm, linear. At a thickness of around 1µm the growth kinetics start to show a parabolic characteristic (Dybkov, 2009). The dissolution of the aluminium during casting is given by:

$$\frac{dx_{dissolved}}{dt} = b_t = b_0 e^{-at} = \frac{c_s k}{\rho \varphi} * e^{-\frac{ks}{v}t} \quad (\text{Eq.2.11})$$

where

$c_s$  = Saturation concentration of A in B at a given temperature (as magnesium and aluminium are completely miscible in the liquid and solid phase,  $c_s$  takes the value '1')

$b_0$  = Saturation concentration at a given temperature

$k$  = Dissolution rate constant

$\rho$  = Density of the  $A_pB_q$  intermetallic compound

$\varphi$  = Content of A in  $A_pB_q$  in mass fractions

$S$  = Surface area of the solid in contact with the liquid

$V$  = Volume of the liquid.

Initially, growth of the layer is less than the rate of dissolution, i.e. no significant growth of the material bond occurs. Equation 2.4 shows that the dissolution of the interface into the liquid magnesium decreases exponentially with time, resembling a parabolic growth rate at longer reaction times.

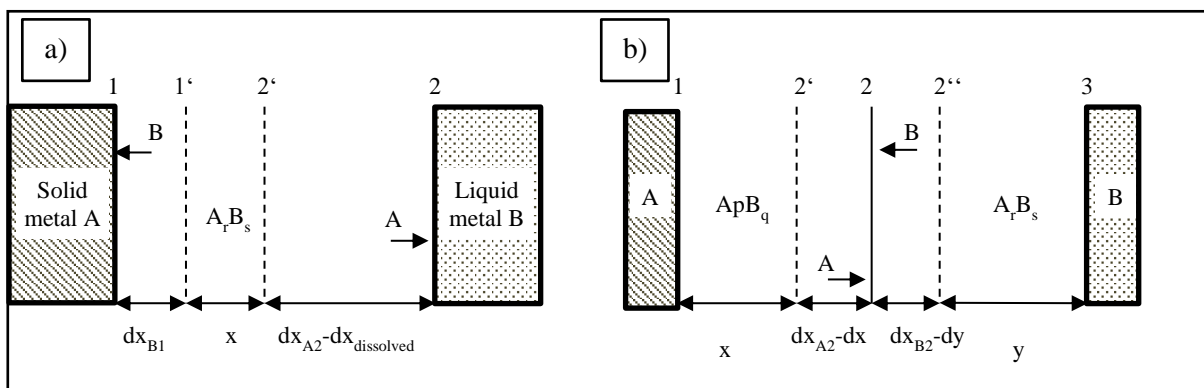


Figure 2.22. Schematics of interfacial growth during: (a) dissolution & crystallisation; and (b) solid state diffusion according to the extensive work of Dybkov (Dybkov and Dybkov, 2004; Dybkov, 2007; Dybkov, 2009).



Upon complete solidification of the magnesium, solid state diffusion becomes the main driving factor of the growth of the interface. A schematic illustration of the diffusion-controlled interfacial growth is shown in figure 2.22. Growth of any  $A_pB_q$  &  $A_rB_s$  (A and B represent the two metals and p, q, r and s the stoichiometric factors) intermetallic compounds can be described by the following non-linear functions:

$$\frac{dx}{dt} = \frac{Ka}{x} - \frac{rgkB}{py} \quad (\text{Eq.2.12})$$

$$\frac{dy}{dt} = \frac{Kb}{y} - \frac{qkA}{sgx} \quad (\text{Eq.2.13})$$

where

$x$  =  $A_pB_q$  layer thickness in the Al-Mg system:  $Al_3Mg_2$

$y$  =  $A_rB_s$  layer thickness in the Al-Mg system:  $Mg_{17}Al_{12}$

$Ka$  =  $A_pB_q$  growth constant

$Kb$  =  $A_rB_s$  growth constant

$g$  = ratio of the molar volume of  $Al_3Mg_2$  and  $Mg_{17}Al_{12}$ .

As shown in figure 2.22, the  $Al_3Mg_2$  layer grows via diffusion of aluminium and its subsequent reaction with  $Mg_{17}Al_{12}$ . Thus the thickness of the  $Al_3Mg_2$  layer increases at the rate  $dxA_2$ . Similarly, the  $Mg_{17}Al_{12}$  layer grows at the rate  $dyB_2$  via the diffusion of magnesium and chemical reaction with  $Al_3Mg_2$  to  $Mg_{17}Al_{12}$ . As both intermetallic compounds,  $Al_3Mg_2$  and  $Mg_{17}Al_{12}$ , are consumed during growth of the material bond, their thickness is reduced by the terms  $dx$  and  $dy$  respectively. The resultant net growth of each layer is the difference between  $dxA_2$  &  $dx$  and  $dyB_2$  &  $dy$ . To calculate the growth rate, knowledge of the  $Ka$  and  $Kb$  growth constants is needed. The constants  $Ka$  (growth constant of  $Al_3Mg_2$ ) and  $Kb$  (growth constant of  $Mg_{17}Al_{12}$ ) can be deduced from experimental data, by measuring the interface thickness dependence with reaction time. However, it can be difficult to measure the growth of the interface thickness precisely, especially in the initial stage, with its characteristic sharp increase. As such the accuracy of the calculation is highly dependent on the accuracy of the experimental data. Data acquired by Tanguet Njiokep, Salamon, and Mehrer (2001) showed that the theoretical calculation of the thickness of the material bond of an Al/Mg compound was in good accordance with the experimental data (Dybkov and Dybkov, 2004). However, there are several discrepancies in the existing literature concerning the interfacial growth in the Al-Mg system. As such the quality of any theoretical calculation is highly dependent on the experimental data used. The discrepancies will be explained in detail in the following section, 2.2.7.

### 2.2.7: Diffusion controlled growth of the material bond in the Al/Mg system

Direct chemical reaction stops after the phases in the interface region reach a thickness of a few crystal-lattice units. Subsequently the growth of the interface is mainly attributed to the reaction diffusion of the aluminium and magnesium. The differing thicknesses of the  $\beta$  and  $\gamma$  intermetallic compounds link them to different growth rates and/or possibly mechanisms. A schematic of the formation of intermetallic compounds in an Al/Mg diffusion couple is shown in figure 2.23.

There are discrepancies in the existing literature concerning the growth rate of the  $\gamma$ -Al<sub>12</sub>Mg<sub>17</sub> phase. Earlier findings by Funamizu and Watanabe (1972), and Tanguet Njiokep, Salamon, and Mehrer (2001), suggested a parabolic  $\sqrt{t}$  dependence of the growth similar to  $\beta$ -Al<sub>3</sub>Mg<sub>2</sub>. With follow-up research determining the activation energy and interdiffusion coefficients of both phases, a model to calculate the thickness of each layer was developed (Brennan et al., 2012). According to this model the  $\beta$  phase displays a higher growth rate and thus thickness compared to the  $\gamma$  phase. The calculated behaviour is in accordance with results observed after heat treating Al/Mg couples for at least 20h (Xiao and Wang, 2015; Brennan et al., 2012). Unlike Al/Mg compound castings, the magnesium-rich phases were observed to dominate the interfacial makeup. The  $\gamma$  phase and  $\gamma$ +Mg phases are several times thicker than the Al-rich  $\beta$  phase, indicating a deviating behaviour from the model for relatively short diffusion times (<10min) and/or low temperatures. This assumption is further supported by the fact that joining aluminium and magnesium at room temperature using a High Pressure Torsion technique results

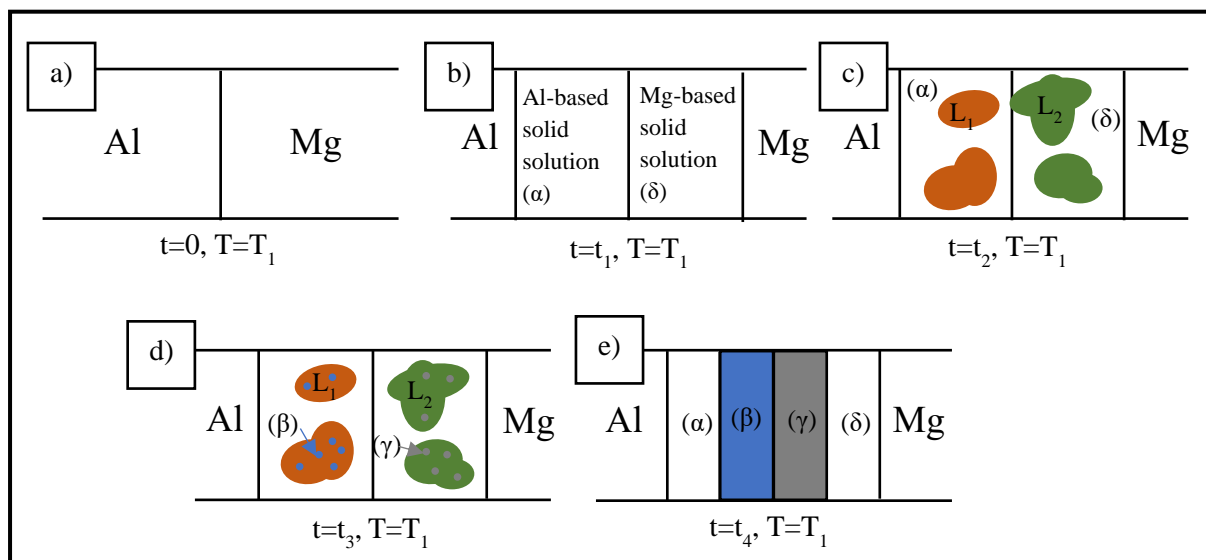


Figure 2.23. Schematic of the formation of intermetallic compounds in an Al/Mg diffusion couple at a constant temperature  $T$ : (a) state of the diffusion couple before experimentation; (b) formation of the Al- and Mg-rich solid solutions on both sides of the material bond; (c) partial melting of the Al- and Mg-rich areas; (d) precipitation of the intermetallic phases  $\beta$  and  $\gamma$  from the Al- and Mg-rich melts; (e) formation of the material bond due to precipitation from the liquid phase and solid state diffusion (Liu et al., 2015).

in a very thin single-phase  $\gamma$ -Al<sub>12</sub>Mg<sub>17</sub> layer (Qiao et al., 2016; Han et al., 2017). More recent research identified the growth mechanisms of the  $\beta$  and  $\gamma$  phases (Xiao and Wang, 2015). Two principal diffusion mechanisms were observed:

1. Lattice diffusion;
2. Grain boundary diffusion.

Growth of the  $\beta$  phase is mainly controlled by lattice diffusion while the  $\gamma$  phase is controlled by lattice diffusion as well as grain boundary diffusion. Other research into Au-Sn and Al-Cu intermetallic compounds link grain boundary diffusion to a non-parabolic growth (Tanaka, Kajihara, and Watanabe, 2007; Yamada et al., 2005). From these findings Xiao and Wang (2015) concluded that, for a given temperature of 400°C, the overall growth of the reaction layer of a pure Al-Mg diffusion couple can be approximated by:

$$l = 0.29t^{0.54} + 0.21t^{0.46} \quad (\text{Eq.2.14})$$

where

$l$  = thickness of the interface [ $\mu\text{m}$ ]

$t$  = annealing time [s].

Phase	Activation energy [kJ/mol]		Average interdiffusion coefficient	Solubility	Growth mechanism	Growth rate	Unit cell	Lattice parameter [nm]
	Brennan et al.	Liu et al.						
$\beta$ -Al <sub>3</sub> Mg <sub>2</sub>	86	127	+	-	Lattice diffusion	Parabolic	Cubic	2.8242
$\gamma$ -Al <sub>12</sub> Mg <sub>17</sub>	165	195	-	+	Lattice diffusion & Grain boundary diffusion	Parabolic/ Non-Parabolic	Cubic	1.05438

Table 2.7: Properties of the  $\beta$ -Al<sub>3</sub>Mg<sub>2</sub> and  $\gamma$ -Al<sub>12</sub>Mg<sub>17</sub> intermetallic compounds

(Brennan et al., 2012; Liu et al., 2015; Gille and Grin, 2018; Mezbahul-Islam, Mostafa, and Medraj, 2014).

As stated, for compound castings the given equation is not accurate, as it only accounts for diffusion-driven growth of the interface; especially since it is possible that the growth of the intermetallic compound layer occurs consecutively, not in parallel (Dybkov, 2007). As the growth of the  $\gamma$  phase is at least partially controlled by grain boundary diffusion, the growth rate of the  $\gamma$  phase could be altered by influencing the grain size of the magnesium (Xiao and Wang, 2015). Additional thermodynamic calculations showed that a critical thickness for the interfacial layer exists, below which only one phase is thermodynamically stable. Thus at low temperatures, due to reduced diffusion, the formation of  $\gamma$ - $\text{Al}_{12}\text{Mg}_{17}$  is thermodynamically more favourable and suppresses growth of the  $\beta$ - $\text{Al}_3\text{Mg}_2$  phase (Qiao et al., 2016). Typical temperatures for the heat treatment experiments of Al/Mg diffusion couples range between 400 and 500°C (Liu et al., 2015; Xiao and Wang, 2015) but both intermetallic compounds are already present in the interface after using temperatures as low as 300°C (Chen et al., 2007). Table 2.7 summarises the most important findings concerning the  $\beta$  and  $\gamma$  phases.

Molecular dynamic simulations of the diffusion behaviour of (pure) Al/Mg compound castings revealed a strong influence of the system's temperature and pressure on the diffusion. At temperatures between the melting points of aluminium and magnesium (923-933K), the aluminium atoms are much more active. At this temperature the bonds between the magnesium atoms are broken up and consequently vacancies form, facilitating diffusion of aluminium into magnesium. This is the reason aluminium atoms have much greater diffusion depths compared to the magnesium atoms. Increasing the system temperatures increases the activity of both metals, and as the bonds between the aluminium atoms are weakened as well, this increases the possible diffusion depth of magnesium into aluminium. By exceeding the melting point of aluminium, the difference in activity between aluminium and magnesium becomes insignificant. This behaviour is reflected in the diffusion coefficients of both metals. With increasing system temperature, the diffusion coefficients also increase. Similarly, an increase in the system's pressure results in an increase of the diffusion coefficient in both metals. Both effects are displayed in figure 2.24. The activation energies calculated were 0.44kJ/mol for aluminium and 7.0kJ/mol for magnesium (Liu, Chen, and Yang, 2015). Liu deduced an equation for the thickness using Einstein's diffusion law. The obtained equation is:

$$L = \sum_{i=Al,Mg} 3\sqrt{2D_i t} \quad (\text{Eq.2.15})$$

where

$D_i$  = Diffusion coefficient of aluminium and magnesium

$t$  = time.

Using this equation, the overall thickness of the interface caused by diffusion can be calculated. The equation shows good agreement with the molecular dynamic simulation conducted by Liu's team. The

thickness of the interface in dependence of diffusion time is displayed in equation 2.15. However, this equation does not account for any reaction kinetics at the interface and thus its accuracy is questionable (Liu, Chen, and Yang, 2015).

Summarised, the growth rate of intermetallic phases is linked to temperature, alloy composition, impurities and number of phases formed in the couple. It is therefore likely that the growth kinetics and thus thickness of the layer can be influenced by the precise control of the melt composition and temperature. So far, a detailed description of the growth of the interface in Al/Mg compound castings, linking all previous research, does not exist.

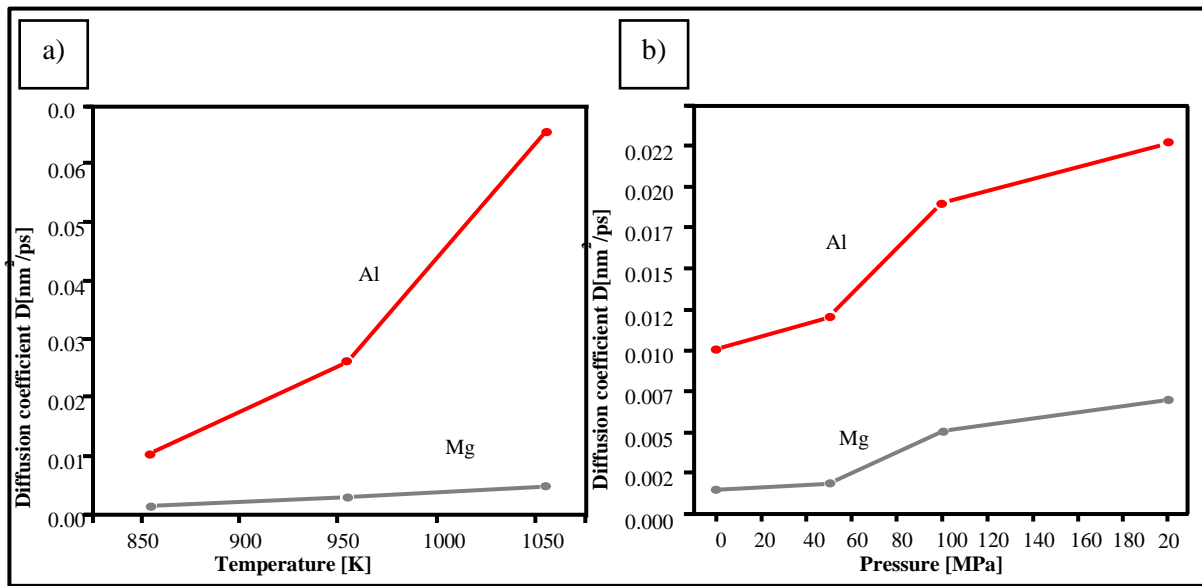


Figure 2.24. (a) effect of the systems temperature on the diffusion coefficient of aluminium and magnesium. (b) effect of the system's pressure on the diffusion coefficients of aluminium and magnesium (Liu, Chen, and Yang, 2015).

## 2.3: Summary

So far the compound casting process has been used to join a number of similar and dissimilar metals. It has been shown that compound casting can be used in a variety of casting processes, ranging from small-scale experimental furnaces up to industry-relevant high pressure die-casting and lost foam casting. As early research concluded that the interface is of great importance for the mechanical properties, recent work was mostly focused on its characterisation (Lao, 2013; Oberschelp, 2012; Bührig-Polaczek et al., 2006). A considerable amount of research has been undertaken in the compound casting of Fe/Al couples, with published research covering various aspects of it (Lao, 2013; Oberschelp, 2012; Zhe et al., 2011; Shahverdi et al., 2002a). In contrast to this, other material combinations, especially Al/Mg compound castings, have received much less scientific scrutiny. From Fe/Mg compound castings it is known that certain alloying elements in magnesium, such as silicon, zinc and aluminium, promote material bonding between the solid iron and liquid magnesium (which is normally chemically inert to Iron). In Fe/Al compound castings, zinc is known to accelerate the formation of the Fe-Al intermetallic compounds (Springer, Szczepaniak, and Raabe, 2015). However, no similar mechanism has been found so far in the Al-Mg system. From the limited amount of existing research concerning Al/Mg compound castings it was concluded that:

1. The compound casting of aluminium and magnesium is feasible using common casting processes like sand-casting and lost foam casting;
2. Coatings or special surface treatments of the aluminium are not strictly necessary, provided the amount of liquid magnesium is great enough to completely wet the aluminium's surface. However, when using very small amounts of magnesium the use of a coating to increase wettability may be necessary.

Despite the reported successful creation of a material bond at the interface of Al/Mg compound castings, many of the underlying mechanisms are not fully understood. It has been established that in compound casting, interfacial formation is the result of two distinct mechanisms.

### **1. Dissolution of the solid phase and subsequent crystallisation of the liquid phase.**

Upon contact of the liquid metal with the solid, part of the solid metal becomes molten and goes into solution with the liquid metal, altering the chemical composition of the liquid near the interface. The amount of solid metal melting is dependent on the type of material and its thermal energy. Depending on the alloys used the liquidus temperature near the interface will be reduced due to a change in its chemical composition. As a consequence, the interface may

solidify later than the bulk of the liquid metal. The thickness of the interface which results from this mechanism is dependent on the amount of material that is dissolved.

## 2. Solid state diffusion.

After solidification, the growth of the interface is governed by the diffusion of atoms across the interface. Like all diffusion processes it is dependent on time and temperature. The two intermetallic compounds  $\beta$  and  $\gamma$ , formed in Al/Mg compound castings, are linked to different growth mechanism rates. Research indicates that initially the  $\gamma(\text{Al}_{12}\text{Mg}_{17})$  phase is the dominating compound at the interface, but at longer reaction times and higher temperatures the  $\beta(\text{Al}_3\text{Mg}_2)$  phase becomes the dominant compound. Even though there is no clear evidence that one of the phases possesses better mechanical properties, there is an indication that the magnesium-rich phase,  $\gamma$ , displays non-brittle characteristics.

Therefore, it is the goal of this research to provide a more profound understanding of the formation of the interface and its properties in Al/Mg compound castings. A major focus of this research will be the investigation of how alloying elements in the aluminium and magnesium alter the formation and morphology of the interface. Characterisation of the morphology of the material bond will be conducted via SEM, EDS, XRD and optical measurements and compared to existing research. As the mechanical properties of any component are vital to its application, the mechanical strength of Al/Mg compound castings will be investigated with micro-hardness measurements and push-out testing, in order to determine the material bond's shear strength.

## 2.4: References

ALJARRAH, M. (2008) *Thermodynamic modelling and experimental investigation of the Mg-Al-Ca-Sr system*. Montreal, Quebec: Concordia University.

ASGAR-KHAN, M. and MEDRAJ, M. (2009) Thermodynamic description of the Mg-Mn, Al-Mn and Mg-Al-Mn systems using the modified quasichemical model for the liquid phases. *Materials Transactions*, **50**(5), pp. 1113-1122.

BENFER, S., STRASS, B., WAGNER, G., and FÜRBEETH, W. (2016) Manufacturing and corrosion properties of ultrasound supported friction stir welded Al/Mg-hybrid joints. *Surface and Interface Analysis*, **48**(8), pp. 843-852.

BOUCHÉ, K., BARBIER, F., and COULET, A. (1998) Intermetallic compound layer growth between solid iron and molten aluminium. *Materials Science & Engineering A*, **249**(1), pp. 167-175.

BRENNAN, S., BERMUDEZ, K., KULKARNI, N. S., and SOHN, Y. (2012) Interdiffusion in the Mg-Al System and Intrinsic Diffusion in  $[\beta]\text{-Al}_3\text{Mg}_2$ . *Metallurgical and Materials Transactions*, **43**(11), pp. 4043-4052.

- BÜHRIG-POLACZEK, A., RÖTH, T., BAUMEISTER, E., NOWACK, N., and SUSSMANN, T. (2006) Hybride Leichtbaustrukturen in Stahlblech-Leichtmetall Verbundguss, *Internationaler Expertenkreis Automobil-Leichtbau 15. Europäische Automobil-Leichtbaukonferenz*, 9-10 May, 2006 2006.
- CAO, R., WEN, B. F., CHEN, J. H., and WANG, P. (2013) Cold Metal Transfer joining of magnesium AZ31B-to-aluminium A6061-T6. *Materials Science and Engineering A*, **560**, pp. 256-266.
- CHEN, M., KUO, C. I., CHANG, C., HSIEH, C., CHANG, Y., and WU, W. (2007) Diffusion and formation of intermetallic compounds during accumulative roll-bonding of Al/Mg alloys. *Materials Transactions*, **48**(10), pp. 2595-2598.
- CHEN, Z., WANG, D., WANG, W., CAO, X., and YANG, W. (2018) Influence of multi-pass rolling and subsequent annealing on the interface microstructure and mechanical properties of the explosive welding Mg/Al composite plates. *Materials Science & Engineering A*, **723**, pp. 97-108.
- DIETRICH, D., NICKEL, D., KRAUSE, M., LAMPKE, T., COLEMAN, M. P., and RANDLE, V. (2011) Formation of intermetallic phases in diffusion-welded joints of aluminium and magnesium alloys. *Journal of Materials Science*, **46**(2), pp. 357-364.
- DIVANDARI, M., and VAHID GOLPAYEGANI, A.R. (2009) Study of Al/Cu rich phases formed in A356 alloy by inserting Cu wire in pattern in LFC process. *Materials and Design*, **30**(8), pp. 3279-3285.
- DURRANT, G., GALLERNEAULT, M., and CANTOR, B. (1996) Squeeze cast aluminium reinforced with mild steel inserts. *Journal of Materials Science*, **31**(3), pp. 589-602.
- DYBKOV, O. and DYBKOV, V. (2004) Analytical treatment of diffusional growth kinetics of two intermetallic-compound layers. *Journal of Materials Science*, **39**(21), pp. 6615-6617.
- DYBKOV, V. (1990) Interaction of 18Cr-10Ni stainless steel with liquid aluminium. *Journal of Materials Science*, **25**(8), pp. 3615-3633.
- DYBKOV, V. (2007) Interfacial interaction and diffusion in binary systems. *Defect and Diffusion Forum*, **263**, pp. 75-80.
- DYBKOV, V. (2009) The growth kinetics of intermetallic layers at the interface of a solid metal and a liquid solder. *JOM*, **61**(1), pp. 76-79.
- EGGELER, G., AUER, W., and KAESCHE, H. (1986) On the influence of silicon on the growth of the alloy layer during hot dip aluminizing. *Journal of Materials Science*, **21**(9), pp. 3348-3350.
- EMAMI, S. M., DIVANDARI, M., ARABI, H., and HAJJARI, E. (2013a) Effect of Melt-to-Solid Insert Volume Ratio on Mg/Al Dissimilar Metals Bonding. *Journal of Materials Engineering and Performance*, **22**(1), pp. 123-130.
- EMAMI, S. M., DIVANDARI, M., HAJJARI, E., and ARABI, H. (2013b) Comparison between conventional and lost foam compound casting of Al/Mg light metals. *International Journal of Cast Metals Research*, **26**(1), pp. 43-50.



FÖRSTER, W., HABISCH, S., BINOTSCH, C., AWISZUS, B., and MAYR, P. (2017) Enhancing the applicability of Al-Mg compounds by using forming and welding technologies. *Procedia Engineering*, **207**, pp. 1659-1664.

FUNAMIZU, Y. and WATANABE, K. (1972) Interdiffusion in the Al-Mg system. *Trans Jap Inst Met*, **13**(4), pp. 278-283.

GALVANISERS ASSOCIATION (2016) *The Galvanising Process*. Available: <http://www.galvanizing.org.uk/learn-more/the-process/> [12 July 2016].

GEBHARDT, E. and OBROWSKI, W. (1953) Reaktionen von festen Eisen mit Schmelzen aus Aluminium und Aluminiumlegierungen. *Zeitschrift fuer Metallkunde*, **44**(1), pp. 12.

GILLE, P. and GRIN, Y. (2018) *Crystal Growth of Intermetallics*. Berlin/Boston: Walter de Gruyter GmbH.

GOTTSTEIN, G. (2007) *Physikalische Grundlagen der Materialkunde*. 2<sup>nd</sup> edn. Heidelberg: Springer Berlin Heidelberg.

GRÖBNER, J., MIRKOVIC, D., OHNO, M., and SCHMID-FETZER, R. (2005) Experimental investigation and thermodynamic calculation of binary Mg-Mn Phase equilibria. *Journal of Phase Equilibria and Diffusion*, **26**(3), pp. 234-239.

HAJJARI, E., DIVANDARI, M., RAZAVI, S. H., EMAMI, S. M., HOMMA, T., and KAMADO, S. (2011) Dissimilar joining of Al/Mg light metals by compound casting process. *Journal of Materials Science*, **46**(20), pp. 6491-6499.

HAJJARI, E., DIVANDARI, M., RAZAVI, S. H., HOMMA, T., and KAMADO, S. (2012) Microstructure Characteristics and Mechanical Properties of Al 413/Mg Joint in Compound Casting Process. *Metallurgical and Materials Transactions A*, **43**(12), pp. 4667-4677.

HAN, J., LEE, H., JANG, J., KAWASAKI, M., and LANGDON, T. (2017) Micro-mechanical and tribological properties of aluminum-magnesium nanocomposites processed by high-pressure torsion. *Materials Science & Engineering A*, **684**, pp. 318-327.

HEUMANN, T. and DITTRICH, S. (1959) Über die Kinetik de Reaktion von festem und flüssigem Aluminium mit Eisen. *Z. Metallkunde*, **50**.

HSIEH, C., CHEN, M., and WU, W. (2013) Mechanical Property and Fracture Behavior of Al/Mg Composite Produced by Accumulative Roll Bonding Technique. *Journal of Composites*, **2013**, pp. 1-8.

KITTNER, K., FEUERHACK, A., FÖRSTER, W., BINOTSCH, C., and GRAF, M. (2015) Recent Developments for the Production of Al-Mg Compounds.

KOBAYASHI, S. and YAKOU, T. (2002) Control of intermetallic compound layers at interface between steel and aluminum by diffusion-treatment. *Materials Science & Engineering A*, **338**(1), pp. 44-53.

KOERNER, C., SCHWANKL, M., and HIMMLER, D. (2014) Aluminum-aluminum compound castings by electroless deposited zinc layers. *Journal of Materials Processing Technology*, **214**(5), pp. 1094-1101.

KORE, S. D., IMBERT, J., WORSWICK, M. J., and ZHOU, Y. (2009) Electromagnetic impact welding of Mg to Al sheets. *Science and Technology of Welding & Joining*, **14**(6), pp. 549-553.

LAO, B. (2013) *Druckgegossene Metallhybridstrukturen für den Leichtbau- Prozess, Werkstoffe und Gefüge der Metallhybriden*. Aachen: Foundry institute RWTH.

LI, C., CHI, C., LIN, P., ZHANG, H., and LIAN, W. (2015) Deformation behavior and interface microstructure evolution of Al/Mg/Al multilayer composite sheets during deep drawing. *Materials and Design*, **77**, pp. 15.

LI, M., GHOSH, S., ROUNS, T.N., WEILAND, H., RICHMOND, O., and HUNT, W. (1998) Serial Sectioning Method in the Construction of 3-D Microstructures for Particle-Reinforced MMCs. *Materials Characterization*, **41**(2), pp. 81-95.

LIU, W., LONG, L., MA, Y., and WU, L. (2015) Microstructure evolution and mechanical properties of Mg/Al diffusion bonded joints. *Journal of Alloys and Compounds*, **643**, pp. 34-39.

LIU, Y., CHEN, Y., and YANG, C. (2015) A study on atomic diffusion behaviours in an Al-Mg compound casting process. *AIP ADVANCES*, **5**(8), pp. 087147-087147-13.

MACWAN, A., JIANG, X. Q., LI, C., and CHEN, D. L. (2013) Effect of annealing on interface microstructures and tensile properties of rolled Al/Mg/Al tri-layer clad sheets. *Materials Science & Engineering A*, **587**, pp. 344-351.

MACWAN, A., PATEL, V. K., JIANG, X. Q., LI, C., BHOLE, S. D., and CHEN, D. L. (2014) Ultrasonic spot welding of Al/Mg/Al tri-layered clad sheets. *Materials & Design (1980-2015)*, **62**, pp. 344-351.

MALLORY, G. O. and HAJDU, J. B. (1990) *Electroless Plating: Fundamentals and Applications*. Orlando, Florida: American Electroplaters and Surface Finishers Society.

MASSALSKI, T. B. (1990) *Binary alloy phase diagrams*. 2<sup>nd</sup> edn. Materials Park, Ohio: ASM International.

MEZBAHUL-ISLAM, M., MOSTAFA, A. O., and MEDRAJ, M. (2014) Essential Magnesium Alloys Binary Phase Diagrams and Their Thermochemical Data. *Journal of Materials*, **2014**.

MONTEIRO, E. J., BARBOSA, M. A., ROSS, D. H., and GABE, D. R. (1991) Pretreatments to improve the adhesion of electrodeposits on aluminium. *Surface and Interface Analysis*, **17**(7), pp. 519-528.

MRÓZ, S., GONTARZ, A., DROZDOWSKI, K., BALA, H., and SZOTA, P. (2018) Forging of Mg/Al bimetallic handle using explosive welded feedstock. *Archives of Civil and Mechanical Engineering*, **18**(2), pp. 401-412.

MURRAY, J. L. (1982) The Al-Mg (Aluminum-Magnesium) system. *Bulletin of Alloy Phase Diagrams*, **3**(1), pp. 60-74.

NATANZON, Y., GORB, M., and DYBKOV, V. (1980) Mechanical strength and heat resistance of stainless steel-aluminium bimetal.

NATIONAL RESEARCH COUNCIL (1997) *Intermetallic Alloy Development: A program evaluation*. Washington, DC: The National Academies Press.

NAYEB-HASHEMI, A. A. and CLARK, J. B. (1985) The Mg-Mn (Magnesium-Manganese) system. *Bulletin of Alloy Phase Diagrams*, **6**(2), pp. 160-164.

OBERSCHELP, C. (2012) *Hybride Leichtbaustrukturen für den Karosseriebau – Gusswerkstofforientierte Anwendungsuntersuchungen für das Druckgießen*. Aachen: Foundry Institute RWTH.

PAPIS, K. J. M., HALLSTEDT, B., LÖFFLER, J. F., and UGGOWITZER, P. J. (2008) Interface formation in aluminium–aluminium compound casting. *Acta Materialia*, **56**(13), pp. 3036-3043.

PAPIS, K. J. M., LÖFFLER, J. F., and UGGOWITZER, P. J. (2009) Light metal compound casting. *Science in China, Series E: Technological Sciences*, **52**(1), pp. 46-51.

PAPIS, K. J. M., LÖFFLER, J. F., and UGGOWITZER, P. J. (2010) Interface formation between liquid and solid Mg alloys—An approach to continuously metallurgic joining of magnesium parts. *Materials Science & Engineering A*, **527**(9), pp. 2274-2279.

PETROV, D. A., MIRGALOVSKAYA, M. S., STRELNIKOVA, I. A., and KOMOVA, E.M. (eds) (1958) *The Constitution Diagram For the Magnesium-Manganese System*. Institute of Materials Science, Academy of Sciences of the Ukrainian SSR.

PIERRE, D. (1999) Doctoral Thesis. University of Lyon.

PIERRE, D., BOSSELET, F., PERONNET, M., VIALA, J. C., and BOUIX, J. (2001) Chemical reactivity of iron base substrates with liquid Mg–Zr alloys. *Acta Materialia*, **49**(4), pp. 653-662.

PIERRE, D., PERONNET, M., BOSSELET, F., VIALA, J. C., and BOUIX, J. (2002) Chemical interaction between mild steel and liquid Mg–Si alloys. *Materials Science & Engineering B*, **94**(2), pp. 186-195.

PIERRE, D., VIALA, J. C., PERONNET, M., BOSSELET, F., and BOUIX, J. (2003) Interface reactions between mild steel and liquid Mg–Mn alloys. *Materials Science & Engineering A*, **349**(1), pp. 256-264.

QI, G., CHEN, X., and SHAO, Z. (2002) Influence of bath chemistry on zincate morphology on aluminium bond pad. *Thin Solid Films*, **406**(1), pp. 204-209.

QIAO, X., LI, X., ZHANG, X., CHEN, Y., ZHENG, M., GOLOVIN, I. S., GAO, N., and STARINK, M.J. (2016) Intermetallics formed at interface of ultrafine grained Al/Mg bi-layered disks processed by high pressure torsion at room temperature. *Materials Letters*, **181**, pp. 187-190.

RAWERS, J. and PERRY, K. (1996) Crack initiation in laminated metal-intermetallic composites. *Journal of Materials Science*, **31**(13), pp. 3501-3506.

ROBERTS, C. S. (1960) *Magnesium and its alloys*. New York: Wiley.

ROBERTSON, S. G., RITCHIE, I. M., and DRUSKOVICH, D. M. (1995) A kinetic and electrochemical study of the zincate immersion process for aluminium. *Journal of Applied Electrochemistry*, **25**(7), pp. 659-666.

RÜBNER, M., GÜNZL, M., KÖRNER, C. and SINGER, R. F. (2011) Aluminium–aluminium compound fabrication by high pressure die casting. *Materials Science & Engineering A*, **528**(22), pp. 7024-7029.

RUPPERT, M., STREBL, M., HÖPPEL, H. W., and GÖKEN, M. (2015) Mechanical properties of ultrafine-grained AlZnMg(Cu)-alloys AA7020 and AA7075 processed by accumulative roll bonding. *Journal of Materials Science*, **50**(12), pp. 4422-4429.

SACERDOTE-PERONNET, M., GUIOT, E., BOSSELET, F., DEZELLUS, O., ROUBY, D., and VIALA, J. C. (2007) Local reinforcement of magnesium base castings with mild steel inserts. *Materials Science and Engineering: A*, **445–446**, pp. 296-301.

SAITO, M., MAEGAWA, T., and HOMMA, T. (2005) Electrochemical analysis of zincate treatments for Al and Al alloy films. *Electrochimica Acta*, **51**(5), pp. 1017-1020.

SCHULZE, G. E. R. (1967) *Metallphysik; Ein Lehrbuch*. Berlin: Berlin Akademie Verlag.

SCHWANKL, M., KELLNER, R., SINGER, R. F., and KÖRNER, C. (2013) The influence of sandblasting on the morphology of electroless deposited zinc layers on aluminium sheets. *Applied Surface Science*, **283**, pp. 202-208.

SHAHVERDI, H. R., GHOMASHCHI, M. R., SHABESTARI, S., and HEJAZI, J. (2002a) Kinetics of interfacial reaction between solid iron and molten aluminium. *Journal of Materials Science*, **37**(5), pp. 1061-1066.

SHAHVERDI, H. R., GHOMASHCHI, M. R., SHABESTARI, S., and HEJAZI, J. (2002b) Microstructural analysis of interfacial reaction between molten aluminium and solid iron. *Journal of Materials Processing Tech*, **124**(3), pp. 345-352.

SINGH, D., SURYANARAYANA, C., MERTUS, L., and CHEN, R. (2003) Extended homogeneity range of intermetallic phases in mechanically alloyed Mg–Al alloys. *Intermetallics*, **11**(4), pp. 373-376.

SLATER, J. C. (1964) Atomic radii in crystals. *The Journal of chemical physics*, **41**(10), pp. 3199-3204.

SMITHELLS, C. J., BRANDES, E. A., and BROOK, G.B. (1992) *Smithells metals reference book*. 7<sup>th</sup> edn. Oxford: Butterworth-Heinemann.

SPRINGER, H., SZCZEPANIAK, A., and RAABE, D. (2015) On the role of zinc on the formation and growth of intermetallic phases during interdiffusion between steel and aluminium alloys. *Acta Materialia*, **96**, pp. 203-211.

SU, H. L., HARMELIN, M., DONNADIEU, P., BAETZNER, C., SEIFERT, H. J., LUKAS, H. L., EFFENBERG, G., and ALDINGER, F. (1997) Experimental investigation of the Mg-Al phase diagram from 47 to 63 at.% Al. *Journal of Alloys and Compounds*, **247**(1), pp. 57-65.

SURYANARAYANA, C., TIWARI, S., and ANANTHARAMAN, T. (1978) NEW METASTABLE PHASE IN THE ALUMINIUM-MAGNESIUM SYSTEM. *Zeitschrift fuer Metallkunde/Materials Research and Advanced Techniques*, **69**(3), pp. 155-156.

TANAKA, Y., KAJIHARA, M., and WATANABE, Y. (2007) Growth behavior of compound layers during reactive diffusion between solid Cu and liquid Al. *Materials Science & Engineering A*, **445**, pp. 355-363.

TANG, Y. C. and DAVENPORT, A. J. (2001) The effect of heat treatment and surface roughness on the zincate treatment of aluminium alloy 6082. *Transactions of the Institute of Metal Finishing*, **79**(3), pp. 85-89.

TANGUEP NJIOKEP, E. M., SALAMON, M., and MEHRER, H. (2001) Growth of intermetallic phases in the Al-Mg system. *Defect and Diffusion Forum*, (194-199), pp. 1581-1586.

TINER, N. (1945) The solubility of manganese in liquid magnesium. (*Metals Technology*), p. 1.

VIALA, J. C., PERONNET, M., BARBEAU, F., BOSSELET, F., and BOUIX, J. (2002) Interface chemistry in aluminium alloy castings reinforced with iron base inserts. *Composites Part A*, **33**(10), pp. 1417-1420.

VIALA, J. C., PIERRE, D., BOSSELET, F., PERONNET, M., and BOUIX, J. (1999) Chemical interaction processes at the interface between mild steel and liquid magnesium of technical grade. *Scripta Materialia*, **40**(10), pp. 1185-1190.

VON GOLDBECK, O. K. (1982) *Iron—Magnesium Fe—Mg. In: IRON—Binary Phase Diagrams*. Berlin, Heidelberg: Springer.

WANG, N., YU, W., TANG, B., PENG, L., and DING, W. (2008) Structural and mechanical properties of Mg<sub>17</sub>Al<sub>12</sub> and Mg<sub>24</sub>Y<sub>5</sub> from first-principles calculations. *Journal of Physics D: Applied Physics*, **41**(19), article id 195408.

XIAO, L. and WANG, N. (2015) Growth behavior of intermetallic compounds during reactive diffusion between aluminium alloy 1060 and magnesium at 573-673 K. *Journal of Nuclear Materials*, **456**, pp. 389-397.

XU, G., LUO, A., CHEN, Y. and SACHDEV, A. (2014) Interfacial phenomena in magnesium/aluminium bi-metallic castings. *MATERIALS SCIENCE AND ENGINEERING A-STRUCTURAL MATERIALS PROPERTIES MICROSTRUCTURE AND PROCESSING*, **595**, pp. 154-158.

YAMADA, T., MIURA, K., KAJIHARA, M., KUROKAWA, N., and SAKAMOTO, K. (2005) Kinetics of reactive diffusion between Au and Sn during annealing at solid-state temperatures. *Materials Science & Engineering A*, **390**(1), pp. 118-126.

ZARE, G. R., DIVANDARI, M., and ARABI, H. (2013) Investigation on interface of Al/Cu couples in compound casting. *Materials Science and Technology (United Kingdom)*, **29**(2), pp. 190-196.

ZHANG, H., CHEN, Y., and LUO, A. A. (2014a) A novel aluminium surface treatment for improved bonding in magnesium/aluminium bimetallic castings. *Scripta Materialia*, **86**, pp. 52-55.

ZHANG, H., CHEN, Y., and LUO, A. A. (2014b) Improved Interfacial Bonding in Magnesium/Aluminium Overcasting Systems by Aluminium Surface Treatments. *Metallurgical and Materials Transactions B*, **45**(6), pp. 2495-2503.

ZHANG, X. P., YANG, T. H., CASTAGNE, S., and WANG, J. T. (2011) Microstructure; bonding strength and thickness ratio of Al/Mg/Al alloy laminated composites prepared by hot rolling. *Materials Science & Engineering A*, **528**(4), pp. 1954-1960.

ZHAO, K. N., LIU, J. C., NIE, X. Y., LI, Y., LI, H. X., DU, Q., ZHUANG, L. Z., and ZHANG, J. S. (2016) Interface formation in magnesium-magnesium bimetal composites fabricated by insert moulding method. *Materials and Design*, **91**, pp. 122-131.

ZHE, M., DEZELLUS, O., GARDIOLA, B., BRACCINI, M., and VIALA, J. C. (2011) Chemical Changes at the Interface Between Low Carbon Steel and an Al-Si Alloy During Solution Heat Treatment. *Journal of Phase Equilibria and Diffusion*, **32**(6), pp. 486-497.

ZHOU, P., GUO, C., WANG, E., WANG, Z., CHEN, Y., and JIANG, F. (2016) Interface tensile and fracture behavior of the Ti/Al<sub>3</sub>Ti Metal-Intermetallic Laminate (MIL) composite under quasi-static and high strain rates. *Materials Science & Engineering A*, **665**, pp. 66-75.

ZYSKA, A., KONOPKA, Z., LAGIEWKA, M., and NADOLSKI, M. (2010) Characteristics of squeeze cast AlZn5Mg alloy castings. *Archives of Metallurgy and Materials*, **55**(3), pp. 969-975.

## Chapter 3: Experimental Methodology

### 3.1: Outline

As discussed in the literature review, interfacial formation in compound castings is a complex process, influenced by a number of factors such as temperature and the choice of material. To assess the importance of these factors, a series of experiments was conducted. The experiments performed were divided into three sub-sections.

1. **Material selection in Al/Mg compound castings.** No profound understanding, on how common alloying elements in the base materials (aluminium and magnesium) affect interfacial formation, exist in the literature. The effect of zinc and silicon on the formation of the material bond was investigated using SEM and EDX characterisation techniques, optical inspections and micro-hardness measurements.
2. **Interfacial phenomena in Al/Mg compound castings.** A number of factors, such as temperature distribution and the effect of the aluminium's intrinsic oxide layer, were found to affect the bonding of compound castings. This section aims at providing a better understanding of these factors. To this end, SEM, EDX and XRD characterisation techniques, optical inspections and micro-hardness measurements were used.
3. **Mechanical properties of the material bond of Al/Mg compound castings.** Mechanical properties of the material bond are of great importance, to assess the possibility of compound castings in actual applications. In this chapter the effect, of differing alloy combinations and temperatures, on the mechanical properties of the bond, was investigated. The strength of the material bond of Al/Mg compound castings was assessed with push-out testing.

The following chapter will first provide a description of all the materials and equipment used. This is then followed by an in-depth description of the experimental methodology used.

## 3.2: Equipment Used

For the experimentation, a number of moulds and furnaces were used. In total four different moulds were used, which hereafter are labelled moulds 1-4. Their exact specifications are listed in section 3.2.1.1.

### 3.2.1: Moulds and furnaces

#### 3.2.1.1: Moulds

Mould 1, shown in figure 3.1, was a hollow cylindrical mould with an inner diameter of 80mm and a wall thickness of 15mm. Mould 1, as well as all other moulds, was made out of tool steel.

Mould 2, also shown in figure 3.1, was a cylindrical mould with a diameter of 30mm and a height of 80mm. A feeder (height 20mm, diameter 30mm) was placed on top to ensure that no solidification related shrinkages and pores were present within the cylinders. The inside of the mould was coated with boron nitride to facilitate the removal of the castings.

Mould 3 was a four-part mould, made from tool steel. The 4 parts formed a wedge-shaped cavity and a feeder on top. The feeder (20mm width, 50mm length and 70mm height) was placed on top to ensure that no solidification related shrinkages and pores were present within the casting. A photograph and schematic of mould 3 is displayed in figure 3.2.

Mould 4 was a rectangular 2-part mould with a cylindrical cavity (diameter 100mm) made from tool steel. At the bottom of the mould was a 5mm deep recess as shown in figure 3.3(b). Aluminium cylinders, cast using mould 4, were placed in the insert which ensured that the aluminium cylinder was

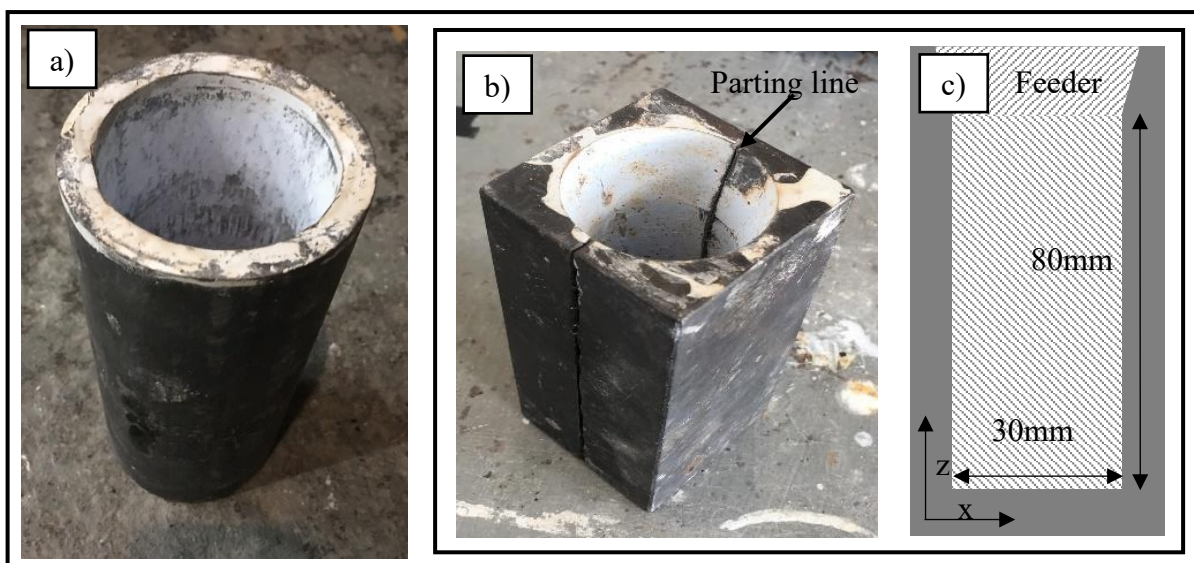


Figure 3.1. Moulds 1 & 2: (a) photograph of mould 1; (b) photograph of mould 2; and (c) view of the schematic along the parting line of mould 2. Due to the design of the moulds, turbulences and resulting oxide films and inclusions could not be avoided, but were deemed not to have a negative impact on the subsequent experimentation.



always in the same position relative to the inlet. The schematic drawings and a photograph of the mould can be seen in figure 3.3. The inside of the mould was coated with boron nitride to facilitate the removal of the castings.

To melt the magnesium alloy, cylindrical steel liners of different sizes were used, depending on the amount of magnesium used. Both liners were 110mm high, and 55mm or 110mm in diameter. Aluminium-based alloys were melted in graphite crucibles of varying sizes, again depending on the amount of aluminium alloy. The graphite crucibles were always coated with boron nitride.

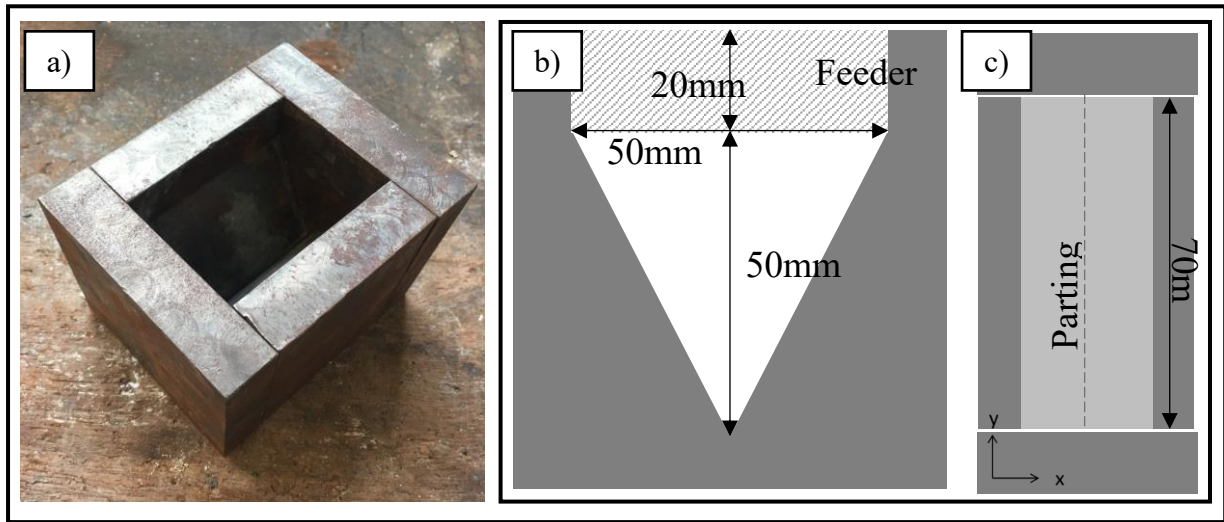


Figure 3.2. Mould 3: (a) photograph of mould 3; (b) side plan view of the schematic of the mould; and (c) top plan view of the schematic of the mould.

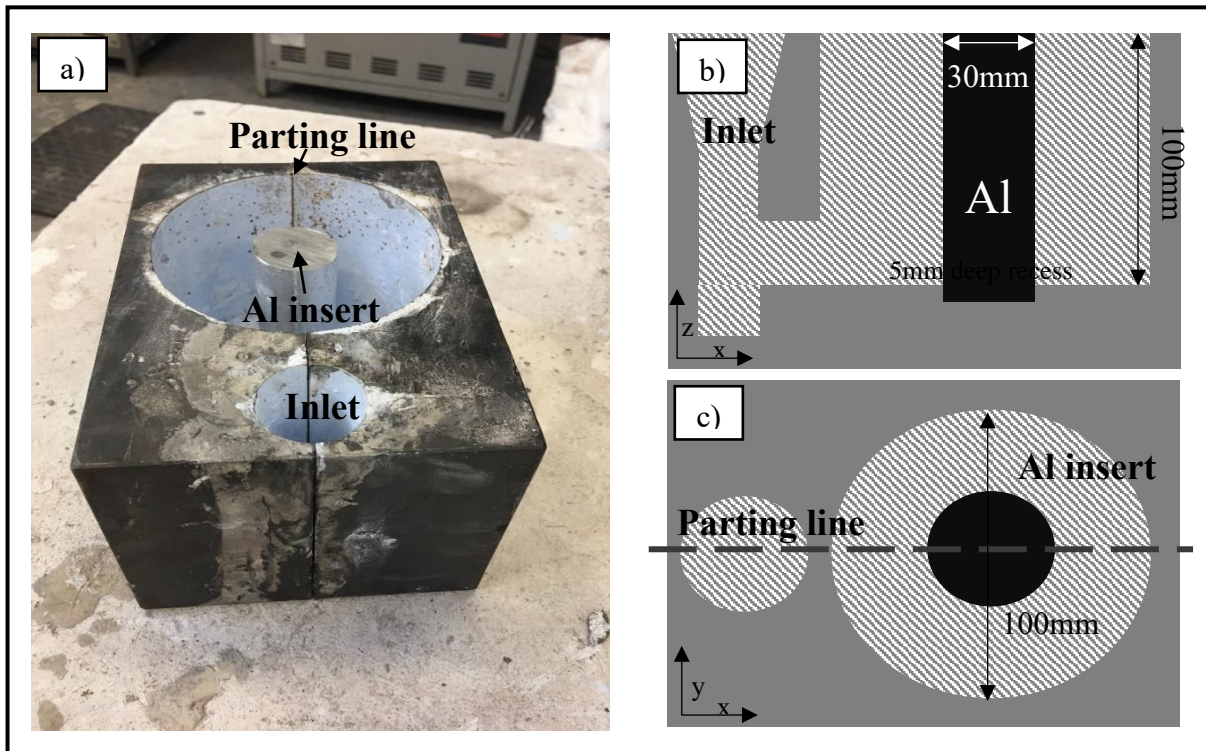


Figure 3.3. Mould 4: (a) photograph of the mould and the Al cylinder insert placed therein; (b) side plan view of the mould along the parting line; and (c) top plan view of the schematic of the mould.

### 3.2.1.2: Furnaces

Two top-loading *Carbolite VCF 12/5* furnaces were used for melting the metals. One furnace was fitted out with a steel liner and a cover gas supply for the melting of magnesium. A round *Nabertherm Top 190* furnace and a *Carbolite Gero* oven were used to preheat the moulds.

### 3.2.1.3: Additional equipment

Larger castings were cut with silicon carbide blades using an *ATM Brilliant 200*. Smaller samples (diffusion couples) were cut using a *Struer Accutom-10 micro-cutter*. The blade was a 91 $\mu$ m thick diamond cup wheel. All samples were ground and polished using an *ATM Saphir 520* machine.

## 3.2.2: Alloys

Throughout all the experimentation, alloys used were either commercially pure alloys/metals sourced from a manufacturer or made in-house using the aforementioned alloys/metals. Commercially pure aluminium, magnesium, zinc, an AlSi50 master alloy and the magnesium alloys AZ31 and AZ91 were used as-received. The exact chemical compositions and sources are listed in table 3.1 below.

<b>Aluminium</b>	<b>%Al</b>	<b>%Si</b>	<b>%Fe</b>		<b>Manufacturer</b>
	99.9	0.04	0.06		
<b>Magnesium</b>	<b>%Mg</b>	<b>%Al</b>	<b>%Zn</b>		Magontec
	99.9				
<b>AZ31</b>	<b>%Mg</b>	<b>%Al</b>	<b>%Zn</b>		Magontec
	Balance	3.09	1.06		
<b>AZ91</b>	Balance	8.95	1.02		
<b>Elektron 21</b>	<b>%Mg</b>	<b>%Nd</b>	<b>%Gd</b>	<b>%Zn</b>	Magnesium Elektron
	Balance	3.25	1.41	0.4	
<b>AlSi50</b>	<b>%Al</b>		<b>%Si</b>		
	50.9		48.8		
<b>Zinc</b>	<b>%Zn</b>				
	99.6				

Table 3.1: List of metals and alloys used, with corresponding chemical compositions and sources where relevant.

## 3.2.3: Characterisation Equipment

### 3.2.3.1: Optical Microscopy (OM)

A *Zeiss Axio Scope A1 AX10* optical microscope was used. The affiliated software was *AxioVision 40V 4.8.2.0*. Optical Microscopy was used to study the thickness and microstructure of the compound castings. Thicknesses were measured with the aforementioned software.

**Sample preparation.** Samples cut from the compound castings were polished using silicon carbide papers and an *ATM Sapphir 520* polishing device. Samples from moulds 1 and 4 were, with diameters of 80 and 100mm, too large for automatic grinding. They were, due to their size, polished by hand, starting with grit 80 for approximately 4min. Step by step, the paper grade was increased up to grit 2000. Water was used as the lubricant throughout all but the last grinding step. To minimise corrosion, the water was replaced with ethanol when grinding to grit 2000. As a final step, the samples were polished using a colloidal silica (0.04 $\mu$ m) and a polishing cloth before being cleaned with ethanol and dried using a hot air drier. Smaller samples with a diameter smaller than 30mm were embedded in a phenolic resin using a *Buehler Simplimet 1000*. These samples were polished similarly to the unembedded ones. Repeated measurement of the length of a reference sample (a Vickers microhardness indent) at several magnifications revealed an upper error margin of ~2%. This in good accordance with values reported by Keeble (2019).

### 3.2.3.2: Scanning Electron Microscopy (SEM)

A *Zeiss Supra 35VP* ultra high field emission gun was used (FEG-SEM). This SEM was equipped with energy-dispersive spectroscopy (EDS), backscatter electron detection (BSE) and electron backscattered diffraction (EBSD). The SEM was used to characterise the chemical composition of the interface and create high-magnification images of phases and precipitates contained within it. An accelerating voltage of 20kV was found to be suitable throughout all sample characterisations. Most compound castings were characterised with backscatter electron detection as it facilitated identification of phases and lessened the impact of the surface quality on characterisation (Reimer, 1985).

EDS spectra were collected using the *TEAM EDAX 4.xxx* software. It was used to identify the chemical composition gradient across the interface, with linescans, and the chemical composition of single spots or areas. EDS is based on the principle that every element has its own unique atomic structure and thus X-ray emission spectrum (Biermann and Krüger, 2014).

**Sample preparation.** Samples characterised with the SEM were prepared as per the method described for optical microscopy.

### 3.2.3.3: X-ray Diffraction (XRD)

A *Bruker D8 Advance* X-ray diffractometer was used. It was equipped with a Cu K $\alpha$ 1 filter and was operated with a voltage of 40kV and current of 50mA. XRD measurements are able to identify the atomic structure of unknown materials using the relationship of the wavelength of electromagnetic radiation, diffraction angle and lattice spacing in crystalline materials, as expressed by Bragg's law. Angles between 20° and 100° were scanned. The results were analysed using the *Diffraction EVA V4* software using the international centre for diffraction database (Cox, Pidgeon 1963).

**Sample preparation.** Solid pieces of metal were embedded in phenolic resin and placed in a sample holder. It was ensured that the sample was level with the top of the holder. The phenolic resin, due to its non-crystalline atomic structure, was expected not to affect the XRD measurements.

#### 3.2.3.4: Optical Emission Spectroscopy (OES)

A *Hitachi Foundrymaster Pro* was used to analyse the bulk chemical composition of the base alloys and compound castings. Where the zinc content, in some of the alloys used and in the resultant material bond in the compound castings, exceeded the calibration range (<6wt%) of the OES, EDS was used instead.

An Optical Emission Spectrometer creates a spark between an electrode and the metallic sample. The spark causes atoms to vaporise and enter a high-energy (excited) state and emit electromagnetic radiation, which is unique to each element. The emitted radiation is split by a diffraction grating into its spectral components. Photomultiplier tubes are used as detectors to measure the intensity of each emission spectrum, which is proportional to the concentration of the element in the sample (Skoog and Leary, 2013).

**Sample preparation.** All samples were polished to grit 80 to obtain an even surface, which is a requirement for an accurate OES measurement.

#### 3.2.3.5: Thermal Analysis

Simultaneous thermal analysis is a combination of differential scanning calorimetry (DSC) and thermogravimetry (TG). The used device was a *NETZCH STA 409 PC luxx*, which uses a heat-flux DSC to measure the temperature difference between the analysed sample and a reference as a function of time. Phase transitions are coupled with emitted or absorbed heat and can be measured by the DSC device. The device was used to identify the melting point of phases found in the material bonds of the compound castings. TG measures the change in mass of a sample as a function of the temperature. Combining it with the DSC allows for a more in-depth analysis of the phase transformations and associated phenomena (e.g. vaporisation) (Hemminger, 1990). TG measurements were not used in this thesis.

The procedure entails placing a small amount of metal in an alumina crucible with a lid. In order to remove the influence of crucible contamination and surrounding events, a baseline correction curve was acquired using an empty crucible before the measurements. A filled and an empty crucible were placed in a chamber, which was purged with helium gas. This process was repeated four times to ensure that no contaminants remained in the chamber. During experimentation, a helium flow of 40mL/min with a pressure of 1.01325bar ensured a non-reactive environment. The samples were heated up and cooled down linearly at a rate of 10°C/min.

**Sample preparation.** A small piece of metal (~0.01g) was cut out of the compound castings using handsaws. After cutting, the sample was rinsed with ethanol and dried with hot air to remove any contaminant stemming from the handsaw and handling.

#### 3.2.3.6: Micro-Hardness Indenter

A *Wilson Vickers Hardness* micro-hardness indenter was used. It is capable of indent forces ranging from 0.3-30N. Vickers micro-hardness measurements utilise a pyramid-shaped measuring head which is lowered onto the specimen's surface with a set force. The penetration depth of the measuring head depends on the hardness of the tested material (International Organisation for Standardisation, 2019). The dimensions of the resulting indent were measured with an optical microscope. Vickers micro-hardness was then calculated using the known applied force and indent dimensions. The dwell time was set to 10s for all hardness measurements and the lowest possible force – 0.3N – was used, as a higher force often resulted in the formation of cracks within the material bond of the inspected samples.

**Sample preparation.** Samples were ground to grit 2000 and briefly polished with OPS to ensure an even and good quality surface to facilitate the optical measurements of the indents.

#### 3.2.3.7: Three-point Bending Machine

An *Instron 5585* Universal Testing System was used for push-out testing. Such machines measure the load applied to a specimen and the displacement caused by this load. This provides information about ductility, yield strength and tensile strength of the material bonds in compound castings. To this end, a disk from a compound casting was placed onto a hollow cylinder. The force was applied to the aluminium and the tool head was lowered with a speed of 8mm/min. A detailed schematic of the used hollow cylinder, as well as the set-up of the push-out testing, is shown in section 3.5. Calibration of the machine revealed that the error margin in the used load range (<35kN) was below 1%.

**Sample preparation.** 15mm high disks were machined from a larger casting (see section 3.5).

#### 3.2.3.8: Numerical Simulation

Numerical simulation is widely used in the foundry industry to reduce development times and improve soundness of a casting. It allows for the prediction of thermal gradients, filling behaviour and solidification (Mi et al., 2013; Junqing et al., 2008). For the numerical simulation, the software package *Magma 5.4*, by Magmasoft, was used. The Magmasoft package was chosen as it is widely used within the foundry industry. Numerical simulation allows a number of process parameters to be calculated, such as temperature distribution and cooling gradients of casting parts, where direct measurements and observations are not practical. The numerical simulation of casting parts using *Magma* can be divided into four parts (Dubois, 2018).

1. Modelling of the geometry: the MagmaSoft package includes a built-in CAD tool, which allows for the creation of (not overly-complex) parts. *Magma* also allows for the import of geometries created with external CAD tools (e.g. *Catia*, *Siemens NX*).
2. Meshing and choosing of parameters: for numerical simulation, a mesh needs to be created based on the modelled geometry. *Magma* uses the Finite Differences Method (FDM) for the calculation, resulting in a mesh of rectangular cells. The number of cells correlates exponentially with computing time. As a consequence, a compromise is needed between resolution and time. After this, the meshing material and process parameters are defined.
3. Calculation: using FDM, *Magma* then calculates the filling, solidification and cooling of the casting parts, within the frame of the chosen parameters.
4. Visualisation: the calculated values for the temperature and melt velocity over time are displayed directly with respect to the geometry of the cast part.

A workstation with 1 CPU core and 32Gb of RAM was used for the numerical simulation. While the filling, solidification and cooling cannot be directly influenced (unlike in similar software packages, such as *Flow 3D*), almost all material data, such as heat transfer coefficients (HTC) can be adjusted. A detailed description of the HTC used can be found in section 3.4.3.

### 3.3: Material Selection in Al/Mg Compound Castings

#### 3.3.1: Selection of a Magnesium Alloy

There is little information in the literature about the impact of different magnesium alloys on the formation of the material bond. One kilogram of commercially pure aluminium was melted in a graphite crucible, coated with boron nitride, using a top-loading *Carbolite* furnace. Temperature of the aluminium melt was measured using a handheld *Maxthermo YC-727* meter and a type K thermocouple. Measurement accuracy of a type K thermocouple is given as  $\sim\pm 5^{\circ}\text{C}$  at  $700^{\circ}\text{C}$ . Once the temperature of the melt reached  $700^{\circ}\text{C}$  it was cast into shape using mould 2. The castings were removed from the mould after solidification and cooled under ambient conditions. The cylindrical castings were cut into 20mm high disks using an abrasive saw. The disks were cleaned with acetone and rinsed with ethanol. Cylindrical mould 1 and the Al disks were preheated to  $200^{\circ}\text{C}$ , in a top-loading *Carbolite* furnace. Before casting, the Al disks were placed in the mould. Two hundred grams of commercially pure magnesium, AZ31, AZ91 and Elektron 21 were melted in a *Carbolite VCF 12/5* furnace under a protective gas ( $\text{SF}_6$  and Nitrogen). The flow rate and mixture of the protective gas used were:

- 6L/min  $\text{N}_2$ ;
- 0.025L/min  $\text{SF}_6$ .

This mixture was used for all experiments. SF<sub>6</sub> causes the formation of a thin film on the melt surface, consisting of MgO and MF<sub>2</sub>. Before casting, the film is mechanically removed; as such, no fluorides or MgF<sub>2</sub> were found within the compound castings throughout all experimentation and characterisation. The alloys were heated to 50°C above their individual liquidus temperatures before being cast onto the aluminium disk. The temperatures of the melts were measured shortly before pouring, with a handheld meter and a type K thermocouple, and are listed in Table 3.2. The castings cooled down under ambient conditions before being removed from the mould.

<b>Magnesium alloy</b>	<b>Pouring temperature [°C]</b>
<b>Mg</b>	667
<b>AZ31</b>	664
<b>AZ91</b>	661

*Table 3.2: Alloys used and pouring temperatures.*

### 3.3.2: Influence of Silicon & Zinc on the Formation of the Material Bond

To assess the influence of the alloying elements silicon and zinc on interfacial formation, a series of experiments was conducted. In these experiments, aluminium alloys containing silicon and zinc were overcast with liquid magnesium to create a continuous material bond. To see the effect of varying amounts of silicon and zinc, the silicon content was set to 1, 6, 15 and 30wt% and the zinc to 6, 15 and 30wt%. The exact compositions and amounts of material produced are given in table 3.3. High amounts of 30wt% zinc and silicon were chosen to determine the effect of an excessive amount on the material bond under extreme conditions.

The AlSi alloys were produced from commercially pure aluminium and an AlSi master alloy containing 50wt% silicon. Similarly, the AlZn alloys were made from commercially pure aluminium and zinc. For both alloys, the aluminium was first melted at 700°C in a graphite crucible coated with boron nitride, using a *Carbolite VCF 12/5* furnace. Once this temperature was reached, the silicon and zinc were added and the melt was intermittently stirred with a graphite ladle for 60min to facilitate a homogeneous distribution of both elements within the aluminium. Due to the high melting temperature of the AlSi30 alloy, the alloy was heated up to 850°C (measured with a handheld meter) before adding the AlSi master alloy. There were some losses regarding the total amount of alloy produced, as it was not possible to remove all the metal from the crucible. After melting and stirring, the AlSi and AlZn alloys were cast into mould 2. The mould was preheated to 250°C before casting, to ensure filling. As silicon and zinc contents over 6wt% were outside the calibration range of the optical spectrometer, it was not possible to validate the chemical composition using this method. Composition of the alloys was confirmed during characterisation.

Each wedge weighed (depending on its composition) approximately 250g (AlSi1) and 350g(AlZn30). After the feeder was cut off, SiC paper was used to set the surface roughness to grit 80. This was to ensure:

1. a similar surface morphology across all samples;
2. the removal of dirt and other impurities on the surface.

The resulting roughened surface was then cleaned with acetone and ethanol. The wedge was placed in cylindrical mould 1 and the entire assembly, consisting of the wedge and mould, was placed in a top loading *Carbolite* furnace. In addition to the effect of silicon and zinc content, the effect of varying heat balances was also investigated. The heat balance of the system was controlled by adjusting the preheat temperatures of the mould and wedge. In order to facilitate a reaction at the interface, the mould and wedge were preheated to 400°C in a first set of experiments. In a second batch of castings, the preheat temperature of the AlZn wedges was lowered to 200°C. All parameters used can be seen in table 3.5. The magnesium alloy AZ31 was heated up to 680°C in a steel crucible under a cover gas (SF<sub>6</sub> and nitrogen). It was initially intended to keep the difference in temperature, between the liquidus temperature of the solid AlSi alloy and the molten AZ31, constant over the varying silicon content. However, due to the very high liquidus temperature of the AlSi30 alloy this was not possible. Safety regulation in the lab prohibited heating the magnesium past 700°C. To minimise oxidation of the magnesium during casting, the casting temperature was set to 680°C. This temperature was also a

Targeted Alloy composition [wt%]	Amount of Aluminium [g]	Amount of AlSi50wt% alloy [g]	Total amount of the produced alloy [g]	Targeted Alloy composition [wt%]	Amount of Aluminium [g]	Amount of Zinc [g]	Total amount of the produced alloy [g]
AlSi1	3479	72	3542	AlZn6	3396	213	3541
AlSi6	3180	430	3570	AlZn15	3180	548	3651
AlSi15	2531	1076	3585	AlZn30	2811	1192	3972
AlSi30	1513	2202	3671				

Table 3.3: Alloy compositions and amounts of material used for the creation of the AlSi and AlZn alloys.

compromise between the low melting alloys (AlZn30 and AlSi15) and the AlSi30 alloy with a liquidus temperature of about 850°C. The melt temperature was continuously measured with a handheld meter and type K thermocouple, and once it reached the casting temperature the AZ31 was cast without a



cover gas into the mould. The pouring temperatures, listed in tables 3.4 and 3.5, are the temperatures measured shortly before pouring, after removal of the mould from the furnace.

To ensure repeatability, the melt was always poured at the same spot relative to the Al wedge. Following the casting, the assemblies were left in the furnace for a specified amount of time, referred to as holding time in tables 3.4 and 3.5. Once the assembly, consisting of mould and casting, was removed from the furnace, the casting was immediately removed from the mould. To stop any temperature-related processes (e.g. solid state diffusion) the castings were quenched with pressurised air (6bar/60s), which was used to cool down the casting to avoid thermal shock near the interface.

Al alloy	Mg alloy	Preheat Temp. [°C]	Holding time [min]	Pouring Temp. [°C]
AlSi1	AZ31	400	30	681
AlSi6				679
AlSi15				678
AlSi30				676

Table 3.4: Parameters for the AlSi wedges overcasting in which one set of experiments was performed. The assembly (AlSi alloy wedge and mould) was preheated to 400°C. The holding time was the amount of time the assembly was left in the furnace after casting and the pouring temperature was the temperature measured just before casting.

Al alloy	Mg alloy	Preheat Temp [°C]	Holding time [min]	Pouring Temp. [°C]	
AlZn6	AZ31	200	15	675	
AlZn15			30	676	
AlZn30			60	671	
AlZn6		400	0		680
AlZn15				678	
AlZn30				669	
AlZn6		400		15	681
AlZn15				30	674
AlZn30				60	673

Table 3.5: Parameters for the AlZn wedges. Three different sets of experiments, with varying preheat temperatures and holding times, were conducted. The AlZn alloy wedge and mould were heated up to the listed preheat temperature. The holding time was the amount of time the assembly was left in the furnace after casting, and the pouring temperature was the temperature measured just before casting.

## 3.4: Interfacial Phenomena in Al/Mg Compound Castings

### 3.4.1: Chemical Reaction of Alumina with Magnesium

Aluminium's intrinsic oxide layer was not found to impede interfacial formation in Al/Mg compound castings. Two mechanisms for this phenomenon were proposed:

1. the solid aluminium adjacent to the alumina layer dissolves in the liquid magnesium, and the alumina is then dispersed within the surrounding melt;
2. as the formation energy for MgO is lower than for Al<sub>2</sub>O<sub>3</sub>, it is thought that the alumina is reduced by the liquid magnesium.

To study the reaction of alumina and liquid magnesium, a solid piece of Al<sub>2</sub>O<sub>3</sub>, as well as Al<sub>2</sub>O<sub>3</sub> powder, were overcast with commercially pure magnesium. Due to practicality and financial reasons, commercially available  $\alpha$ -Al<sub>2</sub>O<sub>3</sub>, used for shot-blasting (the powder) and whetstones (the solid), was used. Purity of both types of Al<sub>2</sub>O<sub>3</sub> was given as 99.9%. Grainsize of the powder was 34-82 $\mu$ m (grade F230), and 1000 $\mu$ m for the whetstone. The chemical composition of the Al<sub>2</sub>O<sub>3</sub> was confirmed via EDS, as high concentrations of oxygen could not be detected by the OES.

A small piece of Al<sub>2</sub>O<sub>3</sub>, weighing around 10g, was cut from the bigger block. It was cleaned with acetone and stored at 300°C for 6h to remove any organic residue. This piece of Al<sub>2</sub>O<sub>3</sub> and 40g of magnesium were placed in a small graphite crucible (diameter:55mm, height:60mm), coated with boron nitride. Both materials were melted in a *Carbolite VCF 12/5* furnace and heated to 660°C under a cover gas (SF<sub>6</sub> and Nitrogen). Once molten, the magnesium in the crucible was left inside the furnace for 30min. Afterwards, the crucible was removed from the furnace and its contents cooled under ambient conditions. The surface of the metal was subsequently covered with sand to prevent oxidation.

The experiments with the Al<sub>2</sub>O<sub>3</sub> powder were conducted similarly. Three crucibles were each filled with 10g of the powder, and 40g of magnesium was placed on top of the powder. After melting, the crucibles were removed after 15, 30 and 60min. With the chosen amount of material, the ratio of magnesium atoms to oxygen atoms was almost 3:1 (approximately  $9.91 \times 10^{23}$  magnesium atoms and  $3.76 \times 10^{23}$  oxygen atoms). The excess of magnesium atoms was chosen to ensure that sufficient magnesium was present to reduce Al<sub>2</sub>O<sub>3</sub> to Al and MgO. The resulting samples were cut along the centre line and polished.

### 3.4.2: AlMgZn Phases

The results from the previous experiments indicated that the magnesium-rich phases  $\phi$  and  $\gamma$  possess higher ductility compared to the aluminium-rich phases. To further investigate these phases, three different alloys within the Mg+ $\phi$ + $\gamma$  phase field were produced from commercially pure magnesium,

aluminium and zinc. The ternary AlMgZn phase diagram and the corresponding boundaries of the  $Mg+\phi+\gamma$  phase field were calculated using the *Pandat* software package. The target chemical compositions for the alloys is displayed in figure 3.4(c).

The magnesium was melted in a small steel liner (diameter:55mm, height:110mm) under a cover gas ( $SF_6$  and nitrogen) in a *Carbolite VCF 12/5* furnace. Once the magnesium was molten the aluminium and zinc were added. The alloys were stirred to ensure an even distribution of elements before being cast into a preheated ( $200^\circ C$ ) cylindrical (diameter:20mm) mould. The alloys were slowly cooled down under ambient atmosphere. Two cylinders of each alloy were cast, resulting in two  $\sim 300g$  castings of each alloy.

A small piece (approximately  $15mm \times 15mm \times 15mm$ ) of each alloy was cut from the cylinders, mounted and polished. To compare the as-cast microstructure of an AlMgZn alloy with the compound casting, a reference sample of the AlZnMg phase, as found at the interface of the AlZn30/AZ31 compound casting, was prepared. The reference sample was cut from a compound casting produced earlier, mounted and polished. The microstructures of the prepared samples were inspected via SEM and XRD. A small amount (39g) of the AlZn30/AZ31 compound casting was kept to be used for thermal analysis.

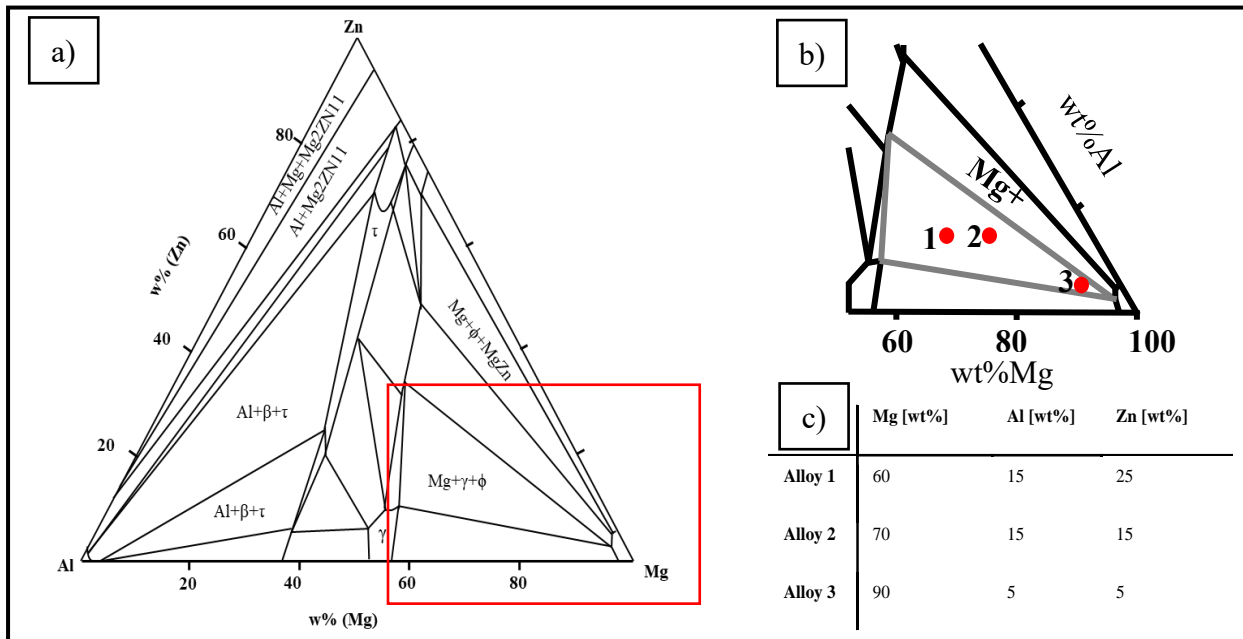


Figure 3.4. (a) Ternary phase diagram of the Al-Mg-Zn system at  $200^\circ C$ , calculated with the *Pandat* software package. The magnesium-rich region is highlighted. (b) Chemical composition of the three alloys within the highlighted  $Mg+\phi+\gamma$  phase field at  $200^\circ C$ . (c) Numerical values for the chemical composition of the three AlMgZn alloys.

### 3.4.3: Thermophysical Description of Interfacial Reaction using Numerical Simulation

Knowledge about the temperature distribution and cooling rates at the interface allows an understanding, and eventually prediction, of growth of the intermetallic layers in the material bond.

While a measurement of temperature directly at the interface is possible with thermocouples, they only allow for the measurement of the temperature from a small area. Numerical simulation was used to gain an understanding of the temperature gradients near the interface throughout the whole casting, and thus complement those that were measured. As the simulation is only an approximation of reality, the comparison and validation via experimentation is essential. As a consequence, cooling curves within the Al/Mg compound castings were recorded and then used in validating the results from the simulation. It is assumed, due to the symmetry of mould 4, that the heat flow is nearly identical in all horizontal directions. Heat loss to the atmosphere and through the bottom of the mould is neglected. Similarly, heat loss through the inlet is also considered to be negligible, as the inlet functions as a hot spot. Hence, cooling curves were recorded at two different spots:

1. directly at the interface at a height of 1mm above the base of the mould and directly opposite the inlet;

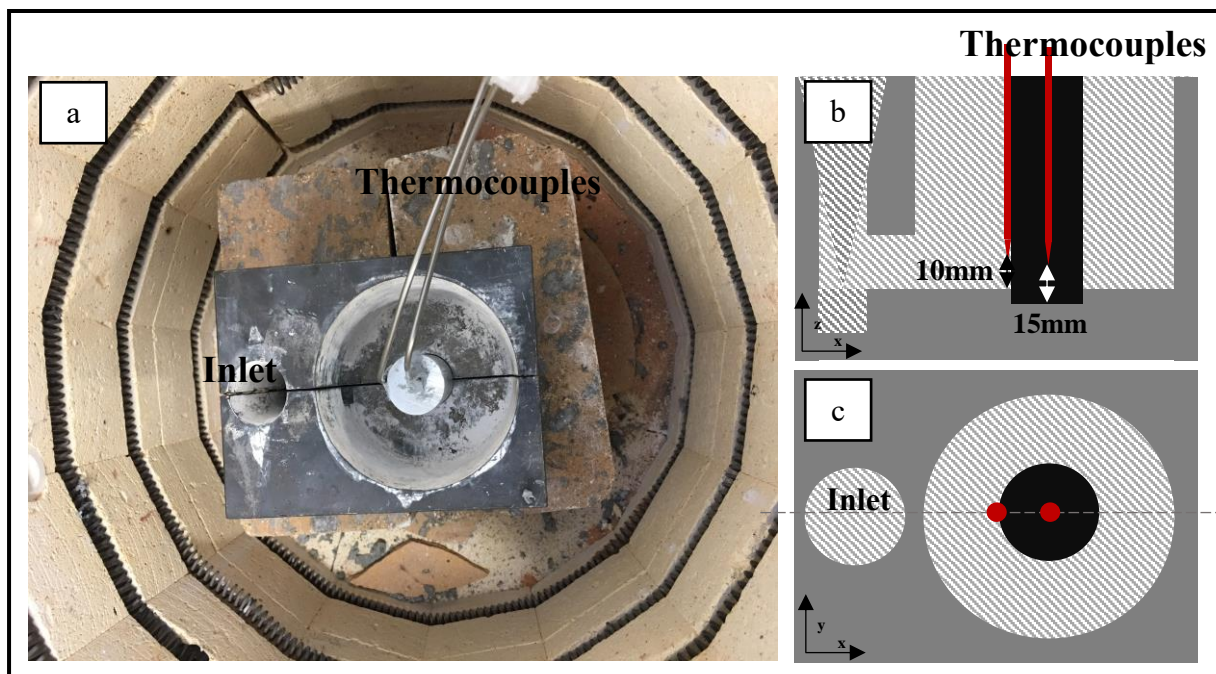


Figure 3.5. Experimental setup for the recording of cooling curves of an Al/Mg compound casting: (a) photograph of the mould and thermocouples before casting; (b) schematic side view, along the parting line, of the positions of the thermocouples; and (c) schematic top view showing the position of the thermocouples.

2. in the middle of the aluminium alloy cylinder at a height of 10mm above the base of the mould (i.e. 15mm from the bottom of the aluminium cylinder).

The whole experimental setup, with the position of the thermocouples, is displayed in figure 3.5. Type K thermocouples with diameters of 3mm were used. They were fixed at the described positions using a silicate glue. These thermocouples were chosen because smaller thermocouples (1.5mm) were difficult to fix to the specified position. The response time of 3mm thick thermocouples is given as 0.55s, which is deemed sufficient considering that the filling, solidification and cooling process is several minutes (~5min) long (Omega Engineering, 2020). Similarly, the impact on the temperature within the mould is considered negligible, considering the small volume of the thermocouples compared to the mould/alloys. However, the thermocouples are anticipated to affect flow of the magnesium melt, and thus interaction with the aluminium alloy, especially opposite the inlet. Consequently, the material bond was not studied in the samples with thermocouples.

For the casting, AZ31 and an AlZn30 cylinder were used. The AlZn30 cylinder was produced from left-over alloys (commercially pure aluminium and zinc) from earlier experiments. The AZ31 was melted under a cover gas ( $\text{SF}_6$  and Nitrogen) and heated to  $660^\circ\text{C}$ . The Al cylinder was placed in the recess of mould 2 and placed in a furnace, which was subsequently heated to  $200^\circ\text{C}$  or  $400^\circ\text{C}$ . The AZ31 was cast without a cover gas into the mould. The temperature was continually recorded (1Hz) with a *Maxthermo YC-727* meter. The temperature was measured until it dropped below  $350^\circ\text{C}$ . This temperature was chosen as a threshold as it is the lowest solidus temperature in the AlMgZn system. The casting was subsequently removed from the furnace and quenched with pressurised air (6bar/120s).

For the numerical simulation of the cooling rate and temperature distribution of the material bond, the *Magma 5.4* software package was used. The mould and casting process were modelled using the CAD tool included in the software package. The created geometry, displayed in figure 3.6, was then meshed;

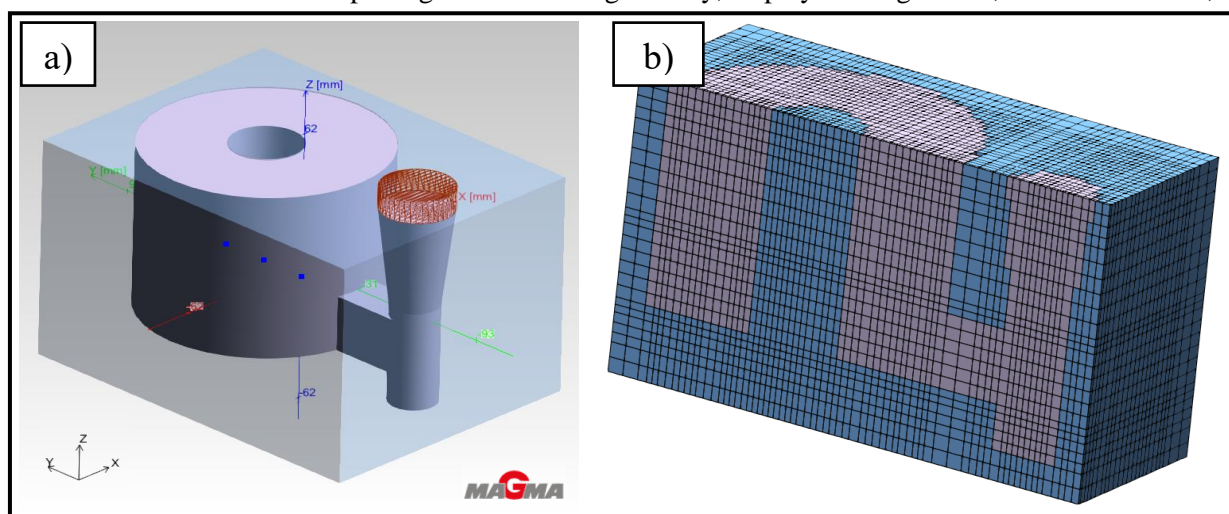


Figure 3.6. Images of mould 4 in Magma 5.4: (a) CAD drawing of the mould. The mould itself is displayed as transparent; and (b) Cross-sectional view along the parting line of the mould after meshing, with the displayed mesh consisting of 101,500 cells.

a mesh size of 101,500 cells (including the 28,900 cavity cells) was found to be a good compromise between computing time and resolution. A critical part for the numeric simulation of casting parts is the gate between the inlet and the actual casting part. The gate controls the filling, and therefore inaccuracies in its modelling and meshing could lead to a number of errors. All parameters were chosen to mirror reality as closely as possible. Thermophysical properties (HTC, heat capacity, thermal conductivity) for the alloys AlZn30 and AZ31 were not available in the Magmasoft database. Therefore, data from the Magmasoft database for pure aluminium and AZ91 were used for an initial simulation. The most important parameters are displayed in table 3.6, with a complete list used in the simulation given in the appendix.

The acquired simulated temperature curves were then compared to the actual measurements. Based on this comparison, the heat transfer coefficient between the Al and Mg alloys, within the Magmasoft database, was adjusted. Using this new set of data, another simulation was run, which was then compared to the actual measurements again. This was repeated for several iterations until the simulated temperature curves were in a close match with those measured, and further manipulation of the parameters did not result in an improved overlap of the two curves. The best match of the simulated and experimental curves was achieved with a constant (over temperature) HTC, shown in figure 3.7.

Casting Temp [°C]	Preheat Temp. [°C]	Pouring time [s]	Cooling time [s]
660	400	20	320
660	200	20	285

Table 3.6: Selection of important parameters used in the numerical simulation of the filling and solidification of an Al/Mg compound casting.

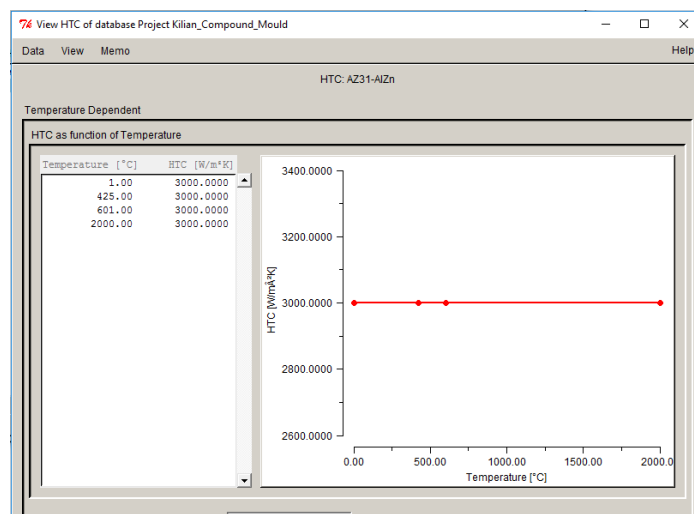


Figure 3.7. Heat transfer coefficient (HTC) between the AZ31 melt and AlZn alloy. A constant HTC provided the best agreement with the experimental results.

### 3.4.4: Growth of the Material Bond via Solid State Diffusion in Diffusion Couples

Growth of the interface via solid state diffusion was assessed with diffusion couples. Aluminium, AZ31 and unused AlZn30 alloy from the previous experiments were melted separately and cast into a cylindrical shape using Mould 2. From these cylinders several disks with a height of 10mm were cut. The surface of the disk was ground to grit 80 before being wiped with acetone, using cotton wool, and rinsed with ethanol. Each diffusion couple consisted of an aluminium and a magnesium disk. The disks were clamped together with a toolmaker's clamp and then placed in a *Carbolite VCF 12/5* furnace with a steel liner. To facilitate a diffusion reaction, the aluminium disk was placed on top. As the heat treatment temperature is above the liquidus temperature of some AlMgZn phases, a cover gas (SF<sub>6</sub> and nitrogen) was used to prevent oxidation. The temperature inside the furnace was continually measured with a handheld meter, and once it reached its desired temperature, the diffusion couple was left inside the furnace for a specified amount of time. After removal from the furnace, the diffusion couples were quenched in water (25°C). The temperature and holding time for each couple was varied as detailed in table 3.7.

Sample Number	Aluminium alloy	Magnesium alloy	Temperature [°C]	Covergas used	Tolerance [°C]	Holding time [min]
1	AlZn30	AZ31	350	✓	+/- 10	1440
2	AlZn30	AZ31	440	-		180
3	AlZn30	AZ31	400	✓		240
5	AlZn30	AZ31	420	✓		240
6	AlZn30	AZ31	420	✓		300
7	AlZn30	AZ31	430	✓		240
8	AlZn30	AZ31	440	-		240
9	AlZn30	AZ31	450	✓		240
10	AlZn30	AZ31	450/420	✓		60/180
11	Al	Mg	400	-		120
12	Al	Mg	450	✓		120
13	Al	Mg	440	✓		120

Table 3.7: List of temperatures, holding times and alloy combinations for every diffusion couple. The diffusion couple was heated from room temperature to the specified temperature. The given holding time is the time after the furnace reached this temperature. The temperature of sample 10 was lowered to 420°C after a holding time of 60min in an attempt to control the diffusion rate.

To assess the difference in the growth of the interface in a compound casting and diffusion couple, another trial was conducted. An Al/Mg compound casting, identical to the ones described above, was produced using Mould 4. To prevent diffusion due to the casting process, the casting was immediately

removed from the mould upon complete solidification and quenched with pressurised air (6bar/180s). A 10mm thick disk was cut out of the casting, the exact location from where the disk – labelled as Disk SSD (solid state diffusion) – was cut out being displayed in figure 3.8. This disk was then subjected to a heat treatment. The disk was placed in a furnace and slowly heated up to 300°C. This lower temperature, compared to the diffusion couples, was chosen as a material bond was already existing in the compound casting, and to prevent partial melting of the disk (as was observed with the diffusion couples). Upon reaching 300°C, the disk was removed (after 15min) from the furnace and quenched in water (25°C). The thickness of the interface was measured with an optical microscope before the disk was returned to the furnace. This action was repeated for 30min and 60min.

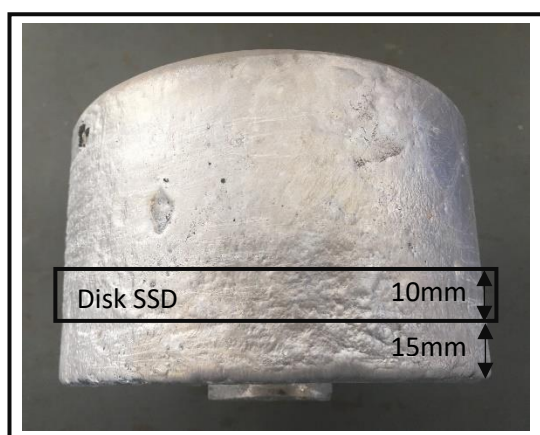


Figure 3.8. Macrograph of the compound casting after removal of gate and inlet with the position from where the disk (SSD), used as a reference sample, was cut.

## 3.5: Mechanical Properties of the Material Bond of Al/Mg Compound Castings

### 3.5.1: Mechanical Strength of the Material Bond

To assess the impact of interfacial thickness and morphology on the bond's mechanical strength, a number of castings were produced. Using mould 4, several Al/Mg compound castings were produced. The cylindrical aluminium inserts were produced with mould 2. After casting, the feeder of the Al cylinder was cut off and the surface roughness set to grit 80 using silicon carbide paper. Cotton wool soaked in acetone was used to clean the surface of the cylinders before they were rinsed with ethanol. The cylinders were placed in the recess of mould 4. The mould and Al insert were then placed in a *Nabertherm Top 190* furnace and heated to a set temperature as specified below. Similar to the previous experiments, the magnesium alloy was heated to temperature under a cover gas ( $\text{SF}_6$  and nitrogen). Upon reaching the desired temperature (all parameters are shown in table 3.8), the magnesium melt was



poured manually into mould 4. After complete filling of the mould, the casting was left in the furnace for a set amount of time.

To modify the material bond and thus achieve a varying thickness and morphology, certain parameters were altered over the course of the castings. The altered parameters were as follows.

1. Alloys used: it was established in the earlier trials that the choice of alloys has an impact on thickness and morphology of the material bond between the two alloys. A number of different combinations were used.
  - Elektron 21 magnesium and 7005 series aluminium alloy were used as both are high-performance materials used in the aerospace and automotive industries.
  - The magnesium- and zinc-rich phases in AlZn alloys showed interesting mechanical properties.
  - The previous experimentation revealed an increased brittleness of compound castings involving AlSi alloys. Thus, no AlSi alloys were used.
2. Melt temperature: it was evident from the experiments detailed in sections 3.3 and 3.4 that a connection between melt temperature and thickness of the interface exists. The higher the difference between melt temperature and solid metal, the more the material is dissolved.
  - Casting temperatures were varied between 660 and 680°C. The lower limit, 660°C, was the lowest temperature at which the mould could be completely filled before the inlet was solidified. It was decided not to exceed 680°C in order to minimise the possibility of oxidisation.
3. Preheat temperature: similar to melt temperature, the preheat temperature of the mould affects the material bonding, as it affects the amount of solid material that is dissolved by the liquid metal.
  - 200°C and 350°C were used as preheat temperatures.
4. Holding time: as solid state diffusion is progressing dependent on temperature and time, the longer the mould remains in the furnace at elevated temperatures after casting, the more diffusion is facilitated.

All parameters and experiments are listed in table 3.8. After casting the gating system and inlet were cut off and a 10mm thick disk, labelled POT (push-out test), was machined out of the casting. The disk was sectioned 5mm from the bottom of the casting, with the exact position shown in figure 3.9(a).

A three-point bending machine was used to exert force on the aluminium and record a load/displacement curve. The POT disks were placed upon a hollow cast iron cylinder and a tool steel disk (height:10mm, diameter:10mm) was used to transfer the force of the machine onto the aluminium cylinder of the compound casting disk. The diameter of the steel disk was chosen to ensure the steel disk was never in contact with the material bond of the compound casting. The exact experimental setup is detailed in

figure 3.9(b). It has been established in the previous chapter that formation of the material bond is a complex interaction of several factors (i.e. heat flow, dissolution of the solid phase), which are difficult to precisely control during experimentation. Consequently, the results have to be interpreted with regard to the anticipated limited reproducibility and representation. Nevertheless, previous researchers have highlighted the usefulness of push-out testing for a qualitative assessment of the mechanical strength of the material bond in compound castings (Sacerdote-Peronnet et al., 2007; Durrant, Gallerneault, and Cantor, 1996; Emami et al., 2013; Hajjari et al., 2011).

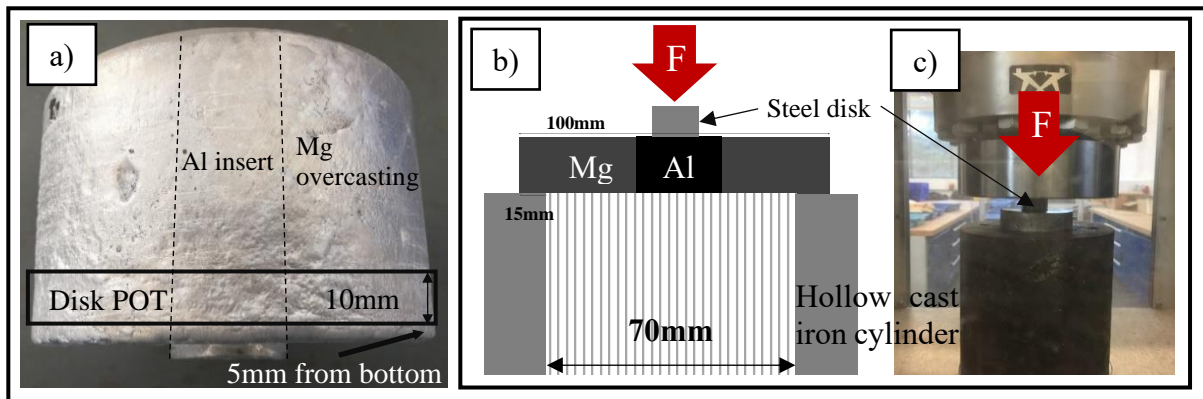


Figure 3.9. (a) Macrograph of a compound casting with the position from where the disks for the push-out tests (labelled Disk POT) were sectioned, indicated. (b) Schematic of the push-out tests. (c) Photograph of the push-out tests.

Number	Compound casting		Casting parameters		
	Al-alloy (insert)	Mg-alloy (overcasting)	Melt temperature [°C]	Preheat temperature [°C]	Holding time [min]
1	AlZn30	Mg	668	350	30
2	Al	E21	679	350	30
3	Al	MgZn30	661	200	15
4	Al	E21	674	200	15
5	Al	AZ31	665	350	30
6	Al	Mg	660	350	15
7	7005	AZ31	670	350	15
8	AlZn15	AZ31	671	350	30
9	Al	E21	675	350	15
10	AlZn15	AZ31	660	350	15
11	AlZn30	AZ31	673	350	30
12	7005	AZ31	669	350	30
13	7005	AZ31	668	200	30
14	AlZn30	AZ31	696	400	15
15	AlZn30	AZ31	665	200	15
16	AlZn30	AZ31	667	350	30
17	Al	AZ31	663	350	30

Table 3.8: Material combinations and casting parameters for the Al/Mg compound castings destined for pushout testing.

### 3.6: References

BIERMANN, H. and KRÜGER, L. (2014) *Moderne Methoden der Werkstoffprüfung*. Weinheim: Wiley-VCH.

COX, J. and PIDGEON, L. (1963) The X-Ray Diffraction Patterns of Aluminum Carbide  $Al_4C_3$  and Aluminum Oxycarbide  $Al_4O_4C$ . *Canadian Journal of Chemistry*, **41**(6), pp. 1414-1416.

DUBOIS, G. (2018) *Modelling and Simulation: Challenges and Best Practices for Industry*. New York: CRC Press.

HEMMINGER, W. (1990) Methoden der Thermischen Analyse. *Berichte der Bunsengesellschaft*, **94**(2), pp. 205-206.

INTERNATIONAL ORGANISATION FOR STANDARDISATION (2019) Available: <https://www.iso.org/obp/ui/-iso:std:iso:6507:-1:ed-4:v1:en/> [27 February 2019]

JUNQING, W., XUN, S., YANG, G., PENGHUA, W., HAILAN, L., LIMEI, B., and XINZHI, S. (2008) Numerical Simulation and Process Optimization for Producing Large-Sized Castings. *中国铸造: 英文版*, **5**(3), pp. 179-185.

KEEBLE, E. (2019) Error and Uncertainty in Metallographic Measurement, in VANDER, G. (ed.) *100 Years of E04 Development of Metallography Standards*. ASTM International, pp. 53-65.

MI, G., LI, C., LIU, Y., ZHANG, B., and SONG, G. (2013) Numerical Simulation and Optimisation of the Casting Process of a Casting-Steel Wheel. *Engineering Review*, **33**(2), pp. 93-99.

REIMER, L. (1985) *Scanning Electron Microscopy*. Berlin: Springer-Verlag Berlin Heidelberg.

SKOOG, D. and LEARY, J. (2013) *Instrumentelle Analytik*. 6<sup>th</sup> edn. Berlin/Heidelberg: Springer-Verlag Berlin/Heidelberg.

## Chapter 4: Material Selection in Al/Mg Compound Castings

### 4.1: Selection of a Magnesium Alloy

Macro- and micro-graphs of the material bond resulting from the overcasting of commercially pure aluminium with magnesium alloys are displayed in figure 4.1. Interfacial thickness varies strongly with the type of magnesium alloy used. The strongest reaction and thus thickest material bond ( $\sim 4000\mu\text{m}$ ) was observed using commercially pure (99.9%) magnesium. Replacing magnesium with AZ31 resulted in a less distinct material bond, while no reaction between the aluminium and AZ91 was observed. As all boundary conditions (pre-heat temperature of the mould, casting temperature and aluminium alloy used) were kept constant, the observed changes in the material bond can be solely attributed to the change in aluminium content in the magnesium alloy. Consequently, reactivity between the metals in compound castings correlates directly with material bond thickness. As displayed in figure 4.1, the material bond of the Al/Mg and Al/AZ31 compound castings consisted of two layers, with the  $\beta$  phase adjacent to the aluminium and the  $\gamma$  phase next to the magnesium. Embedded within the  $\gamma$  phase, eutectic magnesium was present. This ‘dual-layer’ appearance of the material bond, observed in the samples, is in good accordance with results reported in the literature. The presence of both intermetallic phases, and overall morphology, were independent of alloy used. No significant amounts of other chemical compounds were found. Traces of silicon, iron and manganese were present, which can be traced back to impurities in the metals used and the casting process. EDX analysis also detected small amounts of oxygen. The oxygen is thought to be in the form of oxides, resulting either from a reaction of the melt with the atmosphere during casting or as reaction product of the hydrogen absorption of the melt. The

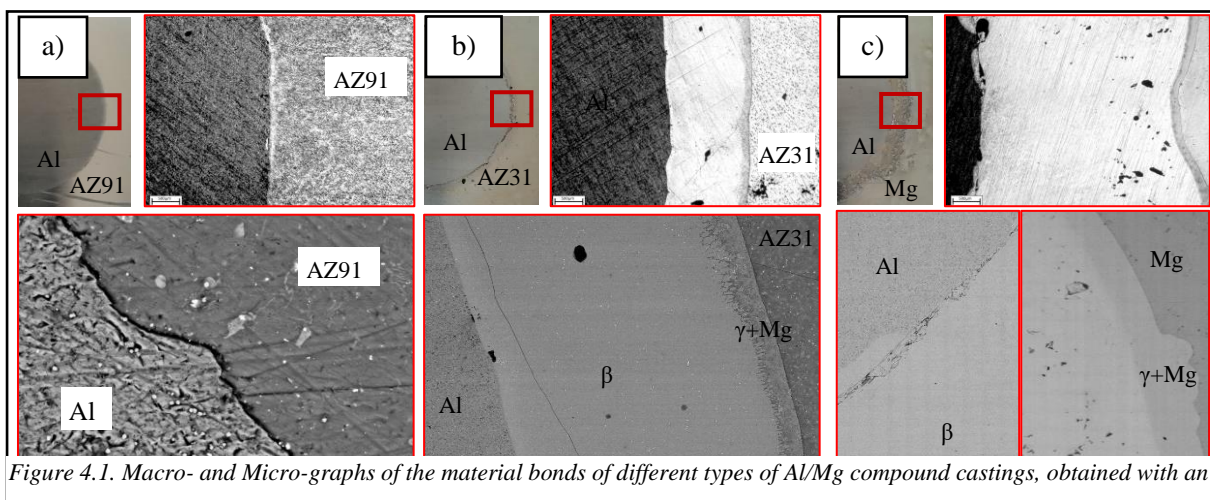


Figure 4.1. Macro- and Micro-graphs of the material bonds of different types of Al/Mg compound castings, obtained with an optical microscope and SEM with BSE detector: (a) Al/AZ91; (b) Al/AZ31; and (c) Al/Mg.

hydrogen level of the magnesium melt was not measured before casting; as such, MgO would have been formed during hydrogen absorption according to the following equation:



The thickness of each phase was measured with an optical microscope, at three different spots; given values are averages. The measured values can be found in table 4.1. The standard deviations of the measurements are given as an indication of the uniformity of the thickness of the material bond. Total interfacial thickness in the Al/Mg compound castings was found to be more than double that of the Al/AZ31. This difference in overall thickness was due to the greater thickness of the aluminium-rich phase  $\beta$  in the Al/Mg compound casting.

The size of the magnesium-rich phase  $\gamma$  was found to be almost identical in the Al/Mg and Al/AZ31 samples (on average  $169 \pm 16 \mu\text{m}$  and  $195 \pm 46 \mu\text{m}$  respectively). It should be noted that the variation in thickness of the  $\gamma$  phase was significantly higher than for the  $\beta$  phase. As discussed earlier the  $\beta$  and  $\gamma$  phases have different growth rates. Therefore, these results indicate that the conditions during castings and solidification favour the growth of the  $\beta$  phase. Despite using ethanol instead of water for the final grinding step and polishing, signs of corrosion are visible on the surface of the magnesium. This rapid corrosion is seen as critical to the mechanical properties of the compound casting, even though it is not found to directly affect material bonding.

Alloy combination		Average thicknesses [ $\mu\text{m}$ ]		
		$\beta$ phase	$\gamma$ phase	total thickness
Al/Mg		3792 $\pm$ 163	195 $\pm$ 46	3987
	Deviation [%]	4.3	23.6	3.7
Al/AZ31		1505 $\pm$ 72	169 $\pm$ 16	1674
	Deviation [%]	4.8	9.9	4.3
Al/AZ91		No reaction	No reaction	No reaction

Table 4.1: List with the thicknesses of the material bonds of Al/Mg, Al/AZ31 and Al/AZ91 compound castings. The standard deviations over the three measurements are given. Deviations can be used as a measure to assess uniformity of the material bond in terms of thickness.

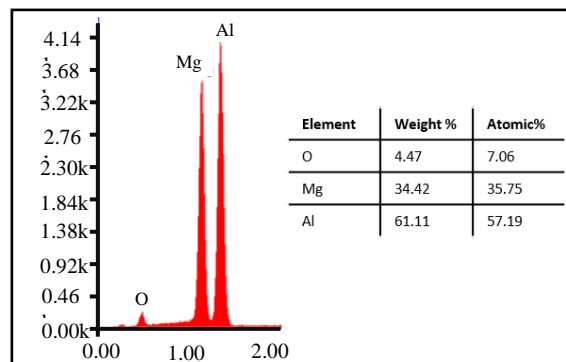


Figure 4.2. EDX analysis of the  $\beta$  phase. The detected oxygen is the result of a reaction of the magnesium with the atmosphere, or hydrogen absorption.

## 4.2: Influence of Silicon and Zinc on the Formation of the Material Bond

The microstructure of an alloy is closely connected to its mechanical properties. It is a common practice to alter the microstructure by adding varying amounts of allotted elements and studying their effect on the mechanical properties. In this chapter, the effects of silicon and zinc on the microstructure of the material bond of Al/Mg compound castings is presented. The effects of increasing amounts of these alloying elements on the phase selection in, and thickness of, the material bond are discussed. The microstructure is then linked to the mechanical properties, which were approximated with Vickers micro-hardness measurements.

The optical macrographs obtained of all samples are shown in figures 4.3 and 4.4. As temperature and composition of the magnesium alloy were kept constant over all experiments, all observed changes can be directly attributed to the aluminium alloy. The figures show that a material bond formed in all samples regardless of alloy used and chemical composition. However, the thickness of the material bond varied significantly with the alloys used. Overcasting an aluminium alloy containing zinc tended to result in a thicker material bond compared to those alloys containing silicon alloys.

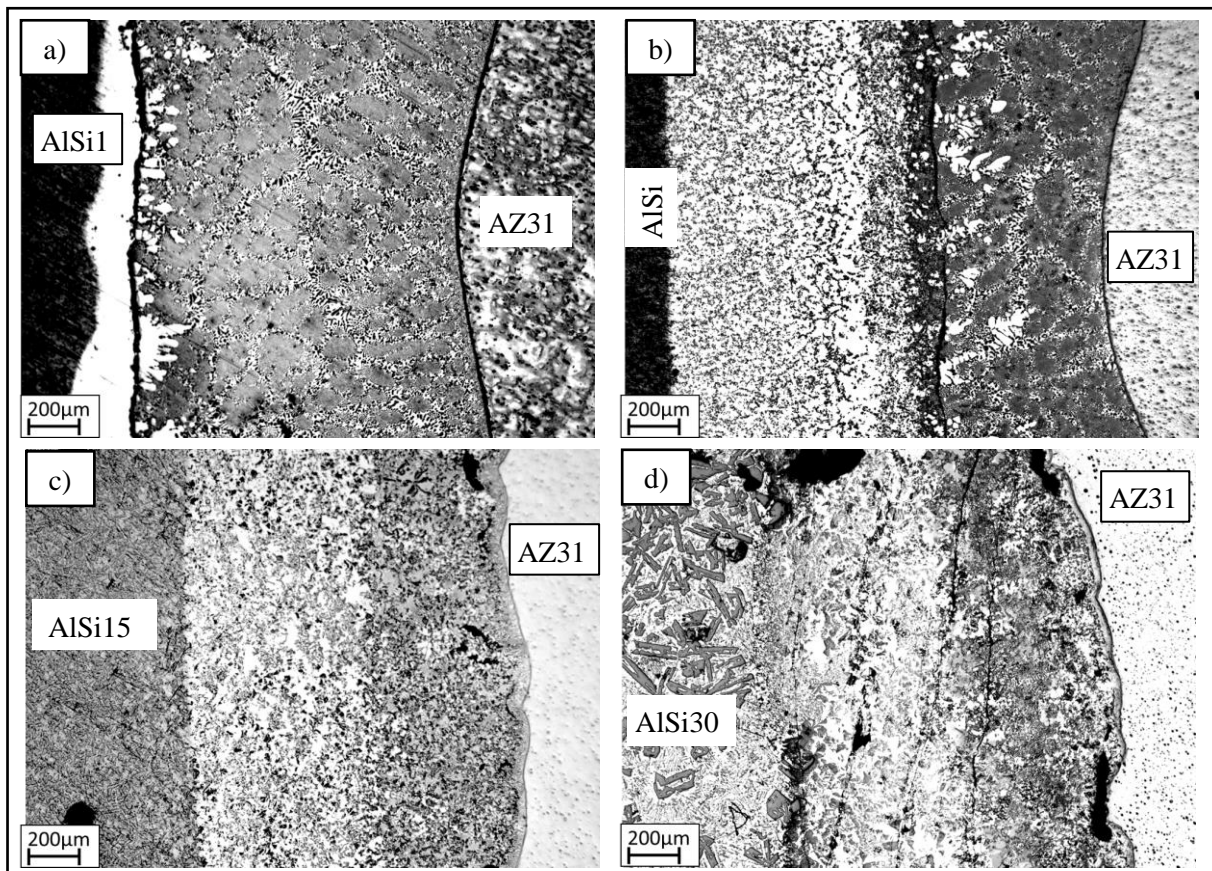


Figure 4.2. Optical micrographs of the material bond in AlSi/AZ31 compound castings:

(a) AlSi1/AZ31; (b) AlSi6/AZ31; (c) AlSi15/AZ31; and (d) AlSi30/AZ31.

Values for the thickness of the material bond over one sample are given in figure 4.5. Values in figure 4.5 are the averages of five separate measurements. Thickness was measured at the visible minimal and maximal thickness in addition to randomly selected points along the whole material bond. The standard deviation was used as a measure of the uniformity of the thickness of the material bond. Overall, higher zinc contents appeared to cause larger thicknesses of the material bond. However, the greatest average thickness, of approximately  $8072 \pm 581 \mu\text{m}$ , was achieved by using an AlZn15 alloy, which surpassed that of an AlZn6 ( $3984 \pm 332 \mu\text{m}$ ) and AlZn30 ( $6815 \pm 544 \mu\text{m}$ ). The thickness of the material bond in AlSi/AZ31 compound castings ranged between  $1295 \pm 104 \mu\text{m}$  for an AlSi30 alloy to  $1144 \pm 235 \mu\text{m}$  for an AlSi1 alloy. No clear trend was observable. While traces of oxygen, thought to be oxides from the casting process or resultant from hydrogen absorption, were found throughout the castings, no larger scale residue of the alumina layer in the form of oxide skins was detected. As the alumina layer is, at  $\sim 4\text{nm}$ , rather thin, it is thought to be finely dispersed within the whole casting (Campbell et al., 1999). Pores of various sizes were found in the material bond of the castings. They can be classified based on their appearance into three categories.

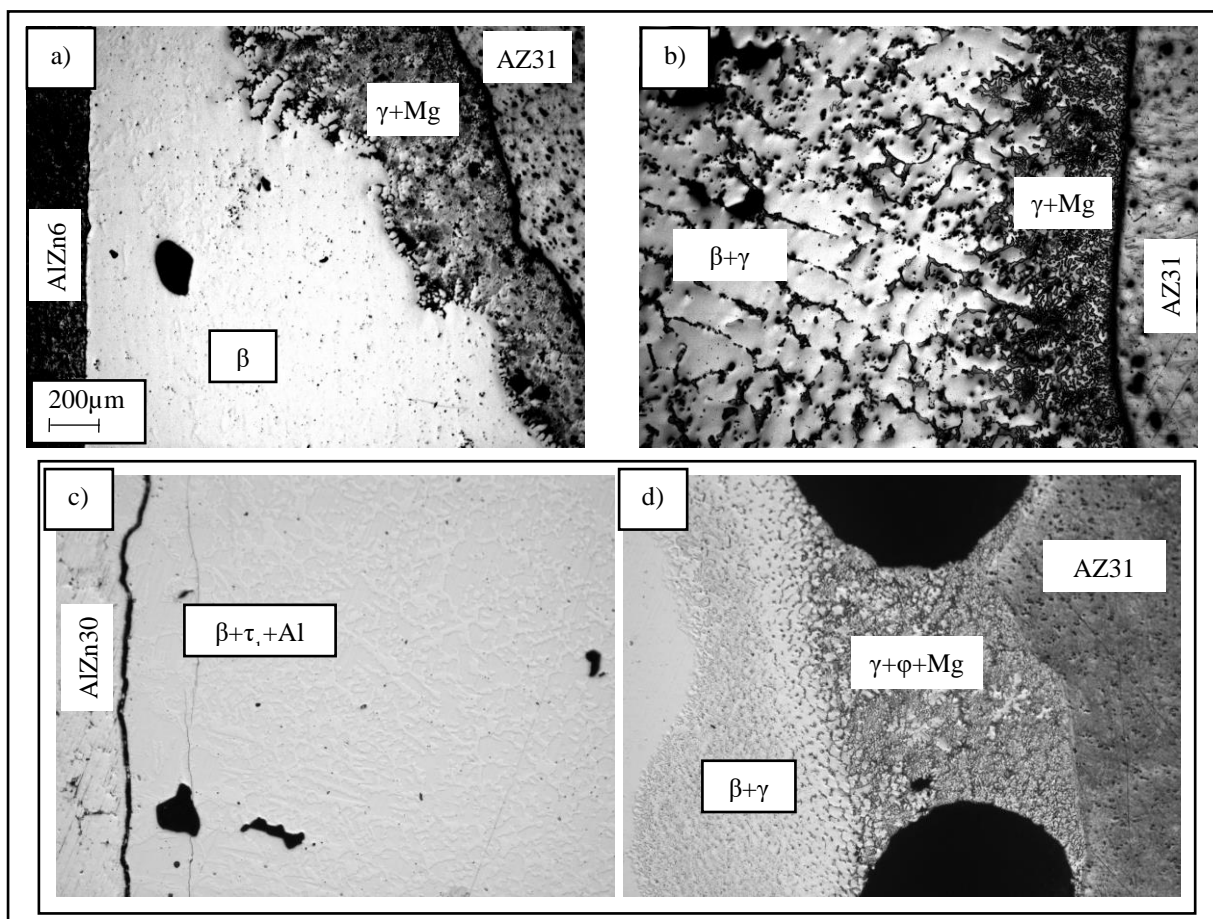


Figure 4.3. Optical micrographs of the material bond in AlZn/AZ31 compound castings:

(a) AlZn6/AZ31; (b) AlZn15/AZ31; (c) aluminium-rich side of the material bond of an AlZn30/AZ31 compound casting; and (d) magnesium-rich side of the material bond of an AlZn30/AZ31 compound casting.



- Pores as a result of the low solidus temperature of the intermetallic phases. The material bond solidifies after the bulk of the magnesium alloy, leading to insufficient feeding and thus shrinkages. Examples of such pores are shown in figures 4.4(a) and 4.4(c).
- Porosity as seen in figure 4.3(c) and 4.3(d) are thought to stem from hydrogen precipitation during solidification. Hydrogen precipitates between the magnesium dendrites, causing the observed non-spherical shape. Moreover, slow cooling rates, such as present in this work ( $\sim 20^{\circ}\text{C}/\text{min}$ , see section 5.4), increase the volume fraction of hydrogen porosity (Anyalebechi, 2013).
- Relatively large ( $\sim 200\text{-}1000\mu\text{m}$ ), evenly-shaped pores were found in the layer adjacent to the AZ31 alloy in AlZn30/AZ31 compound castings (see figure 4.4(d)). As this kind of pore was only found in AlZn30/AZ31 compound castings, they are not believed to be hydrogen porosity. Section 4.2.2 will elaborate further on these pores.

This work was focused on identifying phases found within the material bond, and hydrogen porosity and shrinkage were thus not further investigated.

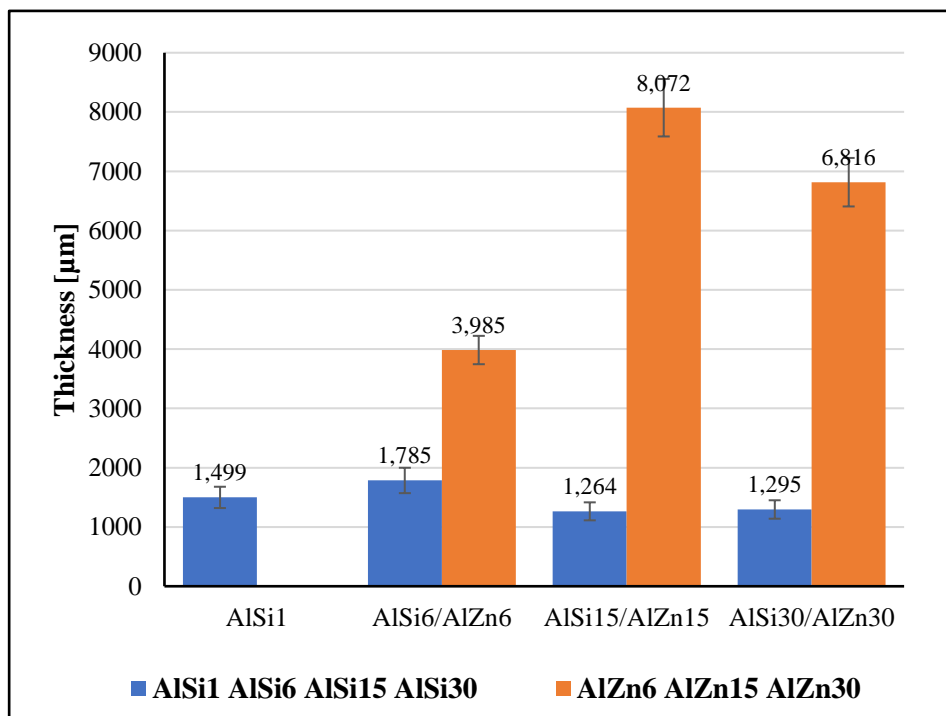


Figure 4.4. Average thickness of the material bond in AlSi/AZ31 and AlZn/AZ31 compound castings. The thickness of the material bond of AlZn/AZ31 compound castings is up to 5x larger compared to AlSi/AZ31 compound castings. The error bars are indicating the standard deviation and thus uniformity of the thickness of the material bond.

## 4.2.1: The Material Bond of AlSi/AZ31 Compound Castings

In this section, the microstructure of the material bond in AlSi/AZ31 compound castings is discussed. The results from the characterisation of the material bond with OM and SEM are presented and the effects of varying amounts of silicon are explained.

Phase identification and characterisation of the material bond was conducted with the SEM's BSE detector. All phases found in the material bond of the AlSi/AZ31 samples were in good accordance with the corresponding Al-Mg-Si phase diagrams, displayed in figures 4.6 and 4.8. The phase diagrams were calculated with the software *Pandat*. The material bond of an AlSi1/AZ31 compound casting and a linescan across it are displayed in figure 4.7. The two intermetallic phases  $\beta$  and  $\gamma$  accounted for the majority of the material bond. As expected, the aluminium-rich intermetallic phase was found adjacent to the aluminium alloy and the magnesium-rich phase next to the AZ31. Contrary to results obtained in the other AlSi/AZ31 compound casings, detailed in the following paragraphs below, the  $\beta$  phase was not found in a separate distinct layer. Rather, the  $\beta$  phase was found in small patches on the aluminium side of the fracture. The presence of eutectic magnesium within a matrix of the  $\gamma$  phase is in good agreement with results reported earlier, as well as in the literature. The silicon was found to exclusively react, as predicted in the phase diagram, with the magnesium, to form  $Mg_2Si$  particles. Closer inspection of the fracture revealed that it propagated along the phase boundary between the two intermetallic phases  $\beta$  and  $\gamma$  as well as along an agglomeration of  $Mg_2Si$  particles. Almost no  $Mg_2Si$  particles were present on the magnesium side of the fracture.

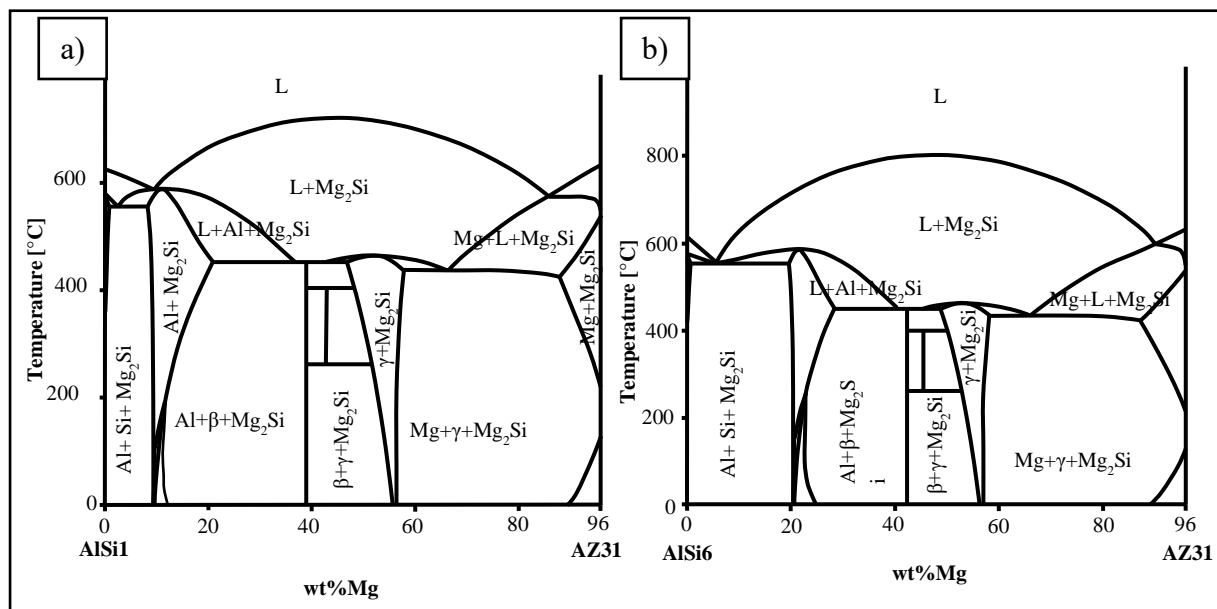


Figure 4.5. (a) Combined AlSi1/AZ31 phase diagram. (b) Combined AlSi6/AZ31 phase diagram.

Both phase diagrams were calculated using the *Pandat* software package.

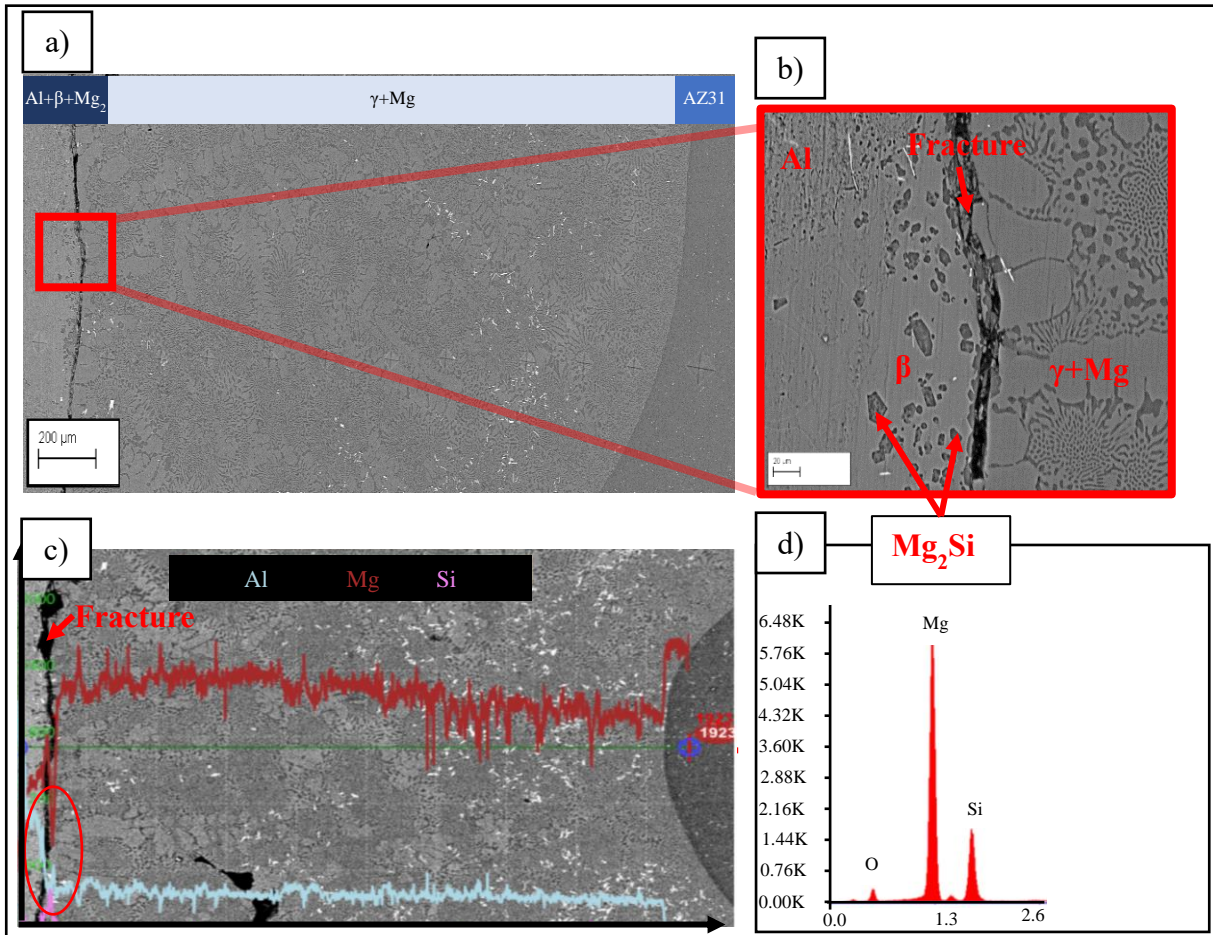


Figure 4.6. SEM micrographs of an AlSi1/AZ31 compound casting. (a) Overview of the whole material bond. It consists of two layers with its constituents marked above the micrograph. On the aluminium side of the fracture the  $\beta$  phase and  $Mg_2Si$  particles were present. On the magnesium side the magnesium-rich phase  $\gamma$  and elementary magnesium were detected. (b) The vicinity of the fracture in greater detail. No aluminium-rich phases or  $Mg_2Si$  particles were found on the magnesium-rich side of the fracture. (c) Linescan, acquired via EDX, across the material bond. A clear drop in aluminium and silicon content at the location of the fracture (circled) is visible. (d) Chemical analysis of the  $Mg_2Si$  particles using EDX.

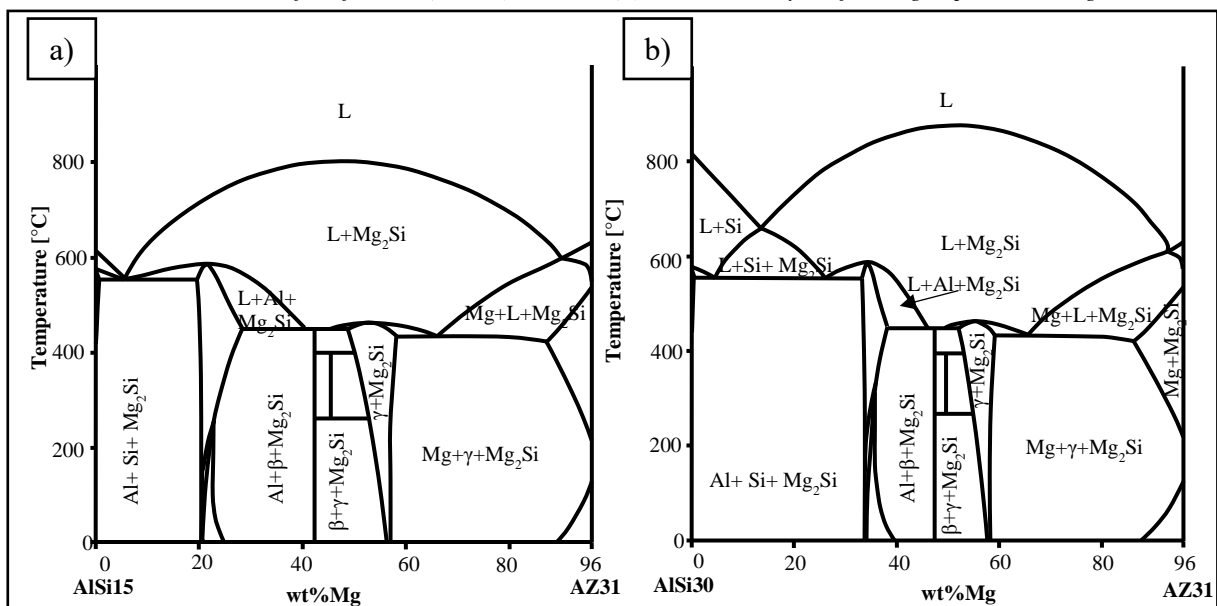


Figure 4.8. (a) Combined AlSi15/AZ31 phase diagram. (b) Combined AlSi30/AZ31 phase diagram.

Both phase diagrams were calculated using the Pandat software package.

This contradiction to the phase diagram can be traced back to fracture impeding the diffusion of silicon across the material bond, and its subsequent reaction to form  $Mg_2Si$ . Similarly, as the fracture prevented the diffusion of the aluminium and magnesium, no distinct concentration gradient of either element was detected. Impurities in the used metals manifest themselves in the material bond as needle- and plate-like structures. These were identified to be mostly manganese- and oxygen-based. As seen in figure 4.9, increasing the amount of silicon from 1wt% to 6wt% resulted in a similar make-up of the chemical composition in the material bond. The main constituents were identified to be the two intermetallic phases  $\beta$  and  $\gamma$ , eutectic magnesium and  $Mg_2Si$ . The formation of an additional distinct layer in the material bond was observed. This third layer consisted of the  $\gamma$  phase but no elementary magnesium was detected. Instead,  $Mg_2Si$  particles were found throughout this layer, embedded within a matrix of  $\gamma$ , forming this additional layer of  $\gamma$  phase and  $Mg_2Si$  particles. Unlike the previous experiment, the layer consisting of the  $\beta$  phase is larger and more distinct. A possible explanation for this behaviour is

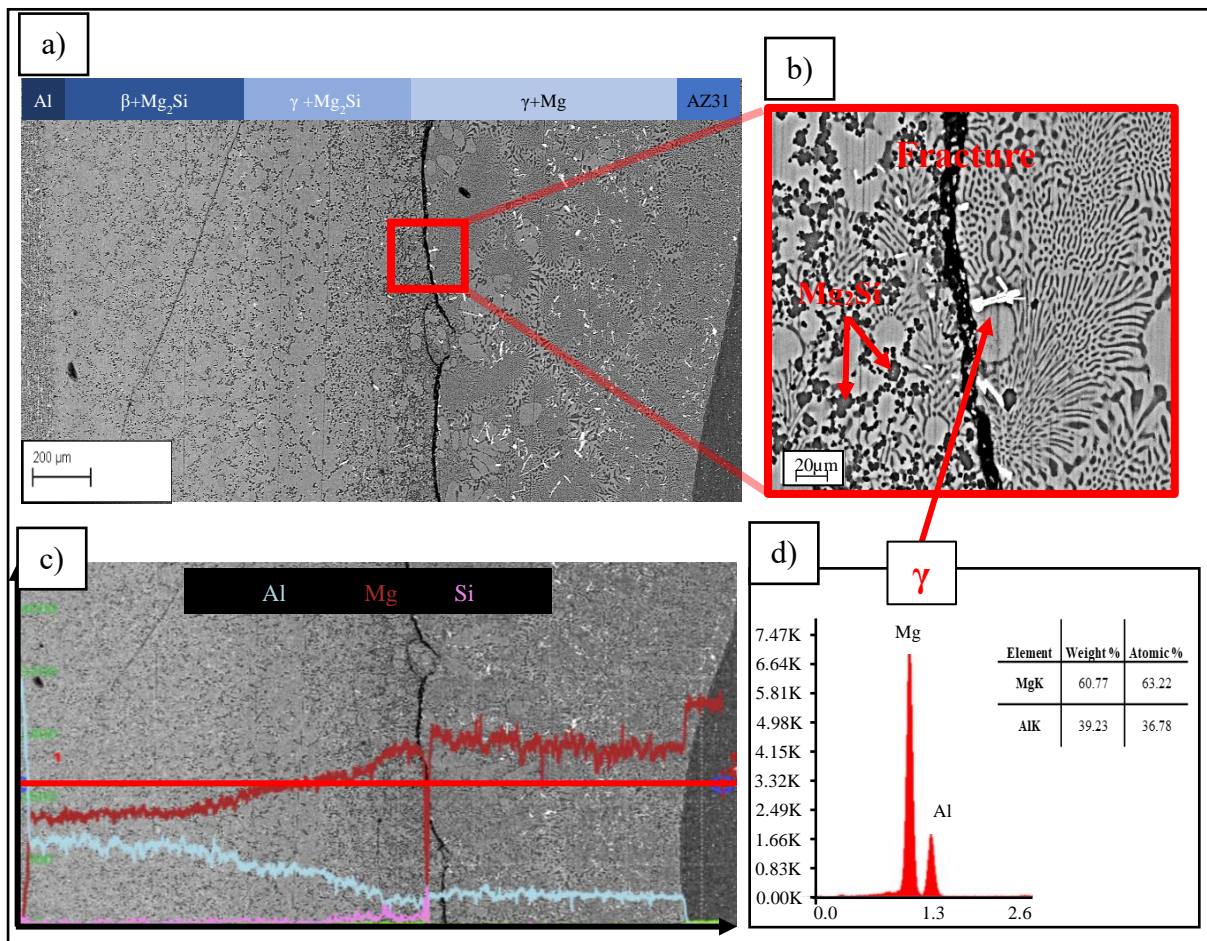


Figure 4.9. SEM micrographs of an AlSi6/AZ31 compound casting. (a) Overview over the whole material bond. The three layers of which it consists and their constituents are marked above the micrograph. The layers were: aluminium-rich intermetallic phase  $\beta$  and  $Mg_2Si$ , magnesium-rich intermetallic phase  $\gamma$  and  $Mg_2Si$  as well as the magnesium-rich intermetallic phases  $\gamma$  and Mg. (b) The vicinity of the fracture in greater detail. No aluminium-rich phases or  $Mg_2Si$  particles were found on the magnesium-rich side of the fracture. (c) Linescan across the material bond. A decrease in silicon content at the location of the fracture (arrowed) is visible. (d) Chemical analysis of the  $\gamma$  phase, as found in the material bond, using EDX.

the fracture that has propagated at the boundary of the new  $\gamma$ +Mg<sub>2</sub>Si and  $\gamma$ +Mg layer. The linescan across the material bond, as seen in figure 4.9, revealed a decrease in the concentration of silicon at the position of the fracture. Almost no silicon and thus Mg<sub>2</sub>Si particles were detected on the magnesium side of the fracture. But unlike the AlSi1/AZ31 compound castings, no change in the aluminium concentration at the fracture was observed. This is due, as will be discussed in chapter 7, to the fact that silicon exclusively reacts to form Mg<sub>2</sub>Si. Mg<sub>2</sub>Si precipitates at higher temperatures (see the AlSi/AZ31 phase diagrams in figures 4.6 and 4.8) compared to the other phases, thus preventing the diffusion of silicon or Mg<sub>2</sub>Si across the material bond. The numerous white needle-shaped structures can be seen in figure 4.8(b) (arrowed) are manganese- and oxygen-based impurities.

Overcasting a hypereutectic AlSi alloy resulted in a change of the microstructure across the material bond. As can be seen in figure 4.10, the bulk of the material bond still consisted of the two intermetallic

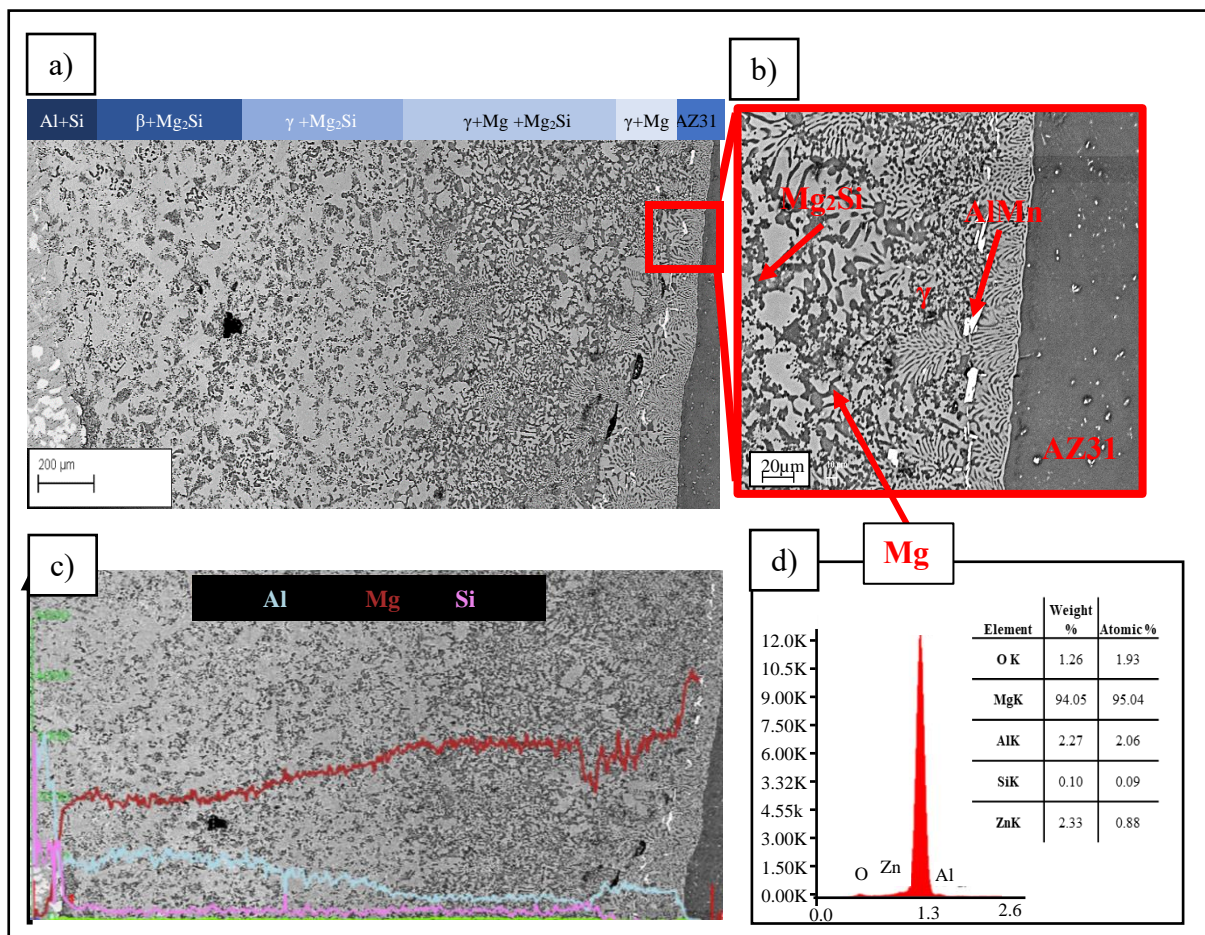


Figure 4.10. SEM micrographs of an AlSi15/AZ31 compound casting. (a) Overview over the whole material bond. The four layers of which it consists and their constituents are marked above the micrograph. The layers were: aluminium-rich intermetallic phase  $\beta$  and Mg<sub>2</sub>Si; magnesium-rich intermetallic phase  $\gamma$  and Mg<sub>2</sub>Si; magnesium-rich intermetallic phase  $\gamma$ , Mg<sub>2</sub>Si and Mg; and magnesium-rich intermetallic phase  $\gamma$  and Mg. No Mg<sub>2</sub>Si was found in this layer. (b) The region of the AZ31 alloy in greater detail. The absence of Mg<sub>2</sub>Si particles in the  $\gamma$ +Mg layer adjacent to the AZ31 alloy is clearly visible. (c) Linescan across the material bond. No fracture was present within the material bond. (d) Chemical analysis of the eutectic magnesium found close to the AZ31 alloy using EDX. The 2at% oxygen either stems from a reaction with the atmosphere during casting or hydrogen absorption.

compounds  $\beta$  and  $\gamma$ . As evident from the figure, the material bond could be divided, based on microstructure and phases present, into 4 distinct layers. Layer 1 consisted of  $Mg_2Si$  particles within the  $\beta$  phase and was adjacent to the AlSi alloy. In layer 2, the main constituent changed from the  $\beta$  to the  $\gamma$  phase. However,  $Mg_2Si$  particles were still found throughout this layer. The third layer consisted of elementary magnesium in addition to the phases found in layer 2. Layer 4 was situated adjacent to the AZ31 and its make-up was similar to that of the previous layer 3. It consisted of the  $\gamma$  phase and magnesium. No  $Mg_2Si$  particles were found in this layer. This is in violation of the calculated phase diagram, as no such combination of the two phases was predicted to exist. This implies that diffusion and reaction kinetics, which are both not considered in equilibrium phase diagrams, play an important role in interfacial formation. Several needle-like structure were found in layer 4, which were identified, using SEM and EDX, to be AlMn compounds. The AlMn impurities are usually found in areas containing elementary magnesium but no  $Mg_2Si$ . Thus, they are usually found close to the AZ31 alloy. This holds true for all four samples. The manganese stems from impurities in the used materials, as it is a common impurity in magnesium alloys. One notable difference of the AlSi15/AZ31 compound casting was the lack of a fracture perpetrating across the material bond. Existing fractures were smaller and more localised. As a consequence, no drop in aluminium or silicon concentration is detected across

the material bond. This confirms the earlier assumption that the  $Mg_2Si$  particles are the result of a diffusion reaction process in the solid state rather than precipitation from the melt.

This makeup is very similar for both hypereutectic alloys. But unlike the previous sample, the material bond in an AlSi30/AZ31 compound casting displayed, as can be seen in figure 4.11, several fractures running parallel to each other across the whole material bond. The fractures propagated along agglomerations of  $Mg_2Si$  particles. The fractures did not prevent diffusion of silicon or aluminium across the bond, as linescans revealed the presence of both elements throughout the material bond and on both sides of the fractures. This indicates that the fractures developed at a later stage. The fractures most likely were caused by mechanical stress, possibly during removal from the mould or cutting, or hot tearing as a result of the brittle  $Mg_2Si$  particles.

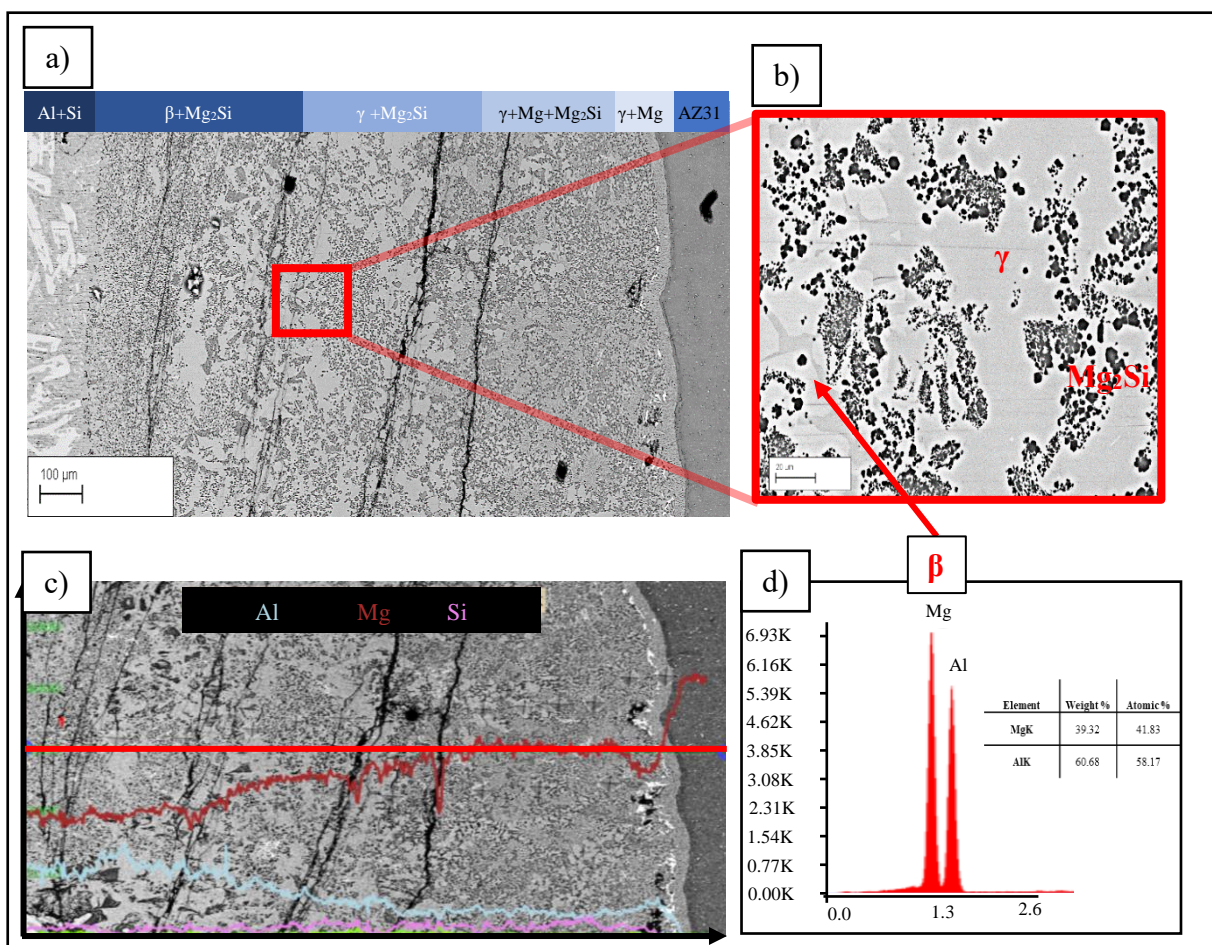


Figure 4.11. SEM micrographs of an AlSi30/AZ31 compound casting. (a) Overview over the whole material bond. The four layers of which it consists and their constituents are marked above the micrograph. The layers were: Aluminium-rich intermetallic phase  $\beta$   $Mg_2Si$ ; magnesium-rich intermetallic phase  $\gamma$  and  $Mg_2Si$ ; magnesium-rich intermetallic phase  $\gamma$ ,  $Mg_2Si$  and Mg; and magnesium-rich intermetallic phase  $\gamma$  and Mg. No  $Mg_2Si$  was found in this layer. (b) Area of transition between the layer with the  $\beta$  intermetallic phase as main constituent and the layer with the  $\gamma$  intermetallic phase as main constituent. (c) Linescan across the material bond. The fractures seem to have little impact on the concentration gradients of the aluminium and silicon. (d) Chemical analysis of the  $\beta$  intermetallic phase EDAX.

In all samples, regardless of silicon content, several different modifications of  $Mg_2Si$  were present in the material bond. These modifications were displayed in figure 4.12 and identified as: primary polyhedral  $Mg_2Si$ ; primary dendritic  $Mg_2Si$ ; binary flake-like  $Mg_2Si$ ; and a fourth modification only present in hypereutectic alloys. This fourth modification stems from a diffusion reaction of silicon in areas where the primary silicon is in direct contact with the material bond. The thickness of each of the four layers for all AlSi samples is noted in table 4.2. The material bond of both the AlSi1 and AlSi6 castings consisted of fewer than four layers. The given values in the table are averages of five measurements of the thickness of each layer. Again, areas with the highest and lowest thickness were chosen to acquire representative data. The standard deviation given in table 4.2 was used as a measure to assess each layer's uniformity of thickness along the interface. While the overall thickness of the material bond was roughly the same as in Al/AZ31 castings, the thickness of the magnesium-rich phases was found to be significantly higher than in the previous experiments. In the AlSi1 and AlSi6 samples, where a fracture prevented the diffusion of silicon across the material bond, layer 4 was the most distinct layer compared to the samples where diffusion of silicon was not impeded. One layer always displayed a noticeably higher deviation from its average thickness than the others. This is an indication that under set conditions, growth of one layer is more stable than the others.

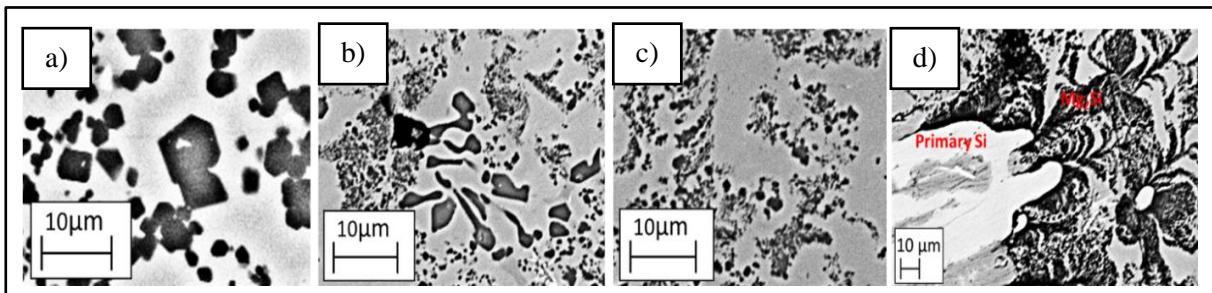


Figure 4.12. Modifications of  $Mg_2Si$  found in the material bond of AlSi/AZ31 compound castings: (a) Primary polyhedral  $Mg_2Si$ ; (b) primary dendritic  $Mg_2Si$ ; (c) binary flake-like  $Mg_2Si$ ; and (d)  $Mg_2Si$  stemming from a diffusion reaction.



Al-alloy	Phases in the material bond	Thickness [ $\mu\text{m}$ ]				Mg <sub>2</sub> Si
		$\beta$ +Mg <sub>2</sub> Si (layer 1)	$\gamma$ +Mg <sub>2</sub> Si (layer 2)	$\gamma$ +Mg+Mg <sub>2</sub> Si (layer 3)	$\gamma$ +Mg (layer 4)	Total
AlSi1		166+/-44	-	-	1284+/-74	1450
	Deviation [%]	26.8	-	-	5.8%	
AlSi6		573+/-13	365+/-25	-	847+/-77	1785
	Deviation [%]	2.3	6.7	-	10.7%	
AlSi15		354+/-10	335+/-6	507+/-15	68+/-22	1264
	Deviation [%]	2.7	1.7	3.1	32	
AlSi30		376+/-26	370+/-22	514+/-39	38+/-4	1298
	Deviation [%]	6.9	6.0	7.6	11.7	

Table 4.2: Thickness in  $\mu\text{m}$  of the material bond in AlSi/AZ31 compound castings. Thicknesses for each layer identified via SEM are given. Not all layers were found in all samples. The standard deviations of the thicknesses are given as a measure to assess the uniformity of the material bond in terms of thickness.

### 4.2.2: The Material Bond of AlZn/AZ31 Compound Castings

In this section the microstructure of the material bond of AlZn/AZ31 compound castings is discussed. The results from the characterisation of the material bond via OM and SEM are presented and the effects of varying amounts of zinc are explained. Figure 4.13 displays a backscatter SEM image of the material bond of an AlZn6/AZ31 compound casting with a preheat temperature of 400°C and no holding time in the furnace. It resembles the results obtained from the overcasting of (commercially) pure aluminium with (commercially) pure magnesium (see section 4.1). The material bond of the sample displays the aforementioned typical ‘dual-layer’ appearance of pure Al/Mg compound castings. The constituents of the material bond were the two intermetallic phases  $\beta$  and  $\gamma$ , and elementary magnesium. Small patches of the  $\gamma$  phase were found within the layer of the  $\beta$  phase. No zinc-rich phases were found. Zinc was evenly dispersed within the  $\beta$  and  $\gamma$  phases. A fracture was observed directly next to the aluminium alloy. Unlike the AlSi samples where the fractures propagated along  $Mg_2Si$  particles, the fracture in the present sample propagated close to the AlZn6/ $\beta$  phase boundary. The linescan of the material bond, as shown in figure 4.14, revealed that the fracture appeared to impede diffusion of aluminium across it. This points to the fact that the fracture originated during or soon after solidification, thus preventing further growth of the aluminium-rich intermetallic phase  $\beta$  and explaining the patches of  $\gamma$  within the  $\beta$  matrix, as magnesium was still able to diffuse in the direction of the fracture.

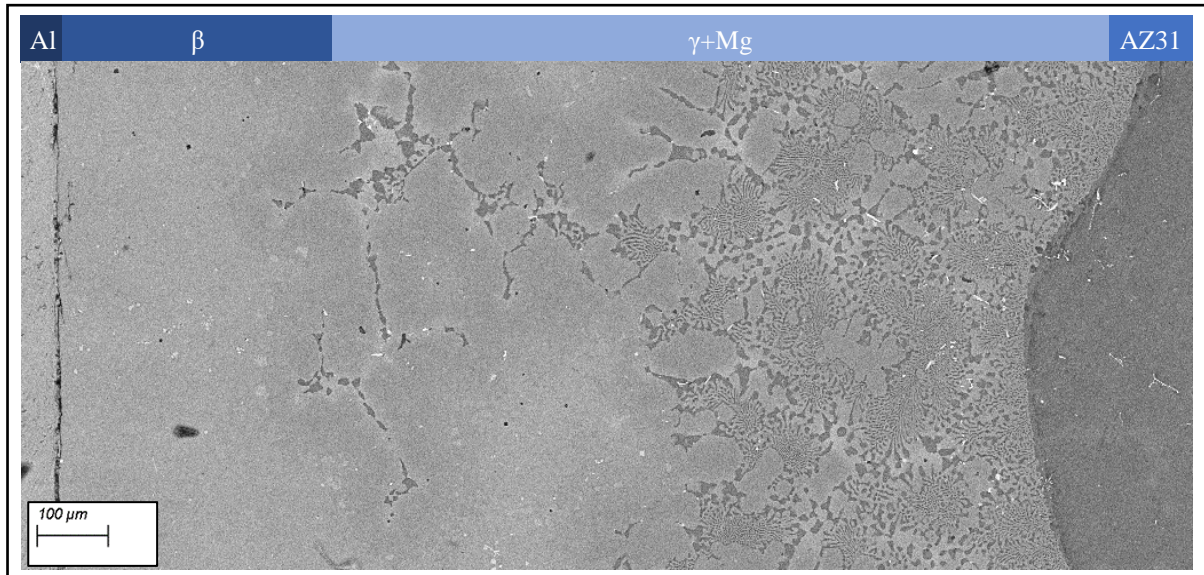


Figure 4.13. SEM micrograph of the material bond of an AlZn6/AZ31 compound casting. The two layers it consists of and their respective constituents are marked above the micrograph: the aluminium-rich intermetallic phase  $\beta$  and the magnesium-rich intermetallic phase  $\gamma$ . Elementary magnesium is found throughout the layer made up of the  $\gamma$  phase. A fracture was observed to form near the AlZn6 alloy and propagating parallel to it along the material bond.

The material bond is less complex than predicted by the AlZn6-AZ31 phase diagram pictured in figure 4.15. It is apparent that the material bond observed deviates from the calculated phase diagram. Neither elementary aluminium nor the AlMgZn phase  $\tau_1$  (in addition to several other phase fields indicated by the phase diagram) were found. It is possible that the described fracture is the cause of this deviation as it disrupted diffusion and thus favoured the formation of the magnesium-rich phase on its opposing side. In addition to the fracture, numerous small and evenly shaped voids, shown in figure 4.16, were present in the layer containing the  $\gamma$  and (elementary) magnesium phases. No such (regular shaped) voids were found in the aluminium-rich phases of the material bond, with the size of the holes varying from ~0.5 to ~1mm. Due to the regularity of their appearance it was deemed unlikely that they are solidification-related shrinkage. While a number of holes and gaps were also found on the aluminium-rich side, their irregular appearance indicated that they are caused by solidification shrinkage.

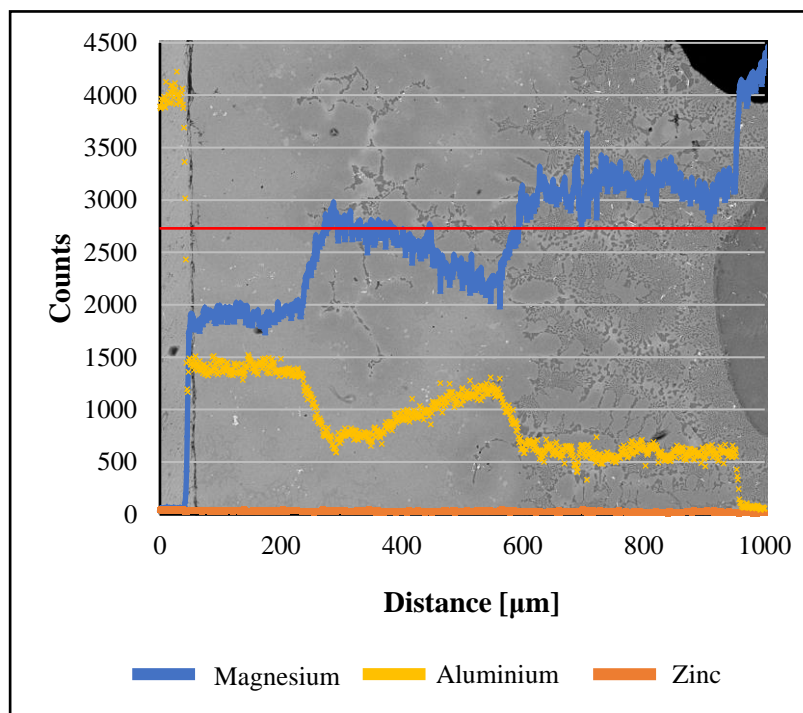


Figure 4.14. Linescan across the material bond of an AlZn6/AZ31 compound casting. The concentration gradients for aluminium, magnesium and zinc are given. Position of the line scan is given by the red line.

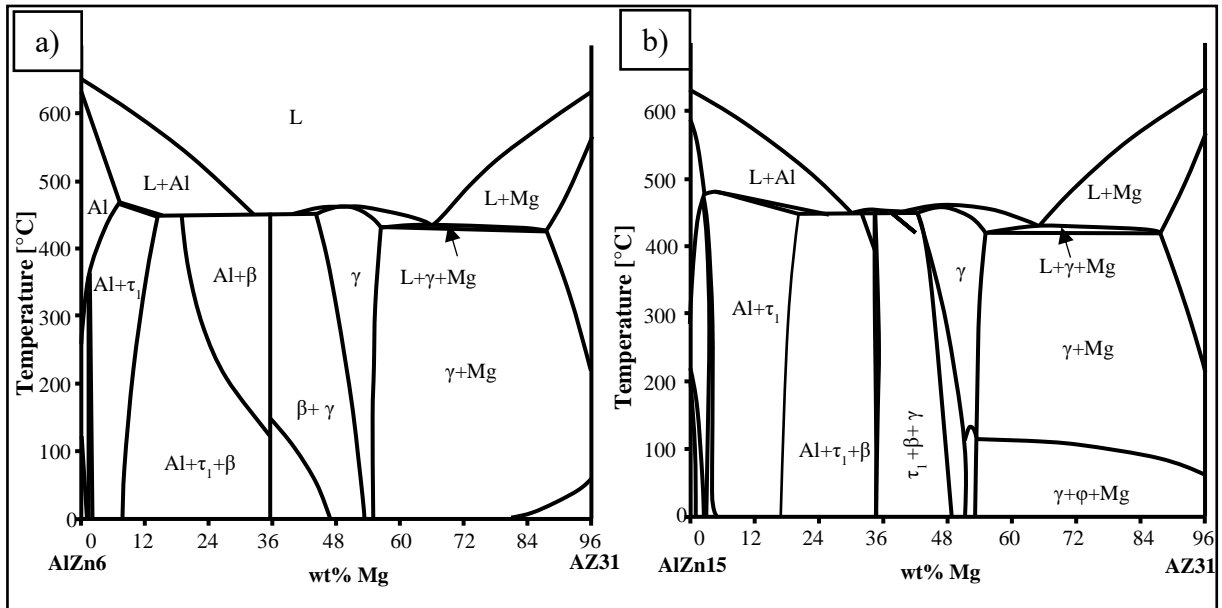


Figure 4.15. (a) Combined AlZn6-AZ31 phase diagram. (b) Combined AlZn15-AZ31 phase diagram. Both phase diagrams were calculated using the Pandat software package.

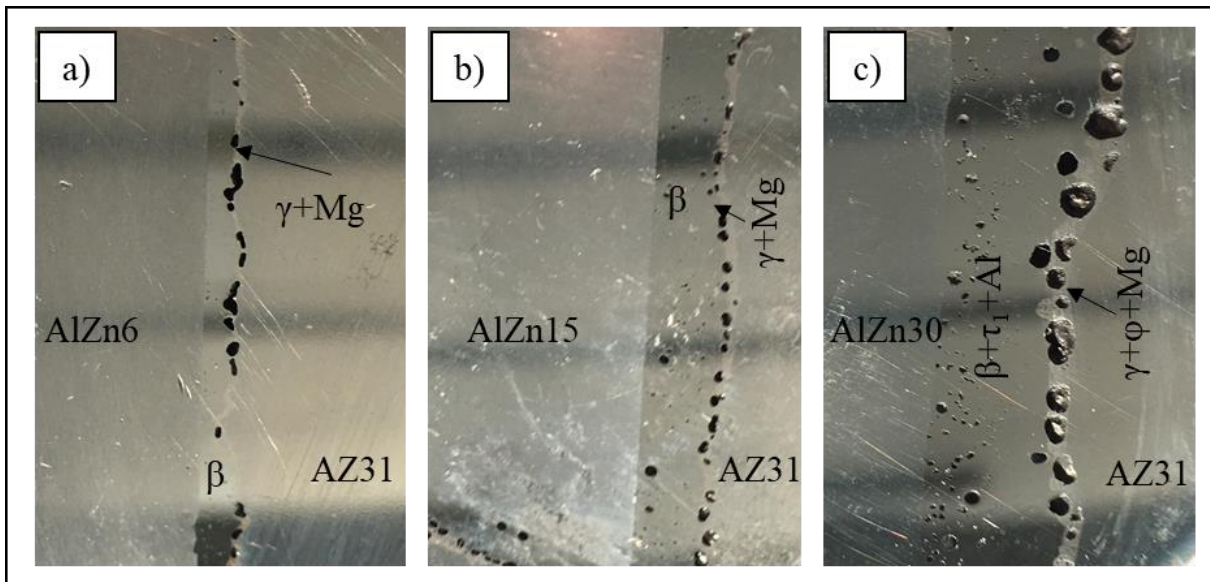


Figure 4.16. Macrographs of the material bond of an: (a) AlZn6/AZ31 compound casting; (b) AlZn15/AZ31 compound casting; (c) AlZn30/AZ31 compound casting. In all three castings, voids on the magnesium-rich side are clearly visible. Typically, said voids were found within the layer consisting of the  $\tau_1+\gamma+Mg$ . The holes appear to increase in size and number with increasing zinc content.

Similarly, as can be seen in figure 4.17, there is little change to the morphology of the material bond when 15wt% zinc is added to the aluminium alloy. According to the binary AlZn15-AZ31 phase diagram, displayed in figure 4.13, the zinc- and magnesium-rich phase  $\phi$  was expected in addition to the  $\tau_1$  phase. However, no such phases were found. Instead an area with its own distinct morphology was observed at the phase boundary of the  $\beta$ - and  $\gamma$ -intermetallic phase. These areas contained 3-6wt% more zinc than the surrounding aluminium-rich  $\beta$  phase with 9-10wt%. Furthermore, 8-10wt% carbon was also detected in these areas. The exact source of the carbon is unknown, but thought to stem from impurities in the metal or from an outside source during melting or casting. No traces of carbon were found in the rest of the material bond, indicating that it was not from the characterisation technique. Similar structures, however, with no carbon, were also observed close by. The remaining zinc is evenly dispersed within the two intermetallic phases. Inspection of the concentration gradient of the aluminium, magnesium and zinc with linescans confirmed an identical make-up compared to the AlZn6/AZ31 compound casting. The material bond consisted mainly of the  $\beta$  phase and a layer of  $\gamma$  and (elementary) magnesium within.

The unit cell of both the intermetallic compounds  $\beta$  ( $a=b=c=2.83\text{nm}$ ) and  $\gamma$  ( $a=b=c=1.054\text{nm}$ ) is several times larger than those of aluminium ( $a=0.4046\text{nm}$ ) and magnesium ( $a=0.32094$  and  $b=0.52108\text{nm}$ ). Due to the large unit cell of the intermetallic compounds and the similar atomic radius of zinc (139pm), compared to aluminium (184pm) and magnesium (173pm), it is thought that the zinc atoms can substitutional or interstitially scatter on the crystal lattice of the  $\beta$  and  $\gamma$  phases. Furthermore, not all sites in the unit cell of the  $\beta$  phase are occupied, leading to a high solubility of zinc atoms (Mezbahul-

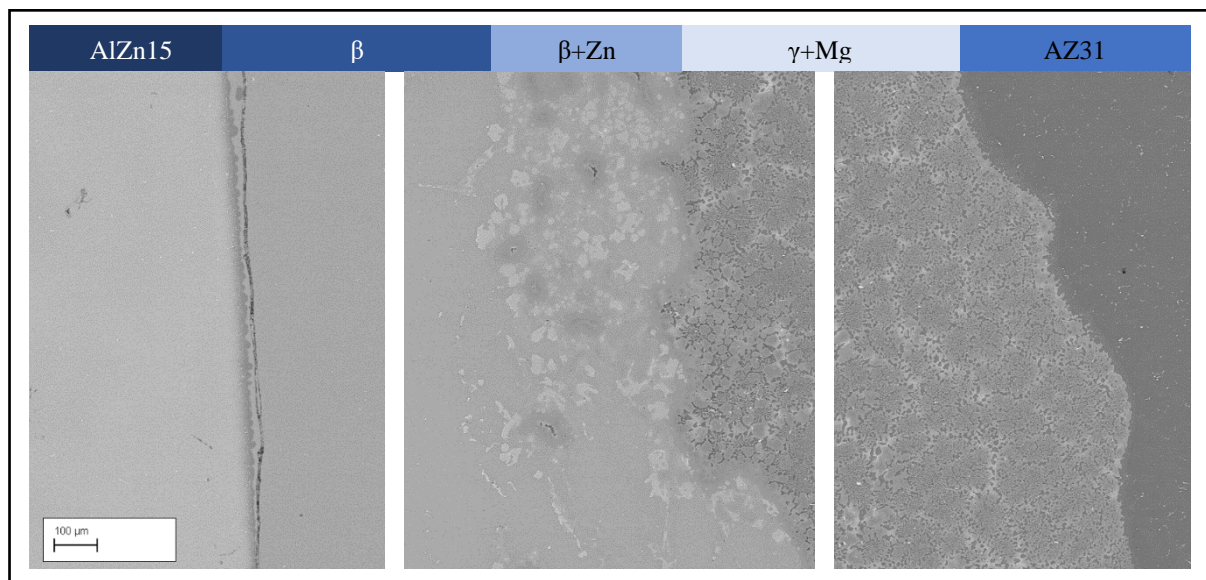


Figure 4.17. SEM micrograph of the material bond of an AlZn15/AZ31 compound casting. The three layers it consists of and their respective constituents are marked above the micrograph: the aluminium-rich intermetallic phase  $\beta$  and the magnesium-rich intermetallic phase  $\gamma$ . Elementary magnesium is found throughout the layer made up of the  $\gamma$  phase. A third layer is found between those two layers. It consists of the  $\beta$  and  $\gamma$  phases with zinc-rich areas located within. A fracture was observed to form near the AlZn6 alloy and propagating parallel to it along the material bond.

Islam, Mostafa, and Medraj, 2014; Gille and Grin, 2018). As in the AlZn6/AZ31 compound casting, a fracture was observed to propagate, in close proximity to and parallel to, the AlZn15/ $\beta$  phase boundary. This fracture caused a decrease in the aluminium concentration, as seen in the linescan shown in figure 4.18, as it prevented the diffusion of aluminium across the material bond. Due to the greater thickness of the intermetallic phase  $\beta$ , it is thought that the fracture originated at a later point of time than in the AlZn6/AZ31 compound casting. Voids on a macroscopic level, resembling those found in the AlZn6/AZ31 compound casting, have been observed inside the magnesium-rich phases as well. The density and number of these cavities increased compared to the AlZn6/AZ31 compound casting. As displayed in figure 4.16(b), the size of the voids was found to be of a similar magnitude to those observed in the AlZn6/AZ31 sample, and varied between  $\sim 0.5\text{mm}$  and  $\sim 1\text{mm}$ . The largest void had a length of  $1130\mu\text{m}$ , while the smallest was measured at around  $340\mu\text{m}$ . Holes and similar defects were also present on the aluminium-rich side of the material bond. These defects displayed an irregular shape and are thus thought to be caused by solidification-related shrinkage.

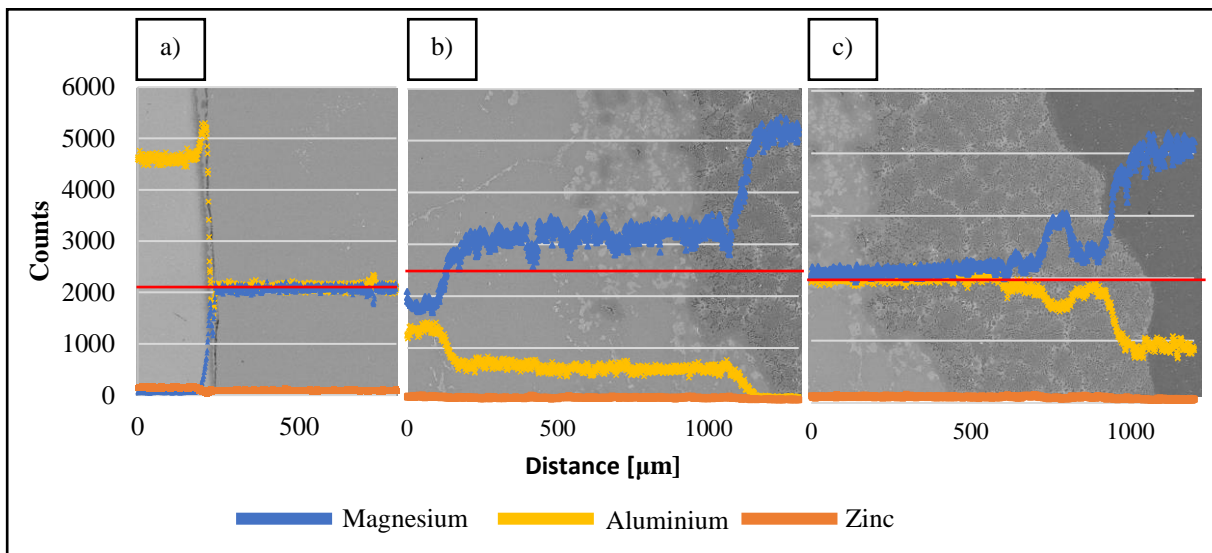


Figure 4.18. Linescan across the material bond of an AlZn15/AZ31 compound casting: (a) AlZn15 and  $\beta$  phase; (b)  $\beta$  phase and  $\gamma$ +Mg phases; and (c)  $\gamma$ +Mg phases and AZ31. Positions of the linescans are given by the red lines. Concentration gradients for aluminium, magnesium and zinc are given. Due to the increased thickness of the material bond, several linescans had to be performed in sequence in order to cover the whole bond. The displayed images do not cover the material bond over the whole thickness. Exact position of the linescans is indicated by the red lines.

A significantly altered bond was acquired after the overcasting of an AlZn30 alloy with AZ31 at a preheat temperature of 400°C. The material bond of such a compound casting is displayed in figure 4.18. As evident from the figure, two new phases were present in the material bond. They were identified as the aforementioned zinc-rich phases  $\tau_1$  ( $\text{Mg}_{32}(\text{Zn},\text{Al})_{48}$ ) and  $\phi$  ( $\text{Mg}_{21}(\text{Zn},\text{Al})_{17}$ ).  $\tau_1$  is the aluminium-rich zinc phase and was observed to form large polyhedral shapes precipitated within a matrix of the  $\beta$  phase. Elementary aluminium is found scattered around the  $\tau_1$  and  $\beta$  phases in small dot-like precipitates. Approaching the magnesium side, the  $\gamma$  phase becomes the main constituent of the material bond. Closer to the magnesium alloy, the magnesium-rich zinc phase  $\phi$  was formed. The  $\phi$  phase was found, similarly to the zinc-rich areas in AlZn15/AZ31 compound castings, spread between the dendrites of the elemental magnesium. The  $\gamma$  phase was still the main constituent of the bond. Figure 4.20 shows the aluminium- and magnesium-rich phases in greater detail. As apparent in the figures, magnesium is found within the  $\phi$  phase in the form of small dot-like precipitates. No traces of other MgZn intermetallic compounds or phases were detected in any of the samples. Numerous, evenly shaped voids as observed in the AlZn15/AZ31 sample were also observed. Again, they were found exclusively in the layer adjacent to the AZ31 (see figure 4.16(c)). However, the size of the holes was found to be noticeably increased ( $\sim 1\text{mm}$  to  $\sim 2\text{mm}$ ). The calculated phase diagram for the AlZn30/AZ31 compound castings, displayed in figure 4.21, is generally reproduced in the acquired material bond. While all the predicted phases were found, several phase fields, such as  $\text{Al}+\tau_1$  or  $\tau_1+\gamma$ , were not. It was noticed that the majority of the bond was made up of the aluminium-rich phases  $\beta+\text{Al}+\tau_1$  even though the corresponding phase field occupies a relatively small space in the phase diagram.

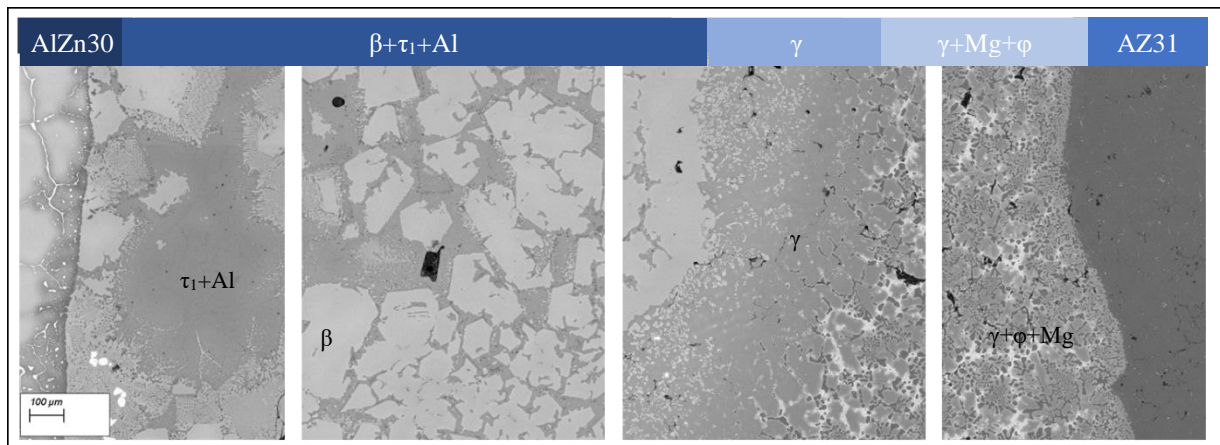


Figure 4.19. SEM micrograph of the material bond of an AlZn30/AZ31 compound casting. The three layers it consists of and their respective constituents are marked above the micrograph: the aluminium-rich intermetallic phase  $\beta$ , an intermediate layer consisting solely of the  $\gamma$  phase and  $\tau_1$ , and the magnesium-rich intermetallic phases  $\gamma$  and  $\phi$ . Elementary magnesium is found throughout the layer made up of the  $\gamma$  phase. The magnesium- and zinc-rich phase  $\phi$  was found to precipitate between the magnesium dendrites.

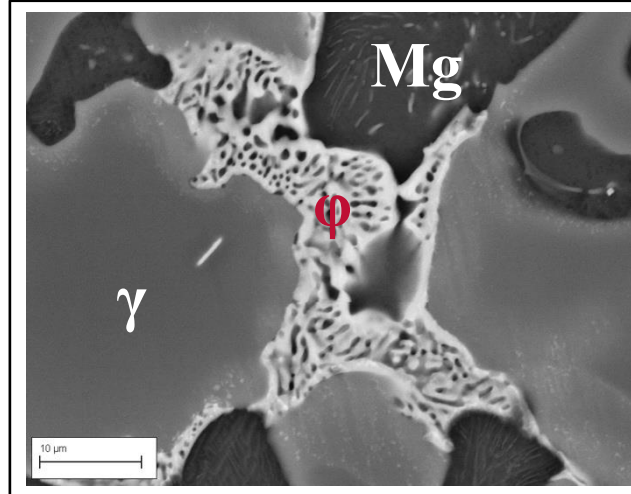


Figure 4.20. Micrograph of the magnesium- and zinc-rich phases  $\phi$  and  $\gamma$  in the layer adjacent to the magnesium alloy.

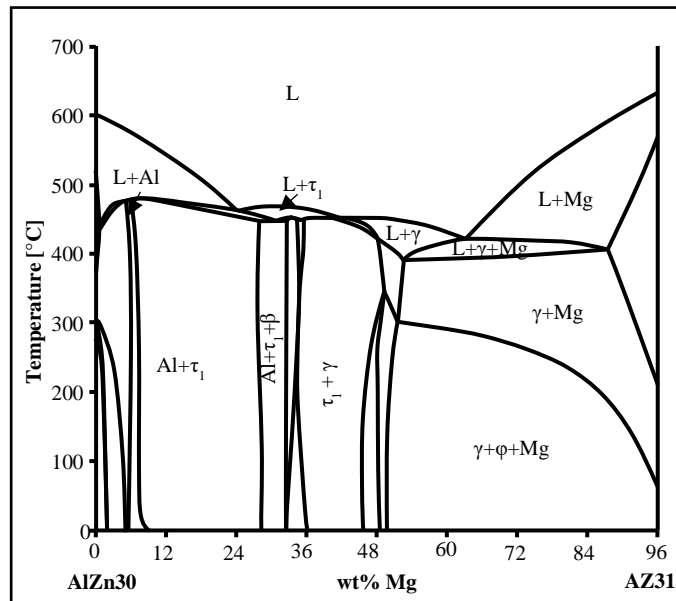


Figure 4.21. Combined AlZn30-AZ31 phase diagram according to the software package Pandat.



According to the phase diagram (which has been confirmed by DSC measurements, detailed in section 4.3) the intermetallic phase  $\phi$  possesses the smallest solidification range of all compounds in the material bond. The  $\phi$  phase, therefore, is the last phase to precipitate in the bond. Similar to the AlZn6/AZ31 and AlZn15/AZ31 castings, a fracture propagated parallel to the AlZn30 alloy. As can be seen in the micrographs, the fracture, unlike in the previous samples, was not found in close proximity to the AlZn30 alloy; instead, it was found within the  $\beta+\tau_1+Al$  layer. Figure 4.22 displays the linescans across the material bond of an AlZn30/AZ31 compound casting. The scans showed a similar level of aluminium concentration on both sides of the fracture. Therefore, the fracture originated after a significant amount of aluminium diffused across the material bond. Hence, the fracture could be the result of the highly brittle nature of the intermetallic phases formed.

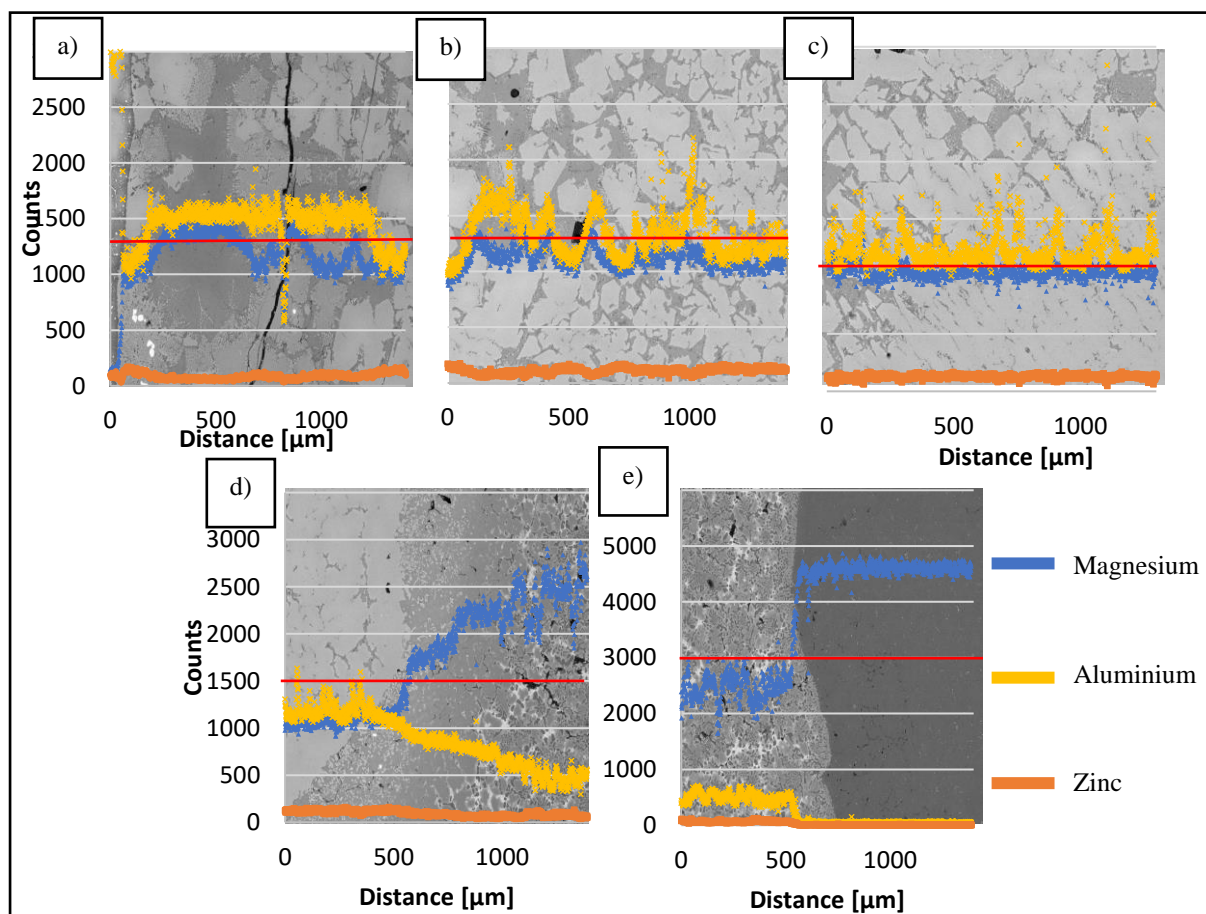


Figure 4.22. Linescans of the material bond of an AlZn30/AZ31 compound casting acquired with EDX: (a) AlZn30 aluminium alloy and  $\beta+\tau_1+Al$  layer; (b)  $\beta+\tau_1+Al$  layer; (c)  $\beta+\tau_1+Al$  layer; (d)  $\beta+\tau_1+Al$  layer and  $\gamma+\phi+Mg$ ; and (e)  $\gamma+\phi+Mg$  and AZ31 magnesium alloy. Exact position of the linescans is indicated by the red lines.

A list with the thickness of each phase in all AlZn/AZ31 compound castings is detailed below in table 4.3. In all inspected samples the thicknesses of the aluminium-rich phases surpasses those of the magnesium-rich ones. Deviations from the average thickness are significantly higher for the magnesium-rich phases. As mentioned above, no simple linear correlation between zinc content and total thickness of the material bond is evident. The given values are averages of five measurements of the thickness of each layer.

A holding temperature of 200°C prevented the formation of the zinc-rich phases  $\tau_1$  and  $\phi$  independent of holding time. Chemically, the material bond resembled that of a pure Al/Mg compound casting. The main constituents in all three samples were the intermetallic phases  $\beta$  and  $\gamma$  in addition to elementary magnesium. While no zinc-rich phases were found, the zinc was found to alter the morphology of the material bond, especially at longer holding times. Figure 4.23(a) shows the material bond of an AlZn30/AZ31 compound casting after a holding time of 15min. It resembles that of pure elements (see figure 4.1). Increasing the holding time to 30 and 60min leads to, as displayed in figure 4.23(b) and 4.23(c), the precipitation and subsequent growth of the  $\gamma$  phase within the layer consisting of the  $\beta$  phase. While the material bond is still dominated by the aluminium-rich phase  $\beta$ , the amount of the magnesium-rich phase  $\gamma$  was found to correlate with holding time. The microstructure of the  $\gamma$  phase within a matrix of the  $\beta$  phase is shown in greater detail in figure 4.24(a). Similar to the AlZn/AZ31 compound castings, numerous holes were present on the magnesium-rich side of the material bond. Figure 4.24(b) displays such a hole, which appears to be the result of the merger of two smaller holes, as seen with an optical microscope.

However, as evident from the calculated phase diagrams, zinc does reduce the range in which  $\beta$  is the equilibrium phase. As such, it is believed that in the presence of zinc, the  $\gamma$  phase is more thermodynamically stable at 200°C. This was not observed in the material bond after annealing for 15min, as the relatively low temperature resulted in a slower diffusion of the zinc across the material bond.

Alloy		Thickness [ $\mu\text{m}$ ]		
		$\beta+\text{Al}(\tau_1)$	$\gamma+\text{Mg}(\phi)$	Total
AlZn6		3566 $\pm$ 86	419 $\pm$ 60	3985
	Deviation [%]	2.4%	14.3%	
AlZn15		7156 $\pm$ 165	916 $\pm$ 111	8072
	Deviation [%]	2.3%	12.1%	
AlZn30		5674 $\pm$ 148	1142 $\pm$ 152	6816
	Deviation [%]	2.6%	13.3%	

Table 4.3: Thickness in  $\mu\text{m}$  of the material bond in AlZn/AZ31 compound castings. Thicknesses for the magnesium-rich and aluminium-rich sides are given. The  $\tau_1$  and  $\phi$  phases were only found in AlZn30/AZ31 compound castings.

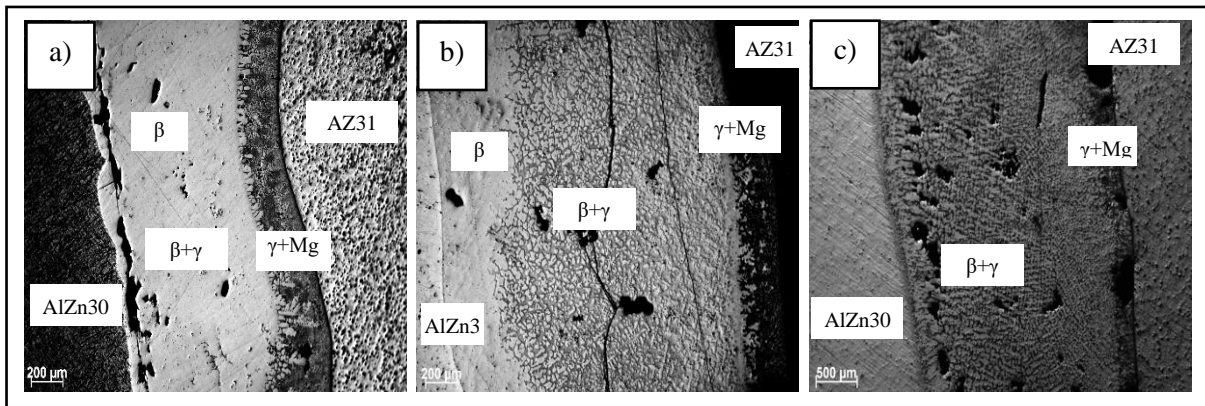


Figure 4.23. Optical micrograph of the material bond of AlZn30/AZ31 compound casting with a preheat temperature of  $200^\circ\text{C}$  after varying holding times: (a) material bond after 15min; (b) material bond after 30min; and (c) material bond after 60min.

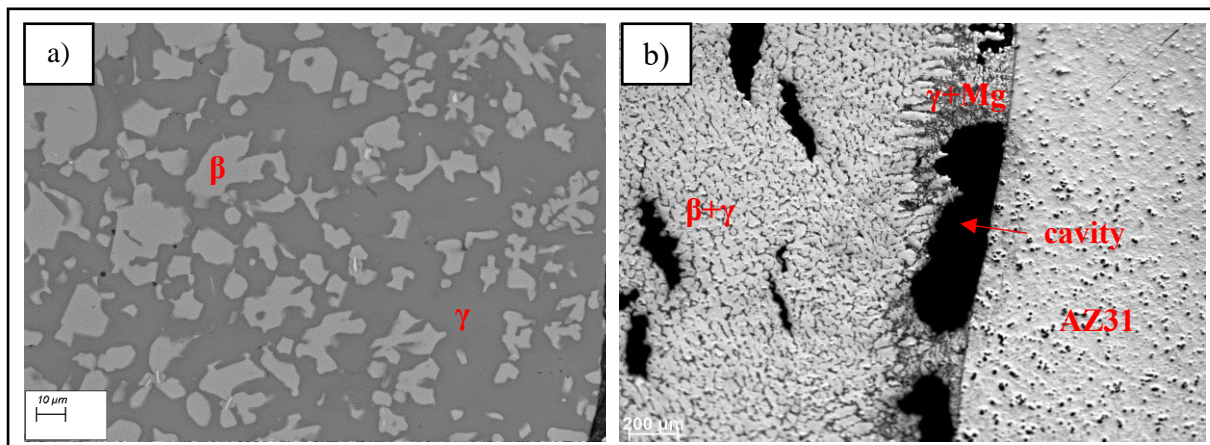


Figure 4.24. Micrographs of the material bond of an AlZn30/AZ31 compound casting after heat treatment at  $200^\circ\text{C}$  for 60min: (a) BSE SEM micrograph of the  $\beta$  and  $\gamma$  phases found in the middle of the material bond; (b) Optical micrograph of Mg+ $\gamma$  layer adjacent to the AZ31 alloy. A 928 $\mu\text{m}$  long cavity (arrowed) is present within the  $\gamma+\text{Mg}$  layer shown in (b). It appears that it was created by the merger of two smaller holes.

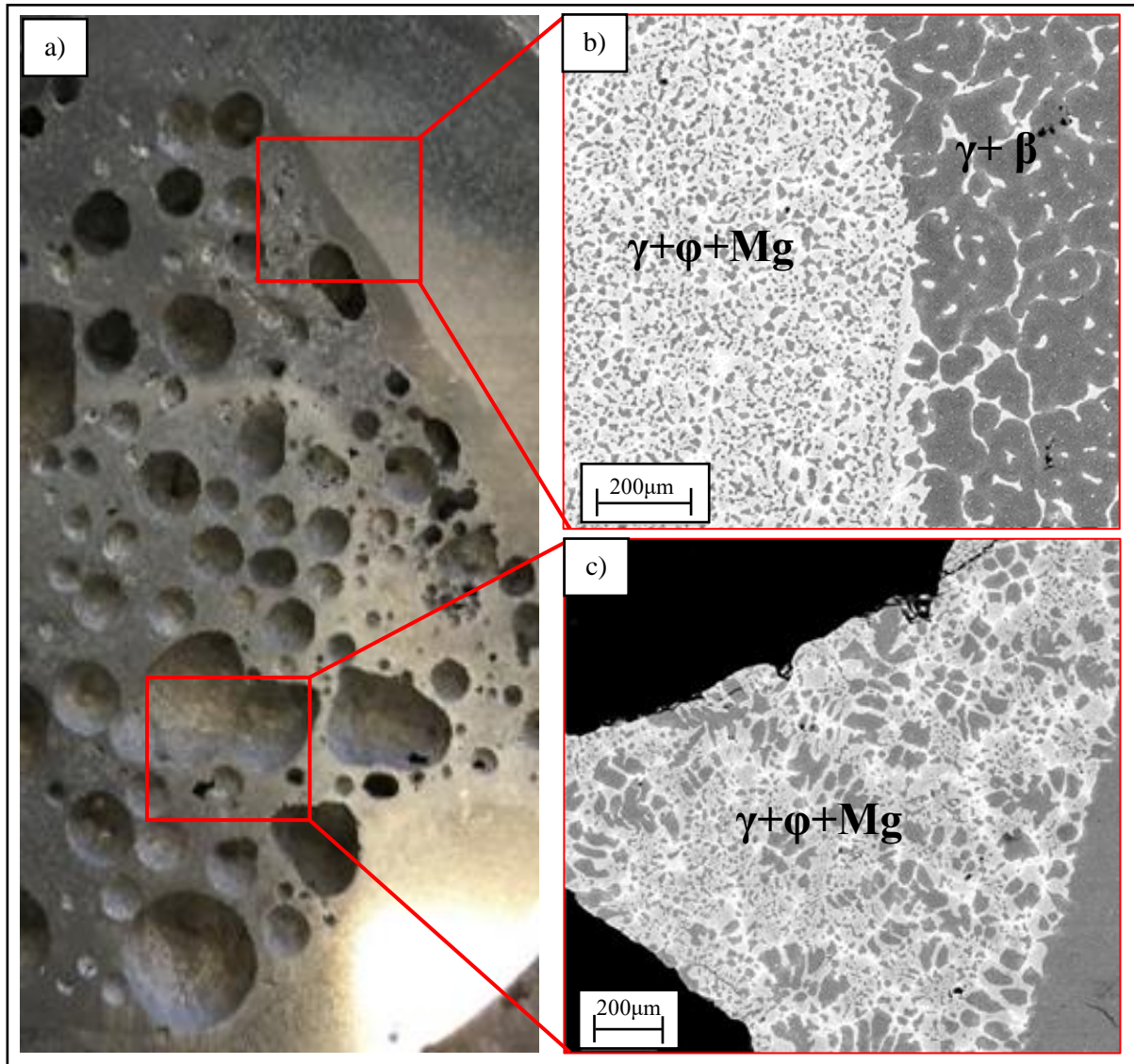


Figure 4.25. Macrograph and micrographs of an AlZn30/AZ31 compound casting after holding it in a furnace at 400°C for 30min after casting. The microstructure of the aluminium alloy is completely transformed into the  $\gamma + \phi + \text{Mg}$  phases. It contained a large density of voids up to 10mm in diameter: (a) macrograph of a cross-section of the compound casting after cutting and polishing; (b) micrograph of the material bond, with the AZ31 alloy transformed into  $\gamma + \beta$  phases; and (c) micrograph of the AlZn wedge showing a complete transformation of the material bond where no elementary aluminium was found throughout the whole casting.

Increasing the holding temperature to 400°C, regardless of holding time, led to the complete transformation of the microstructure of the aluminium and magnesium alloy. Figure 4.25 shows a cross-section of an AlZn30/AZ31 sample after 30min of holding time in the furnace at 400°C. The microstructure of the AlZn30 alloy (Al+Zn) is completely replaced with a microstructure consisting of magnesium-rich phases  $\gamma$  and  $\phi$  as well as elementary magnesium. Within these phases numerous evenly shaped voids were found. Their morphology resembled those observed in the AlZn15 and AlZn30 castings. These holes varied in size from a couple of mm up to 20mm in diameter. Furthermore, the AZ31 microstructure (Mg) is transformed into  $\gamma$  and  $\beta$ . Elementary zinc is found in solid solution within the  $\gamma$  phase. No elementary aluminium or aluminium-rich  $\tau_1$  phase was detected in the cross-section. Aluminium is exclusively found in the two magnesium-rich intermetallic phases. As can be seen in figure 4.25, no transition zone is found in the material bond of the two phase groups. This transformation of the microstructure was also observed after 15min at 400°C, although to a lesser extent, indicating that the transformation takes place relatively quickly. Holding times of 60min did not result in any further changes. Based on the regular appearance of these voids it is unlikely that they originated from a solidification process. It is unlikely that the observed voids are the result of hydrogen porosity as:

- no (hydrogen) porosity was observed in the AlZn30 alloy before the overcasting with AZ31;
- the voids were only observed in AlZn30/AZ31 compound castings – lower zinc contents prevented their formation;
- no inter-dendritic pores (typical for hydrogen porosity in magnesium) were observed.

Thicknesses of the aluminium- and magnesium-rich phases of an AlZn30/AZ31 compound casting after different holding times are listed in table 4.4. A clear correlation between holding time and thickness of the material bond was evident. The increase in thickness was attributed mostly to the growth of the aluminium-rich phase  $\beta$ . This is in good accordance with earlier observations and results reported in the literature. Voids and fractures were present in all inspected samples. As previously reported, evenly shaped cavities were found adjacent to the AZ31 alloy surrounded by magnesium and  $\gamma$  phase. Voids located near the aluminium alloys displayed a more irregular shape. Fractures were often found propagating along these voids, while no fractures were detected propagating along the voids adjacent to the magnesium alloy.

Holding time [min]	Thickness [ $\mu\text{m}$ ]		
	Al-rich	Mg-rich	Total
15	1067 $\pm$ 100	323 $\pm$ 67	1390 $\pm$ 52
30	1567 $\pm$ 200	335 $\pm$ 19	1902 $\pm$ 180
60	2267 $\pm$ 814	350 $\pm$ 21	2617 $\pm$ 712

Table 4.4: Thickness in  $\mu\text{m}$  of the material bond of an AlZn30/AZ31 compound casting after different holding times. Preheat and holding temperature was 200°C. This was chosen to avoid the formation of the described large-scale voids found with a preheat temperature of 400°C.

### 4.3: Micro-hardness of the Material bond in AlZn/AZ31 and AlSi/AZ31 Compound Castings

Mechanical properties of the material bond are approximated using Vickers micro-hardness measurements. A linear correlation between indentation hardness and tensile strength is described in the literature for steels (Pavlina and Van Tyne, 2008). A similar linear relationship between Vickers hardness and yield stress and tensile strength was found to exist in aluminium alloys as well (Tiryakioğlu et al., 2015). Thus, hardness is considered a good indicator for the performance of the material bond under load.

The cracks and fractures present at the material bond in most samples indicate an increased brittleness. Gradients of the Vickers micro-hardness for all AlZn/AZ31 and AlSi/AZ31 compound castings are displayed in figures 4.26-4.33. A load of 0.3N was chosen, as higher loads resulted in fractures, originating from the indents. Furthermore, increasing the load resulted in a larger indent and reduced the possible number of measuring points that could be obtained across the material bond. Vickers micro-hardness measurements only provide the hardness for a specific area. As such, the hardness of each measurement spot is dependent on the type and percentage of the phases the indenter collides with. The smaller the indent, the higher the influence of the phases hit by the indenter. Small impurities or segregation of the elements during solidification could also have an impact on the hardness. As such, the measured hardness might not be representative of the surrounding material. To verify the acquired hardness values, three measurements across the sample in areas with the same microstructure were performed. The presented values, in figures 4.26-4.33, are from one measurement series across the material bond. Spots, where significant deviations from the other two series of measurements were observed, are mentioned where necessary. Average values for the hardness measurements of each layer, identified in section 4.1, are displayed in table 4.25 for the AlSi alloys and table 4.26 for the AlZn

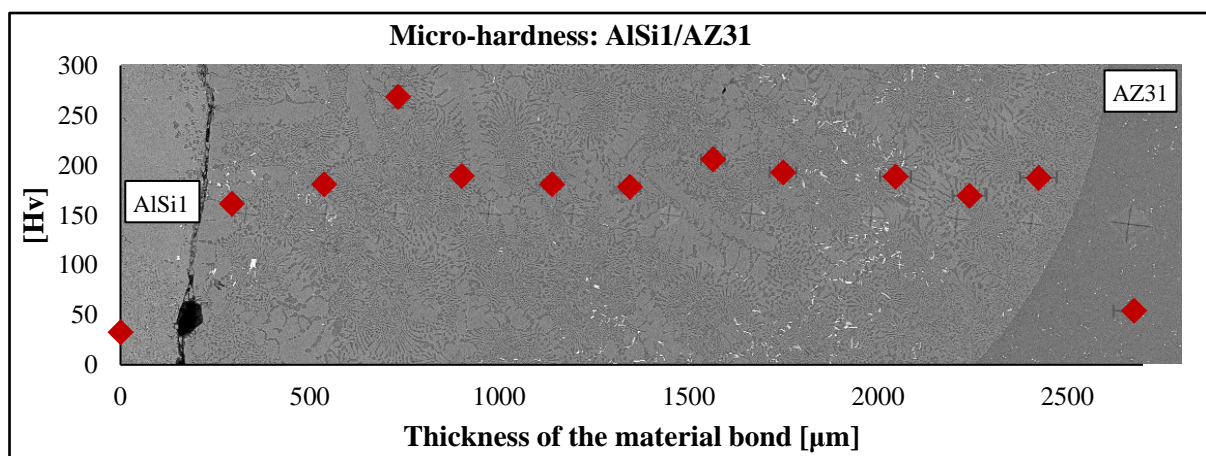


Figure 4.26: Micro-hardness in Hv across the material bond of an AlSi1/AZ31 compound casting. The peak is caused by the indenter partially hitting a Mg<sub>2</sub>Si particle.

alloys. In both alloy systems the hardness of the material bond is several times higher than those of the two base metals. This is caused by the intermetallic phases  $\beta$  and  $\gamma$  as well as the ternary phases  $Mg_2Si$ ,  $\tau_1$  and  $\varphi$ . As mentioned previously, a 2% error was assumed on measurements with an optical microscope, resulting in a 4% error of the calculated Vickers micro-hardness.

Beyond the strength increase as a result of the addition of 1wt% silicon (due to solid solution strengthening), no linear correlation between hardness and increase in silicon content exists in AlSi/AZ31 compound castings. An increase in silicon does not strictly lead to an increase in hardness or vice versa. As the microstructure of the AlSi1/AZ31 casting (see figure 4.27) is rather uniform, with

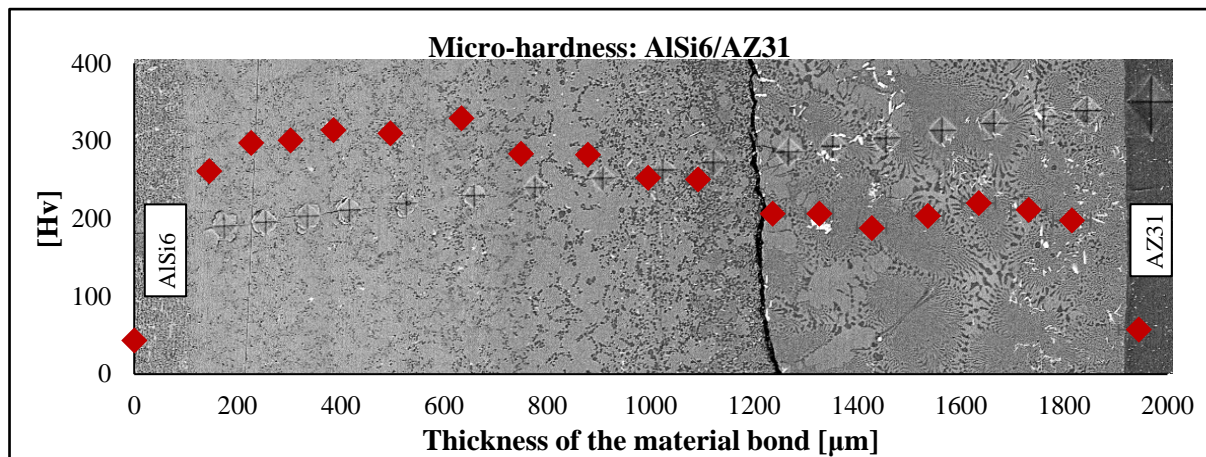


Figure 4.27. Micro-hardness in Hv across the material bond of an AlSi6/AZ31 compound casting. Hardness on the aluminium-rich side of the fracture was higher than on the magnesium-rich side. This may be an indication of the harder aluminium-rich intermetallic phase  $\beta$ .

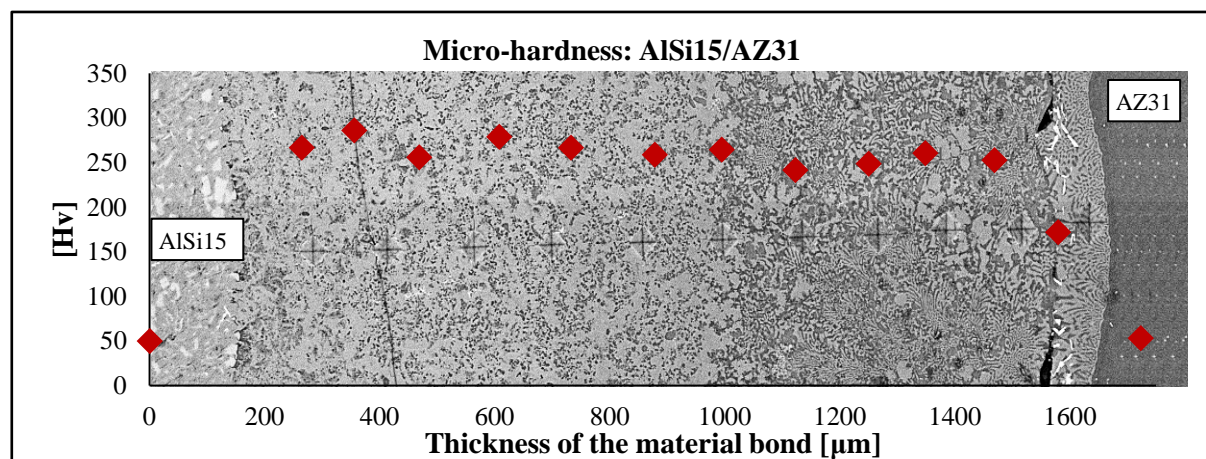


Figure 4.28: Micro-hardness in Hv across the material bond of an AlSi15/AZ31 compound casting.

the exception of the fracture, across the material bond, the hardness gradient displays almost constant values. The spike in the gradient is caused by the indenter partially hitting an  $Mg_2Si$  particle. This is an indication that the hardness of the  $Mg_2Si$  is higher than that of the  $\gamma$  intermetallic phase. The AlSi6/AZ31 casting displays a more complex hardness gradient. The aluminium-rich side of the material bond



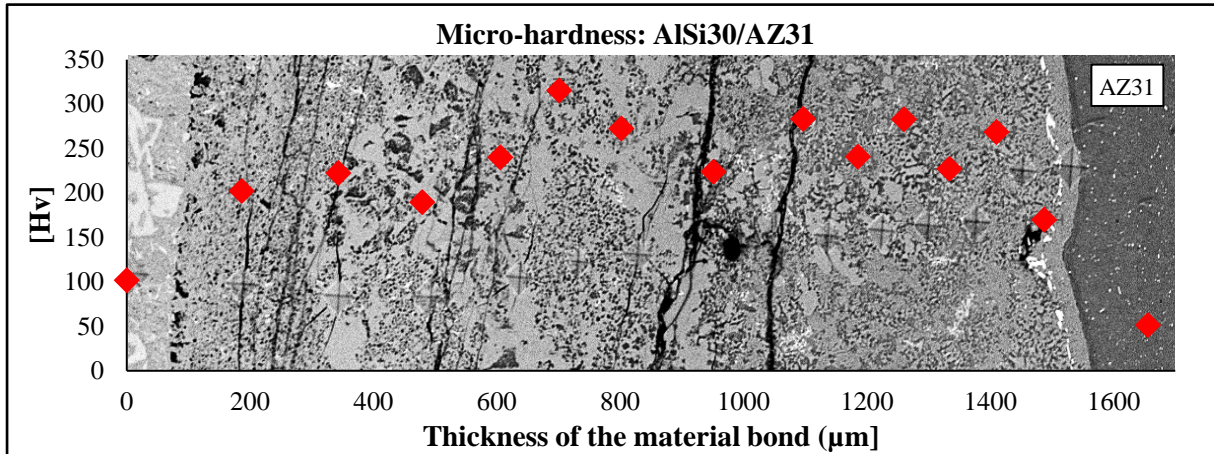


Figure 4.29. Micro-hardness in Hv across the material bond of an AlSi30/AZ31 compound casting.

displays the highest hardness values. From here the hardness decreases proportionally with respect to the increase in the magnesium content. As the gradient of the magnesium concentration on the magnesium side of the fracture is almost constant, there is no clear gradient in the hardness.

Alloy	Hardness [Hv]			
	$\beta$ +Mg <sub>2</sub> Si (layer 1)	$\gamma$ +Mg <sub>2</sub> Si (layer 2)	$\gamma$ +Mg+Mg <sub>2</sub> Si (layer 3)	$\gamma$ +Mg (layer 4)
AlSi1	181(+/-13)	-	-	169(+/-8)
AlSi6	298(+/-22)	257(+/-18)	-	209(+/-10)
AlSi15	271(+/-13)	259(+/-4)	256(+/-7)	152(+/-5)
AlSi30	223(+/-14)	264(+/-48)	231(+/-25)	170(+/-6)

Table 4.5: Average values of the hardness of each layer found in AlSi/AZ31 compound castings. The standard deviations over three measurement series are given.

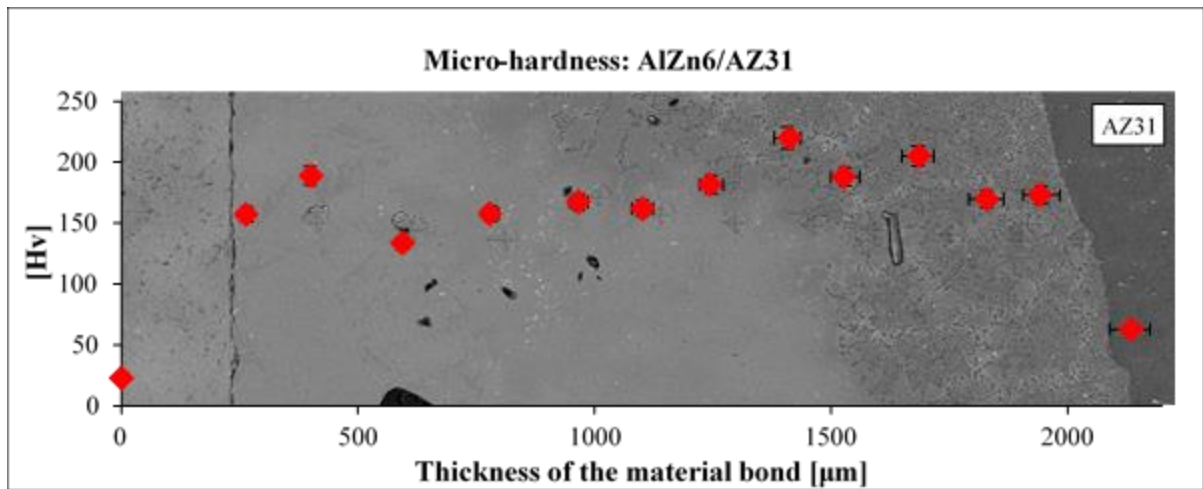


Figure 4.30: Micro-hardness in Hv across the material bond of an AlZn6/AZ31 compound casting.

Despite the varying microstructure across the material bond of the AlSi15/AZ31, the hardness gradient is quite uniform with the values ranging from  $\sim 250 \pm 10$  to  $\sim 280 \pm 11$  Hv. The aluminium-rich side appears to be (in the magnitude of  $\sim 10$  to  $\sim 20 \pm 1$  Hv) slightly harder than the magnesium-rich one. Also, a clear drop in hardness can be observed in the  $\gamma$ +Mg layer, due to the relatively high percentage of magnesium and the lack of hard  $Mg_2Si$  particles. As can be seen in figure 4.29, the increased amount of  $Mg_2Si$  has led to an increased brittleness in the AlSi30/AZ31 casting, which in turn has led to a significant number of fractures across the material bond, with several of the fractures originating from the indents of the measurements. When the indenter partially hit one of the fractures, the resulting hardness value would be lower than anticipated. As a consequence, the hardness gradient is rather inconsistent, with a number of deviations.

The hardness of the AlZn/AZ31 compound castings is significantly lower than that of the castings containing silicon. The highest values were around  $300 \pm 12$  Hv for an AlZn15/AZ31 casting, and the

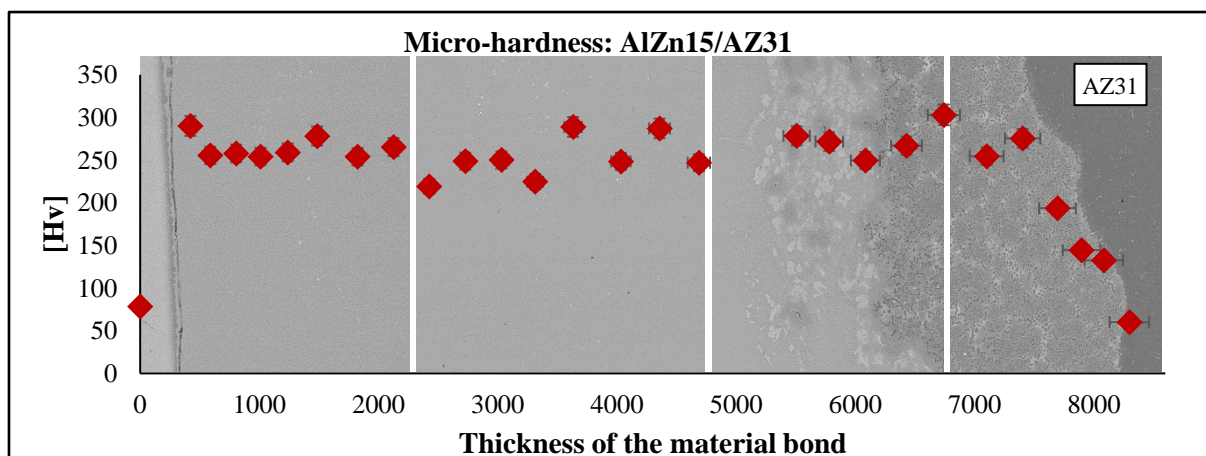


Figure 4.31: Micro-hardness in Hv across the material bond of an AlZn15/AZ31 compound casting.

lowest value was around  $133 \pm 5 \text{Hv}$  for an AlZn6/AZ31 casting. Again no linear correlation between zinc content and hardness was measurable. Hardness in the AlZn/AZ31 compound castings is dependent on the two intermetallic phases, and, in the case of AlZn30/AZ31, the  $\tau_1$  and  $\phi$  phases. In contrast to all previously reported results, the areas with the higher hardness in the AlZn6/AZ31 sample tended to be on the magnesium side, with no clear trend in the gradient of the hardness. The highest average hardness of the material bond was achieved by the AlZn15/AZ31 casting. Hardness fluctuated between  $250 \pm 10$  and  $300 \pm 12 \text{Hv}$  across the whole material bond. With an average of  $206 \pm 26 \text{Hv}$ , the hardness of the AlZn30/AZ31 casting was between that of the AlZn6/AZ31 ( $\sim 174 \pm 23 \text{Hv}$ ) and AlZn15/AZ31 ( $\sim 250 \pm 34 \text{Hv}$ ). The two AlMgZn phases  $\tau_1$  and  $\phi$  displayed a similar level of hardness to the  $\beta$  and  $\gamma$  phases. This explains the somewhat even gradient of the hardness. Due to the larger thickness of the material bonds in AlZn/AZ31 compound castings, the micrographs shown in figures 4.30-4.32 were stitched together from several separate micrographs. As such, the values for the hardness do not necessarily correspond with the spot shown above/beside them.

Values of the hardness of each layer found in AlZn/AZ31 compound castings are shown in table 4.6. They are the averages of the measurement series presented in figures 4.30-4.32 and two additional measurement series. As can be seen in the figures, the indents of the hardness measurement on the magnesium-rich side (right-hand side in the figures) display no cracks or deformation at the edges. This was not observed on the aluminium-rich side. Many indents had visible cracks or signs of deformations at the edges despite the low load (0.3N) used. This is an indication that the  $\gamma$  phase possesses increased ductility compared to the  $\beta$  phase, while retaining a similarly high level of hardness.

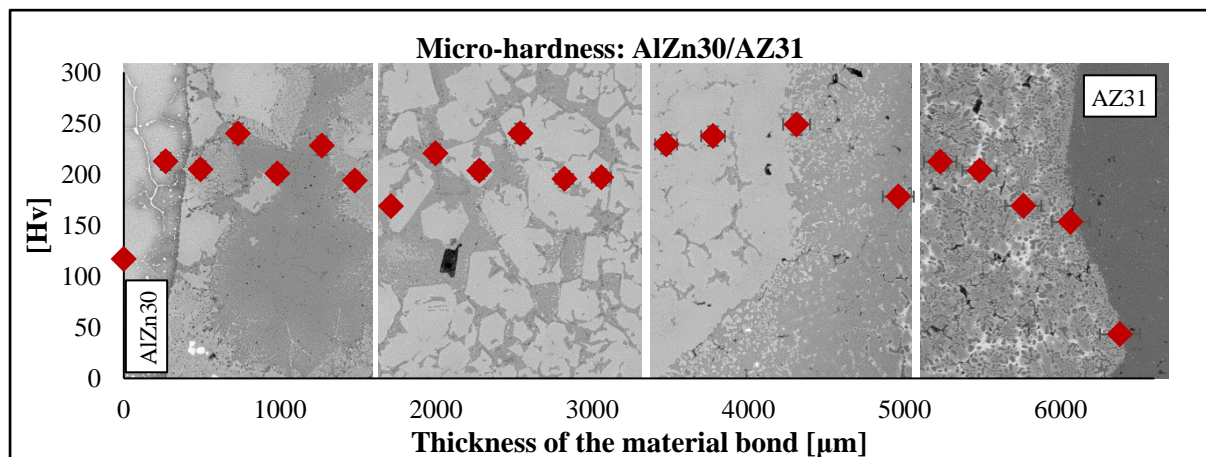


Figure 4.32. Micro-hardness in Hv across the material bond of an AlZn30/AZ31 compound casting.

Alloy	Hardness [Hv]	
	$\beta$ +Al(+ $\tau_1$ )	$\gamma$ +Mg(+ $\phi$ )
<b>AlZn6</b>	174(+/-24)	188(+/-19)
<b>AlZn15</b>	255(+/-20)	241(+/-53)
<b>AlZn30</b>	219(+/-23)	184(+/-24)

*Table 4.6: Average values of the hardness of each layer found in AlZn/AZ31 compound castings. The standard deviations over three measurement series are given.*

## 4.4: Conclusion

- A material bond was observed to form when overcasting commercially pure aluminium with a magnesium alloy. No special surface treatment was necessary for a chemical material bond to occur.
- The intermetallic phases  $\beta$  and  $\gamma$  were the main constituents of the material bond. They were found in layers adjacent to the aluminium and magnesium respectively. Elementary magnesium was found to precipitate in the layer containing the  $\gamma$  phase. The  $\beta$  phase was found to be the dominant phase in the bond.
- Annealing of an AlZn30/AZ31 compound casting at 400°C resulted in the complete transformation of the microstructure. Numerous, large (up to 2cm in diameter), evenly shaped holes were present in the aluminium alloy.
- The phases that make up the material bond displayed a low solidus temperature. The material bond solidifies after the magnesium alloy, leading to defects such as solidification-related shrinkages and pores. Some of the pores, found near the magnesium dendrites, were identified as stemming from hydrogen porosity.
- Additional defects included fractures and evenly shaped voids. Fractures were found propagating in close proximity to the aluminium side of the bond. Fractures were deduced to either originate during cooling or after solidification. The regular shaped voids, not thought to stem from solidification, were found throughout all compound castings. They are thought to stem from an imbalanced diffusion process in the solid state. They were found on the magnesium-rich side of the material bond.
- Growth of the material bond is a complex interaction between chemical reactions, dissolution and crystallisation, segregation and solid state diffusion. The thickness of each phase varied with the process parameters (casting and preheat temperature, holding time). The  $\beta$  phase was generally found to be the dominant phase in the bond.
- Adding silicon and zinc as ternary elements resulted in the formation of new chemical compounds.  $Mg_2Si$  particles were formed when adding silicon, and the zinc-rich intermetallic phases  $\tau_1$  and  $\phi$  when adding zinc. The phases  $\beta$  and  $\gamma$  were found to be able to dissolve and contain a significant amount of zinc in solid solution. Consequently, only in the presence of large quantities of zinc (>15wt%) did the aforementioned zinc-rich phases form.
- Localised mechanical testing confirmed the brittle nature of the bond, with the hardness of the bond found several times higher than that of the aluminium and magnesium alloys used. Testing was done using Vickers micro-hardness measurements, as Vickers hardness correlates with tensile strength. It was evident that the material bond was susceptible to fractures and cracks, which were a common occurrence.

- The found defects (shrinkages, hydrogen porosity, fractures) are thought to weaken the soundness, and thus mechanical strength, of the material bond. Mechanical strength and soundness of the material bond is further discussed in chapter 6.

## 4.5: References

ANYALEBECHI, P. N. (2013) Hydrogen-induced gas porosity formation in Al–4.5 wt% Cu–1.4 wt% Mg alloy. *Journal of Materials Science*, **48**(15), pp. 5342-5353.

CAMPBELL, T., KALIA, R. K., NAKANO, A., VASHISHTA, P., OGATA, S., and RODGERS, S. (1999) Dynamics of Oxidation of Aluminum Nanoclusters using Variable Charge Molecular-Dynamics Simulations on Parallel Computers. *Physical Review Letters*, **82**(24), pp. 4866-4869.

GILLE, P. and GRIN, Y. (2018) *Crystal Growth of Intermetallics*. Berlin/Boston: Walter de Gruyter GmbH.

MEZBAHUL-ISLAM, M., MOSTAFA, A. O., and MEDRAJ, M. (2014) Essential Magnesium Alloys Binary Phase Diagrams and Their Thermochemical Data. *Journal of Materials*, **2014**.

PAVLINA, E. and VAN TYNE, C. (2008) Correlation of Yield Strength and Tensile Strength with Hardness for Steels. *Journal of Materials Engineering and Performance*, **17**(6), pp. 888-893.

TIRYAKIOĞLU, M., ROBINSON, J. S., SALAZAR-GUAPURICHE, M. A., ZHAO, Y. Y., and EASON, P. D. (2015) Hardness–strength relationships in the aluminum alloy 7010. *Materials science & engineering, A, Structural materials: properties, microstructure and processing*, **631**, pp. 196-200.

## **Chapter 5: Interfacial Phenomena in Al/Mg Compound Castings**

### **5.1: Outline**

It has been established in chapter 4 that the formation of the material bond in Al/Mg compound castings is the result of chemical reactions and the formation of new phases according to the corresponding phase diagrams. Over the course of the experimentation described in chapter 3, a number of interesting observations (deemed interesting enough to warrant further investigation) were made. These observations concerned:

1. aluminium's oxide and what is happening to it during casting;
2. the magnesium- and zinc-rich phases showing signs of improved ductility compared to the aluminium-rich phases;
3. the impact of the casting process on the formation of a material bond;
4. temperature distribution along the material bond being found to have a significant impact on the formation of the material bond and its growth.

## 5.2: Chemical Reaction of Alumina with Magnesium

As elaborated on in the literature review, aluminium's oxide layer is reported to negatively impact compound castings involving aluminium. This however has not been observed in the present study. No traces of aluminium's oxide layer were found throughout the castings. Hence, a set of experiments was conducted to assess what happened to the alumina layer during casting.

According to the Ellingham diagram shown in figure 5.1, at temperatures below  $\sim 1500^{\circ}\text{C}$  magnesium oxide is thermodynamically more stable than aluminium oxide (Stratton, 2013). Thus it is expected that the alumina layer is reduced to elementary aluminium and magnesium oxide. The reduction of alumina to Al and MgO should follow the following equation:



A common impurity in cast aluminium alloy is Al-Mg spinel ( $\text{MgAl}_2\text{O}_4$ ); the corresponding chemical reaction equation is:



Photographs of cut samples, each containing a piece of  $\text{Al}_2\text{O}_3$  overcasted with AZ31, are displayed in figure 5.3. As can be seen in the photographs, the piece of  $\text{Al}_2\text{O}_3$  showed no signs of a chemical reaction with the magnesium. Inspection via SEM revealed an  $\sim 100\mu\text{m}$  thick reaction zone at the interface of the  $\text{Al}_2\text{O}_3$  piece with the magnesium. However, as revealed with a map of the elemental distribution at the interface using EDX, the magnesium could also just have penetrated the surface of the  $\text{Al}_2\text{O}_3$ , thus creating the visible reaction zone. As such, no proof of a chemical reaction between the two materials is evident. Micrograph and map of the elemental distribution of aluminium, magnesium and oxygen are displayed in figure 5.4.

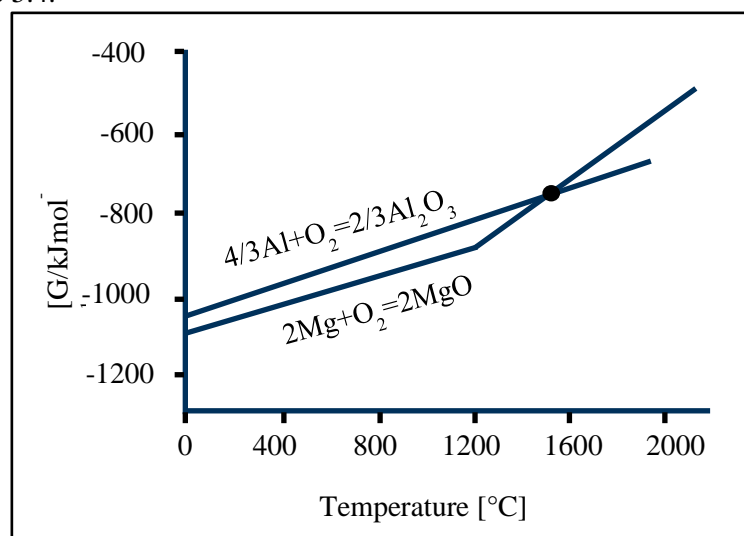


Figure 5.1. Free energy of the formation of aluminium and magnesium oxide as a function of the temperature according to the Ellingham diagram (Stratton, 2013).



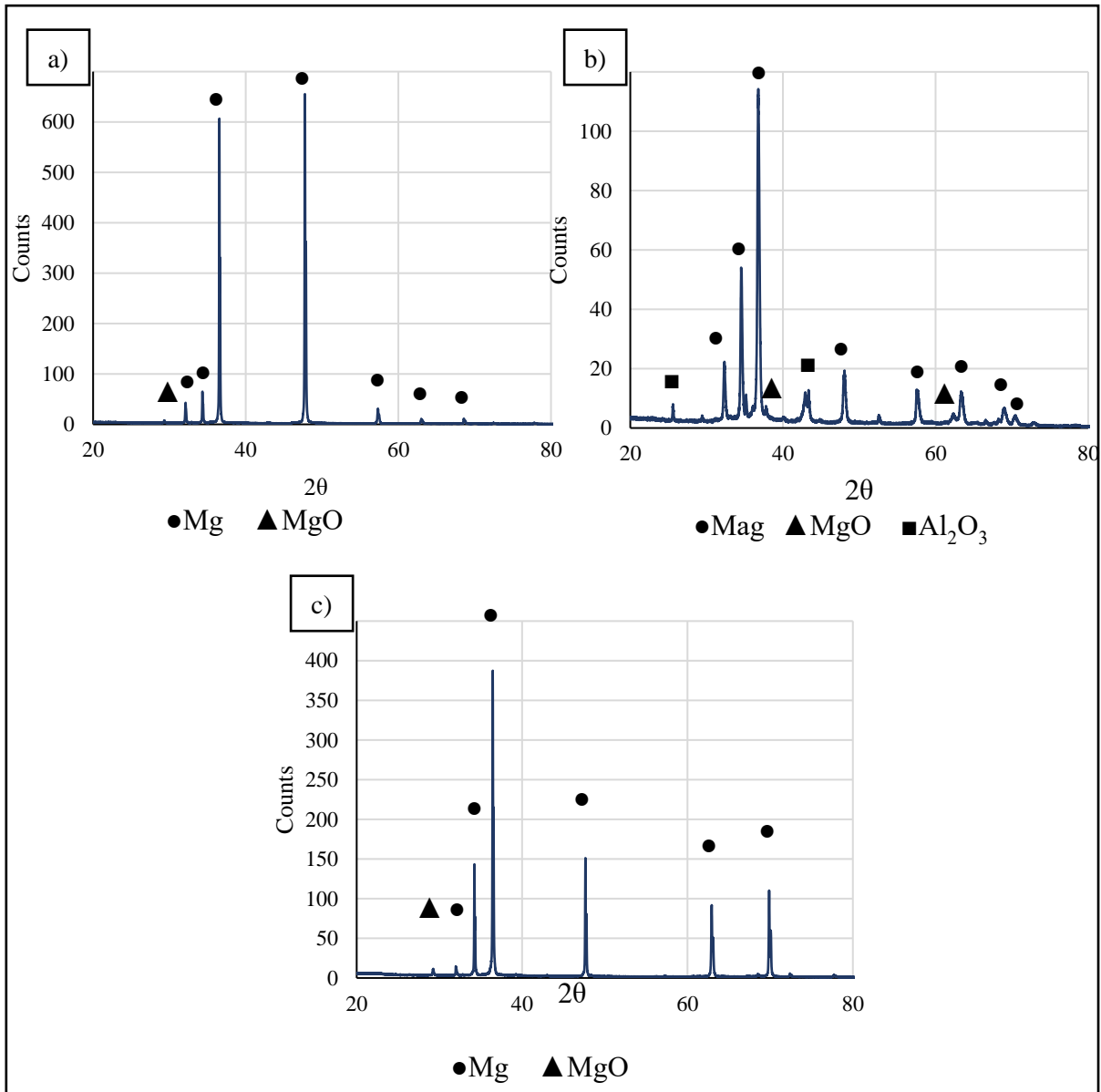


Figure 5.2. X-Ray Diffraction (XRD) patterns of the  $Al_2O_3$  powder overcast with magnesium after a reaction time of: (a) 15min; (b) 30min; and (c) 60min.

As shown in figure 5.3, overcasting the  $\text{Al}_2\text{O}_3$  powder resulted in the visible formation of dross on the

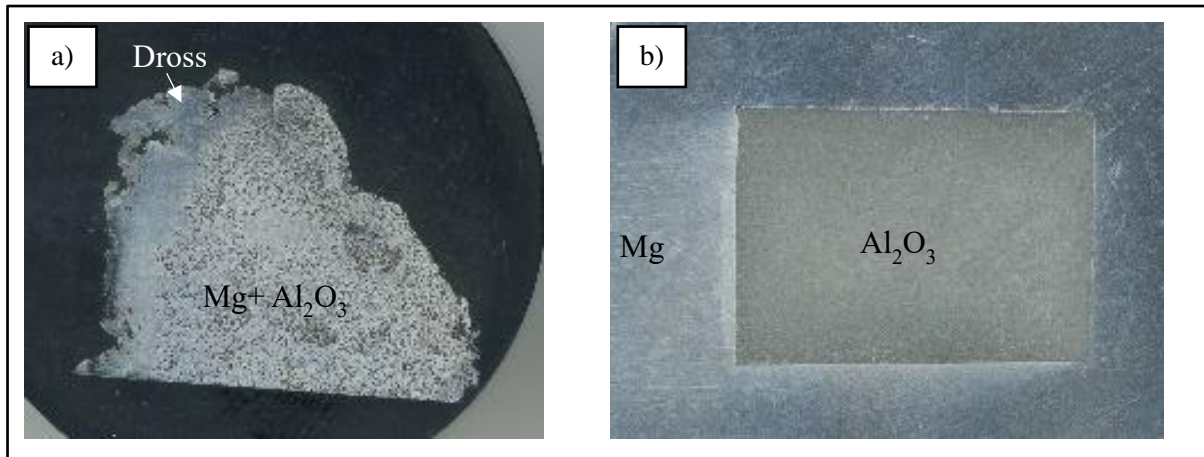


Figure 5.3. Macrographs of: (a) the overcasting of an  $\text{Al}_2\text{O}_3$  powder with magnesium. Appearance of the sample hints to the presence of a reaction zone; and (b) the overcasting of a piece of  $\text{Al}_2\text{O}_3$  with magnesium. The dark colour of the  $\text{Al}_2\text{O}_3$  piece stems from polishing with SiC paper. No reaction zone is visible.

surface of the liquid magnesium. As a cover gas was used, this hints at a chemical reaction within the liquid magnesium. The diffraction curves, displayed in figure 5.2, display no proof of a chemical reaction. While the presence of MgO was confirmed in all three samples, the peak intensity associated with MgO was not distinct in any of the samples. The exact source of the MgO is inconclusive. While it could be the reaction product of magnesium with  $\text{Al}_2\text{O}_3$ , as theorised, it could also stem from the oxide skin of the magnesium. No  $\text{Al}_2\text{O}_3$  was identified in the samples removed from the furnace after 15 and 60min. Similarly, the XRD was unable to identify any elementary aluminium, in all three samples. As only a relatively small amount (compared to the amount of magnesium) of aluminium was present, the aluminium is dissolved in the magnesium melt. During solidification, it precipitates on the magnesium crystal lattice, rather than forming its own phase. The aluminium atoms cause a slight distortion of the magnesium lattice, resulting in a small shift of the magnesium peaks in the diffraction pattern. Intensity of the peaks, indicating the presence of MgO and  $\text{Al}_2\text{O}_3$ , is more distinct in the sample removed from the furnace after 30min. Even though all samples were cut from the same place, segregation of the melt and  $\text{Al}_2\text{O}_3$  particles, due to stirring, could have led to deviating microstructure across the three samples. It is possible that some oxides floated to the surface of the liquid melt, forming the observed dross. Overall, almost no differences between the three holding times were detected. As visible on the micrographs, the  $\text{Al}_2\text{O}_3$  tended to form clusters. No traces of AlMg spinels were found in any of the diffraction patterns or micrographs. The reaction between aluminium's oxide layer and the magnesium melt to form magnesium oxide (and aluminium) has not been directly observed. Lacking any direct evidence, the reduction of the oxide layer will be further discussed in chapter 7 using results reported in the literature and the observations described in this section.

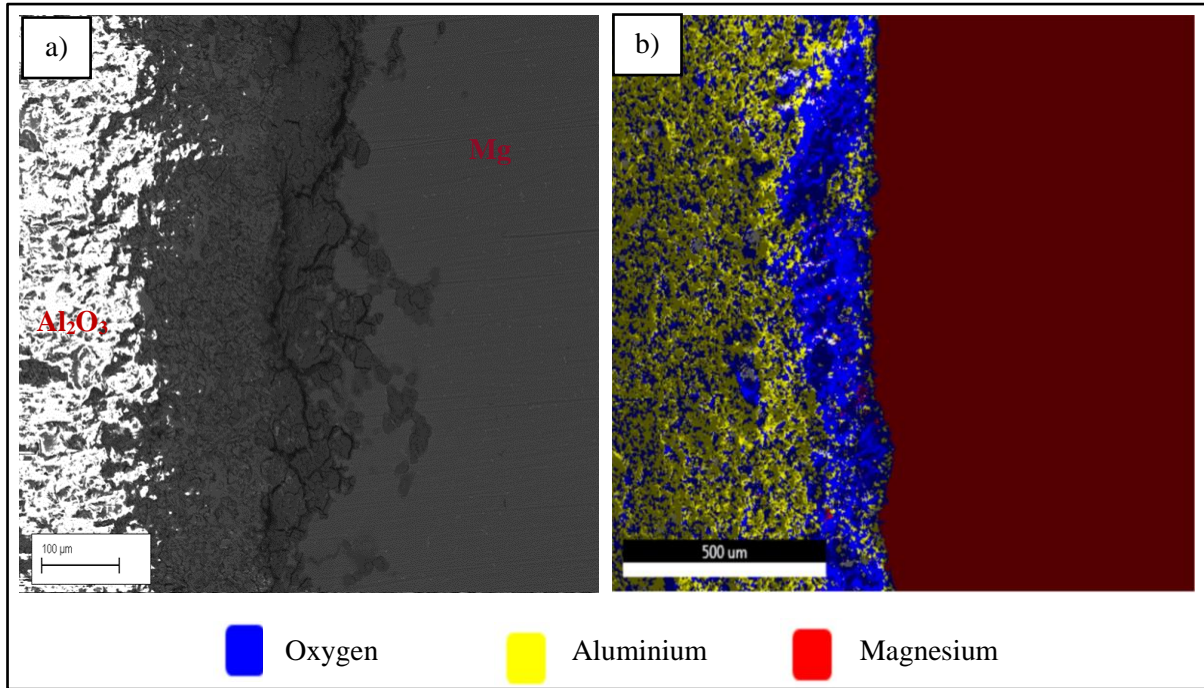


Figure 5.4. (a) Secondary SEM micrograph, of the interface of a solid piece of  $\text{Al}_2\text{O}_3$  and (commercially) pure magnesium, obtained with Secondary Electron Imaging. (b) Map of the elementary distribution at the interface.

### 5.3: AlMgZn Phases

Phases on the magnesium side of the material bond showed signs of improved ductility compared to the aluminium-rich phases. The Mg+ $\phi$ + $\gamma$  phases displayed a high hardness (with an average of 210 Hv, roughly on the same level as the  $\beta$  phase with an average of 230Hv) while retaining some form of ductility. It is believed that the combination of hard intermetallic phases  $\phi$ + $\gamma$  and soft magnesium is responsible for this increase in ductile behaviour. In this chapter, the results concerning the study of the microstructure of the AlMgZn phases are presented.

Images acquired via optical microscopy and SEM for the three alloys, produced as described in chapter 3, are shown in figure 5.5. Compared to the microstructure of the reference sample, displayed in figure 5.6, the microstructure of the three AlMgZn alloys displays significant differences. More importantly, the microstructures of the AlMgZn alloys differ from one another. For consistency (with previous hardness measurements), mechanical properties were approximated using Vickers micro-hardness measurements. The given values for hardness are the average of ten separate measurements taken

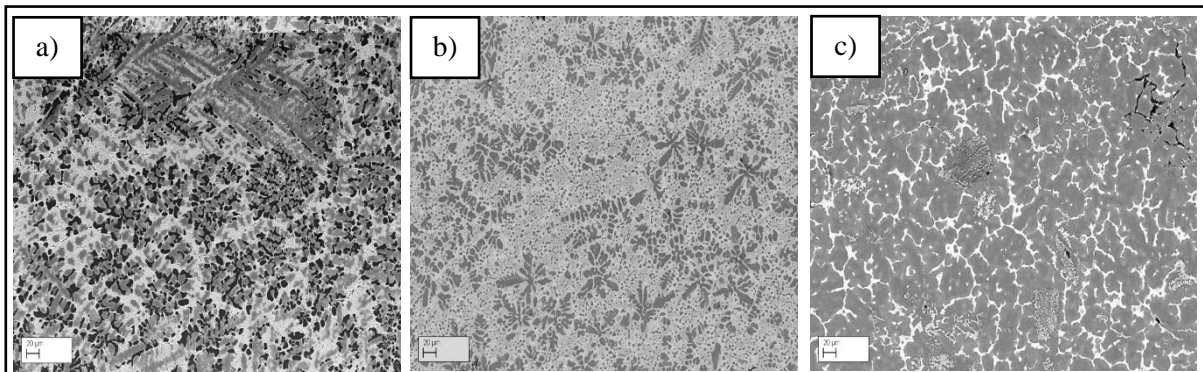


Figure 5.5. SEM backscatter micrographs of all three AlMgZn-alloys:  
(a) alloy 1 (Mg60Zn20Al15); (b) alloy 2 (Mg70Al15Zn15); and (c) alloy 3 (Mg90Al5Zn5).

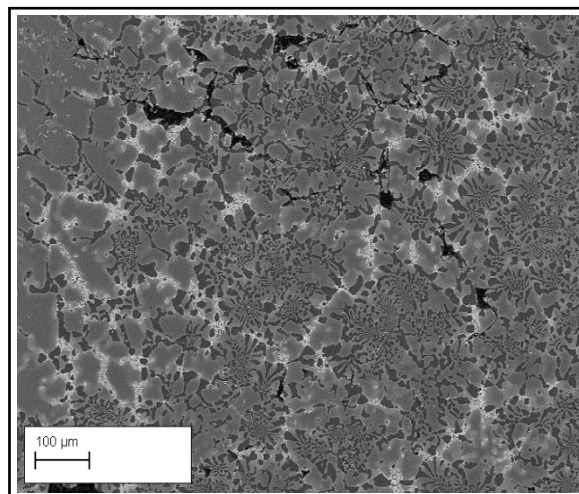


Figure 5.6. SEM backscatter micrograph of the microstructure of the Magnesium-rich side of an AlZn30/AZ31 compound casting. The chemical composition and phases observed are similar to the three AlMgZn alloys displayed in figure 5.5.

randomly in different locations across the samples. It was expected that the microstructure of all three alloys would be similar, as chemical composition placed all three alloys in the same phase field. Chemical composition of the three alloys is listed in table 5.1. It was verified with EDX as the composition was outside the calibration range of Optical Emission Spectroscopy. The listed values are the averages of three separate measurements taken across the samples. The three alloys tended to oxidise quickly when exposed to the atmosphere. As a result, oxides and thus oxygen were common impurities. Besides oxygen, 1.6-1.7wt% carbon was detected in alloy 2. As carbon was not present in the other alloys, which were produced from the same base material, it was thought to originate from impurities during melting or casting.

	Weight per cent [wt%]			
	Al	Mg	Zn	Impurities
<b>Alloy 1</b>	15.66	61.02	22.07	Balance
<b>Alloy 2</b>	14.95	70.99	12.29	Balance
<b>Alloy 3</b>	4.61	87.27	5.82	Balance

Table 5.1: Chemical composition of the three AlMgZn alloys. The composition was measured with EDX as the composition of the alloy was outside the calibration range of OES. Due to the high affinity of magnesium to oxidise, oxygen was a common impurity.

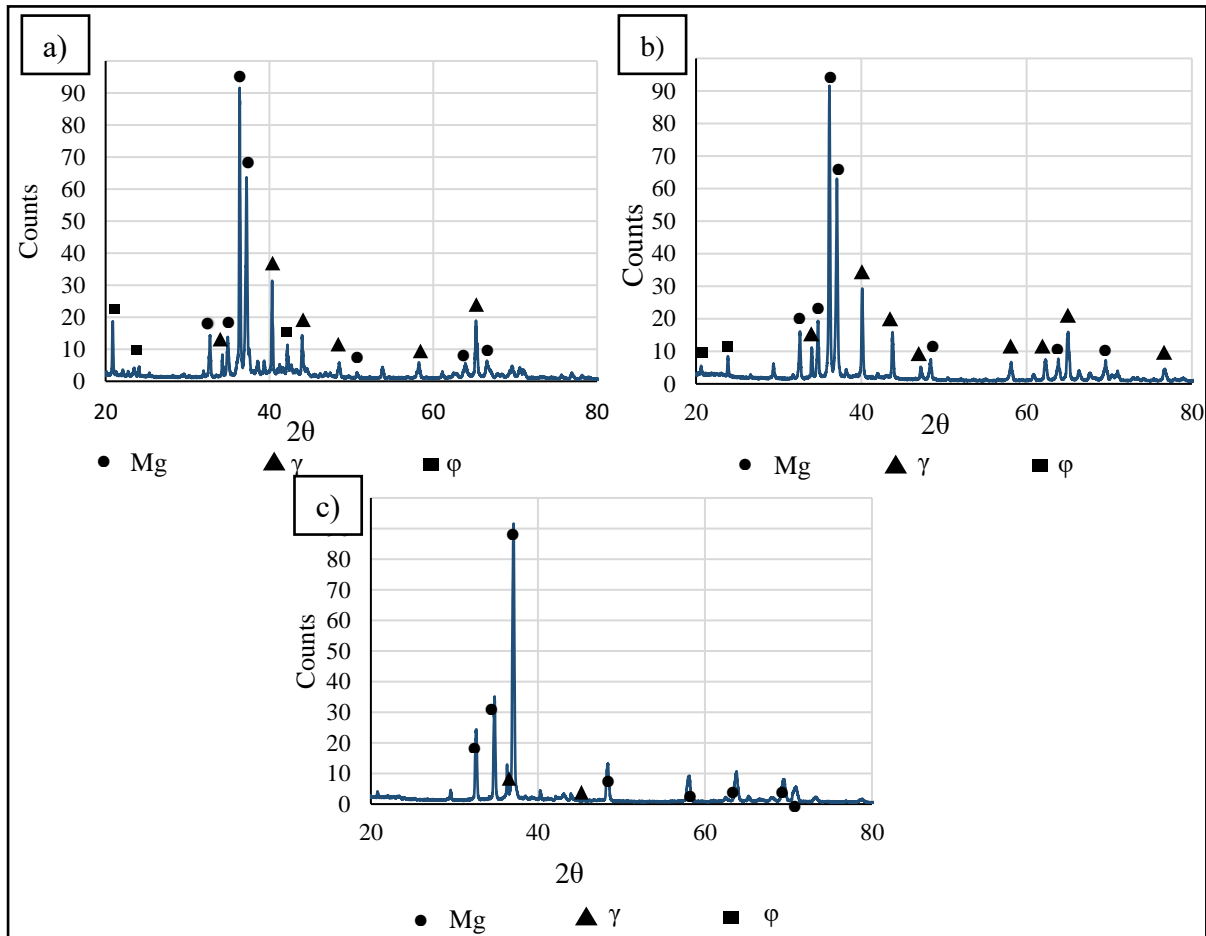


Figure 5.7. X-Ray Diffraction (XRD) patterns for all three AlMgZn alloys: (a) alloy 1 (Mg60Al20Zn20); (b) alloy 2 (Mg70Al15Zn15); and (c) alloy 3 (Mg90Al5Zn5).

Even though the microstructure of alloy 1 resembles the reference sample most closely, a number of differences are visible. In alloy 1 elementary magnesium is more finely dispersed and the dendrites are smaller. The  $\phi$  phase is also more evenly distributed and additionally the  $\gamma$  phase is less distinct. The micro-hardness of the alloy was measured at 182Hv, which is a similar value to that measured in AlZn/AZ31 compound castings (see chapter 4). While the same phases can also be found in alloy 2, its microstructure is vastly different. Elementary magnesium constitutes only a small part of it. The majority of the microstructure consists of the  $\phi$  and  $\gamma$  phases. Hardness was 146Hv on average, lower than in alloy 1, but still within a comparable range with other AlZn/AZ31 compound castings. Even though all three phases,  $\gamma$ ,  $\phi$ , and Mg, are supposed to be present in alloy 3, only the presence of two phases,  $\gamma$  and Mg, was confirmed. Elementary magnesium was the main constituent of the material bond, with the  $\gamma$  phase forming dendrites. No significant amount of the  $\phi$  phase was discovered. Hence, the hardness of the alloy was 70Hv, considerably (up to 60% ) lower than those of the other two alloys and the material bond present in AlZn/AZ31 compound castings. According to the phase diagram, the microstructure in all three alloys was expected to be similar. The deviations in phases found, and thus hardness described, indicate that the formation of the equilibrium phases predicted by the phase diagram is impeded. As a consequence, it must be concluded that phase diagrams are of limited use for predicting existing phases in Al/Mg compound castings containing relatively large amounts of zinc.

The height of the liquid metal in the crucible before and after solidification was marked. Based on the differences between the height of the liquid and solid metal in the crucible, the volume of the liquid and solid phases can be approximated. It should be noted that while a clear decrease in height between the liquid and solid was detected, the given values were measured by hand and are thus not to be considered exact. The crucible was cylindrical with an internal diameter of 60mm. Values for the height of the liquid and solid metal in the crucible are listed in table 5.3, and a clear difference between the volumes in the liquid and solid state was observed; but due to the rather imprecise nature of the measurements, the given values should not be considered precise. The DSC trace for the reference sample is displayed in figure 5.8. As expected from the phase diagram, the two phases  $\phi$  and  $\gamma$  display a very low solidus temperature. From the DSC trace, the solidus temperature of the  $\phi$  phase was measured to be 367°C, with the  $\gamma$  phase starting to melt shortly after. The melting range of both phases was measured to be 367-433°C.

	<b>Alloy 1</b>	<b>Alloy 2</b>	<b>Alloy 3</b>
<b>Microhardness [Hv]</b>	182.8+/-6Hv	146.6+/-16Hv	70.5+/-4Hv

Table 5.2: Micro-hardness of the three alloys in Hv.

AlMgZn alloy	H <sub>liquid</sub> [mm]	V <sub>liquid</sub> [mm <sup>3</sup> ]	H <sub>solid</sub> [mm]	V <sub>solid</sub> [mm <sup>3</sup> ]	ΔV [%]
1	45	127234	39	110269	15
2	51	144199	44	124407	15
3	32	90477	25	70685	28

Table 5.3: Height of the AlMgZn alloy in a cylindrical mould in the liquid and solid state was measured manually. The liquid-solid volume contraction was calculated using these values. An error of +/-2mm is assumed on the measurements.

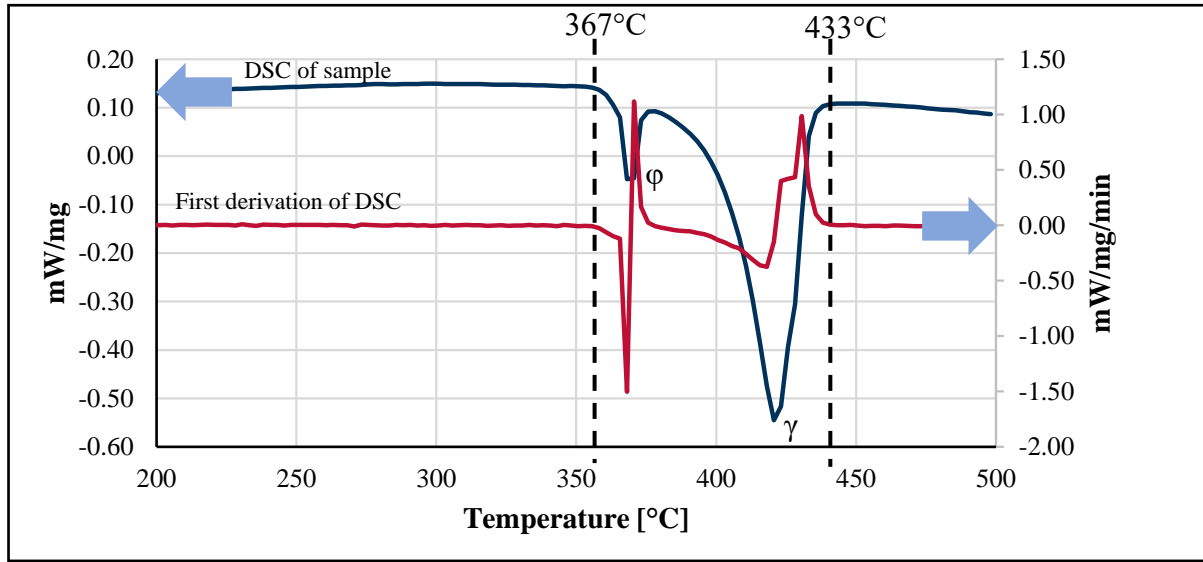


Figure 5.8. DSC curves of the heating of the magnesium-rich side of an AlZn30/AZ31 material bond. The solidification range of the magnesium-rich phases  $\gamma$  and  $\phi$  is marked with the dashed lines. The sample was heated up at a constant rate of 10°C/min.

## 5.4: Thermophysical Description of Interfacial Reaction using Numerical Simulation

Temperature is thought to play an important role in the formation of the material bond in compound casting. As a consequence, the temperature distribution along the Al/Mg interface was approximated by direct temperature measurement and calculated with numerical simulation. The curves and gradients acquired with numerical simulation will be referred to hereafter as calculated curves/gradients.

The cooling curve for the AlZn/AZ31 compound casting is displayed below in figure 5.9. No cold shuts were present in the casting and consequently the casting temperature of 660°C was deemed high enough to ensure proper filling of the mould. The highest measured temperature opposite the inlet was 615°C, using a casting temperature of 660°C, while the temperature loss of the liquid metal to the surrounding atmosphere and mould was 45°C. As expected, there is an offset between the temperature measured in the middle of the Al cylinder and opposite the inlet. The temperature measured inside reached its peak of 580±5°C 15 seconds after the outside measured temperature reached its peak of 615±5°C. The whole experimental setup displayed a degree of inertness to temperature changes, due to the relatively large amount of melt and slow reactivity of the thermocouples used, resulting in a low cooling rate. Due to the low cooling rate the curves would only coincide with each other after approximately 370s. The average cooling rate was calculated to be 22.89±0.1°C/min. The temperature was measured until the temperatures reached 350°C, the lowest solidus temperature of the Al-Mg-Zn system. Due to the low cooling rate of the experimental setup, the system was not sensitive enough to record the recalescence of the magnesium alloy during cooling and solidification. Adding the liquidus and solidus temperatures

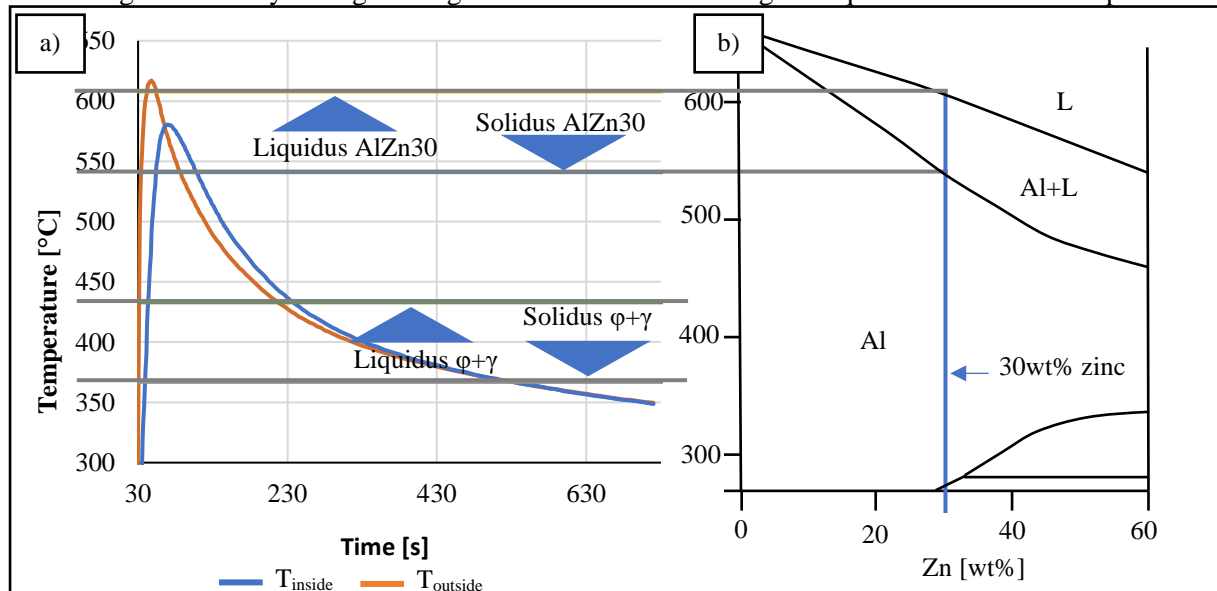


Figure 5.9. (a) Cooling curves measured in an AlZn30/AZ31 compound casting. The  $T_{outside}$  curve displays the temperature at the interface while the  $T_{inside}$  curve was acquired via thermocouple measurement in the middle of the Al cylinder. (b) Relevant section of the Al-Zn phase diagram. The measured pouring temperatures are above the solidus temperature of an AlZn30 alloy.



of the AlMgZn phases determined in the previous chapter, and of the AlZn30 alloy, to the recorded temperature curves yields additional information as displayed in figure 5.9. The temperatures recorded at the interface rise above the liquidus temperature of the AlZn30 alloy for a short time (15s). This time window was deemed too narrow to cause the complete melting of the AlZn30 alloy, but due to the wide solidification range of the alloy, partial melting of the surface is likely to have occurred. The temperature in the middle of the cylinder was found to be above the alloy's solidus temperature. Based on these observations, the cooling conditions allow for at least the partial melting of the AlZn30 alloy.

Comparing the measured cooling curves with the one simulated with the Magmasoft package yields figure 5.10. According to the Magmasoft package, the average cooling rate was  $21.24 \pm 0.1^\circ\text{C}/\text{min}$ . This calculated cooling rate was found to be similar to that measured. The calculated curve however deviated at several points from the measured one. The peak temperature opposite the inlet was reached at 14s after pouring began, 36s faster than the actual measurements. Depending on their diameters, thermocouples display inertness to temperature changes. On the other hand, the reactivity of simulated thermocouples in Magmasoft is instantaneous. As such, as soon as the thermocouple comes into contact with the melt, the thermocouple records the simulated melt temperature. The varying peaks at the top of the simulated curve are thus the result of the turbulent filling of the mould. It should also be noted that pouring by hand is less consistent than the simulated pouring.

The plateau beginning at around  $430^\circ\text{C}$  in the cooling curve cannot be explained by this deviating reactivity of the thermocouples. A plateau usually indicates some form of recalescence or phase transformation. According to the ternary Al-Mg-Zn phase diagram, some AlMgZn alloys display a solidus temperature around this temperature. However, Magmasoft does not calculate a mixing or chemical reaction between the two metals. As such, the plateau in the calculated curve is probably due to the deviating heat balance between simulation and reality. Temperature losses to the environment are generally lower in the simulation than in reality, causing the described plateau around the preheat-temperature of the mould. Overall, as can be seen in figure 5.10, the calculated temperature on the outside of the Al cylinder is in fairly good accordance with the experimental measurements. Matching the peak of the simulated curve with the measured one confirmed a very similar gradient of both curves, up until the discussed plateau at  $450^\circ\text{C}$ . The calculated temperature in the middle of the Al cylinder followed a similar gradient to the simulated curve opposite the inlet. The maximum calculated temperature is  $565^\circ\text{C}$ , slightly lower than the measured  $580^\circ\text{C}$ . The offset was, at 36s, identical to the one on the outside. After the peak, at around 85s, the two calculated curves approach and overlap one another. During experimentation, this overlap was not observed until approximately 5min ( $\sim 300\text{s}$ ) later. In an attempt to achieve a better match between the calculated and measured gradients, the heat transfer coefficient (HTC) between the liquid magnesium and the solid aluminium was manipulated in Magmasoft. A changed HTC resulted in a slightly depressed or elevated (in the range of  $4\text{-}10^\circ\text{C}$ ) gradient, but the overall shape of the gradient did not change. An almost identical behaviour for the

temperature gradient on the outside of the Al cylinder was also observed. Under these conditions, changes in the HTC between the liquid magnesium and the mould did not translate into a changed gradient either. Within the boundary conditions used, the HTC seems to have only a limited impact on solidification and cooling. The mass of the mould and the magnesium was suspected to be too small for a changing HTC to have a significant impact. The described discrepancies between the calculated and recorded data persisted even after numerous iterations of the parameters used. These discrepancies were attributed to Magmasoft, showing that it does not mirror certain aspects of the casting and solidification of compound castings. The model does not accommodate the following.

1. Dissolution of the aluminium cylinder: the Al cylinder is treated as a permanent mould with regard to the numerical simulations. Melting, or the solid to liquid state transformation, is not modelled in Magmasoft.
2. Diffusion in the solid state: the diffusion of aluminium, magnesium and zinc across the material bond, and any subsequent reaction with intermetallic phases, is not modelled.
3. Formation of intermetallic phases: chemical reactions and associated reaction kinetics are disregarded in Magmasoft. While the resulting enthalpy from the solidification of the liquid metal is included in the simulation, the latent enthalpy of fusion of the AlZn alloy is not.

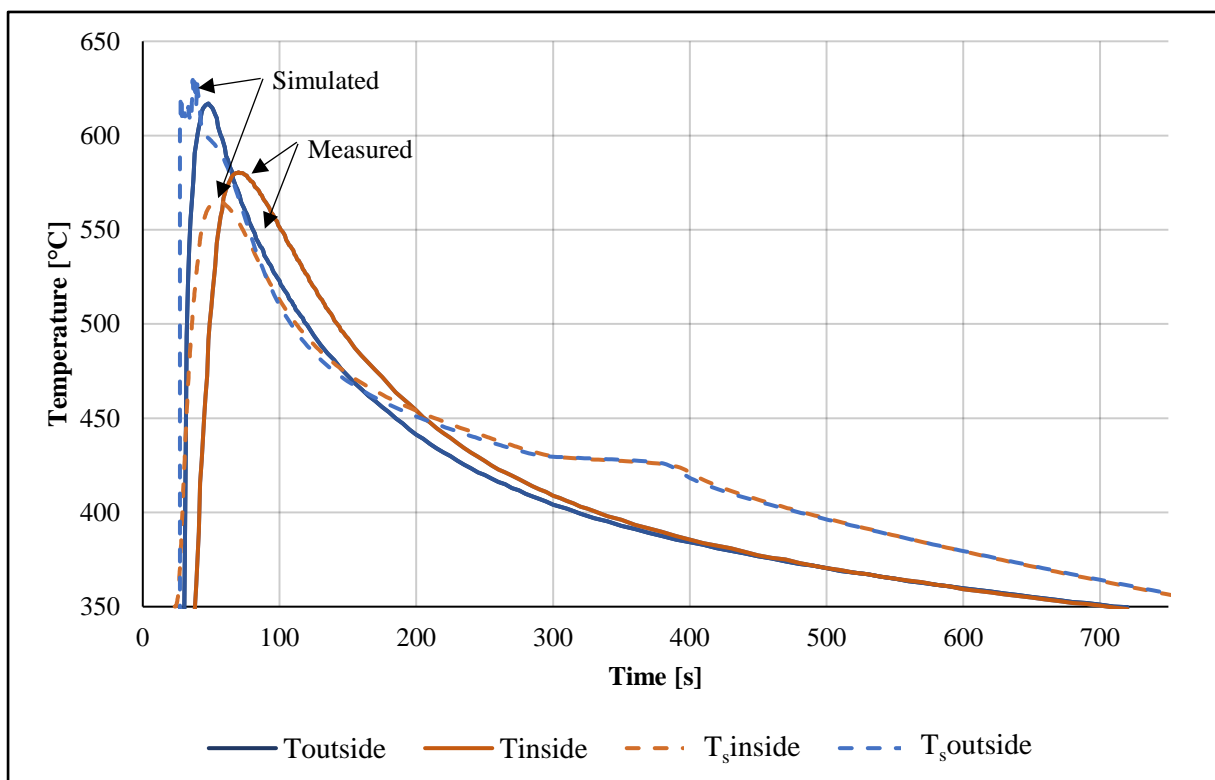


Figure 5.10. Measured ( $T_{outside}$  and  $T_{inside}$ ) and simulated with Magmasoft ( $T_{sinside}$  and  $T_{soutside}$ ) cooling curves of an AlZn30/AZ31 compound casting. Temperature was measured in the inside and at the surface of the AlZn30 cylinder.

4. Insufficient material data: aluminium alloys with a very high zinc content are not in general commercially used, and consequently their exact thermophysical properties are mostly unknown.

Despite these discrepancies, the gradient calculated at the interface ( $T_{s, \text{outside}}$ ) with Magmasoft, displayed in figure 5.10, is considered to be in acceptable agreement, in terms of maximum temperature and cooling rate, with the measured values for temperatures above 450°C. As such, the Magmasoft model is suited to assess the temperature at the Al/Mg interface during pouring and solidification. The temperature distribution within the casting and mould at the end of pouring, according to Magmasoft, is displayed in figure 5.11. According to the calculated temperature gradient between the inlet and the opposite side of the Al cylinder, temperature loss is negligible. This observation is in agreement with the experimental results. Thickness and characteristics of the material bond were found not to be strictly correlated to the distance from the inlet.

After filling, it was assumed that the hottest spot in the casting would be near the inlet, as it is the last area to be filled. However, the calculated temperature distribution displayed a slightly different behaviour. While, immediately after the end of the filling, a hot spot was found in the predicted location, with progressing cooling the hot spot migrated around the cylinder. Consequently, there is no localised area along the surface of the Al cylinder where the cooling conditions are significantly different.

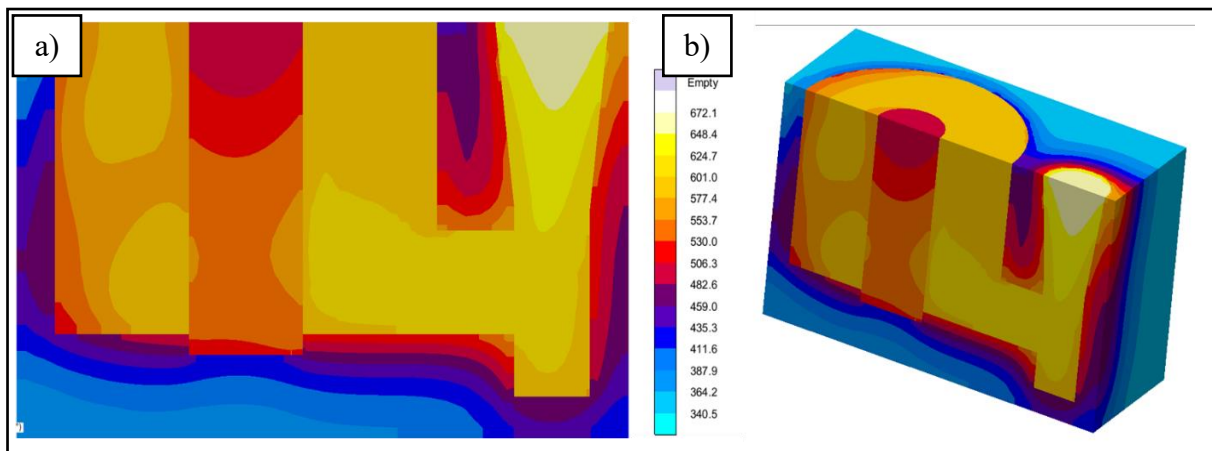


Figure 5.11. Temperature distribution within the casting and mould at the end of pouring: the loss of temperature, according to the simulation, around the surface of the Al cylinder was negligible. (a) Side plan view of the temperature distribution along the parting line of the mould. (b) Schematic view of the temperature distribution along the parting line and top of the mould.

## 5.5: Growth of the Material Bond via Solid State Diffusion in Diffusion Couples

Al/Mg diffusion couples were the subject of extensive research, in order to compare the results to Al/Mg compound castings. The data from the literature, presented in chapter 1, about diffusion couples and compound castings, differ – in terms of growth and thickness of the material bond – from the results presented in this thesis. As differing processes were used, this chapter aims to discern the impact of the process (casting and diffusion bonding) on the formation of the material bond.

The diffusion couples were assessed on the morphology and overall appearance of the material bond. Based on the reaction of both metals, the diffusion couples were classified into four different categories.

1. **Diffusion couples with successful bonding.** At 450°C and while using a cover gas, the formation of a continuous material bond was observed. The overall appearance of the two samples indicated the presence of a large liquid phase. Additionally, several voids and fractures were scattered throughout the material bond.
2. **Oxidisation of the diffusion couple.** At temperatures above 440°C, both disks, without using a cover gas, would completely melt and oxidise. Little more than powdery residues (assumed to be oxides) of the whole couple remained.
3. **Partial melting of the diffusion couple.** At temperatures between 420°C and 440°C, the centre of two disks partially melted. Despite the presence of a liquid phase, no material bonding occurred. The two disks fell apart upon removal from the furnace.
4. **No material bonding.** At temperatures below 420°C, no material bonding occurred between the two disks. In some couples however, marks in the centre of the two disks, indicating a limited chemical reaction, were found.

A complete list of the results of the experimentation with the diffusion couples is shown in table 5.4. Temperature control during the experiment proved vital, as too low a temperature would result in no reaction and thus no bonding, and too high a temperature resulted in the melting and oxidation of both disks. The oxide layer on the aluminium disk is thought to hinder the diffusion and reaction between the two metals. A certain amount of thermal energy (e.g. 450°C in the current experimentation) is needed to break down the alumina and make diffusion possible. The intermetallic compounds  $\beta$ ,  $\gamma$ ,  $\phi$  and  $\tau_1$ , formed during the diffusion reaction, display a very low solidus temperature, typically 367°C-433°C (see the phase diagrams in chapter 3). Therefore, the melting is a result of the reaction of both metals and the forming of the aforesaid compounds. The best result (actual material bonding) was achieved by reducing the temperature by 30°C (from 450°C to 420°C) during the experiment. This was done to reduce the rate of diffusion of the aluminium and magnesium.

Sample Number	Al-alloy	Mg-alloy	Result	Category
1	AlZn30	AZ31	No reaction	4
2	AlZn30	AZ31	Complete oxidisation of both disks	2
3	AlZn30	AZ31	No reaction	4
4	AlZn30	AZ31	No reaction	4
5	AlZn30	AZ31	No reaction	4
6	AlZn30	AZ31	Partial melting	3
7	AlZn30	AZ31	Partial melting	3
8	AlZn30	AZ31	Complete oxidisation of both disks	2
9	AlZn30	AZ31	Successful material bonding	1
10	Al	Mg	No reaction	4
11	Al	Mg	Complete oxidisation of both disks	2
12	Al	Mg	Successful material bonding	1

Table 5.4: List of all conducted diffusion experiments and their respective results. The results are classified into four categories: 1) diffusion couples with successful bonding; 2) oxidisation of the diffusion couple; 3) partial melting of the diffusion couple; and 4) no material bonding.

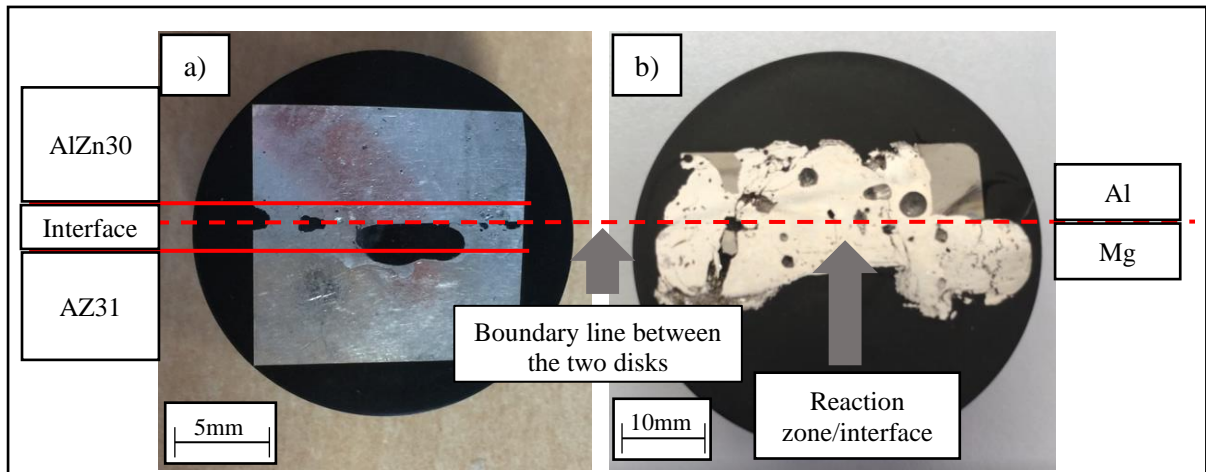


Figure 5.12. Macrographs of the diffusion couples where material bonding was observed: (a) AlZn30/AZ31 diffusion couple (Sample Number 9) – the formation of a distinct material bond was observed with several voids and gaps evident; (b) Al/Mg diffusion couple (Sample Number 12) – no distinct material bond was formed, but instead the large reaction zone almost completely consumed both metals.

Successful bonding was only achieved in two cases, with an AlZn30/AZ31 and an Al/AZ31 diffusion couple. Macrographs of both couples, after cutting, are displayed in figure 5.12. Upon removal from the furnace, a partially liquid phase was observed in both diffusion couples. For safety reasons, both couples were cooled down under ambient atmosphere, until the liquid phases completely solidified, before being quenched in water. While a distinct material bond was visible in the AlZn30/AZ31 couple, several prominent gaps and a void were found therein as well. The morphology of the material bond is explained by the presence of the liquid phase, observed immediately after removal from the furnace. Chemical analysis and phase identification were performed with EDX and XRD. An SEM BSE micrograph can be seen in figure 5.13. Unlike compound castings, the magnesium-rich phases  $\phi$  and  $\gamma$ , as well as elementary magnesium, make up the bulk of the material bond, while the aluminium-rich phase  $\beta$  is only found within a thin (10-15 $\mu\text{m}$  thick) layer adjacent to the aluminium. The aluminium- and zinc-rich phase  $\tau_1$  was not found in this thin layer.

Similarly to AlZn/AZ31 compound castings, the zinc-rich phase  $\phi$  was found forming between the dendrites of the elementary magnesium. But unlike compound castings, the  $\phi$  phase was more spread out and less concentrated. The appearance of the Al/AZ31 diffusion couple suggests that a considerable part of the couple partially melted and then reacted to form Al-Mg intermetallic phases. As a consequence, a large reaction, and thus material bond, formed. The whole AZ31 disk was transformed in the process, while small parts of aluminium remain near the edges of the disk. Again the interface/reaction zone contains multiple fractures and voids. The most prominent of the voids was a nearly circular void with a diameter of 3.96mm. As solidification-related pores and shrinkage rarely display such a uniform shape, it is likely that the cavities observed are caused by a different mechanism. The spherical shape of the pores might indicate hydrogen porosity. However, neither of the disks used

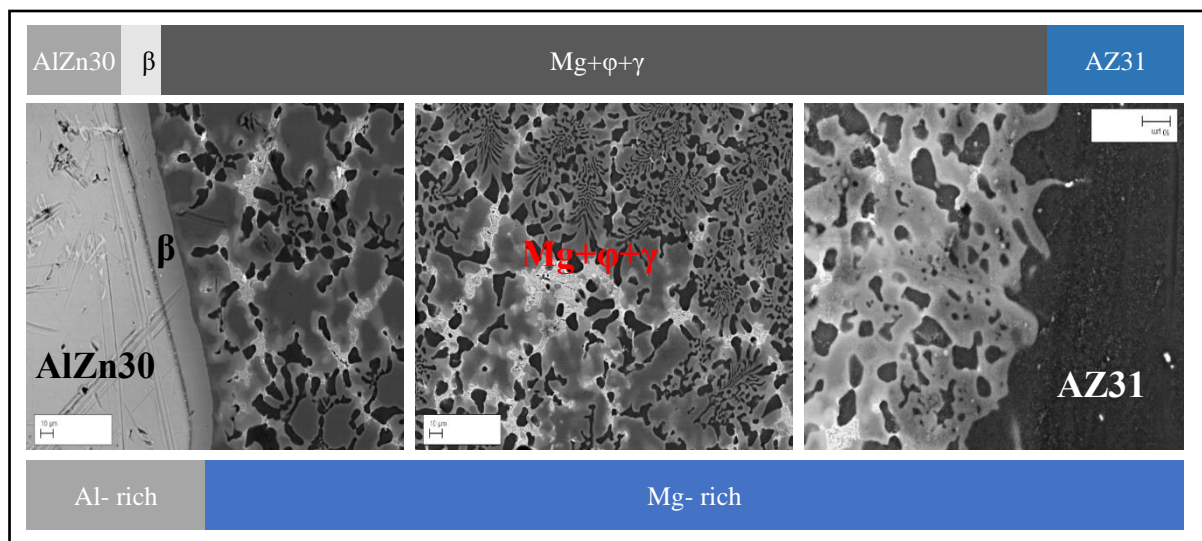


Figure 5.13. Micrograph of the AlZn30/AZ31 diffusion couple. The main constituents of the interface are the magnesium-rich phases  $\gamma$  and  $\phi$ , and elementary magnesium. The aluminium-rich phase  $\beta$  is only found in a small layer adjacent to the AlZn30 alloy. This is in contrast to what was observed in compound castings, where the  $\beta$  phase was found alongside the  $\tau_1$  phase. The  $\tau_1$  phase was not found in the material bond of the diffusion couple.

for the diffusion experiment displayed any hydrogen porosity prior to heating up, and it is thought unlikely that enough hydrogen is absorbed (under cover gas), at the temperatures used (<450°C), to form the observed pores.

Compared to the diffusion couple, the material bond acquired with compound casting displayed fewer voids and fractures, as well as a more uniform thick material bond. The values for the thickness of the  $\beta$  and  $\gamma$  phases in the diffusion couples are shown in table 5.5. Unlike the growth of the material bond in AlZn/AZ31 compound castings discussed in chapter 4, a clear correlation between holding time and thickness of the material bond was observed. This is not surprising, as this heat-treatment experiment differs from the compound casting in a number of ways.

1. Temperature regime: with a temperature of 300°C, the temperature used in the heat treatment was higher than the pre-heat/holding temperature used in the AlZn/AZ31 compound castings.
2. Type of alloy: the liquidus temperature of AlZn alloys is lower than pure aluminium, and zinc is known to possess a very high diffusion coefficient, which was thought to translate into an increased thickness of the material bond. This however was not observed.

The increase in thickness was exclusively caused by the growth of the  $\beta$  phase, with the thickness of the  $\gamma$  phase not increasing with holding time. These results confirmed observations in chapter 4, as well as in results reported in the literature (see section 2.2.7). Under the described conditions, only the aluminium-rich intermetallic phase  $\beta$  grows, while growth of the magnesium-rich intermetallic phase  $\gamma$  is hindered. The details of the growth mechanism, however, remain unclear. It will be shown in the following chapter that the material bond mostly grows in the direction of the magnesium. It can thus be deduced that the  $\gamma$  phase grows at the same rate, as it is consumed by the  $\beta$  phase.

Holding time [min]	Thickness [ $\mu\text{m}$ ]		
	$\beta$	$\gamma$	Total
15	865+/-124	247+/-16	1092+/-133
30	1344+/-43	211+/-17	1590+/-43
60	1756+/-772	225+/-94	1971+/-874

Table 5.5: Thickness of the  $\beta$  and  $\gamma$  phases in Al/Mg diffusion couples after a holding time of 15, 30 and 60min.

## 5.6: Conclusion

- The alumina layer was not found to impede the formation of the material bond. The process of reducing  $\text{Al}_2\text{O}_3$  to MgO was not directly observed.
- The material bond acquired via diffusion experiments using a diffusion couple varied greatly from the material bond acquired with compound casting. Unlike in compound castings, the magnesium-rich phases were dominant in the material bond of the AlZn30/AZ31 diffusion couple, with only a  $\sim 15\mu\text{m}$  thick layer containing the aluminium-rich phases being found. Furthermore, the aluminium- and zinc-rich phase  $\tau_1$  was not found in the AlZn30/AZ31 diffusion couple, whereas it was present in the AlZn30/AZ31 compound castings.
- Using an identical heating and cooling regime, the microstructure of the three AlMgZn alloys, in the same phase field, varied with chemical composition.
- DSC measurements confirmed the low solidus temperature of the magnesium-rich phases found in the material bond of compound castings.
- A stark difference (15%-28%) in the volume of the liquid, and the volume of the solid state of AlMgZn alloys, was detected. Highest contraction, with 28%, was observed in the Mg90Al5Zn5 alloy. This difference in volume might partially explain the holes and voids found in the studied samples.
- Numerical simulation confirmed a relatively uniform solidification and cooling of the compound casting. Commercial simulation packages for casting and solidification are not ideally suited to model the complex interactions in compound castings, as satisfactory agreement between the measured and simulated curves was only achieved at elevated temperatures ( $>450^\circ\text{C}$ ).

## 5.7: References

STRATTON, P. (2013) Ellingham diagrams – their use and misuse. *International Heat Treatment and Surface Engineering*, 7(2), pp. 70-73.



## Chapter 6: Mechanical Properties of the Material Bond of Al/Mg Compound Castings

### 6.1. Mechanical Strength of the Material Bond

The strength of a bond between two metals is of great importance, as it determines the overall strength of the compound casting. Ideally, the strength of the bond is equal to or higher than the strength of the aluminium and magnesium alloy. Shear strength is widely used for the characterisation of the strength of welds (Fujii et al., 2016; Kulekci et al., 2011). Moreover, according to Schmid's law, shear strength directly relates to tensile strength in metals (Budynas et al., 2015). Thus, shear strength is used in the present study to characterise the strength of the material in Al/Mg compound castings.

Macrographs of all the disks after machining and polishing, and their interfacial thicknesses, are listed in table 6.4 at the end of the chapter. The thickness of the interface was measured in the four locations illustrated in figure 6.1. One spot was directly opposite the inlet, and another on the opposing side of the Al cylinder. The other two spots were at a 90° angle to both spots on both sides. The thicknesses of the aluminium- and magnesium-rich phases were measured optically. To assess segregation during solidification, and concentration gradients in the chemical composition within the casting, the chemical composition was measured with an OES. Positions where compositions were measured are indicated by roman numerals (I, II, III, IV), also shown in figure 6.1.

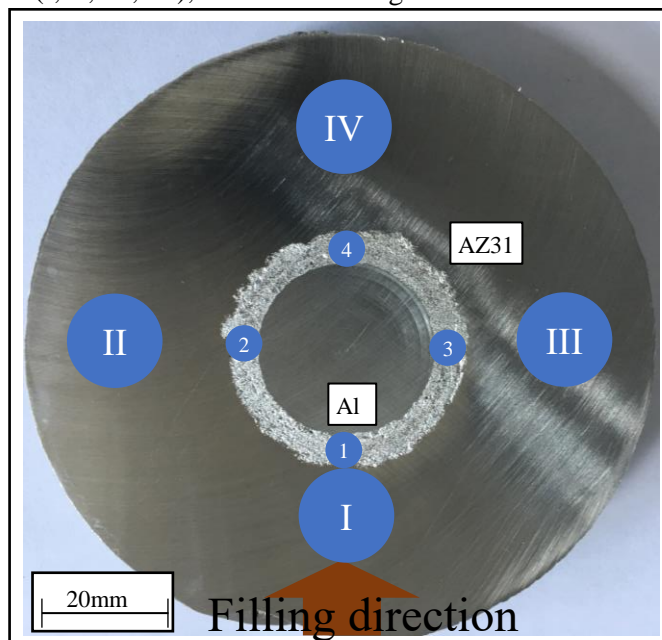


Figure 6.1. Macrograph of the locations for measurement of the thickness of the material bond and chemical compositions of the magnesium alloy. I, II, III, IV indicate the locations where the chemical compositions were measured. 1, 2, 3, 4 indicate the locations where the interface thicknesses were measured.

Sample No	Alloys		Position											
	Al	Mg	1			2			3			4		
			Mg	Nd	Gd	Mg	Nd	Gd	Mg	Nd	Gd	Mg	Nd	Gd
2	Al	E21	93	3.2	1.5	93	3.2	1.5	93.8	3.2	1.5	92.9	3.2	1.5
4	Al	E21	92.8	3.2	1.34	92.7	3.2	1.5	92.9	3.2	1.5	93	3.2	1.39
9	Al	E21	94.9	3.2	1.48	94.4	3.2	1.45	94.7	3.2	1.46	95.3	3.2	1.38

	Al	Mg	Al	Mg	Zn	Al	Mg	Zn	Al	Mg	Zn	Al	Mg	Zn
5	Al	AZ31	3.40	95.2	0.50	3.5	95.2	0.41	3.6	94.7	0.40	3.56	95.9	0.49
7	7005	AZ31	3.34	95.4	0.491	3.47	95	0.458	3.45	95	0.47	3.38	95.4	0.473
8	AlZn15	AZ31	3.41	95.4	0.50	3.56	95.2	0.525	33.7	95.4	0.458	3.31	95.6	0.457
10	AlZn15	AZ31	3.38	95.2	5.42	3.38	95.4	0.535	3.29	95.3	0.564	3.2	95.4	0.505
11	AlZn30	AZ31	3.3	96.1	0.34	4.1	95.2	0.523	3.42	95.8	463	3.4	95.5	0.465
12	7005	AZ31	5.23	93.1	0.659	3.86	94.3	0.701	3.92	94.6	0.69	3.6	95	0.565
13	7005	AZ31	3.56	95.2	0.544	3.57	95.2	0.528	3.68	95	0.541	3.7	94.8	0.54
14	AlZn30	AZ31	12	76.2	7.63	4.13	94.4	0.623	12	39.5	8	3.98	94.6	0.635
15	AlZn30	AZ31	3.25	94.8	0.611	3.41	94.9	0.501	3.27	95.3	0.5	3.38	95.3	0.474
16	AlZn30	AZ31	3.72	95	0.572	3.61	95.1	5.74	3.62	95.1	0.56	3.56	95.2	0.536
17	Al	AZ31	4.29	94.1	0.557	4.69	93.8	0.513	3.62	94.9	0.528	3.71	94.7	0.548

Table 6.1: Chemical composition in wt% at the four different spots (denoted by 1, 2, 3, 4 in figure 6.1) for each sample. Due to the increased thickness of the material bond in sample 14, no measurement inside the magnesium alloy was possible.

Note: E21 refers to the alloy Elektron21 (a magnesium alloy with nominally 0.2-0.5wt% zinc, 2.6-3.1wt% neodymium and 1.0-1.7wt% gadolinium).

Sample Nr.	Alloys		Position												
	Al	Mg	1			2			3			4			
			Al	Mg	Zn	Al	Mg	Zn	Al	Mg	Zn	Al	Mg	Zn	
12	7005	AZ31	Side 1	5.23	93.1	0.659	3.86	94.3	0.701	3.92	94.6	0.69	3.6	95	0.565
			Side 2	3.56	95.1	0.561	4.25	93.8	0.751	3.75	94.6	0.611	3.67	94.9	0.544

Table 6.2: Chemical composition in wt% of sample 12 on both sides of the disk.

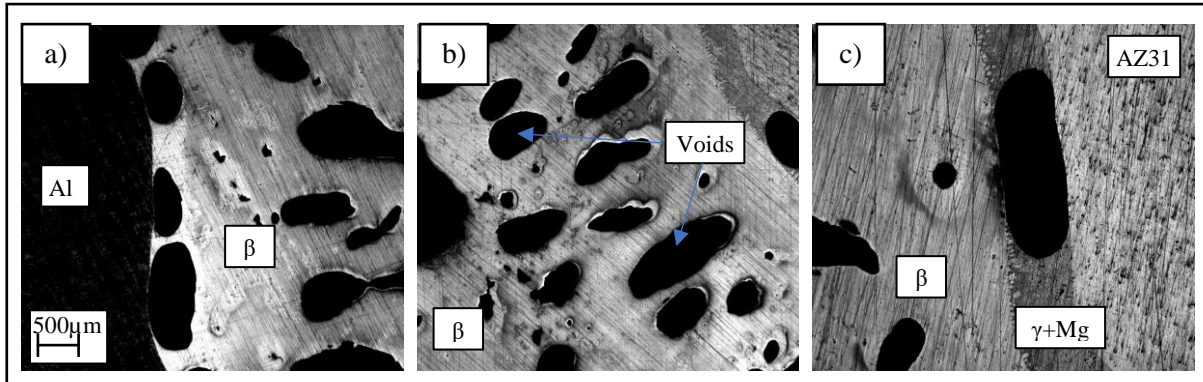


Figure 6.2. Overview of the defects in an Al/AZ31 compound casting: (a) voids in the aluminium-rich side, adjacent to the aluminium alloy; (b) middle of the interface with the voids orientated towards the centre of the casting; and (c) voids in the magnesium-rich side, adjacent to the alloy.

The chemical composition measured from the four locations (I, II, III, IV) presented in table 6.1 revealed a significant drop in zinc content and a small increase in the aluminium content in the Mg alloy of the castings. Lacking any other possible sources, the increase in aluminium is thought to arise from the diffusion, either in the liquid or solid state, of aluminium from the Al cylinder across the material bond. Similarly, the decrease in zinc content is explained by its diffusion into the material bond. In the AZ31 alloys, the decrease in zinc content was measured to be around 0.5%. Small differences in the chemical composition at the spots I, II, III and IV on the opposing sides of the disk were measured and are shown in table 6.2. The differences over the height were roughly on the same level as those across the circumference (~0.5wt% Al, ~0.5wt% Mg and 0.05wt% Zn). Hence, no predominant direction of segregation of the three elements was detected.

As can be determined from table 6.4, the thickness varied around the circumference of the Al cylinder. Based on all results, no clear correlation between interfacial thickness and position was evident. Originally it was expected that the interface at the initial contact area between the solid Al cylinder and the liquid melt would be greatest. However, this was not observed. As seen with sample 15 in table 6.4, no interface was formed at position 1. Thus, it seems likely that the melt velocity at the solid/liquid interface plays an important role in the formation of the material bond, as any reaction product between the magnesium melt and aluminium insert is washed away, thus preventing the formation of a distinct material bond. The largest average thickness, with around 22.5mm, was observed in sample 14 (see table 6.4). As visible in the macrograph, the interface was not uniform, and the variation in thickness around the Al cylinder was significant. At position 1, the interface completely replaced the magnesium alloy. In other castings, the thickness of the material bond was found to be uniform. Sample 17 was an example of such a regular interface. Fractures and voids of varying size were found in almost all samples. Size, form and locations of the cavities were found to be mostly identical to the ones reported in the earlier experiments in section 4.2.2. Upon closer inspection of the Al/AZ31 compound casting disk (sample 17) a pattern in the voids was discernible. Oval-shaped holes in the middle of the interface were found directed towards the centre of the compound casting disk.

To interpret the acquired results from the push-out testing, the differing material behaviour under stress had to be considered. The hardness measurements in chapter 4 revealed an increased brittleness of the material bond in comparison to the base alloys. Thus, it was assumed that the material bond would display the lowest mechanical properties and as such the interface would be the place where the disk would fail. In the absence of a material bond, or after failure of it, friction between the two metals would offer some degree of resistance to being pushed out. Plotting the absolute maximum load at failure in [N] against average interface thickness yields a scatter-plot as displayed in figure 6.3. As the push-out of the Al cylinder would necessitate the complete failure of the interface, the average interface thickness was deemed a suitable value for correlation with the maximum load. At first sight, no clear correlation between interface thickness and push-out resistance was present. However, a number of tendencies were detected.

1. The maximum load was measured after a displacement of 0.4-1.4mm.
2. In samples with a very thin interface (samples 3&9), push-out resistance was found to be the lowest, with a maximum measure force of 5.51kN for sample 3 and 8.28kN for sample 9. After failure of the material bond, friction between the Al cylinder and surrounding metal would cause further resistance to being pushed out, as observed with sample 3.
3. Generally, samples with a thicker interface displayed a higher push-out resistance. The maximum measured force during push-out testing was around 33kN for sample 2 with an average interface thickness of around 1.9mm.
4. Lowest measured force was 5.7kN with an average thickness of the material bond of 0.6mm in sample 3.
5. Sample 14 was unique, due to its increased interface thickness and highly irregular material bond. Its push-out resistance was less than 10kN, below the average of all samples, indicating that no direct correlation of the thickness of the material bond with its mechanical strength exists.

Interestingly, even chemical composition seemed to have little impact on mechanical strength of the material bond in compound castings. The same material combination was used for samples 2 & 9 (Al/E21), but they failed at vastly different loads. Sample 2 failed at 32kN and sample 9 at ~8kN. Similarly, AlZn30/AZ31 compound castings (samples 14, 15 and 16) failed at vastly different loads (27kN, 21kN and 13kN respectively). The thickness of the material bond was also not found to correlate with strength of the material bond. The fact that all samples failed in the material bond close to the Al-cylinder, regardless of material bond thickness, further confirms the uncoupled nature of thickness and strength. Due to the low uniformity of the material bonds, correlating the maximum load with average thickness may not provide the most meaningful results. Results from push-out or shear tests in the

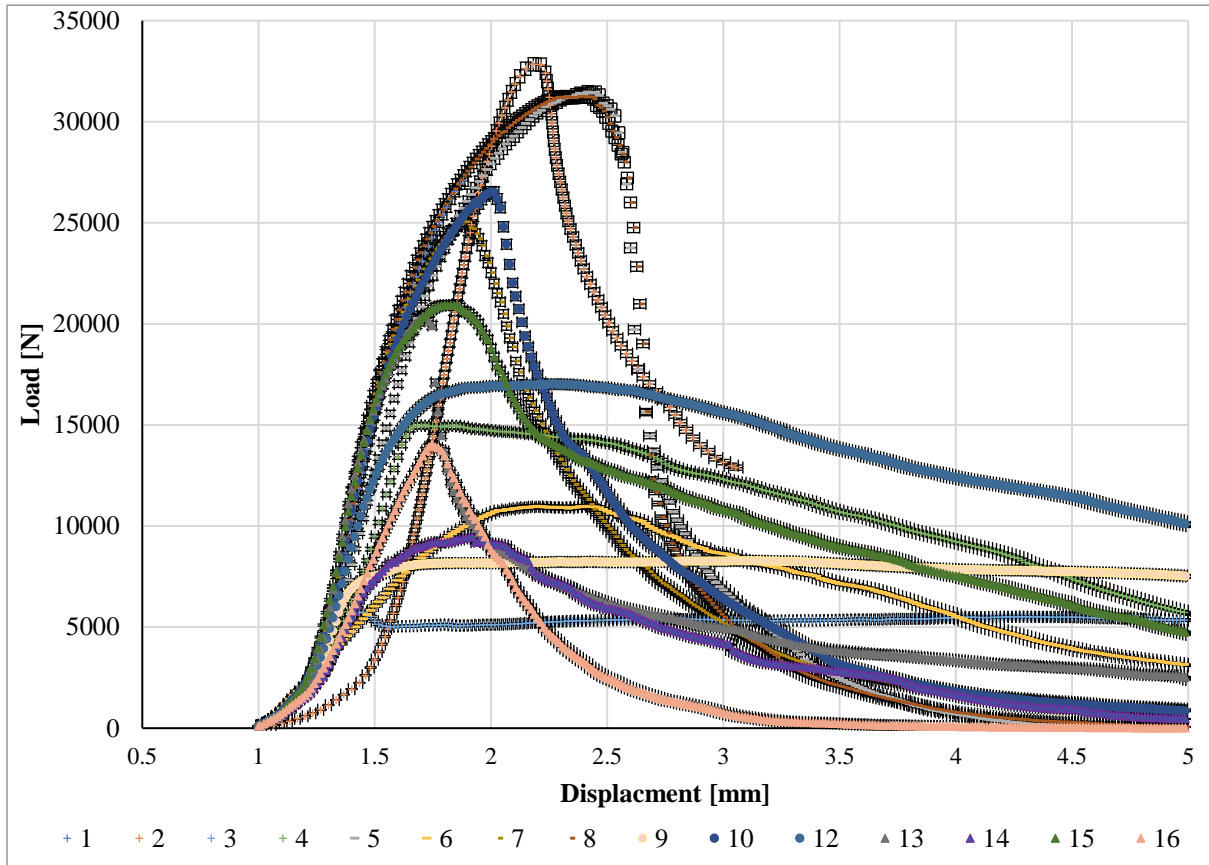


Figure 6.3. Load-displacement curves for all 17 push-out samples. Absolute strength of the interface of all 17 samples in N.

literature are usually given in [MPa] with respect to the corresponding profile/surface involved in the material bonding. All samples failed in close proximity ( $\sim 1\text{mm}$ ) or directly adjacent to the Al cylinder, within the aluminium-rich intermetallic phases. Thus, these phases were identified as the weak spot of the material bond. The surface involved in the material bonding can be approximated by using the circumference of the Al cylinder, with:

$$2\pi r * h = A \quad (\text{Eq.6.1})$$

where

A = effective contact area between the aluminium and magnesium

r = radius of the Al cylinder

h = height of the disk.

The diameter of the Al cylinder was 30mm, referred to as  $D_{\text{Initial}}$ . With a given height of 15mm the effective surface for material bonding can thus be calculated with:

$$2\pi 15\text{mm} * 15\text{mm} = C \quad (\text{Eq.6.2}).$$

As evident from the macrographs in table 6.4, the diameters of the Al cylinders shrank, due to the aluminium being partly consumed by the growing material bond. The resulting new diameter was labelled  $D_{true}$ . It was measured optically from the cut disks, seen in table 6.4. In some samples, the resulting shape of the Al cylinder was oval rather than circular. In these cases, the surface was approximated according to the ellipse approximation of Ramanujan, using the width (parameter  $a$ ) and height (parameter  $b$ ) of the ellipse (Villarino, 2005). In other samples, very little of the aluminium was consumed, resulting in no overall change in the diameter. This new diameter, and the resulting surface of the circumference, are listed in table 6.3. In samples where the Al cylinder displayed an oval shape the ellipse parameters  $a$  and  $b$  are given instead. This approach disregards the effects of the defects and voids within the interface. It was expected that these voids and defects, located in the interface region, have a detrimental impact on the strength of the interface, as they can reduce the effective bonding surface  $A$ . Their exact impact on the strength of the interface in the present samples is difficult to assess as it is unknown how many defects are present at the interface near the casting. The effect of the lateral strain (or Poisson ratio) during compression was deemed not to have a significant effect on the results, as no noticeable change in the height of the Al cylinder was measured after the push-out testing.

Sample	$D_{true}$ or $a/b$ [mm]/	$C$ [mm]	$A$ [mm <sup>2</sup> ]
1	26.5/26.3	82.94	1244.08
2	28.8/29.5	91.58	1373.71
3	30	94.25	1413.72
4	27.4/28	87.02	1305.37
5	27.5	86.39	1295.91
6	25	78.54	1178.10
7	28.3/30	91.60	1373.95
8	28.3/30	91.60	1373.95
9	28.5/28.9	90.16	1352.47
10	26.5	83.25	1248.78
11	24/28.9	83.27	1249.10
12	28.6/28.2	89.53	1343.04
13	30	94.25	1413.72
14	22.7/29.5	82.34	1235.157
15	28.5	89.53	1343.03
16	26.9	84.51	1267.63
17	27	87.97	1319.48

Table 6.3: Diameters,  $D_{true}$ , of the Al cylinder in the push-out disks after machining. In some samples the resulting shape of the Al cylinder was oval rather than circular. In these cases, the ellipse-parameters  $a$  and  $b$  are given instead of  $D_{true}$ .  $C$  is the circumference of the Al cylinder after machining.  $A$  is the effective contact area between the aluminium and magnesium, responsible for bonding. Diameters were measured optically; as such an error of 2% is assumed in all measurements.

Plotting the acquired push-out resistance in MPa over the surface changes the appearance of the scatter plot, as displayed in figure 6.4(b). Notably, the points are less scattered than in figure 6.4(a). However, no correlation between bonding surface and push-out resistance was detectable. The overall trend observed in the push-out resistance/thickness remained unchanged when considering the bonding area and the corresponding push-out resistance. Samples with a low resistance in absolute terms (<15kN) also displayed low resistance (<15MPa) when considering their bonding surface. Meanwhile, the opposite was also true for samples with a high resistance, which would display a high push-out resistance with respect to the bonding area. Based on these results the sequence of the failure for the material bond was observed to generally follow the following sequence.

1. As soon as a force was applied to the bond, metallic cracking was heard, confirming the brittleness of the material bond. A linear increase in the beginning of a load/displacement curve usually indicates elastic deformation. No such linear increase was detected in any sample.
2. As displayed in figure 6.5, the aluminium alloy of some samples showed signs of plastic deformation. As the material bond was failing simultaneously to the deformation of the aluminium alloy, no sign of this behaviour was observed in the load/displacement curves.
3. Once the interface was completely broken, friction between the Al cylinder and the disk was the only resistance to the measuring head. As the Al cylinder continued to be pushed out, friction between the two components lessened until the end of testing. The reduction in friction is indicated, by the falling load after passing through the peak in the load/displacement curve, in figure 6.3.

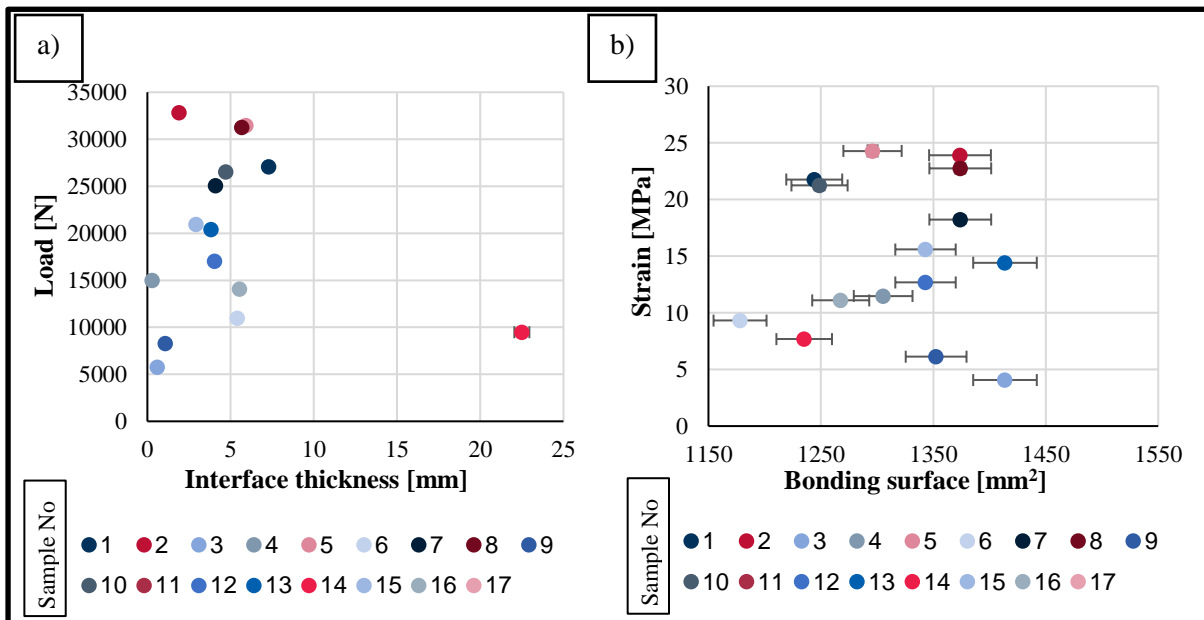


Figure 6.4. (a) Load in N at failure of the compound casting over thickness of the material bond. (b) Strain in MPa over the bonding surface between the aluminium and magnesium. Bonding surface was calculated for each sample separately.

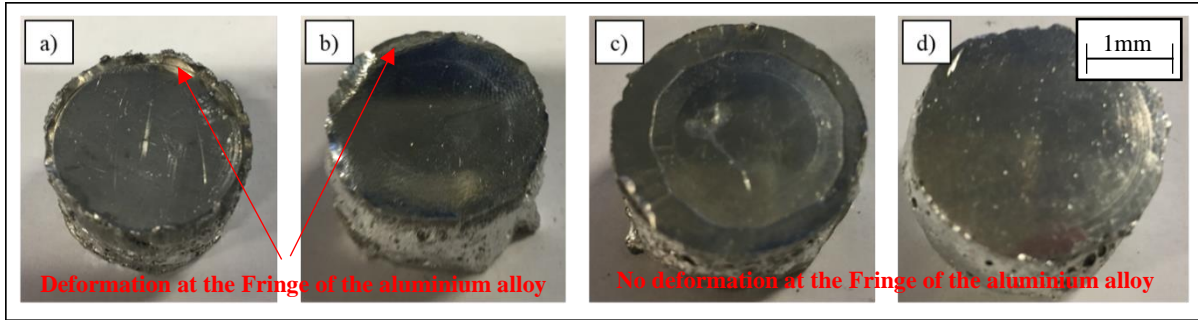


Figure 6.6. Al cylinders after push-out testing: (a) Al/AZ31, sample 5; (b) 7005/AZ31, sample 12; (c) Al/Mg, sample 6; and (d) AlZn30/AZ31, sample 16. Visible plastic deformation on the fringes of the cylinder is visible in the 'soft' Al cylinders of samples 5 and 2. No visible plastic deformation was observed in sample 2, due to the high-strength 7005 alloy, or sample 16, due to the relatively low load at failure.

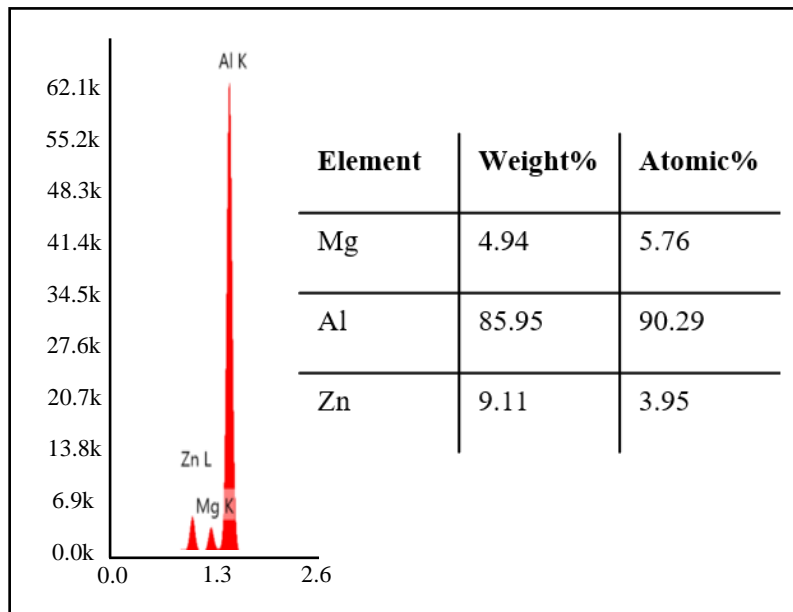


Figure 6.5. Chemical composition of the fringe of an AlZn15 cylinder. Magnesium was found to infiltrate the aluminium alloy and zinc content was ~6wt% lower than in the original alloy.

As no correlation between process parameters and push-out resistance was detected, no repeat or follow-up tests were conducted. Figure 6.5 displays the Al cylinder for four samples after push-out testing was complete. As is evident from the figure, the outer fringes of the aluminium alloy deformed under load in samples 5 and 12. The alloy's yield strength is thus lower than the ultimate tensile strength (UTS) of the material bond. The maximum load measured, for the two samples, was 23.9MPa. In the published literature, the yield strength of pure aluminium is given as approximately 7-11MPa (Polmear, 1995). This leads to the conclusion that the fringes of the Al cylinder are infiltrated by magnesium which leads to an increase in the mechanical strength due to solid solution hardening.

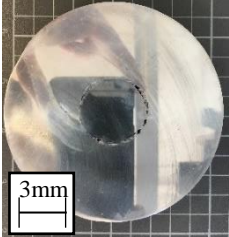
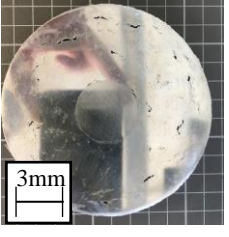
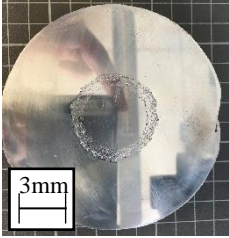
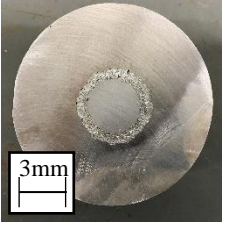
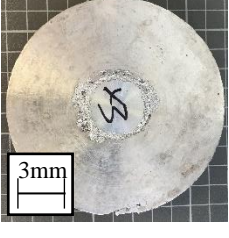
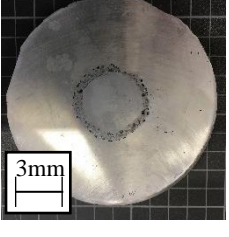
EDX analysis of an area at the fringes and thus close to the material bond of an AlZn15 alloy is shown in figure 6.6. The presence of ~5wt% of magnesium confirms the diffusion of magnesium into the Al cylinder. A decrease in the zinc content near the material bond was also detected, indicating that zinc

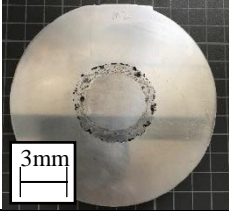
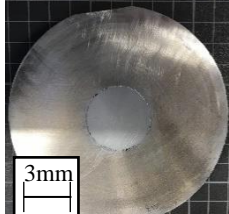
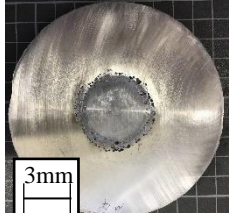
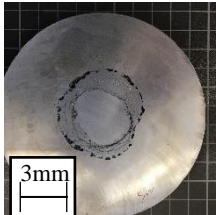
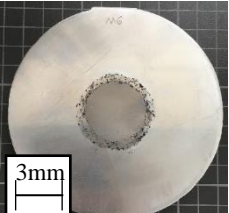
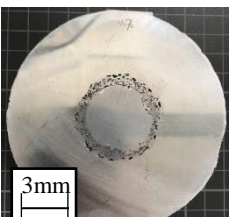


diffuses into the material bond from the aluminium alloy. This, however, was not observed in the remaining samples. In some cases, the aluminium alloy did not display any visible plastic deformation. As no strain gauges were used during the push-out testing, minor plastic deformation cannot be ruled out. Due to their high strength, 7005 series alloys did not display any significant kind of deformation. Similarly, in samples that failed at a low load (11kN), the Al cylinder showed no sign of deformation either.

## 6.2. Conclusion

- The average thickness of the material bond of the push-out disks varied from 0.3 to 22.5mm.
- The highest measured push-out resistance was 23MPa. Best results were achieved with an interface thickness of around 5mm.
- In samples with an interface thickness of below 1mm, the load/displacement curves indicate that the mechanical strength of the material bond was determined to be based on friction between the two metals.
- Above the minimum interface thickness, the interface strength was found to be mostly independent from interface thickness.
- During push-out testing the samples always failed on the aluminium-rich side of the bond.
- In some samples, plastic deformation of the Al cylinder was observed. This was usually observed in samples that displayed increased push-out resistance.

Sample No	Alloys		Interface thickness [ $\mu\text{m}$ ]					Macrographs of the push-out disks
			1	2	3	4	Average	
	Cylinder	Overcasting						
1	AlZn30	Mg	5716	9095	<b>5812</b>	8564	<b>7296</b>	
2	Al	Elektron21	2200	1821	1900	1715	<b>1909</b>	
3	Al	MgZn30	609	711	598	534	<b>613</b>	
4	Al	Elektron21	278	282	278.53	286	<b>281</b>	
5	Al	AZ31	6442	5888	6130	5285	<b>5936</b>	
6	Al	Mg	5401	5300	4822	6178	<b>5425</b>	
7	7005	AZ31	5981	5746	1703	2972	<b>4101</b>	

<b>8</b>	AlZn15	AZ31	4670	5955	6011	6056	<b>5673</b>	
<b>9</b>	Al	Elektron21	794	851	1406	1238	<b>1072</b>	
<b>10</b>	AlZn15	AZ31	3562	5461	3539	6296	<b>4714</b>	
<b>11</b>	AlZn30	AZ31	7062	5628	4407	9124	6555	
<b>12</b>	7005	AZ31	3935	4109	3540	4564	<b>4037</b>	
<b>13</b>	7005	AZ31	3786	4109	3046	4355	<b>3824</b>	

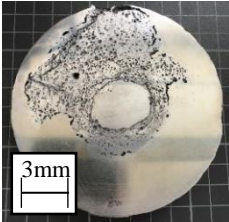
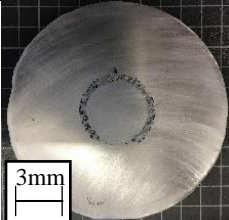
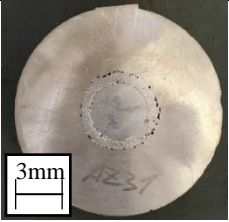
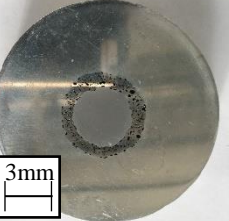
14	AlZn30	AZ31	37000*	11000*	29000*	13000*	22500	
15	AlZn30	AZ31	0	4178	3538	3984	2925	
16	AlZn30	AZ31	5766	6036	5632.5	4692	5531	
17	Al	AZ31	6375	6299	6828	6297	6449	

Table 6.4: Overview of all compound casting conducted for push-out testing. Sample number, material combination, thickness at four locations around the interface and average interface thickness are given. Thickness was measured using an optical microscope, except for sample 14, which was measured using a ruler.

### 6.3. References

BUDYNAS, R. G., NISBETT, J. K., TANGCHAICHIT, K., and SHIGLEY, J. E. (2015) *Shigley's mechanical engineering design*. 10<sup>th</sup> edn. New York, NY: McGraw Hill Education.

FUJII, H., GOTO, Y., SATO, Y., and KOKAWA, H. (2016) Microstructure and lap shear strength of the weld interface in ultrasonic welding of Al alloy to stainless steel. *Scripta Materialia*, **116**, pp. 135-138.

KULEKCI, M., ESME, U., ER, O., and KAZANCOGLU, Y. (2011) Modelling and prediction of weld shear strength in friction stir spot welding using design of experiments and neural network. *Materialwissenschaft und Werkstofftechnik*, **42**(11), pp. 990-995.

POLMEAR, I. J. (1995) *Light alloys: metallurgy of the light metals*. 3<sup>rd</sup> edn. Oxford: Butterworth Heinemann.

VILLARINO, M. (2005) *Ramanujan's Perimeter of an Ellipse*. Available at <https://arxiv.org/abs/math/0506384> [20 June 2005]

## Chapter 7: Discussion

### 7.1: Introduction

Formation, growth and the resultant mechanical properties of the material bond have been investigated in this thesis. Considerable deviations from results previously reported in the literature concerning the thickness of the material bond and its growth rates have been found. In this study, the thickness of the material bond in the castings was several times the magnitude of the thickness of the material bond found in diffusion couples and compound castings. Figure 7.1 displays the thicknesses of the material bonds achieved with Al/Mg diffusion couples and compound castings according to this study, and two results from the literature. The thicknesses reported by Xiao and Wang (2015) are from an Al/Mg diffusion experiment, while Liu, Chen, and Yang provided results from a compound casting process (Xiao and Wang, 2015; Liu, Chen, and Yang, 2015). Other results from the literature also deviate significantly from the results from the current study (Tanguiep Njiokep, Salamon, and Mehrer, 2001; Dybkov and Dybkov, 2004). While researchers around Emami and Hajjari reported a thickness of up to 1800 $\mu\text{m}$  in an Al/Mg compound casting, those results are still below the results from the current study (Emami et al., 2013b; Hajjari et al., 2011). Some of the differences can possibly be attributed to the different methodologies employed. Xiao and Wang (2015), and Tanguiep Njiokep, Salamon, and Mehrer (2001), used constant temperatures of 300 $^{\circ}\text{C}$  and 400 $^{\circ}\text{C}$  in their diffusion experimentation. However, Liu, Chen, and Yang (2015) used compound casting to develop their growth model and there

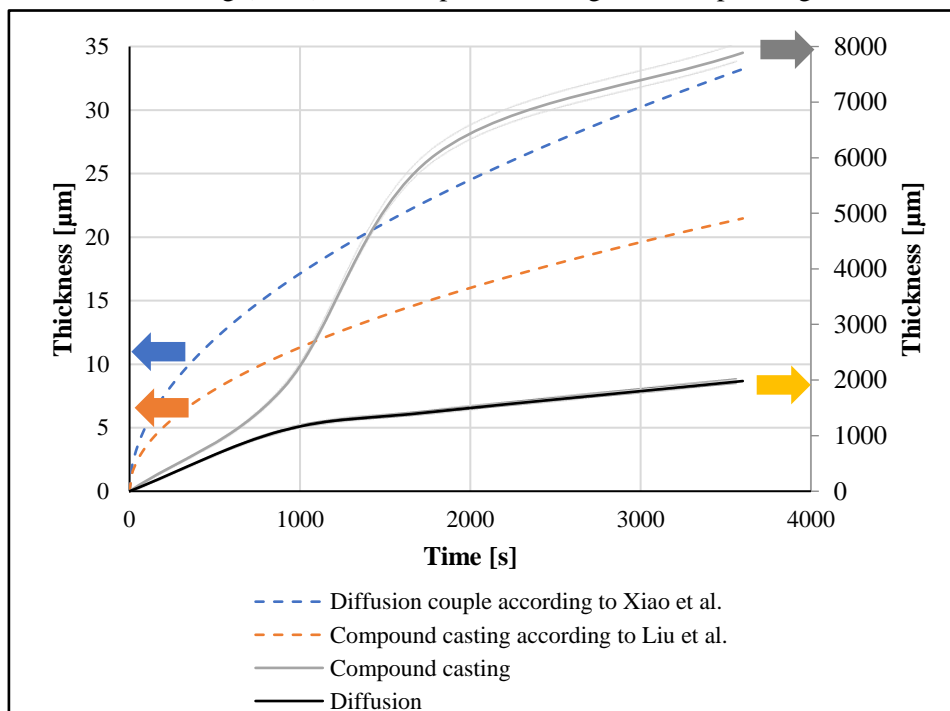


Figure 7.1: Total thickness of the material bond over time according to the literature and this study (the thin lines indicate the error band). The data series from this study refers to the right hand axis and both data series from the literature refer to the left hand side (Xiao and Wang, 2015; Liu, Chen, and Yang, 2015).

are still major deviations from the values reported in the current study. Another possible reason for the deviations is the scale of the experiments. Liu, Chen, and Yang (2015) used only a small (20x15x3mm) piece of aluminium, and an unspecified small amount of magnesium. Similarly, the amounts of magnesium used by Zhang, Chen, and Luo (~3g) and Xu et al. (2.5g) were significantly smaller than the amount used in the current study (~300g) (Liu et al., 1996).

Despite these discrepancies, there are a number of observations from the current study that are in good accordance with the literature. From the results presented in chapter 4 it is known that in Al/Mg compound castings, the intermetallic  $\beta$  phase is the dominant phase in the material bond of such compound castings; in AlZn6/AZ31 compound castings the aluminium-rich layer constitutes almost 90% of the material bond. This is in good accordance with the results on diffusion couples and compound castings from the literature, as reported by Dybkov, Xiao and Wang, and Liu, among others (Liu, Chen, and Yang, 2015; Dybkov and Dybkov, 2004).

However, the strongly deviating thickness between the literature and the current study indicates that there are contributing factors in the production of compound castings that have yet to be identified. It was indicated in chapter 4 that the formation of the material bond is believed to be a complex interaction between several metallurgical reactions and processes, such as wettability, dissolution and crystallisation. Based on observations made during experimentation, and building on the work of previous researchers (Xu et al., 2014; Emami et al., 2013b; Hajjari et al., 2011), the formation of a material bond has been divided into three distinct stages, which will be discussed in the following sections.

1. **Initial contact of melt and solid metal.** The first reaction in Al/Mg compound casting is the interaction between aluminium's oxide layer and the magnesium melt. The limited wettability between the two materials, as described in the literature, was found not to impede the formation of a material bond. This behaviour will be discussed further in sections 7.2.1 and 7.2.2. In addition, the inconclusive experimental results concerning the reduction of the alumina layer are elaborated on.
2. **Dissolution of the solid metal and solidification of the melt.** Exposure to the magnesium melt leads to the dissolution of the aluminium alloy therein. The importance of this dissolution process is discussed as it causes the formation of a concentration gradient within the melt, which in turn may affect the solidification of the material bond. It will be discussed in section 7.2.3 why this stage is an important part in the formation of the material bond.
3. **Growth of the material bond due to solid state diffusion.** Growth of the material bond continues upon complete solidification of the melt. It is controlled by the diffusion of atoms across the material bond.

Section 7.6 will, based on the results presented in chapter 4, discuss the effects of the alloying elements silicon and zinc on the formation of the material bond in Al/Mg compound castings.

1. **Silicon.** In section 7.6.1, the impact of silicon on formation and growth of the material bond will be elaborated on. It will be explained that the solid state diffusion and subsequent reaction to  $Mg_2Si$  is the main process resultant from the addition of silicon.
2. **Zinc.** Section 7.6.2 will demonstrate that zinc, unlike silicon, has a profound impact on the dissolution of the Al alloy by the Mg melt, and the subsequent precipitation from the liquid phase. Furthermore, based on these observations, a model explaining the formation of the regular shaped voids is presented and explained.

In section 7.7, the soundness and mechanical strength of the material bond in Al/Mg compound castings is discussed, with focus on the following points.

1. **The soundness of the material bond.** The material bond in compound castings was found to be susceptible to fractures, cracks and voids.
2. **The mechanical strength of the material bond.** The strength of the material bond is of vital importance for any actual application of compound casting. In this section the results, and their significance, from the push-out testing in chapter 6, will be discussed.

The discussion is then concluded by a critical assessment about the viability of Al/Mg compound casting, by identifying weaknesses and briefly discussing potential means of addressing them.



## 7.2: Reactions at the Solid/liquid Interface in Al/Mg Compound Castings

As shown in chapters 4 and 5, material bonding occurred without the removal of the oxide layer or any other special surface treatment, e.g. zincate or zinc plating, as proposed by a number of researchers (Xu et al., 2014; Rübner et al., 2011). Aluminium's intrinsic oxide layer thus has to show at least some degree of reactivity with the liquid aluminium, as the initial wetting of the alumina and its subsequent reaction/dissolution was not directly observed in the current study. The following sections, 7.2.1 and 7.2.2, aim to explain the processes at this early stage of the formation of the material bond, using reports from the literature and observations from the current study.

### 7.2.1: Wetting of the Aluminium Alloy by the Melt

According to the literature, wettability of a liquid metal on an oxide substrate was proven to directly correlate with the reactivity between the two, and as such is a good measure for it (Eustathopoulos, 2015). Wettability and thus reactivity between a liquid metal and a solid substrate is characterised by the equilibrium contact angle  $\theta$ , pictured in figure 7.3. The angle  $\theta$  is the angle between the solid substrate (aluminium/alumina), the liquid metal (magnesium) and vapour (Eustathopoulos, 2015). In chemically non-reactive systems, the angle  $\theta$  can be expressed by both Young's (equation 7.1) and the Young Dupree Equation (equation 7.2):

$$\cos\theta_y = \frac{\sigma_{SV} - \sigma_{SL}}{\sigma_{LV}} \quad (\text{Eq.7.1})$$

$$\cos\theta_y = \frac{W_a}{\sigma_{LV}} - 1 \quad (\text{Eq.7.2})$$

where

$\sigma_{SV}$ : Surface energy of the solid [J/m<sup>2</sup>]

$\sigma_{LV}$ : Surface energy of the liquid [J/m<sup>2</sup>]

$W_a$ : Adhesion energy<sup>1</sup> of the system [J/m<sup>2</sup>].

From equations 7.1 and 7.2, wettability can be defined as the result of competing adhesive forces between the magnesium and Al<sub>2</sub>O<sub>3</sub> (promoting wettability) and cohesive forces within the magnesium (limiting wettability). Due to the metallic bonding, the cohesive forces between the magnesium atoms are stronger than the adhesive forces between the magnesium and alumina (Eustathopoulos, 2015). Moreover, it is known that ionocolavent oxides like alumina display little wettability with pure liquid metals (Eustathopoulos and Drevet, 1994) and that the reaction of magnesium with alumina takes place

---

<sup>1</sup> Adhesion energy is defined as the energy needed to create two free surfaces by removing a liquid from a solid.

at a slow pace (Jynge and Motzfeldt, 1980). This leads to the limited wettability and reactivity between aluminium and a magnesium melt, as reported by Zhang and others (Xu et al., 2014; Rübner et al., 2011). This discrepancy in the reactivity (as manifested by the presence or lack of a material bond between magnesium and aluminium) between the literature and the current study, is traced back to the following effects.

1. Wettability and thus reactivity between aluminium and  $\text{Al}_2\text{O}_3$  increases with contact time between the aluminium and  $\text{Al}_2\text{O}_3$  (Sangghaleh and Halali, 2009). As such, the relatively long solidification time ( $\sim 2$ min, see figure 4.10) in this study's experimentation, and thus increased contact time, promotes a reaction between the magnesium and  $\text{Al}_2\text{O}_3$ .
2. Due to the process and the amount of magnesium alloy used ( $\sim 300$ g) for each compound casting, the energetic equilibrium directly at the interface is vastly different from the conditions used by Zhang, Chen, and Luo ( $\sim 3$ g) and Xu et al. (2.5g). The kinetic energy of the melt is the square of its velocity times mass and as such the kinetic energy is higher than the cohesive forces of the magnesium (1.516eV/atom), thus forcing the melt to completely wet the aluminium even in the absence of a chemical reaction (Liu et al., 1996).

As can be seen in figure 7.3(a), the simulated melt velocities are, as expected, highest directly opposite the inlet, where the melt first comes in contact with the Al cylinder. In several castings, no material bond was found to form at this position. This leads to the conclusion that an upper limit for the melt velocity, where no reaction at the interface occurs, must exist. An example of such a location can be seen in figure 7.3(b). The high velocity is thought to impede any chemical interaction, and in case of a reaction the resultant phases are broken off and washed away, preventing the forming of aluminium-

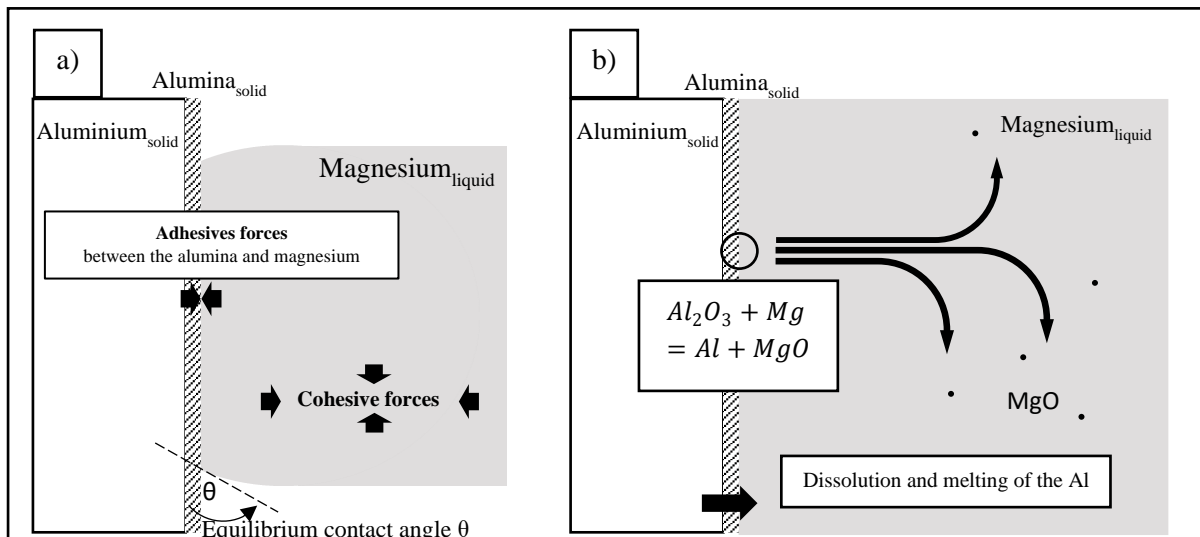


Figure 7.2. Schematic representation of the reactions at the solid/liquid interface. (a) Factors affecting wettability upon initial contact of the melt and aluminium are the adhesive forces at the Al-Mg boundary and the cohesive forces between the Mg atoms. (b) At increased contact times between liquid magnesium and solid aluminium, the alumina layer is being reduced by the magnesium to MgO and elementary Al. Part of the solid aluminium can then be molten or dissolved by the melt.

rich areas in the magnesium melt. According to Magmasoft, the velocity of the melt at the point of initial contact (between melt and insert) and shortly thereafter was between 500-650m/s. Under these conditions, a material bond was formed in 16 of 17 samples (see figure 5.4). Thus, the melt velocity at the point of contact should not exceed 650m/s in order to achieve a distinct material bond. As detailed later in section 7.3, the formation of aluminium-rich areas in the magnesium melt is important for the formation of a material bond. As the melt is cooling down during filling of the mould, the local temperature may become too low for a chemical reaction between the melt and aluminium alloy to occur once it falls below a critical value.

Replacing the oxide layer with a coating (zinc electroplating) significantly increased wettability of the aluminium alloy with the magnesium (Xu et al., 2014). However, as demonstrated in this study a coating is not strictly necessary when producing larger scale (>400g) compound castings.

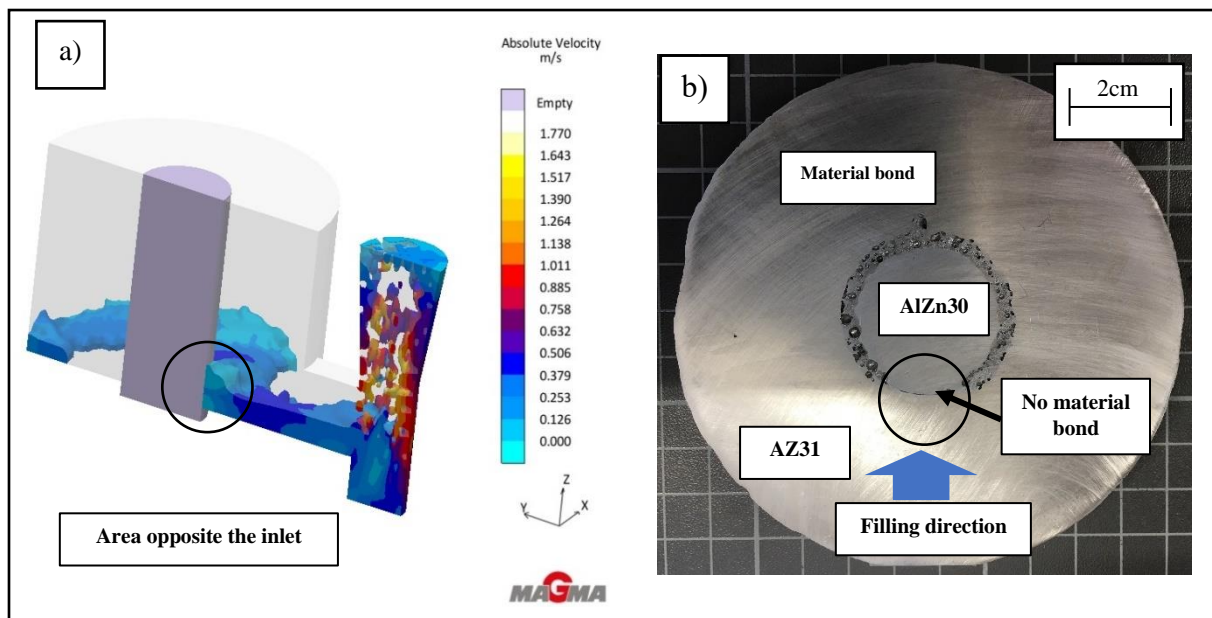


Figure 7.3. (a) Velocity of the melt 2s after pouring commenced, as simulated with Magmasoft. The highest melt velocities were found opposite the inlet. (b) Macrograph of an AlZn30/AZ31 compound casting. No material bond was present in the area with the highest melt velocity.

### 7.2.2: Chemical Interaction with the Alumina Layer

As all experimentations within this thesis were performed under an ambient atmosphere, aluminium's intrinsic oxide layer was thought to affect, somehow, the formation of a material bond at the Al-Mg interface. However, it has been demonstrated in the experiments presented in chapters 3-5 that the alumina layer did not impede interfacial formation. Specifically, no evidence of the oxide layer was found in Al/Mg compound castings on a macroscopic level, through inspections with an optical and electron microscope. Based on that observation, two different mechanisms are proposed for the removal of the oxide layer in Al/Mg compound castings. Both mechanisms are schematically displayed in figure 7.2.

It is theorised that due to the very low thickness of the alumina layer, around 4nm, that parts of the aluminium directly beneath the alumina layer are melted by the heat of the liquid melt (Campbell et al., 1999). Due to alumina's high melting temperature (2077°C), the alumina layer itself is not melted, but rather mechanically broken up due to the flow of the melt and dispersed therein. It is unlikely that partial melting of the aluminium is solely responsible for removing the oxide layer. If so, it would be expected that material bonding in Al/Al compound castings would also occur, which has not been reported in the literature (Rübner et al., 2011). Similarly, a reaction and eventually the formation of a material bond in Al/Mg diffusion couples (see chapter 5) was observed at temperatures below the alloys' respective liquidus temperatures, meaning that melting of the aluminium beneath the oxide layer was not responsible for the removal of the layer. Furthermore, oxide skins in aluminium castings are up to 5000µm in size and thus should be visible with the naked eye (Friedrich, 2015). No such inclusions were observed in the Al/Mg compound castings, either with OM or SEM. Thus, even though no direct chemical reaction between the magnesium melt and alumina was observed in this work, it is deemed likely that the alumina layer is reduced by a chemical reaction with the liquid magnesium.

As briefly discussed in chapter 5, in the temperature range used in experimentation (~650°C- ~700°C) magnesium oxide is thermodynamically more stable than aluminium oxide. According to the Ellingham diagram pictured in figure 5.1, at temperatures below ~1500°C the following reaction is expected to take place.



Following from Eq.7.3, the presence of elementary aluminium in the diffraction patterns (see figure 5.2) would have been evidence of the chemical reduction reaction of Al<sub>2</sub>O<sub>3</sub> to MgO and Al. The lack of aluminium in the diffraction patterns can be explained by the small amount contained within the samples. At low concentrations of aluminium, it is dissolved in the magnesium matrix and as such not detectable by X-Ray diffraction.

According to the literature, in the presence of liquid magnesium MgO is the only stable phase.  $\text{Al}_2\text{O}_3$  and  $\text{MgAl}_2\text{O}_4$  (Al-Mg spinel) are predicted to be reduced to MgO (Schramm et al., 2018). McLeod and Gabryel (1992) concluded that at thermodynamic equilibrium, the reduction of  $\text{Al}_2\text{O}_3$  with magnesium shifts towards the formation of  $\text{MgAl}_2\text{O}_4$  with decreasing magnesium content. As an abundance of magnesium was detected near the interface in all experimentation presented in the current study, the formation of MgO was assumed. This formation of MgO is supported by the calculated Gibbs free energy of formation of both MgO and  $\text{MgAl}_2\text{O}_4$  (McLeod and Gabryel, 1992). The Gibbs free energy of the formation of MgO at 900°C is calculated to be:

$$\Delta G_{MgO} = -123 \text{ kJ/mol} \quad (\text{Mounib et al., 2014}).$$

AlMg spinels are a common impurity in aluminium alloys. They are usually formed as a reaction product of MgO and aluminium. It is also possible for AlMg spinels to form as a reaction of the  $\text{Al}_2\text{O}_3$  layer with magnesium (Friedrich, 2015). The Gibbs free energy of this formation at 900°C was calculated to be:

$$\Delta G_{MgAl_2O_4} = -256 \text{ kJ/mol} \quad (\text{Mounib et al., 2014}).$$

At the lower temperatures used in the current study (~650°C to ~700°C), due to the abundance of available magnesium, the formation of MgO (over  $\text{MgAl}_2\text{O}_4$ ) is still the thermodynamically favourable reaction (McLeod and Gabryel, 1992). The ideal size of particles for detection by XRD measurements is 10-50µm (Pecharsky and Zavalij, 2009).  $\text{MgAl}_2\text{O}_4$  spinels are 0.1-100µm in size and typically several times larger than MgO particles, which are 0.1-5µm in size; thus, the former are easier to detect by X-Ray diffraction (Friedrich, 2015). However, no  $\text{MgAl}_2\text{O}_4$  spinels were detected in the experimentation with alumina, detailed in section 5.1. The lack of the  $\text{MgAl}_2\text{O}_4$  spinels thus indicates that under the conditions used, the MgO phase was thermodynamically more favourable than  $\text{MgAl}_2\text{O}_4$  spinels. This then indicates that the findings of MacLeod and Gabryel (1992) and Mounib et al. (2014) are also applicable to Al/Mg compound castings. The thermodynamic calculations, as well as the experimental observations presented in this thesis, are further confirmed by additional results in the literature (Schramm et al., 2018). MgO particles, from the reduction reaction, range in size from several hundred nm up to one µm. They display a higher stability in the magnesium matrix than in the  $\text{Al}_2\text{O}_3$  matrix and thus are dispersed within the magnesium melt (Mounib et al., 2014). The low thickness of the  $\text{Al}_2\text{O}_3$  layer (~4nm) on the surface of the aluminium would only result in a small, relative to the casting, amount of MgO and aluminium, which is then dispersed within the surrounding melt. Their small size and dispersal within the magnesium melt make direct detection, even with an electron microscope, difficult, explaining the difficulty in observing the reaction directly. Due to the low thickness of the alumina layer and thus the small amount of oxide formed by it, it is thought that the mechanical properties are not negatively affected by its presence (Zhou et al., 2019).

Observations made in the experimentation with diffusion couples, detailed in section 5.4, revealed a strong temperature dependency for the reaction of the metals with each other. At low temperatures no reaction and thus no material bonding occurred, indicating that some form of activation energy is needed for the reduction reaction to start. As this was also observed for long diffusion times (24h, see sample 1 in table 5.4), very slow reaction kinetics are believed not to be responsible for the inertness of the metals. Upon reaching this minimum temperature, the reduction process between the  $\text{Al}_2\text{O}_3$  layer and melt can commence. Observations made in section 5.3 identified the minimum temperature to be  $\sim 420^\circ\text{C}$ . This is in good accordance with calorimetric measurements of the reaction between magnesium and  $\text{Al}_2\text{O}_3$ . The temperature range of the chemical reaction was reported by Mounib et al. (2014) to be between  $400^\circ\text{C}$  and  $550^\circ\text{C}$ . The exact reaction kinetics depend on a number of variables, such as time, temperature, the relative amounts of  $\text{Al}_2\text{O}_3$  and magnesium, and in what form (e.g. powder) both materials are present. The larger the surface available for reaction, the faster the reduction takes place (Mounib et al., 2014). The liquidus temperature of the intermetallic phases  $\beta$  ( $\sim 450^\circ\text{C}$  in the binary Al-Mg system) and  $\gamma$  ( $\sim 437\text{-}458^\circ\text{C}$  in the binary Al-Mg system) is within this temperature range of  $400^\circ\text{C}$ - $550^\circ\text{C}$ . As such, temperatures that are high enough to chemically reduce the  $\text{Al}_2\text{O}_3$  layer also cause the partial or complete melting of any AlMg phases formed at the interface. This is further facilitated by alloying elements such as zinc, that reduce the liquidus temperature, leading to the melting and possible oxidation of the material bond. In compound castings, it was found that melting and dissolution is a major factor in the formation of the material bond, and this will therefore be discussed in detail in the next section. In diffusion couples, however, the melting of the AlMg phases at the interface leads to voids and defects in the couple, reducing its soundness. As such, the temperature and temperature range for the bonding of the diffusion couple should be minimised, yet high enough to ensure the chemical reduction of the  $\text{Al}_2\text{O}_3$  layer, to prevent the melting of the formed AlMg phases. To avoid a liquid phase, researchers commonly used a temperature of  $400^\circ\text{C}$  and an oxygen-free atmosphere to join aluminium and magnesium via solid state diffusion (Tanguet Njiokep, Salamon, and Mehrer, 2001). As the alumina layer was also removed (to facilitate reaction between both metals) during the experimentation described in the literature, it remains unclear if the  $\text{Al}_2\text{O}_3$  layer would be reduced to MgO and Al at  $400^\circ\text{C}$  (Xu et al., 2014).

The reduction of  $\text{Al}_2\text{O}_3$  to MgO was not directly observed in the experimentations in the current study. This lack of direct evidence is attributed to the small size of the MgO particles. Nevertheless, there is enough evidence, from experimentation (see chapters 3 and section 4.1) and the literature (Mounib et al., 2014), to assume that a reduction reaction happens in Al/Mg compound castings.

### 7.3: Dissolution of the Solid Metal and Solidification of the Melt

The solid aluminium alloy is continually heated up by the melt, at first via radiation, from the melt before contact, and then, upon direct contact with the melt, heat conduction. Despite alumina's low thermal conductivity ( $\sim 32\text{W/mK}$  for 99.9% pure alumina), its low layer thickness means that it is not expected to significantly impede the heat transfer between melt and aluminium alloy. In any case, as argued in the previous section, the  $\text{Al}_2\text{O}_3$  layer is eventually removed via a chemical reaction with the magnesium melt, or washed into the melt, allowing for a direct heat transfer between melt and solid aluminium insert.

The temperature at the Al/Mg interface (according to the measurements presented in chapter 5) was, with a maximum of  $\sim 615^\circ\text{C}$ , not high enough to completely melt a substantial amount of the aluminium insert. As was shown in figure 5.9, the maximum measured temperature was above the liquidus and solidus temperature of the AlZn30 alloy. However, as the temperature at the interface exceeded the liquidus and solidus temperatures of the alloy for only a short amount of time ( $\sim 10\text{s}$  and  $50\text{s}$  respectively), no melting beyond a few grams of the aluminium alloy is thought to have occurred. Partial melting of the aluminium in some areas can still occur, as a temperature of  $615^\circ\text{C}$  is above the solidus temperature of the AlZn30, AlSi6, AlSi15 and AlSi30 alloys. In these cases, small amounts of the secondary phases (zinc in AlZn alloys, silicon in hypoeutectic AlSi alloys and aluminium in hypereutectic AlSi alloys) possibly melt. In the absence of extensive melting of the aluminium alloy, the majority of the interfacial reaction is believed to stem from the dissolution of the aluminium alloy into the magnesium melt. The dissolution of a metal into a liquid melt can be separated into two stages. The first stage is the diffusion and dissolution of single atoms into the melt on a small scale (Yan and Fan, 2001). It is controlled by the interfacial reaction, which is linear with reaction time. This is followed by the diffusion of atoms from the solid metal, as well as the melt, into the reaction layer, and subsequent dissolution of this layer into the melt. At this stage, the material bond is established and growing. The direct chemical reaction stops after the intermetallic compound layer in the material bond reaches a thickness of a few crystal-lattice units (Dybkov, 2007). Dissolution of the solid aluminium is then diffusion-controlled and proportional to the square root of time (Yan and Fan, 2001).

The dissolution of a solid metal into a metallic melt is governed by three material-specific parameters (Eremenko and Natanzon, 1970). These are the diffusion coefficient  $D$ , the thickness of the diffusion boundary layer  $\delta$  and the solubility  $c$ . The first two parameters,  $D$  and  $\delta$ , were found to have only a slight impact on the dissolution. As such, dissolution of a solid metal in a liquid melt is mostly governed by the solubility of the solid metal in the melt (Eremenko and Natanzon, 1970).

The dissolution of the aluminium into the magnesium melt at a given temperature can be described using the following equation (Bircumshaw and Riddiford, 1952; Dybkov, 1990):

$$\ln\left(\frac{c_s - c_0}{c_s - c}\right) = k \frac{St}{V} \quad (\text{Eq.7.4})$$

where

$C$  = concentration of the aluminium in the magnesium melt

$C_s$  = saturation concentration

$C_0$  = initial concentration of the aluminium in the magnesium melt

$k$  = dissolution rate constant at a given temperature

$S$  = solid metal surface [mm]

$V$  = melt volume [mm<sup>3</sup>]

$t$  = time [s].

Flow/velocity of the melt, according to the numeric simulation, continuously decreases with temperature until viscosity prevents any molten metal flow. This leads to an increase in the aluminium concentration in the magnesium melt near the interface, as the dissolved aluminium is not transported away by the melt flow. The concentration of aluminium decreases with distance from the Al/Mg interface into the melt. According to models developed to understand the durability of a solid metal exposed to a metallic melt, under these experimental conditions a thin layer precipitates due to heterogeneous nucleation on the surface of the solid aluminium. As this thin layer, in the case of Al/Mg

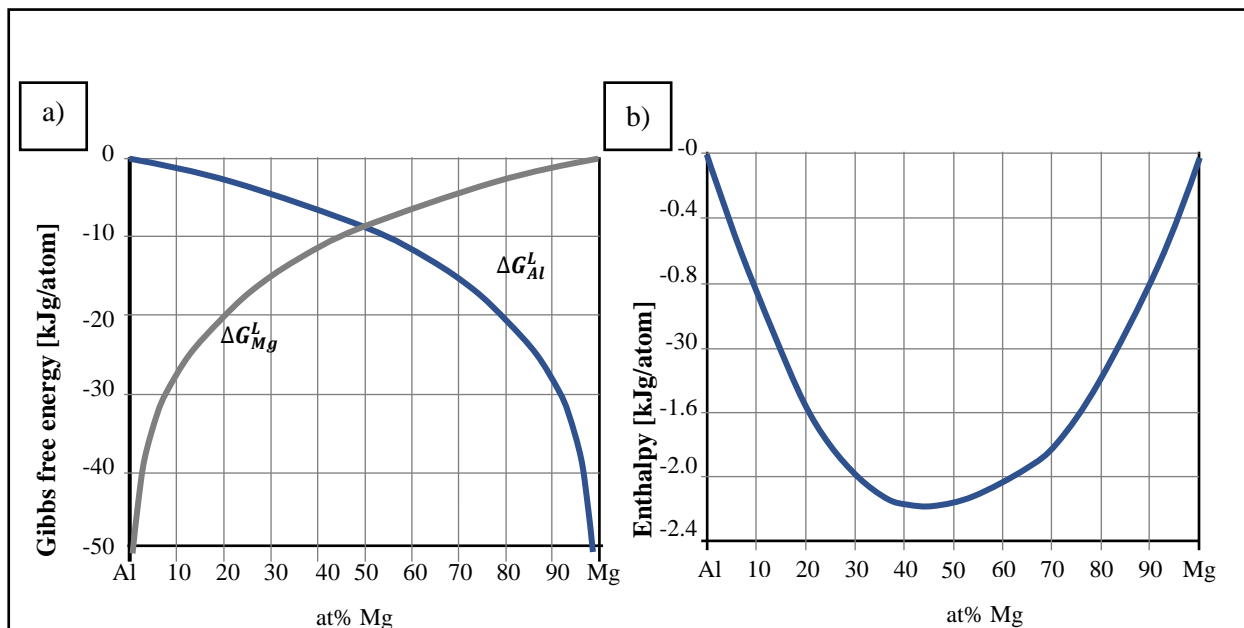


Figure 7.4. (a) Gibbs free energy of mixing of aluminium and magnesium dependent on magnesium content. (b) Enthalpy mixing of aluminium and magnesium dependent on magnesium content (Agarwal and Sommer, 1991; Moser et al., 1998).



compound castings, mostly consists of aluminium, it is expected to be made up of the  $\beta$  phase. Depending on the temperature gradient and heat extraction at the solid/liquid interface, parts of the  $\beta$  phase are then again dissolved into the melt or broken off due to the flow of the melt (Yan and Fan, 2001). However, for the formation of a material bond it is imperative that parts of the solid aluminium insert are dissolved into the melt as well. This was demonstrated in chapter 4, where no dissolution and thus formation of a material bond was observed at the interface of an Al/AZ91 compound casting. Formation of a material bond is thus directly linked to the ability of the magnesium melt to dissolve aluminium.

Even though aluminium and magnesium are completely miscible in each other in the liquid state, the lack of a material bond can be explained when regarding mixing enthalpy and the Gibbs free energy of mixing for both metals. The mixing enthalpy and Gibbs free energy of mixing of aluminium and magnesium are displayed in figure 7.4 (Agarwal and Sommer, 1991; Moser et al., 1998). It is evident that higher concentrations of aluminium in the magnesium alloy lead to a lower Gibbs free enthalpy of mixing. Similarly mixing enthalpy shows a strong correlation with aluminium/magnesium concentration. While magnesium is completely miscible with aluminium in the solid and liquid phase, this change of the Gibbs free energy causes a change in the solubility of the aluminium alloy in the melt. Gibbs free energy is temperature dependent and thus an increase in temperature decreases the Gibbs free energy of the reaction and thus results in the dissolution of more solid aluminium. The tendency to form a material bond in Al/Mg compound casting is therefore mostly dependent on temperature and chemical composition. The thickness of the material bond in compound casting

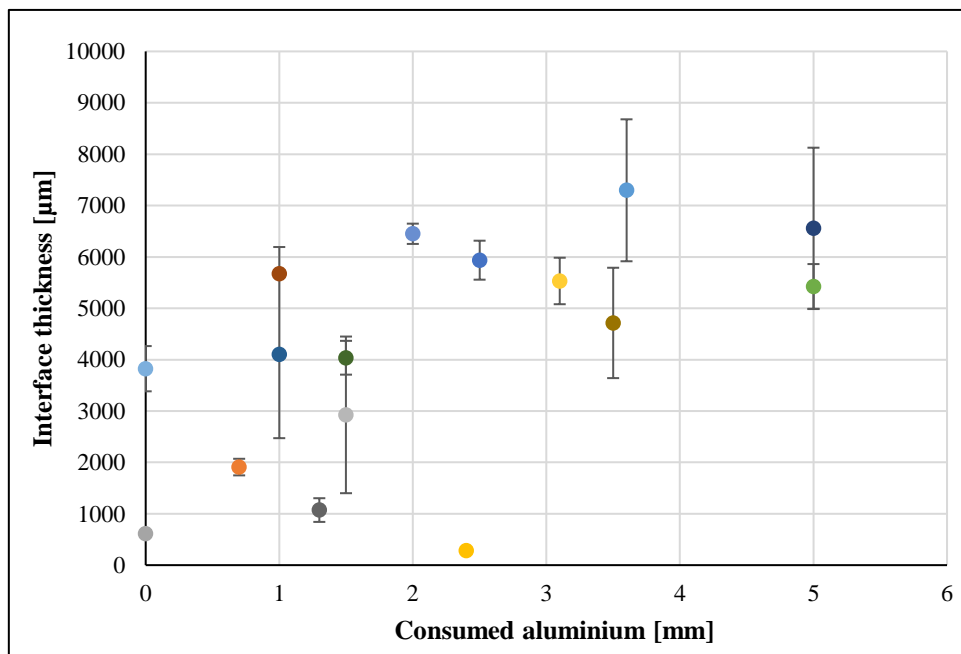


Figure 7.5. Thickness of the material bond in correlation with amount of aluminium consumed. The displayed data was collected from the push-out samples in chapter 6. Consumed aluminium is the difference in diameter of Al cylinders before and after being overcast with a magnesium melt. The error bars indicate the standard deviation of the interface thickness along the circumference of the cylinders. The deviation is used to assess uniformity of the thickness of the material bond.

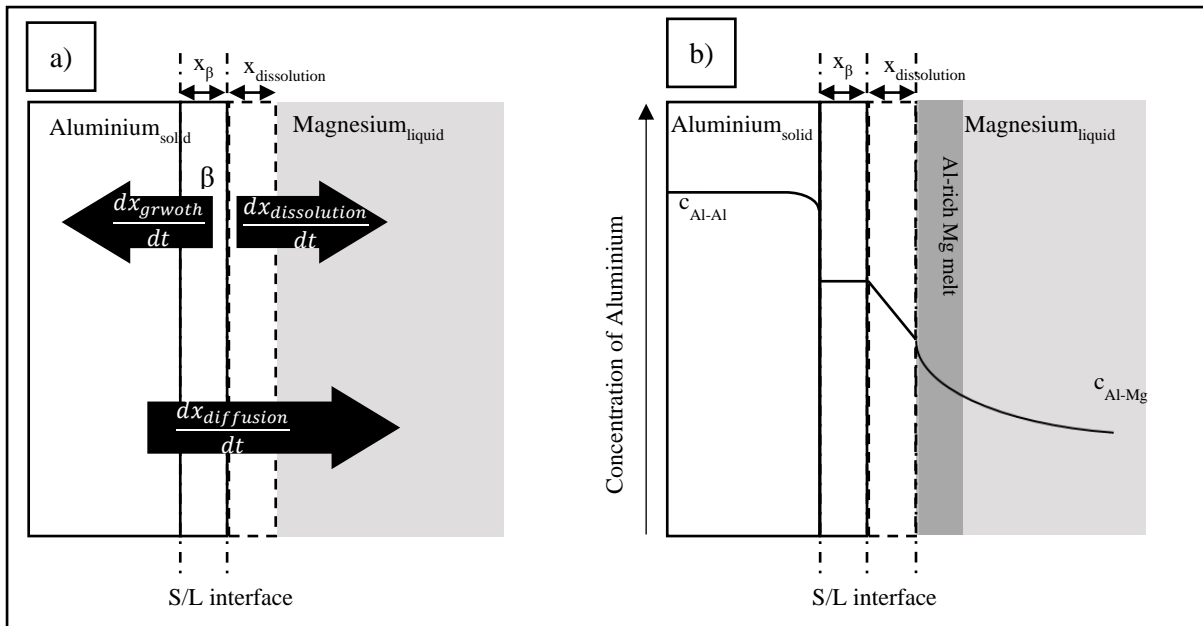


Figure 7.6. (a) Schematic representation of the reaction in the early stage of Al/Mg compound castings. S/L is the solid/liquid interface.  $x_{\beta}$  is the thickness of the intermetallic phase  $\beta$ .  $x_{dissolution}$  is the thickness of the dissolution layer.

(b) Concentration gradient of the aluminium  $c_{Al}$  across the interface according to measurements from this study (see chapter 3), Zhu (2014), and Kulkarni and Luo (2013).

correlates directly with the amount of solid aluminium dissolved and can thus be influenced by altering the reactivity between the metals involved. This can be achieved in Al/Mg compound casting by adjusting (e.g. increasing or decreasing) the aluminium content in the magnesium alloy. The less aluminium present in the magnesium alloy, the more aluminium can be dissolved by the magnesium melt, resulting in a more distinct material bond. This correlation can be clearly seen in the results presented in chapter 4. Commercially pure magnesium would dissolve the most aluminium and thus form the thickest bond. The amount of dissolved aluminium (either due to dissolution into the melt or diffusion) was approximated by measuring the decrease in diameter of the Al cylinders after overcasting with a magnesium melt (see table 6.3). Correlating this decrease in diameter with the thickness of the material bond yields figure 7.5, confirming the assumed connection. Thus, by controlling the amount of aluminium being dissolved into the melt, the thickness of the material bond can to a certain degree also be controlled. This can be achieved, as already mentioned, by altering the aluminium concentration in the magnesium and by controlling the temperature; the lower the temperature and higher the Al content in the Mg alloy, the thinner the resulting material bond.

Alternatively, as evident from equation 7.4, increasing the volume of the magnesium melt (relative to the liquid/solid contact area) allows for more aluminium to be dissolved into the melt, and thus provides a more distinct material bond. As a consequence, the geometry and scale of the experimental setup have a direct impact on the formation of the material bond and its morphology. This has to be taken into account when comparing the results of different researchers in the area of compound castings.

According to Dybkov (2007) the direct chemical reaction between the aluminium insert and magnesium melt ceases after the thickness of the reaction layer becomes greater than a few crystal lattices. Diffusion must then become an important factor of growth of the material bond. The mechanisms of the diffusion-related growth of the  $\beta$  and  $\gamma$  phases have been comprehensively discussed in chapter 2. Due to the high temperature in the initial stages of Al/Mg compound castings, the formation of the  $\beta$  phase is inevitable, which is ultimately detrimental to the mechanical strength of the material bond, as will be discussed later in section 7.7.2.

At this early stage of interfacial reaction, the total net growth of the interface is thus the growth of the  $\beta$  phase. Its growth rate is the sum of its growth in the direction of the solid and liquid, and the rate  $\beta$  is dissolved by the melt at the solid/liquid interface. A schematic of the reaction at the interface is displayed in figure 7.6. In this early stage of material bonding, the thickness of the material bond is a function of its dissolution into the magnesium melt at the solid liquid interface, and its growth in the direction of the aluminium alloy. Its net growth,  $dx_{total}$ , over time, can then be given as:

$$\frac{dx_{total}}{dt} = \frac{dx_{\beta}}{dt} = \frac{dx_{gro}}{dt} - \frac{dx_{dis}}{dt} \quad (\text{Eq.7.6})$$

where

$dx_{\beta}$  = growth of the  $\beta$  phase

$dx_{gro}$  = growth of the material bond

$dx_{dis}$  = rate of dissolution.

The rate of dissolution is given by a modified form of equation 6.4 (Dybkov 2009):

$$\frac{dx_{dis}}{dt} = b_0 e^{-at} = \frac{c_s k}{\rho \varphi} e^{-\frac{ks}{V}t} \quad (\text{Eq.7.7})$$

where

$c_s$  = solubility of aluminium in magnesium at a given temperature

$k$  = dissolution rate constant at a given temperature

$\rho$  = density of  $\beta$  intermetallic phase

$\varphi$  = content of aluminium in  $\beta$  in mass fraction

$s$  = surface area of the aluminium in contact with the magnesium

$V$  = volume of the magnesium

$t$  = time.

The growth of a single intermetallic phase is given by Wang et al. (2015) as:

$$\frac{dx_{growth}}{dt} = x^2 = 2kt \quad (\text{Eq.7.8})$$

where

$x$  = thickness of the intermetallic layer

$k$  = experimental layer growth rate constant

$t$  = time [s].

At the solid/liquid interface (see figure 7.6(a)), the material bond is continuously dissolved or melted by liquid melt, until the melt completely solidifies at  $\sim 450^\circ\text{C}$  (the solidus temperature of the  $\beta$  phase in the binary Al-Mg system). Additionally, diffusion of aluminium into the magnesium melt was reported to be facilitated due to the high number of vacancies in the magnesium (Liu, Chen, and Yang, 2015). This diffusion and dissolution of aluminium into the magnesium melt causes the formation of a concentration gradient within the melt. A sharp drop in the aluminium concentration gradient was observed in the diffusion couple, as seen in figures 7.7 and 7.12. A similar sharp drop between the  $\beta$  phase and the melt, caused by convection within the melt, was reported by Zhu (2014) and also described in diffusion couples by Kulkarni and Luo (2013). The change in chemical composition near the interface consequently alters the liquidus temperature of the melt according to the Al-Mg phase diagram. Resulting from this drop in the liquidus temperature of the aluminium-rich melt near the interface, the melt solidifies later than the remaining magnesium melt. This behaviour will be discussed in depth at the end of this section, and in the subsequent sections, as it is of great importance for the formation of a material bond in Al/Mg compound castings.

The chemical concentration of AlSi/AZ31 and AlZn/AZ31 compound castings, described in detail in section 4.2, follows the aforementioned gradient. A schematic of the described concentration gradient across the interface is displayed in figure 7.10. It is, as previously mentioned, in relatively good agreement with the chemical compositions described in the literature (Zhu 2014; Kulkarni and Luo, 2013). Concentrations of aluminium across the  $\beta$  phase are quite consistent, with no distinct concentration gradient observable. Approaching the magnesium-rich side, the aluminium concentration was found to decrease almost linearly.

Upon reaching a temperature below the liquidus temperature of the  $\beta$  phase ( $\sim 450^\circ\text{C}$ ) the solid/liquid interface will grow in the direction of the melt. From the work of Fukui and Maeda (1998) it is known that the concentration of the aluminium behind the advancing solidification front is higher than the equilibrium concentration in the melt. Thus it is the precipitation of the aluminium-rich phase that advances the growth of the material bond. Aluminium continues to diffuse across the interface and dissolves in the remaining melt. As a result, aluminium-rich areas near the solid/liquid interface are

continuously formed. The  $\beta$  phase then precipitates from the melt, driving further growth of the interface in the direction of the melt. This process is repeated until the aluminium concentration in the melt at the solid/liquid interface is too low to form the aluminium-rich  $\beta$  phase. The amount of  $\beta$  phase and thus its thickness in the interface is therefore linked to the amount of aluminium diffusing across the interface and dissolving into the melt. Both mechanisms are time/temperature dependent, explaining the correlation between elevated temperatures and amount of  $\beta$  phase.

The correlation between high temperature and thickness of the  $\beta$  phase was further shown in the push-out disks discussed in chapter 6 (see table 6.4 for sample details). The high casting and preheat temperatures would lead to an increased thickness of the  $\beta$  phase. Plotting the sum of casting and preheat temperature over thickness of the  $\beta$  phase yields figure 7.7. The sum of casting and preheat temperature was chosen to include the fact that different preheat temperatures were used in the experimentation. The thicknesses of the  $\beta$  phase are the averages of four measurements from different positions around the circumference of the Al cylinder, as detailed in chapter 6. With the exception of sample 14, the pouring temperature only varied by  $16^\circ\text{C}$ . As three different preheat temperatures were used, the results are grouped within three distinct clusters as seen in figure 7.7.

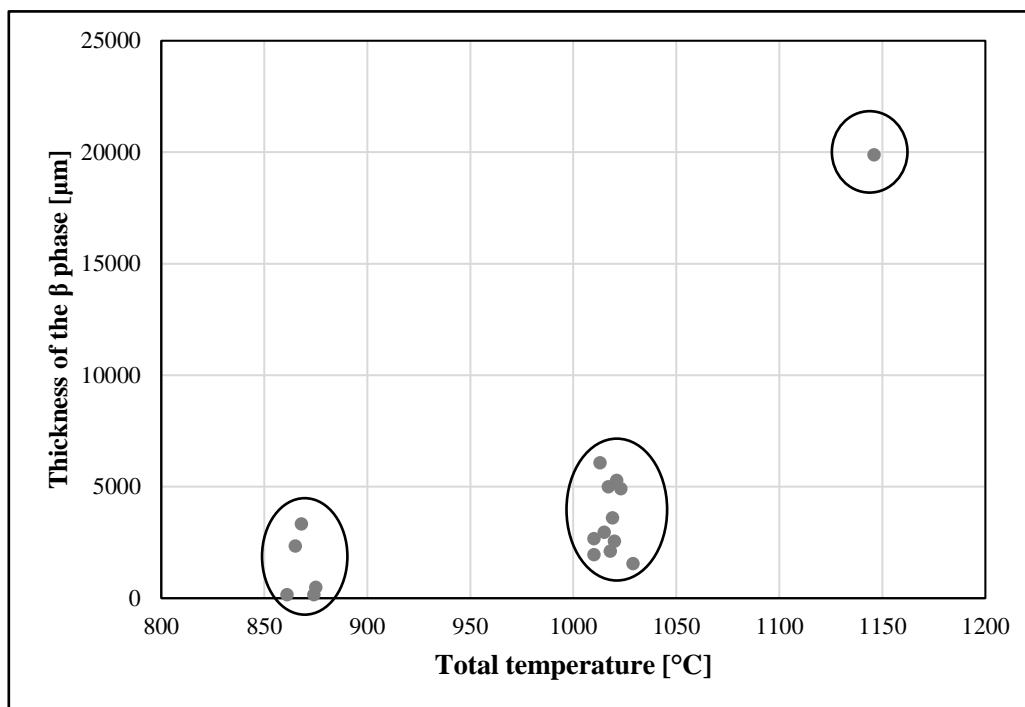


Figure 7.7. Correlation between temperature and interface thickness. Total temperature is the sum of the casting and preheat temperatures. Sample data was taken from table 5.4. The result can be grouped into three clusters, which are marked in this figure. It can be deduced that a direct correlation between temperature and thickness of the  $\beta$  phase within the material bond exists.

It has been shown in the previous section (see figure 7.6) that growth of the  $\beta$  phase is facilitated by the presence of a liquid phase. However, this liquid phase is not strictly necessary for  $\beta$  intermetallic compounds to form, as its presence is confirmed in various solid state diffusion experiments (Mola and Dziadoń, 2008; Brennan et al., 2012; Wang et al., 2015).

Dissolution of aluminium in the melt is dependent on temperature. The decrease in temperature due to continuous cooling near the solid/liquid interface leads to less aluminium being dissolved in the melt. Furthermore, it is evident from equation 7.7 that dissolution of the aluminium into the melt also decreases exponentially with time. Similarly, diffusion of aluminium into the melt is in addition impeded by the continuous cooling at the solid/liquid interface. Thus the concentration of aluminium near the solid/liquid interface decreases with the increasing reaction time and decreasing temperature. On the magnesium-rich side, decreasing the temperature below 650°C leads to the precipitation of primary magnesium. Elementary magnesium has always been found on the magnesium-rich side of the material bond, as can be seen in the micrographs presented in chapter 3. Further decreases in temperature of the magnesium-rich melt results in the precipitation of the magnesium-rich  $\gamma$  phase. The  $\gamma$  phase starts precipitating from the magnesium-rich melt once the local temperature falls below its liquidus temperature (437-458°C in the Al-Mg binary system). As the  $\gamma$  phase was always observed to exist alongside the primary phase (magnesium) the lower limit of temperature of the solidification reaction is 437°C.

The temperature distribution within the compound casting at the time of the precipitation of the  $\beta$  phase is seen in figure 7.8. It is apparent from the numerical simulation that the hot spot of the compound castings lies on the aluminium-rich side of the casting. Due to the change in chemical composition and

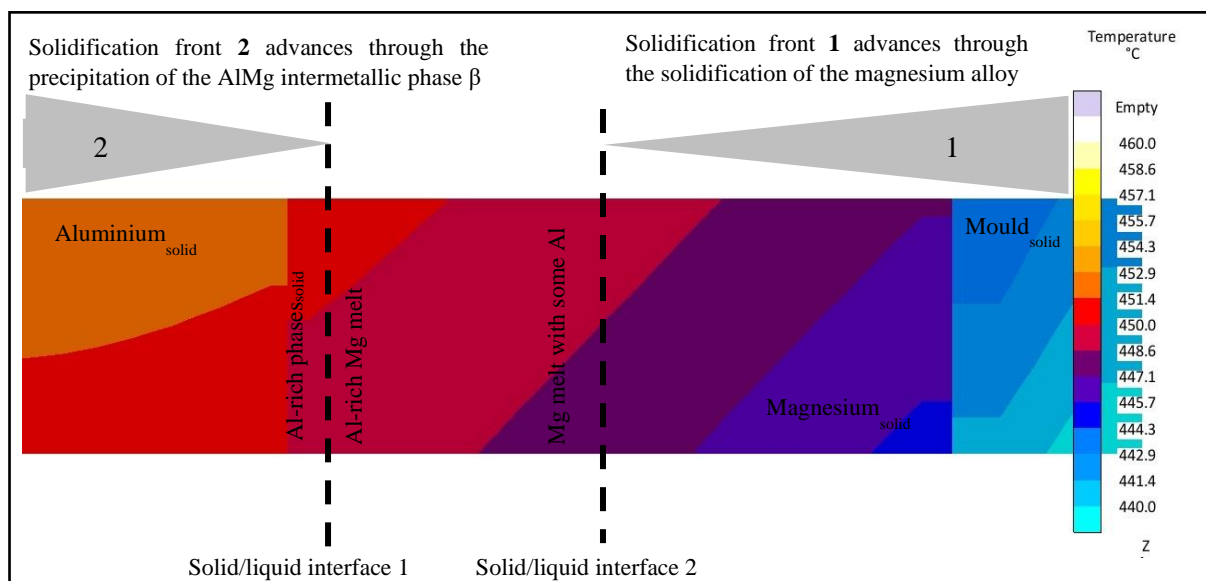


Figure 7.8. Schematic of the solidification fronts of Al/Mg compound castings 3min after pouring ended. Solidification of the compound casting is driven by two converging solidification fronts. The temperature distribution was calculated using Magma 5.3.

thus liquidus temperature, the affected melt solidifies at a significantly lower temperature. Exact temperature of the solidification depends on the melt's chemical composition, but would lie between 660°C and 540°C. The result is two converging solidification fronts. A schematic display of the two solidification fronts is depicted in figure 7.8.

1. The concentration of aluminium (and additional alloying elements) in the melt decreases with distance to the solid/liquid interface 1. Thus the liquidus temperature of the magnesium melt changes in dependence on distance from the solid/liquid interface. At solid/liquid interface 2, the magnesium melt starts solidifying upon falling below the alloy's liquidus temperature. For a commercially pure magnesium, and AZ31 alloy, this would be 650°C and 631°C respectively. The solidification front will then advance in the direction of the solid/liquid interface 1. When the solidification front reaches the aluminium-rich melt, magnesium will precipitate from the melt as the primary phase. Further cooling results in the formation of the magnesium-rich intermetallic  $\gamma$  phase at ~437°C.
2. As the solid aluminium alloy acts as a heat sink, a second solidification front is formed at the solid/liquid interface, which moves towards the magnesium melt and solidification front 1. The aluminium-rich melt starts to solidify at temperatures ranging from 660°C to the eutectic temperature of ~450°C, forming the  $\beta$  phase.

The magnesium-rich phases are thus the last to form in the material bond. More specifically, the last reaction in the Al-Mg system to occur is the eutectic solidification at 437°C. The thickness of the magnesium-rich phases is thus directly dependent on the amount of eutectic or near-eutectic melt. It is widely known that the last melt to solidify in castings contains numerous defects. Engineers and foundrymen go to great lengths to achieve a directed solidification, with the feeder being the last part in the casting to contain melt. The magnesium-rich phases, thus those that solidify last, within the material bond, displayed a number of defects, as observed in figures 4.15 and 6.2 and described in chapters 4 and 6. While a number of these defects are not directly attributable to the solidification process, the soundness of the material bond in the area that solidifies last is thought to be affected negatively.

The thickness of the layer containing the magnesium-rich phases  $\gamma$  – and, in the presence of zinc,  $\phi$  – can thus be selectively grown by increasing the time the liquid melt remains near the solid/liquid interface (i.e. below the solidus temperature of the  $\beta$  phase). This can be achieved either by carefully controlling the advancing solidification front or by altering the solidification range of the magnesium-rich melt by adding alloying elements. The addition of zinc was shown to increase the relative thickness of the layer containing the magnesium-rich phases, by lowering the solidus temperature of the melt. This has not been observed when adding silicon to the compound casting. The effect of both elements on the solidification of the material bond will be discussed in detail in section 7.6.

## 7.4: Growth of the Material Bond due to Diffusion in the Solid State

Once the last remaining melt has solidified, solid state diffusion becomes the driving force of the growth of the material bond. According to the literature, equation 7.8 becomes insufficient to describe the growth of two layers in compound castings. Equations 2.5 and 1.6 from section 2.2.5 can then be used to describe growth of both intermetallic layers. This mathematical model is the result of the extensive work by Dybkov. Even though this approach was proven to be in good accordance with experimental data for diffusion couples and metal-solder experiments, its predicted growth of the material bond was found not to match the observed growth in the current study. The models and the experiments from which this approach was developed were based on the use of a constant reaction temperature. The non-stationary heat-flux present in compound castings is not considered in this model. Rather, the thickness of the material bond was found to correlate with the square of time, as described in equation 7.8. Consequently, the Dybkov's model is unsuited to predict the growth of the material bond in Al/Mg compound casting with a non-stationary heat flux.

The diffusion of both aluminium and magnesium was found to be closely linked to the temperature (Liu, Chen, and Yang, 2015). Thus, the temperature regime in the solid state is an important factor in controlling the growth of the material bond and thus explaining the deviating values for growth and thickness, in the literature and in the current study. In the solid state, the growth of the material bond is expected to mirror the growth of diffusion couples. As such, the material bond grows according to the principles of diffusion of aluminium and magnesium as discussed in section 2.2.7. The contribution to the total thickness of the material bond from the casting process, due to its higher temperatures, is significantly greater than that of solid state diffusion, due to the higher atomic mobility in the liquid

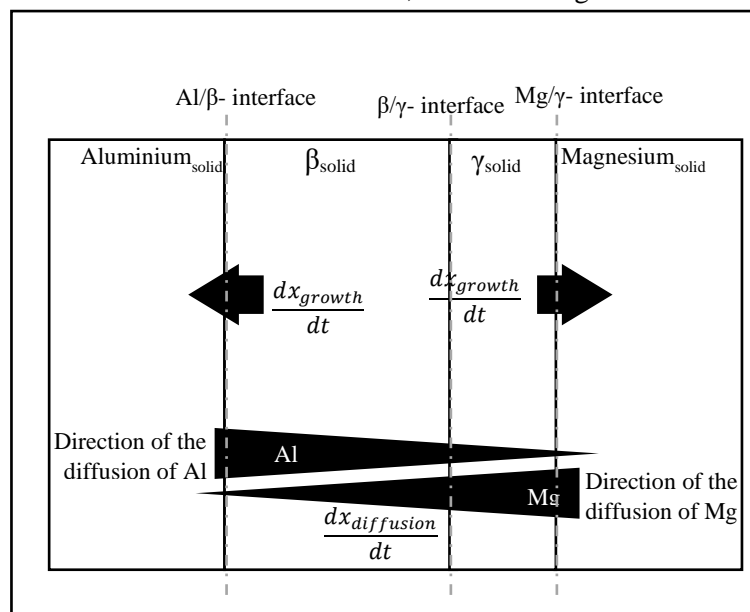


Figure 7.9. Schematic of the growth of the material bond due to solid state diffusion. Diffusion of aluminium and magnesium across the material bond is the driving force of growth in the solid state.



state. As schematically depicted in figure 7.9, the growth of the material bond is the sum of the growth rates of both the intermetallic phases. It is known that the diffusional mobility of magnesium in the solid state is higher than that of aluminium (Zhao et al., 2011; Robson, Panteli, and Prangnell, 2012). Despite this, it was observed in this study that the material bond predominantly grows in the direction of the magnesium alloy and little growth occurs in the direction of the aluminium insert. This behaviour can be traced back to two mechanisms.

1. As discussed in chapter 2.2.7, at temperatures between the melting points of aluminium and magnesium (923-933K), the aluminium atoms are more active and can more easily diffuse into the magnesium. This is the result of the temperature breaking up the bonds between the magnesium atoms, and the subsequent formation of vacancies (Liu, Chen, and Yang, 2015). Consequently, the material bonds in Al/Mg compound castings are dominated by the aluminium-rich phases, due to the said dissolution and diffusion of aluminium into the magnesium in the liquid state.
2. As previously stated, due to the casting process the aluminium-rich phases dominate the material bond. Consequently, as depicted in figure 6.9, the distance between the Al/ $\beta$  and  $\beta/\gamma$  interfaces is greater than the distance between the Mg/ $\gamma$  and  $\beta/\gamma$  interfaces. According to Fick's first law (see equation 2.7 in section 2.2.5) the diffusion flux correlates with distance in the solid state. Therefore, after solidification, the distance between the  $\gamma/\beta$  and  $\gamma/\text{Mg}$  interfaces is shorter and thus the diffusion flux of the available aluminium direction of the magnesium is less hindered by distance compared to the diffusion of the magnesium, despite magnesium's higher diffusional mobility.

Eventually this, as observed with the diffusion couples (see section 4.4) and the castings for push-out testing (see chapter 5), leads to the material bond growing predominantly in the direction of the magnesium, moving the  $\beta/\gamma$  and  $\gamma/\text{Mg}$  interfaces in the same direction. Generally, this was observed in all samples; and it was measured in an exemplary fashion in table 5.4. The concentration profiles of aluminium and magnesium, in compound castings after complete solidification, measured in this study, can be seen in figure 7.10. Comparing it to the data from diffusion experiments conducted by Kulkarni and Luo (2013) reveals similar findings. However, several deviations exist; most notably, the jump in the concentration gradient at the  $\beta/\gamma$  interface, observed in diffusion couples, was not present in the compound castings (see figures showing the linescans in chapter 4). The existing differences can be traced back to the fact that the material bond in compound castings precipitated directly from the liquid melt, while in diffusion couples it was the result of diffusion in the solid state (Kulkarni and Luo, 2013). Overall, the concentration gradients, in compound castings, across the material bond, were more continuous than observed in diffusion couples by Kulkarni and Luo.

In summary, the thickness of the material bond was found to be mostly dependent on the casting process, not solid state diffusion. The impact of diffusion on formation and growth of the material bond is somewhat limited as:

1. no additional phases or layers are formed as a result of diffusion;
2. in the timeframe considered in this study (<60min), thickness of the material bond due to diffusion was significantly lower compared to the resultant thickness of the compound casting process – this is evident from figure 6.1, where thickness due to diffusion was ~1500 $\mu\text{m}$  (30min, 300°C) and thickness due to compound casting and diffusion was ~7500 $\mu\text{m}$ .

Due to the differing growth mechanism, discussed in chapter 2.2.7, large grains (>10 $\mu\text{m}$ ) facilitate the growth of the  $\gamma$  phase compared to the growth of the  $\beta$  phase. The refinement of the grain size could then potentially allow the  $\gamma$  phase to grow exclusively, which is linked to improved mechanical properties as discussed in chapters 4 and 6 (Wang et al., 2015). This would, however, require precise control over the temperature at the material bond; which was not achieved in this study, due to a lack of the necessary equipment and because of safety regulations, and which will be difficult to achieve in commercially sized castings. There are also indications that the addition of erbium facilitates the formation of the  $\gamma$  phase in MgAl alloys (Li et al., 2014). The effect of erbium on the Al-Mg intermetallic phases was investigated after the researcher pointed out the beneficial effects of other rare earth elements, such as neodymium, yttrium and cerium, on intermetallic phases (Guo et al., 2007). It remains unclear if erbium affects the growth of the material bond, as its increased atomic radius (232pm) compared to zinc and aluminium hinders its diffusion in the solid state. At temperatures around ~700°C erbium is dissolved in a magnesium melt and thus it is then possible for it to precipitate alongside the AlMg intermetallic phases during solidification (Raghavan, 2007).

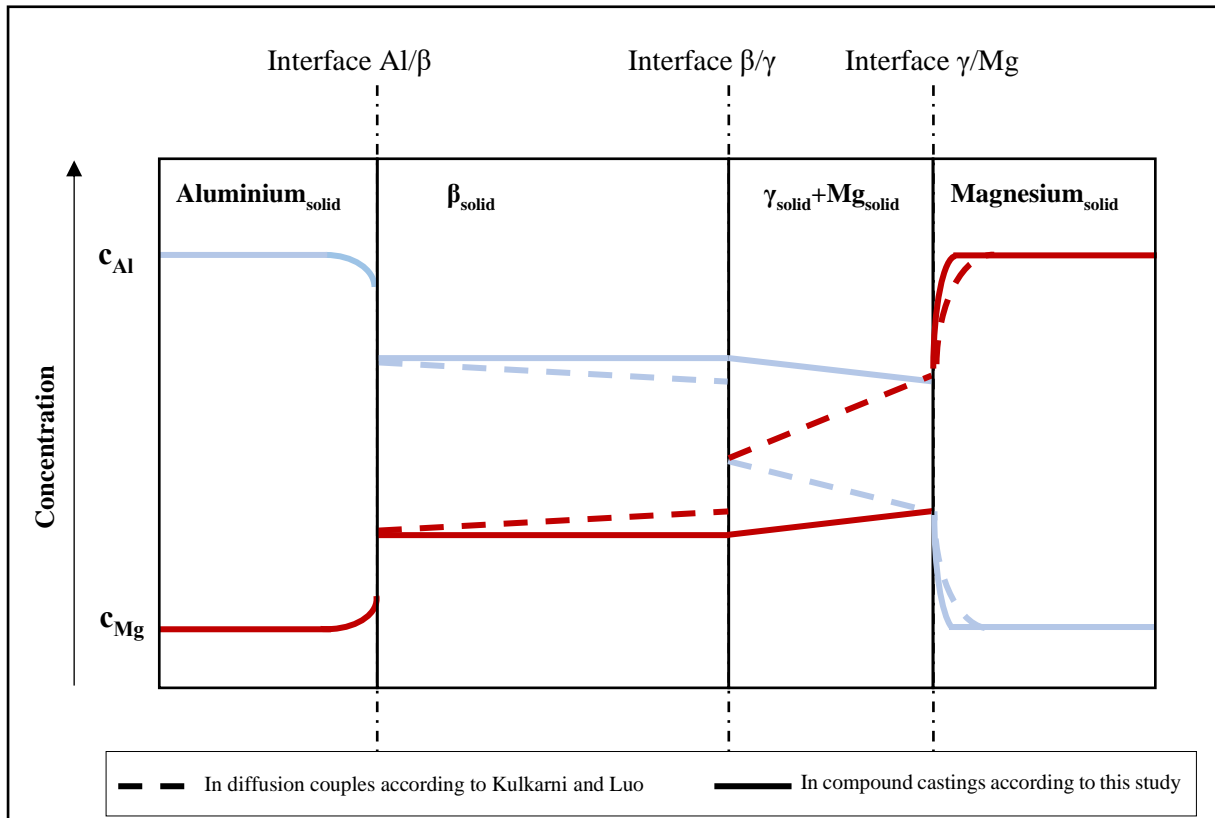


Figure 7.10 Schematic of the material bond after solidification in Al/Mg compound castings. The concentration gradient across the bond as found in this study (solid line) and according to Kulkarni and Luo (2013) (dashed line). Overall, the concentration gradient in compound castings is more continuous than in diffusion couples. The red line (solid and dashed) denotes the concentration of aluminium ( $C_{\text{Al}}$ ) and the blue line (solid and dashed) the concentration of magnesium ( $C_{\text{Mg}}$ ).

## 7.5: Formation of the Material Bond in Al/Mg Compound Casting – Summary

Aluminium's intrinsic oxide layer was not found to impede any reaction between the aluminium alloy and a magnesium melt. The oxide layer is reduced by the magnesium to magnesium oxide and elementary aluminium, and subsequently dispersed within the entire surrounding melt. The forming of the material bond in Al/Mg compound castings follows a different route than through the joining of Al/Mg via solid state diffusion. In compound castings the material bond is the result of the dissolution of aluminium in the magnesium melt, while in diffusion couples solid state diffusion is responsible for the formation of a material bond. The loss of temperature during solidification eventually leads to the precipitation of the aluminium-rich  $\beta$  phase and then the magnesium-rich  $\gamma$  phase. The amount of aluminium dissolved in the magnesium melt during casting is directly correlated with the resultant thickness of the material bond. Thus solubility of the aluminium in the magnesium is the most important factor determining the bond's thickness. However, in diffusion couples the diffusion of aluminium and magnesium, and the subsequent reaction in the solid state, is the only source of growth. As explained in the previous section and displayed in figure 6.12, in compound castings, as opposed to diffusion couples, no jumps in the concentration gradient across the material bond are present. At temperatures above  $\sim 450^\circ\text{C}$  the  $\beta$  phase is formed. As this temperature is exceeded in the compound casting process, the formation of this phase is unavoidable. Once the temperature on the aluminium-rich side of the material bond falls below the solidus temperature of the  $\beta$  phase ( $\sim 450^\circ\text{C}$ ), this phase precipitates from the melt. The magnesium-rich phase  $\gamma$  precipitates on the magnesium-rich side of the bond once the melt reaches  $437^\circ\text{C}$ . Overall thickness of the material bond correlates with the amount of aluminium dissolved in the melt and thus with the time a liquid phase (that is able to dissolve aluminium) is present in the material bond. Ultimately, the thickness of each phase within the material bond depends on the cooling rate, temperature regime, time and alloy composition.

## 7.6: Impact of Alloying Elements on the Formation of the Material Bond

The addition of ternary elements to compound castings results in the formation of compounds as predicted by the corresponding ternary phase diagrams. However, even large amounts (up to 30wt%) of an additional ternary element will not change the overall make-up of the formed material bond, with the intermetallic phases  $\beta$  and  $\gamma$  remaining the primary constituents. The impact of Zn and Si as alloying elements is specifically discussed in the following sections.

### 7.6.1: Silicon

The liquidus temperatures of the AlMgSi ternary system are displayed in figure 7.11 (Feufel et al., 1997). As evident from this figure,  $Mg_2Si$  precipitates from the melt at relatively high temperatures (Kumar et al, 2005). The eutectic temperature on the magnesium side of the MgSi binary system is  $637.6^\circ\text{C}$ , compared to  $437^\circ\text{C}$  in the AlMg binary system (Djurđević et al., 2013). From the temperature measurements presented in section 5.3 it is known that the temperature of the magnesium-rich melt near the solid/liquid interface is below the liquidus temperature of  $Mg_2Si$  (depending on chemical composition,  $\sim 580$  to  $\sim 900^\circ\text{C}$ ) already, after the initial contact of magnesium melt and aluminium alloy. Thus  $Mg_2Si$  is the first phase to form during the cooling of the material bond.

As  $Mg_2Si$  is the only stable phase containing silicon in the magnesium corner of the AlMgSi ternary phase diagram, any silicon that is dissolved by the melt reacts with the magnesium to form  $Mg_2Si$  (Kumar et al., 2005). The  $Mg_2Si$  then precipitates from the melt close to the solid aluminium

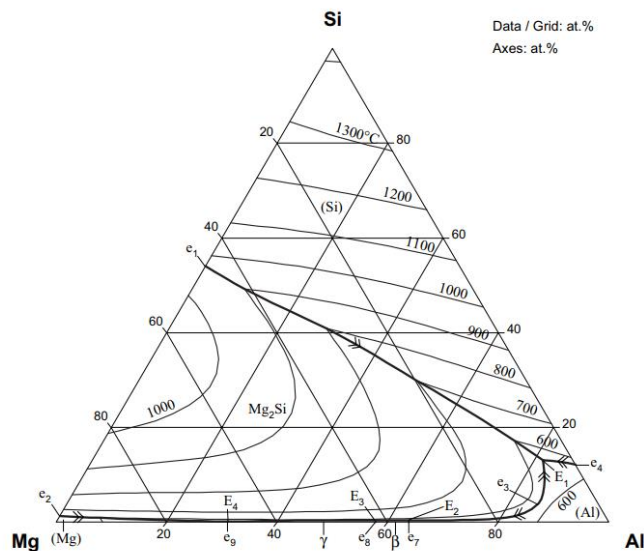


Figure 7.11. Liquidus surface of the AlMgSi ternary system according to Kumar et al. (2005), based on experimental data from Feufel et al. (1997).

insert/magnesium melt interface. Thus, unlike aluminium, silicon is not accumulated in the magnesium melt near the solid/liquid interface.

As a consequence, upon solidification of the material bond it is mostly free of silicon/ $Mg_2Si$ . This can be seen in the samples where a fracture (figures 3.6 and 3.8) propagated along the material bond. On the magnesium-rich side of the fracture, little to no silicon was detected. The presence of aluminium, in excess of the aluminium content of the AZ31 alloy, on the magnesium-rich side, indicates that the fracture originated at some point after solidification, as diffusion of aluminium was possible. This suggests that, while the dissolved aluminium is able to migrate away from the solid/liquid interface in the melt, silicon is not; or only at a very low speed. Consequently, the  $Mg_2Si$  detected in the material bond of AlSi/AZ31 castings is the result of the diffusion of silicon into and across the material bond in the solid state. If a fracture is present within the material bond, the diffusion of silicon and thus formation of  $Mg_2Si$  is prevented. Figure 7.12 depicts the phase distribution in the material bond of an AlSi/AZ31 compound casting from this study (see section 3.2.1), and of a diffusion-welded AlSi1MgMn/AZ31 couple by Dietrich et al. (2011). In diffusion-welded couples,  $Mg_2Si$  particles are only found in close proximity to the AlSi1/ $\beta$ -phase interface and not, as in this study, dispersed within the material bond. This indicates that the diffusion of silicon is facilitated by the higher temperatures of the compound casting process.

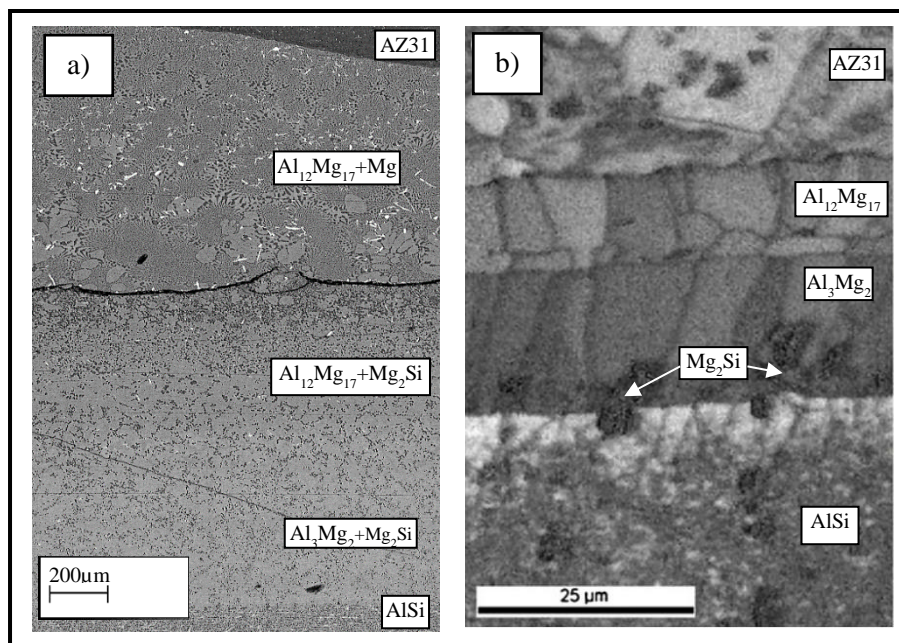
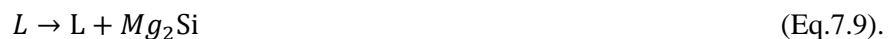


Figure 7.12. Material bond in AlSi/AZ31 couples: (a) AlSi6/AZ31 compound casting from this study; and (b) AlSi1/AZ31 diffusion-welded couple according to Dietrich et al. (2011). The differing distributions of  $Mg_2Si$  particles are attributed to the joining processes (compound casting/diffusion welding).

As detailed in section 4.2.1, silicon is found exclusively in the form of  $Mg_2Si$ , with no evidence of silicon dissolving within the intermetallic phases  $\beta$  and  $\gamma$ . According to the corresponding binary Mg-Si and ternary Al-Mg-Si phase diagrams, silicon has no solid solubility in either magnesium or the two intermetallic phases  $\beta$  and  $\gamma$ . A micrograph and chemical analysis of the  $\beta$  phase showing evidence of the presence of silicon can be seen in figure 4.10. These observations suggest that  $Mg_2Si$  is, in the presence of magnesium, thermodynamically stable, i.e. the more favourable phase. Therefore, the formation of  $Mg_2Si$  is the driving force of silicon diffusion across the interface. As is evident from table 4.2, the total interface thickness was found to remain almost constant, with increasing silicon content in the aluminium insert. It was argued in section 6.3 that the thickness of the material bond is greatly affected by the amount of metal dissolved by the magnesium melt. As silicon is not dissolved (or if dissolved, precipitates immediately in the form of  $Mg_2Si$ ) in the melt, the silicon content has little impact on the thickness of the material bond.

Figure 7.14 displays the overlapping AlSi/AZ31 phase diagrams as calculated with *Pandat*. According to these calculations, silicon does not affect the solidus temperature of the solidification reactions on the magnesium side significantly;  $\pm 10^\circ C$  in the considered range of silicon content. More specifically, the solidus temperatures on the aluminium-rich ( $\sim 450^\circ C$ ) and magnesium-rich ( $\sim 437^\circ C$ ) sides of the bond remain almost constant. A complete overview of the sequence of solidification in AlSi/AZ31 compound castings, described in the following paragraphs, can be found in table 7.1.

$Mg_2Si$ , from the addition of even small amounts of silicon, precipitates at temperatures between  $\sim 580^\circ C$  (in the AlSi1/AZ31 system) and  $\sim 900^\circ C$  (in the AlSi30/AZ31 system). As such, the precipitation of  $Mg_2Si$  is the first reaction that occurs near the solid/liquid interface:



On the aluminium-rich side, this reaction is followed by the formation of the  $\beta$  intermetallic phase at  $\sim 550^\circ C$  (with the AlSi15 and AlSi30 alloys) and  $\sim 450^\circ C$  (with the AlSi1 and AlSi6 alloys):



Sequence of phase formation in AlSi/AZ31 compound castings				
Aluminium-rich side			Magnesium-rich side	
	Temperature range [ $^\circ C$ ]	Reaction	Temperature range [ $^\circ C$ ]	Reaction
1	580-900	$L \rightarrow L + Mg_2Si$	520-630	$L \rightarrow L + Mg$
2	450-550	$L + Mg_2Si \rightarrow Mg_2Si + \beta + Mg_2Si$	437-460	$L \rightarrow Mg + \gamma$
				$L + Mg \rightarrow Mg + \gamma$
				$L \rightarrow \gamma$

Table 7.1: reaction sequence of the solidification on the aluminium-rich and magnesium-rich sides in AlSi/Mg compound castings. As chemical composition varies across the material bond, the approximate temperature ranges, according to the Al-Mg-Si phase diagram, of each reaction are given.

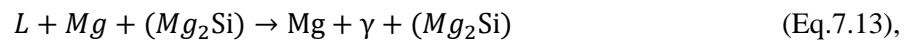
On the magnesium-rich side, magnesium precipitates first from the melt. As silicon is not thought to be able to diffuse away from the solid/liquid interface, no  $Mg_2Si$  precipitates on the magnesium-rich side:



The melt then, depending on chemical composition, solidifies at temperatures between  $\sim 437^\circ\text{C}$  and  $460^\circ\text{C}$ , as the following:



or



or

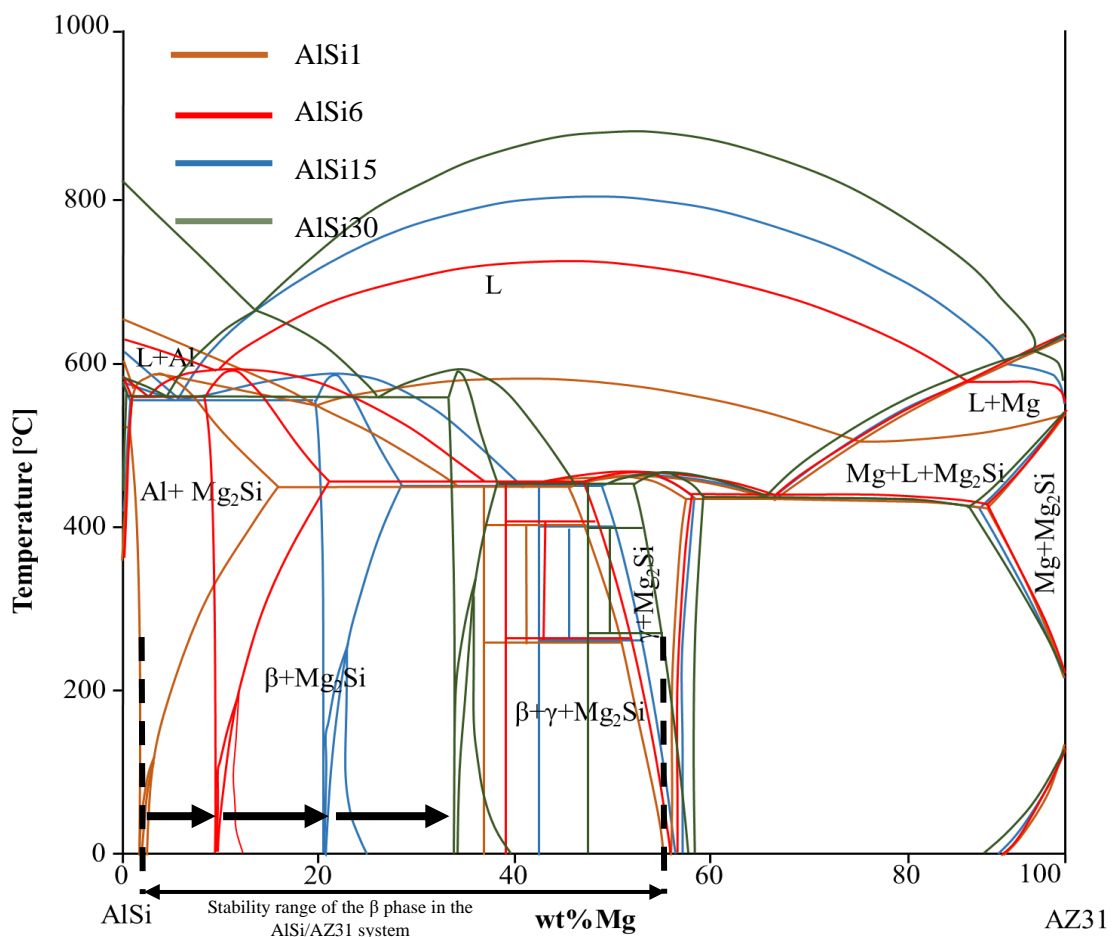


Figure 7.12. AlSi-AZ31 phase diagrams. The effect of silicon on the solidus temperature is negligible. Stability range of the  $\beta$  phase decreases with increasing silicon content. An increase in silicon results in the reduction (arrowed) of the stability range of the  $\beta$  phase.



However, the temperature ranges in which the  $L+Mg+Mg_2Si$  phases are stable increase with silicon content, by around  $90^\circ\text{C}$ . An increase in the solidification freezing range of the melt is associated with hot cracking, which is detrimental to the mechanical properties and will be discussed later in section 7.7. Additionally, the phase diagrams according to *Pandat* predict that an increase from 1wt% to 6wt% silicon reduces the stability range of the  $\beta$  phase by  $\sim 15\%$  in the AlMgSi ternary system. Consequently, silicon (up to 30wt%) reduces the range of stability of this phase field by up to 60%. The non-linear gradient of the aluminium concentrations in the material bond causes deviations from the phase diagram, i.e. the missing Al+Si+ $Mg_2Si$  phase field. Specifically, the jump in aluminium concentration between the AlSi alloy and the aluminium-rich side of the material bond results in the formation of the  $\beta$  phase as the primary phase on this side of the material bond. As a result, the magnesium-rich phases are more dominant in material bonds of Al/Mg compound castings containing silicon. As can be seen in table 3.2, in the presence of silicon the magnesium-rich phases are thicker than the aluminium-rich ones. This is not observed in Al/Mg compound castings containing zinc, or no alloying elements. As the temperature of the eutectic solidification of the  $\gamma$  phase remains almost unchanged, it is still the last reaction to happen at the interface. Upon complete solidification of the material bond, the thermal energy is insufficient to cause diffusion of silicon into the  $\gamma$  and Mg phases, explaining the lack of silicon. As no silicon was found dissolved in the intermetallic phases (see figure 3.10) the liquidus and solidus temperatures of the melt remain unchanged.

As was shown in figures 4.13 and 4.24, large holes and voids that were present throughout all AlZn/AZ31 compound castings were mostly absent in compound castings with silicon. As the holes have been linked to the Kirkendall effect, which is caused by imbalanced diffusion, their absence in the material bond has been attributed to the low diffusivity of silicon in the present case (Aloke, 2004).

$Mg_2Si$  particles are widely reported to increase the strength of an aluminium alloy (Yan et al., 2012); but in the course of the current study it was found that the combination of intermetallic phases  $\beta$  and  $\gamma$  with  $Mg_2Si$  causes embrittlement of the material bond. More precisely, a microstructure of this composition displays a very high level of hardness,  $>300\text{Hv}$  (see section 4.3). By comparison, an aluminium alloy with 20wt%  $Mg_2Si$  was reported to possess a Vickers hardness of just  $\sim 150\text{Hv}$  (Zainon, Ahmad, and Daud, 2016). As a result, the fractures caused by embrittlement and propagating along the phase boundaries and agglomerations of  $Mg_2Si$  particles were common in all castings containing silicon.

### 7.6.2: Zinc

The two zinc-rich phases ( $\tau_1$  and  $\phi$ ) were observed to form at high concentrations of zinc. The  $\tau_1$  was found to contain 10-42%at, and the  $\phi$  17-28%at zinc (Liang et al., 1998; Liang, Chen, and Chang, 1997; Su et al., 1997). According to the chemical analysis of the material bond of AlZn/AZ31 compound castings presented in chapter 4, large amounts of zinc (up to 16wt%) were found to dissolve in the two

intermetallic phases  $\beta$  and  $\gamma$ . The zinc atoms – due to the relatively similar atomic radius of zinc (139pm) compared to aluminium (184pm) and magnesium (173pm) – are believed to be scattered substitutionally in the crystal lattice of both intermetallic phases. The large unit cell of the intermetallics ( $\beta$ :  $a=b=c=2.83\text{nm}$  and  $\gamma$ :  $a=b=c=1.054\text{nm}$  (Mezbahul-Islam, Mostafa, and Medraj, 2014; Gille and Grin, 2018)) can thus incorporate a large amount of zinc (up to 16wt%). Even in the absence of the zinc-rich phases  $\tau_1$  and  $\phi$ , the presence of an even a relatively small amount of zinc (6wt%) was found to increase the thickness of the interface (see table 4.3). This behaviour can be explained by studying the ternary AlZn-AZ31 phase diagrams (figures 4.14 and 4.20) in chapter 4.

1. The eutectic point in the Al-Zn phase diagram is at ~94wt% zinc. Increasing the zinc content thus lowers the liquidus temperature of the AlZn insert. The constant pouring temperature (+/- 6°C, as listed in table 2.5) of the experimentation in this study, in combination with the different AlZn inserts, results in an increase in time for which a solid/liquid interface exists (assuming near-constant cooling rates). Consequently, according to equations 7.4 and 7.5, the amount of solid metal dissolved into the magnesium melt increases, which then leads to an increase in interface thickness as explained in section 7.3.
2. The activation energy for the diffusion of zinc is ~1.25eV, considerably lower than other metals (Erdélyi et al., 1978). As a consequence, compared to aluminium and magnesium, zinc possesses a higher diffusivity (Kammerer et al., 2014). The presence of zinc thus increases the diffusion-driven growth of the material bond, in the liquid state via diffusion of zinc from the AlZn insert into the magnesium melt, and in the solid state via solid state diffusion.
3. In contradiction to the ternary AlMgZn phase diagram, the zinc-rich phases  $\phi$  and  $\tau_1$  were not found to form at a lower preheat temperature of 200°C. At this temperature, dissolution and diffusion of zinc into the melt is found to be reduced, resulting in a decrease in thickness (from 6818 $\mu\text{m}$  at 400°C to ~1390 at 200°C) of the bond compared to higher temperatures. As such, insufficient zinc to form the zinc-rich phases ( $\tau_1$  and  $\phi$ ) is present near the solid/liquid interface. Increasing the preheat temperature of the mould from 200 to 350°C was found to be necessary to form the zinc-rich phases. The temperature at the solid/liquid interface at the end of casting, according to numerical simulation, detailed in section 5.3, for two different preheat temperatures, can be seen in figure 7.13. As evident from this figure, the temperature near the interface is ~40-60°C higher with a preheat temperature of 350°C. According to the simulation, this difference persisted near the material bond until it was completely cooled to ambient temperature.

It is evident from these observations that the zinc-rich phases precipitate directly from a zinc-rich melt. As such, their formation is dependent on the dissolution of the solid AlZn insert into the Mg-based melt at the solid/liquid interface during casting, and the subsequent diffusion of zinc into the magnesium melt. As both mechanisms are dependent on or promoted by the presence of a liquid phase, the longer the melt is liquid, the more zinc is dissolved therein. Decreasing the preheat temperature resulted in a faster cooling and consequently less zinc being dissolved in the melt. This in turn prevented the formation of the zinc-rich phases  $\tau_1$  and  $\phi$ . The solidus temperature of the  $\phi$  phase was, at 367°C,

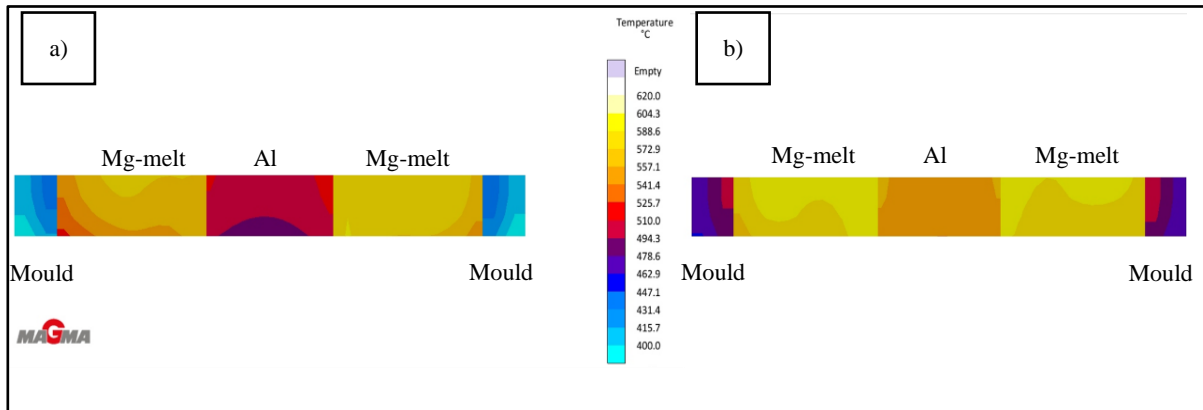
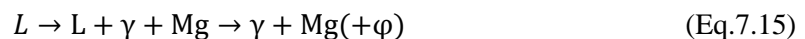


Figure 7.13. (a) Temperature distribution at the cross-section of an Al/Mg compound casting with a preheat temperature of 200°C. (b) Temperature distribution at the cross-section of an Al/Mg compound casting with a preheat temperature of 350°C.

considerably lower than that of the  $\gamma$  phase at 433°C. From this it follows that the magnesium-rich side of the material bond is not completely solidified until reaching the aforementioned critical temperature of 367°C. Al/Mg compound castings, without any zinc, solidify at 437°C, the eutectic temperature of the Al-Mg binary system, and thus they solidify considerably earlier. Considering the cooling curves displayed in figure 5.11, the material bond in compound castings with 30wt% zinc are completely solidified approximately 5min after Al/Mg compound castings without zinc; which in turn facilitates further diffusion of zinc. As seen in figure 7.14, increasing the amount of zinc delays the complete solidification of the magnesium-rich side of the material bond. More specifically, zinc lowers the temperature of the following reactions by up to ~30°C (at 30wt% zinc):



and

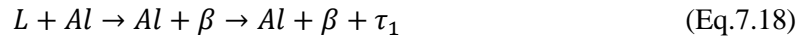


As a consequence, even in the absence of the formation of the zinc-rich phases, zinc lowers the liquidus temperature of the melt by ~30°C, depending on chemical composition, thus increasing the time of liquid/solid interaction. This in turn increases the thickness of the magnesium-rich phases relative to the total thickness of the interface, as shown in figure 7.14. The sequence of solidification for AlZn/AZ31 compound castings is displayed in table 7.2. Unlike the magnesium-rich phases, zinc has

little impact on the temperature range of the solidification of the aluminium-rich phases. An increasing amount of zinc does lower (up to ~40°C with an AlZn30/AZ31 compound casting) the temperature of the initial solidification reaction of the primary phase:



Zinc, however, has no impact on the solidus temperature of the solidification. Depending on the exact chemical composition, the  $\tau_1$  phase precipitates from the melt at ~450°C. In AlZn30/AZ31 compound castings the solidification, according to the phase diagrams calculated with *Pandat*, follows the following sequences:



or



As was shown in chapter 4, in the AlZn6/AZ31 and AlZn15/AZ31 compound castings no zinc-rich phases precipitated under the conditions used; nor was elementary aluminium detected in the layer containing the  $\beta$  phase. Thus in AlZn6/AZ31 and AlZn15/AZ31 compound castings the aluminium-rich melt solidifies following the reaction:



Sequence of phase formation in AlZn/AZ31 compound castings				
Aluminium-rich side		Magnesium-rich side		
Temperature range [°C]	Reaction	Temperature range [°C]	Reaction	
1	>450	L→L+Al	430-630	L→L+Mg
			430	L→L+Mg+ $\gamma$
			430-450	L→L+ $\gamma$
2	450	L+Al→Al+ $\beta$ + $\tau_1$ L+Al→Al+ $\beta$ →Al+ $\beta$ + $\tau_1$	410-450	L+Mg→L+Mg+ $\gamma$
	450	L→L+Al→ $\beta$ (in AlZn6 and AlZn15/AZ31 compound castings)	390-450	L+ $\gamma$ →L+Mg+ $\gamma$
3	No additional phases formed	367	L+Mg+ $\gamma$ →Mg+ $\gamma$ + $\phi$	
			L+ $\gamma$ →Mg+ $\gamma$ + $\phi$	

Table 7.2: reaction sequence of the solidification on the aluminium-rich and magnesium-rich sides in AlZn/Mg compound castings. As chemical composition varies across the material bond, the approximate temperature range, according to the Al-Mg-Zn phase diagram, of each reaction is given. The zinc-rich phases  $\tau_1$  and  $\phi$  were only found in AlZn30/AZ31 compound castings

Measurements of the chemical composition (see tables 6.1 and 6.2) revealed that zinc displayed a clear tendency to diffuse into the material bond. The zinc found in the material bond did not exclusively stem from the dissolution of the AlZn insert. It was found that the zinc content of AZ31 was  $\sim 0.5\text{wt}\%$  lower than the initial zinc content of the AZ31 alloy. Zinc is, at a concentration below  $51.3\text{wt}\%$ , continuously dissolved by the remaining (Al+Zn-rich) magnesium melt during solidification of the AZ31 alloy. This possibly leads to the observed chemical segregation, which could be due to the large unit cells of the  $\beta$  and  $\gamma$  phases (less closely packed than the aluminium and magnesium unit cells) facilitating the diffusion of zinc into them. In all compound castings containing zinc, evenly shaped holes were found within the magnesium-rich phases (consisting of elementary magnesium, the intermetallic phase  $\gamma$  and the AlMgZn phase  $\phi$ ). These voids, seen in figure 3.13, were found specifically within a matrix of magnesium- and zinc-rich phases. The number and size of the cavities were found to increase with zinc content. The presence of similarly shaped holes has been reported in the material bonds of other compound castings, such as Al/Fe (Viala et al., 2002; Zhe et al., 2011), Al/Pt (Radi, Barna and Lábár, 1996) and Au/Sn compound castings (Nakahara and McCoy, 1980). The voids were linked to an imbalanced diffusion process, known as the Kirkendall effect (Aloke, 2004) and are referred to as Kirkendall voids. Kirkendall voids are observed to form after extended periods of heat treatment. Zhe

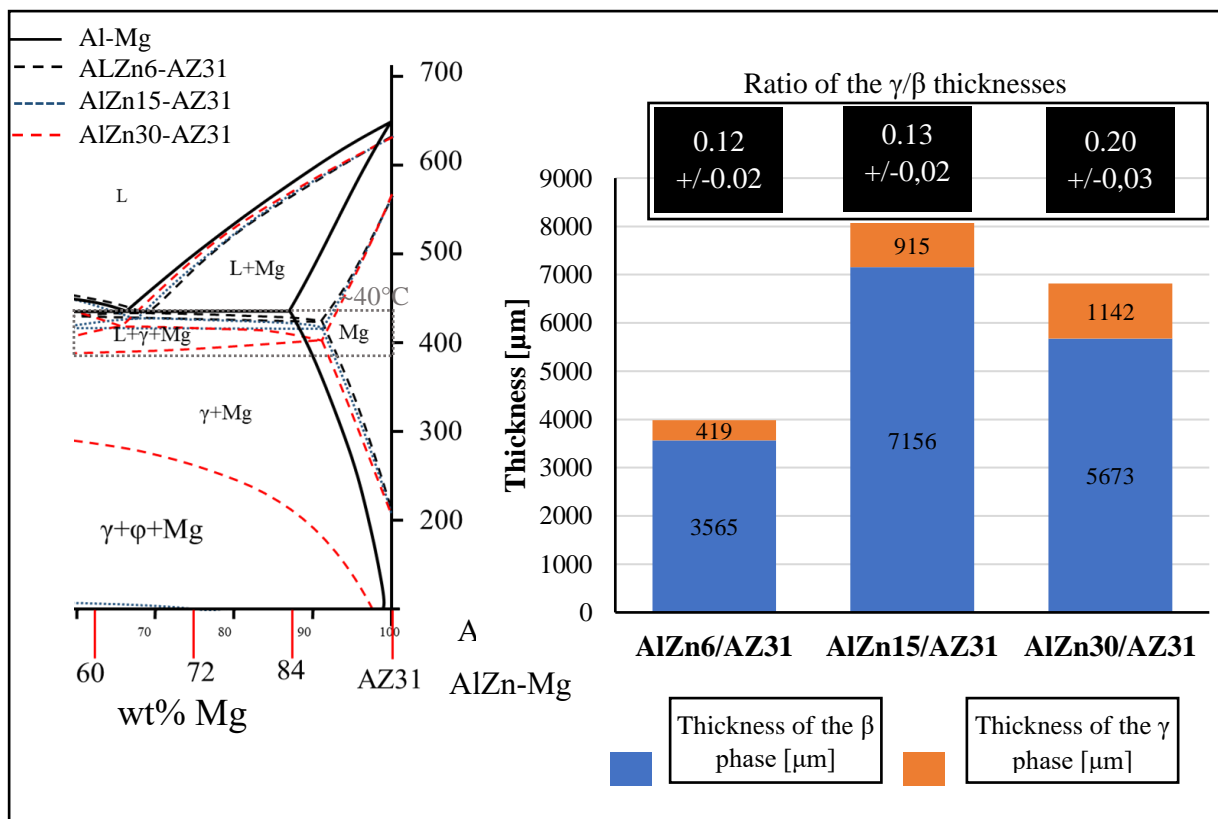


Figure 7.14. (a) Magnesium-rich side of the AlZnX/AZ31 phase diagram. As highlighted, zinc increases the solidification range of the magnesium-rich side of the material bond. As shown, the solidus temperature is lowered by  $\sim 40^\circ\text{C}$  in the presence of 30wt% zinc. (b) Thickness of the  $\gamma$  phase in relation to thickness of the  $\beta$  phase. Higher values for the ratio indicate an increased thickness of  $\gamma$  phase in the material bond. This increased thickness of the  $\gamma$  phase is caused by the increased solidification range, allowing more time for the diffusion of zinc.

et al. observed such voids after the heat treatment of an Fe/Al compound casting for 160h. The formation of the holes in the current study took place at a much faster pace (<30min), possibly indicating that the presence of zinc accelerated their formation. However, in his extensive research of the solid/liquid reaction, Dybkov concluded that the Kirkendall effect is unobservable in compound castings (Dybkov, 2002, 2007).

In the current study, it was demonstrated in figure 7.15 that zinc is not found evenly distributed within the  $\gamma$ +Mg phases. This figure reveals that zinc is more commonly found in areas close to the magnesium dendrites. This leads to the formation of zinc-rich areas within the matrix of  $\gamma$ +Mg. These zinc-rich areas possess a different solidification range than the surrounding magnesium-rich matrix. The difference of the volume of the magnesium-rich AlMgZn phases, presented in table 4.3, in the solid and liquid states, was found to be far greater than the volume contraction of aluminium (7%) and magnesium (4%) (Altenpohl, 1965; Glatzel, 2012). Considering the greater volume contraction during solidification of the magnesium-rich AlMgZn phases, and the appearance of the described voids, it is possible that the voids are formed during the solidification of the magnesium- and zinc-rich phases. Areas with an increased zinc content would solidify after the  $\gamma$  phase and the contraction of these phases would then cause the formation of the voids. However, as mentioned before in section 4.2.2, solidification-related shrinkages are rarely observed to be as evenly shaped, as they usually follow the solidification front and thus the temperature gradient (Mercury Castings, 2019; Pequet, Rappaz, and Gremaud, 2002).

A combination of 30wt% zinc and an elevated preheat temperature (350°C) caused the complete transformation of the microstructure and the formation of large and distinct holes, as discussed in section 4.2.2. It is believed that these larger voids are formed by the same mechanism as the smaller ones seen in figure 4.13. Ultimately, all of the evenly shaped holes are caused by a combination of imbalanced diffusion, segregation and delayed solidification of zinc-rich areas within the melt near the solid/liquid interface. Based on the results from experimentation presented in sections 4.2.2, 4.3 and 5.4, a model describing the formation of these voids has been developed. A schematic of the model can be seen in figure 7.16. To understand the formation of the voids, it is important to realise the following.

- As discussed in section 7.3 (and schematically displayed in figure 7.8), solidification in Al/Mg compound castings is advanced by two converging solidification fronts.
- Zinc is continuously dissolved by any remaining melt during casting and solidification. This dissolved zinc then migrates within the melt according to the principles of diffusion. Accordingly, the concentration of the zinc in the melt decreases with increasing distance from the solid/liquid interface.

The AZ31 (or magnesium) melt starts to solidify at the mould/melt interface at its liquidus temperature, and then the solidification front advances in the direction of the AlZn30 alloy. The zinc concentration in the melt ahead of the solidification front increases due to the dissolved zinc from the AlZn30 and

AZ31 alloys. As detailed above, an increase in zinc causes the decrease of the solidus temperature for the solidification reaction ( $L \rightarrow L + \gamma + \text{Mg} \rightarrow \gamma + \text{Mg}$ ). As a result, the zinc-rich areas of the melt remain liquid within the solidified  $\gamma$  and Mg phases. As the solidification front continues to advance in the direction of the AlZn30 insert, zinc is continuously dissolved by the remaining melt. This dissolution of zinc and additional diffusion of it further lowers the melt's solidus temperature; DSC measurements in this study identified the lowest solidus temperature be 367°C. Diffusion of aluminium and magnesium across the (mostly) solidified material bond takes place at the same time and causes the formation of low-melting (zinc- and magnesium-rich) areas ahead of the solidification front (see figure 7.15).

Areas already solidified might remelt, as a result of the lowering of the liquidus temperature of this area due to the diffusion of zinc and aluminium. As these areas remelt, the advancement of the solidification front, and the local re-melting and re-solidification just described, causes the migration of these zones, consisting of the (solidified)  $\gamma$  and Mg phases and zinc-rich melt, towards the AlZn30 insert. Once the local temperature drops below 367°C the remaining zinc-rich melt solidifies without re-melting. The volume contraction during solidification is compensated by the remaining melt. This melting and solidifying of the melt is repeated until the AlZn30 alloy is completely transformed (to the  $\gamma+\phi+\text{Mg}$ -phases), resembling the microstructure seen in figure 4.24. The volume contraction of zinc-rich AlMgZn alloys is significant (>15% (see section 4.2.)). Consequently, as this contraction of the melt cannot be compensated by any remaining melt, voids are formed. It was previously noted that the observed voids are too evenly shaped to be entirely caused by solidification. If they were solely caused by the volume contraction, a transition zone in the microstructure adjacent to the voids would be expected. This has not been observed, as can be seen in figure 3.24. Thus it is thought that upon solidification zinc diffuses out of the recently solidified zinc-rich phases, as these areas are oversaturated with zinc. This imbalanced diffusion (Kirkendall effect), in addition to the volume contraction, then causes the growth voids and the eventual formation of the evenly shaped holes. Direct observation of the transformation is difficult as it takes place at a relatively high speed (<15min). To observe an intermediate step in the transformation of AlZn30/AZ31 compound castings would require water quenching to stop diffusion. However, quenching the castings with water was prohibited due to safety concerns.

The diffusion of zinc is the driving force for the transformation of the microstructure in AlZn30/Mg compound castings. In the Mg hcp solid solution, zinc diffuses faster than both magnesium and aluminium, and interestingly also increases the diffusivity of magnesium and, to a lesser extent, aluminium (Kammerer et al., 2016). Similarly, an increasing zinc content also increases the diffusivity of zinc and aluminium in the fcc solid solution (Cui et al., 2006). Due to zinc's high diffusivity, the transformation of the microstructure takes place at a fast pace (<30min in the present study, as opposed

to 16h as reported by Zhe et al. (2011)). It can thus be concluded that, in compound castings, two criteria must be satisfied to observe the formation of the evenly shaped (Kirkendall) voids.

- **High diffusivity.** The transformation of the microstructure of the AlZn30 insert necessitates the diffusion of aluminium, magnesium and zinc across the material bond.
- **Low solidus temperature.** The reduction of the lowest solidus temperature from 437 (in the Al-Mg binary system) to 367°C (in the Al-Mg-Zn ternary system) increases the time, assuming a similar cooling rate, that a liquid phase exists in the material bond.

Both criteria are met in AlZn30/Mg compound castings, as the  $\phi$  phase displays a very low solidus temperature and zinc possesses the aforementioned high diffusivity. A certain minimum amount of zinc (>15wt%) was found to be necessary for the  $\phi$  phase to form, as the intermetallic phases  $\beta$  and  $\gamma$  are able to dissolve a significant amount of zinc in solid solution. The exact amount is dependent on the amount of magnesium present and the diffusion depth of the zinc (which is mainly dependent on temperature). As such it is important to consider the effects of diffusion on the morphology of the material bond in compound castings.

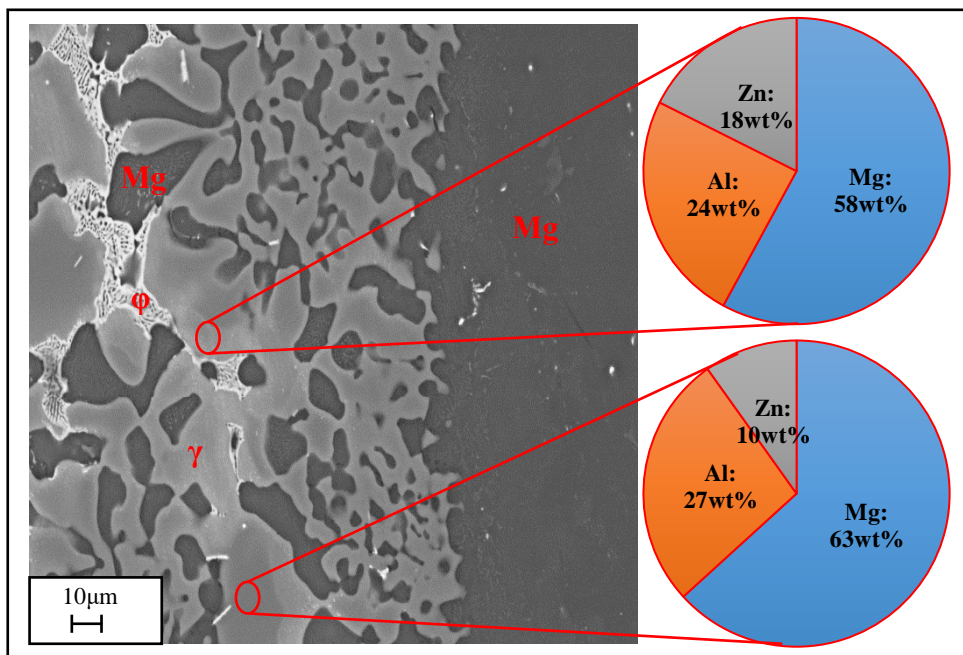


Figure 7.15. SEM micrograph of the magnesium-rich side of the material bond. Zinc-rich and poor areas (circled) were identified with EDX within the  $\gamma$  matrix. The corresponding chemical compositions of a zinc-rich and a zinc-poor area are displayed on the right-hand side.



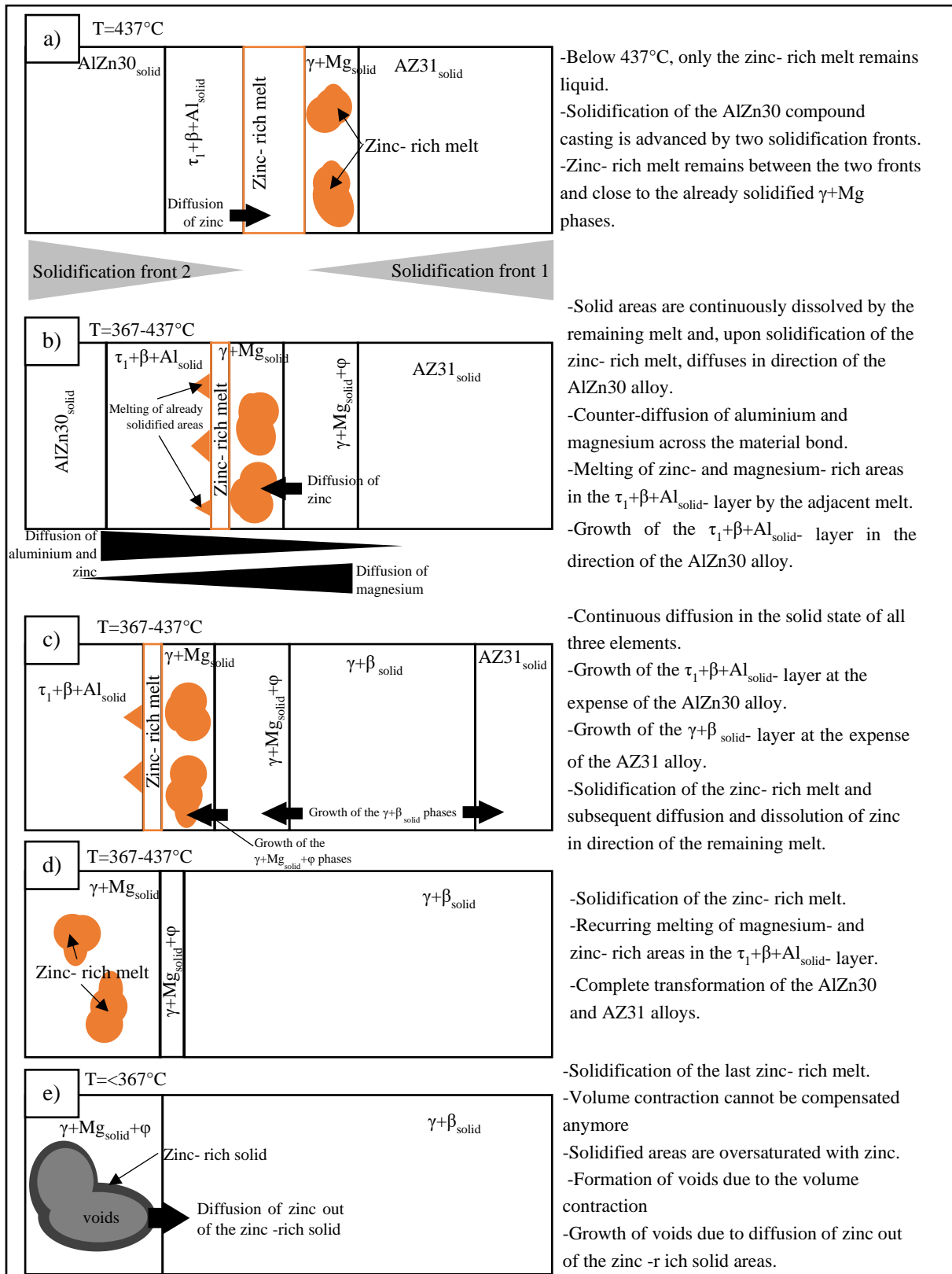


Figure 7.16. Schematic of the model to show the formation of the regularly shaped voids observed in AlZn30/AZ31 compound castings. The model was developed based on the results from chapters 3 and 4. According to the model, the void formation can be classified into 5 distinct steps: (a) after solidification of the  $\gamma$  phase with only zinc-rich melt remaining; (b) change of chemical composition due to diffusion of aluminium, magnesium and zinc; (c) continuous melting and solidification of parts of the material bond; (d) transformation of the AlZn30 insert; and (e) formation and growth of voids due to volume contraction and diffusion.

## 7.7: Soundness and Mechanical Strength of the Material Bond in Al/Mg Compound Castings

### 7.7.1: Soundness of the Material Bond of Al/Mg Compound Castings

According to the (obsolete) ISO 7722 standard, soundness in castings refers to the casting being ‘free from faults, such as porosity, cavities or detrimental discontinuities with regard to intended use’. Thus, the numerous fractures and pores demonstrated in chapter 3, present in Al/Mg compound castings, reduce the soundness of the casting. Two types of fractures are found within Al/Mg compound castings:

1. fractures as a result of hot cracking originating during solidification and cooling (Kobayashi, 1998);
2. fractures caused by mechanical stress during removal from the mould, or from cutting (Liu and Kou, 2015, 2017).

Hot crack fractures are created by the contraction of the melt during solidification and occur when insufficient liquid melt, needed to fill the gaps, remains near the solidification front. The tendency of an alloy to suffer from hot cracks is dependent on its chemical composition and volume contraction (Lange, 2001). As such, it was expected that the high volume contraction found in Al-Mg-Zn (see table 4.3) would result in hot crack fractures. However, the fractures in AlZn/AZ31 compound castings appear to have originated after the complete solidification of the material bond, as the fractures did not impede diffusion of zinc across the bond. According to Liu and Kou (2015, 2017), elements with a high diffusivity (zinc in the present case) reduce the crack susceptibility, possibly explaining the absence of hot crack fractures in AlZn/AZ31 compound castings. Compound castings with silicon displayed numerous fractures. As these fractures prevented the diffusion of silicon across the material bond, they are thought to have originated during the solidification of the bond and are thus linked to hot cracking.

Inducing a mechanical load onto the material bond results in the weakest part of the bond failing. The fracture is initiated when the Ultimate Tensile Strength (UTS) of the material bond’s weakest section is exceeded. These fractures due to mechanical stress would propagate either along phase boundaries (e.g. close to the Al/ $\beta$  or  $\beta$ / $\gamma$  interface), or, in the presence of silicon, along agglomerations of Mg<sub>2</sub>Si particles. During push-out testing the compound castings always failed near the aluminium-rich side of the material bond. This shows that the aluminium-rich phases are more prone to fail, specifically the aluminium-rich  $\beta$  phases, and, in the presence of zinc, the  $\tau_1$  phases.

Besides the mechanical properties of the material bond, its mechanical strength is also affected by pores. Pores in the material bond of Al/Mg compound castings are the result of:

1. imbalanced diffusion in the solid state (Kirkendall voids), as discussed in section 6.6.2;

2. volume contraction during solidification (solidification-related shrinkages) (DeGarmo, Black, and Kohser, 2008).

Due to the lower solidus temperature of the intermetallic phases (e.g. the  $\beta$  and  $\gamma$  phases) in the material bond, the bond solidifies after the magnesium melt. Thus, the volume contraction during solidification can only be compensated by the remaining melt at the interface. Engineers and designers go to great lengths to prevent porosity in castings. It is questionable if any of the traditional approaches to minimise porosities (such as feeders, design of feeding paths within the casting, or chills to control the solidification front) would be effective in compound castings, as:

1. feeders are only effective in close proximity to the area which is supposed to be fed with liquid melt (DeGarmo, Black, and Kohser, 2008);
2. controlling the direction of the solidification of the material bond will be more difficult in compound castings with more complex geometries.

The material bond in the AlSi/AZ31 compound castings showed a lesser tendency to contain pores. Silicon is one of the few elements that expand during solidification, and thus counters the volume contraction. The addition of silicon, however, results in the formation of  $Mg_2Si$  particles, which increase hardness. As evident from figures 3.25-3.28,  $Mg_2Si$  is  $\sim 50Hv$  harder than the  $\beta$  and  $\gamma$  phases. However, increased hardness is an indication of increased brittleness, and the embrittlement of the material bond makes it more prone to fracture (Hughes, 2009). The push-out testing performed in chapter 5 revealed that pores in the material bond reduce the effective bonding surface, which ultimately reduces the strength of the material bond in the compound castings. As such, any pores are detrimental to the strength of the material bond, regardless of their exact origin.

### 7.7.2: Mechanical Strength of the Interface of Al/Mg Compound Castings

There are many reports in the literature linking the thickness of the material bond, and thus the intermetallic phases, to the bond's strength. Reducing the thickness of the intermetallic layer and thus the material bond was linked to an improvement in the stability and mechanical properties of the bond (Choi et al., 2011; Emami et al. 2013a; Hajjari et al., 2011; Panteli et al., 2013; Wang et al., 2015). A correlation between the thickness of the material bond (thus intermetallic phases) and the mechanical properties (push-out resistance in this study) was not found in the experimentation outlined in chapter 5. In fact, as is evident from figure 5.4, the results indicate that if the resultant material bond is too thin ( $<500\mu m$ ), or not encompassing the whole interface, push-out resistance is lower than in samples with a thicker interface. In such samples, the recorded load on the sample would almost linearly decrease with the displacement (see figure 5.5). Pushing-out the Al cylinder would result in a decrease of the bonding area, thus friction, between the Al cylinder and the magnesium alloy. As a constant push-out speed was used, this resulted in the observed linear decrease in the load. This behaviour indicates that

in samples with a very low thickness, the friction between the two metals provides more resistance to being pushed-out than the actual material bond.

Push-out resistance of the Al/Mg compound castings was, with a maximum of 25MPa, somewhat similar to the 29MPa reported by Emami et al. and Hajjari et al.; however, the described correlation that a thinner material bond would lead to a higher pushout resistance was not observed (Emami et al., 2013a; Hajjari et al., 2011). It has been demonstrated throughout this study that the coating of the aluminium alloy is not necessary to facilitate a reaction at the interface. Results from Xu et al. (2014) indicate that a coating could be beneficial for the mechanical strength of the material bond. The authors reported a maximum shear strength of over 60MPa for an AlSi17/AM60 compound casting. However, the experimental casting process used resulted in a significantly smaller casting, with an increased soundness within the material bond, compared to the castings in the current study. As such, the higher shear strength of the bond may not be solely attributable to the coating, but rather to the increased soundness of the material bond (Xu et al., 2014). The ultimate tensile strength (UTS) for a number of select alloys and Al/Mg couples, as well as the highest measured UTS from this study, are displayed in figure 7.17. It should be noted that the strength of Al/Mg couples is considerably lower than that of aluminium and magnesium alloys.

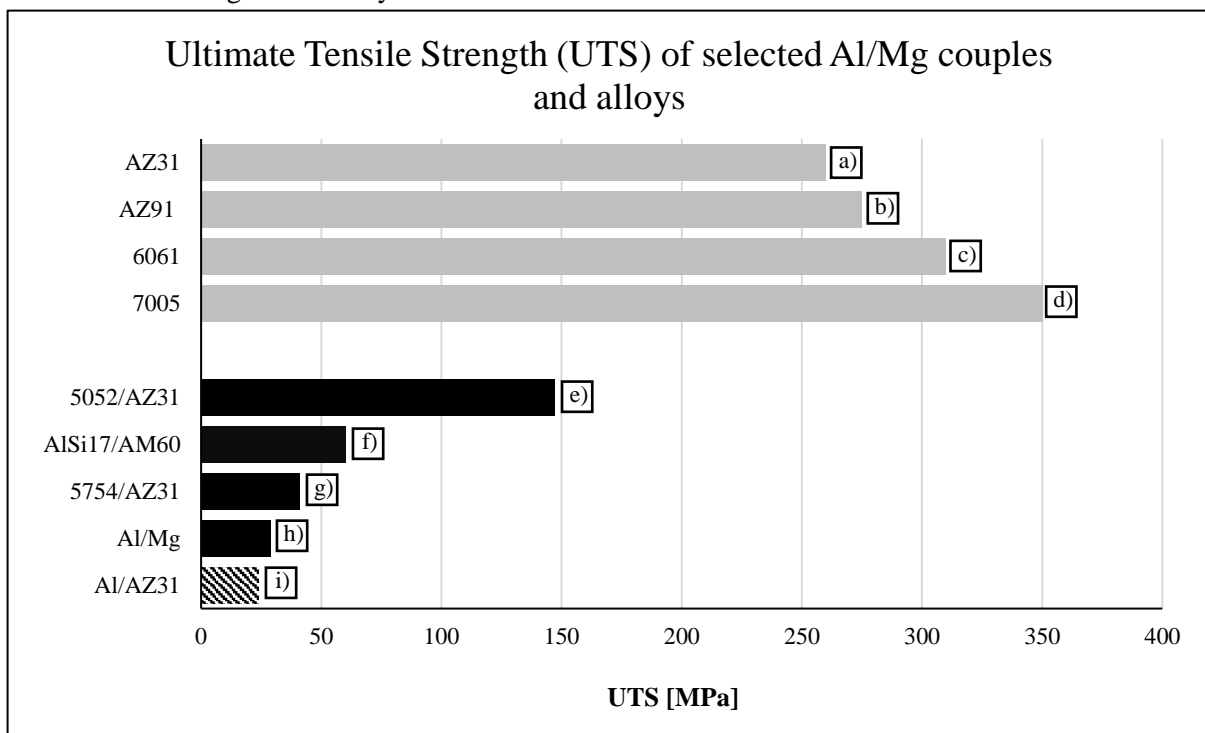


Figure 7.17. Ultimate tensile strength (UTS) of selected Al/Mg couples and alloys. UTS of Al/Mg couples from this study (shaded) and from the literature (black), as well as the UTS of selected alloys (grey) are displayed: (a) extruded AZ31 magnesium (Bauccio, 1993); (b) die-cast AZ91 magnesium (Bauccio, 1993); (c) 6061 aluminium (ASM International, 1990); (d) 7005 aluminium (ASM International, 1990); (e) friction stir welded 5052/AZ31 couple (Morishige et al., 2008); (f) AlSi17/AM60 compound casting (Xu et al., 2014); (g) ultrasonic spot welded 5754/AZ31 couple (Patel, Bhole, and Chen, 2012); (h) commercially pure Al/Mg compound casting (Emami et al., 2013a); and (i) commercially pure Al/AZ31 compound casting from this study (see chapter 6).

The push-out testing (see figure 5.4) revealed that the type of aluminium and magnesium alloy appears to have only a minor impact on the strength of the material bond. Despite the bond's higher hardness (compared to the aluminium and magnesium alloys), failure of the compound castings always originated in the material bond close to the aluminium insert. Therefore, its mechanical strength is determined by the strength of its constituents; the  $\beta$  and  $\gamma$  intermetallic phases in Al/Mg compound castings. In this study the material bond was observed always to fail near the aluminium alloy, within the layer consisting of the aluminium-rich  $\beta$  phase; and, in the presence of sufficient amounts of zinc, the  $\tau_1$  phase. An exemplary sample of the failed castings is seen in figure 5.5. It is apparent from this figure that the material bond failed inside the aluminium-rich phases ( $\beta$  and  $\tau_1$ ) adjacent to the aluminium insert. This behaviour was exhibited throughout all compound castings, independent of casting parameters and alloy selection. It is in good agreement with observations made during the measurement of the micro-hardness in section 3.3, which identified the  $\gamma$  phase as possessing a higher degree of ductility than the  $\beta$  phase, while retaining high hardness. This is confirmed in calculations by Wang et al. (2008) which identified the  $\gamma$  phase as non-brittle. The presence of secondary phases such as  $\tau_1$  and  $\phi$  was found to have little impact on the behaviour of the bond under load.

The  $\beta$  phase is the limiting factor in terms of mechanical stability. It was discussed in section 6.3 that the thickness of the  $\beta$  phase can be somewhat controlled by carefully adjusting casting parameters (casting temperature of the melt, and preheat temperature of the aluminium alloy). However, the formation of at least a thin layer of this phase is unavoidable, due to the high temperatures involved in the casting process. To improve the mechanical strength of the material bond in compound castings, the mechanical properties of the aluminium-rich phases (mainly the  $\beta$  phase) have to be improved. Due to the unfavourable properties of the  $\beta$  phase, this phase is avoided rather than improved in castings.

At temperatures above 150°C, the ductility of the  $\gamma$  phase increases further. This softening of the intermetallic  $\gamma$  phase at elevated temperatures can possibly also improve push-out resistance and thus strength of the material bond (Li et al., 2015; Mathur, Maier-Kiener and Korte-Ketzel, 2016). The strength of the material bond is not improved by increasing the mechanical properties of the  $\gamma$  phase, as the bond's strength would still be limited by the strength of the  $\beta$  phase.

Many intermetallic phases (e.g. titanium aluminides) display high creep resistance due to their strong atomic bonding and resultant high melting point (Kassner and Pérez-Prado, 2004; Ashby, Shercliff, and Cebon, 2014). Due to the low melting points of the  $\gamma$  phase and  $\beta$  phase, they are expected to display low creep resistance. Thus, it is doubtful if Al/Mg compound castings are suited for applications at elevated temperatures.

## 7.8: Discussion remarks - An Assessment of the Viability of Al/Mg Compound Castings

One of the main benefits identified by early research into compound castings was the good economic viability of the components due to the high function integration (i.e. a single component can fulfil several requirements) (Tayal et al., 2012; Bührig-Polaczek et al., 2006). In this regard, Al/Mg compound castings offer several advantages over the compound casting of different material combinations (e.g. Al/Al, Al/Cu compound castings).

1. Al/Mg compound casting offers the highest potential for weight savings.
2. Contrary to the published findings, the removal of the alumina layer was not necessary for bonding to occur. This study has shown that the alumina layer is reduced by the magnesium melt, and thus no special treatment is necessary.

However, while a material bond was achieved, Al/Mg compound castings display several drawbacks. The main drawbacks encountered in Al/Mg compound castings are either caused by the material (aluminium/magnesium) or the casting process (conventional gravity casting was used in this study).

**Material related drawbacks.** An increase in the brittleness of the material bond caused by the presence of intermetallic phases, especially the  $\beta$  phase, was always present in Al/Mg compound castings. Consequently, fractures and cracks are commonly found in the material bond of all compound castings. Even in the absence of fractures and cracks, the resulting mechanical strength is, at ~25Mpa, relatively low. The presence of elements with a high diffusion coefficient (e.g. zinc) leads to an imbalanced diffusion, which may then cause the formation of Kirkendall voids, weakening the material bond further.

**Process related drawbacks.** The dissolution of aluminium in the magnesium melt causes the liquidus temperature to drop. Thus, the melt in the material bond is the last liquid phase to solidify. As a consequence, the volume contraction during the solidification of the melt cannot be compensated. Pores are formed and shrinkages occur as a result, thus reducing the soundness of the casting. The thickness of the material bond directly correlates with the amount of aluminium-rich melt near the solid/liquid interface. Turbulence and fluctuating melt velocities, due to the casting process, thus result in a material bond of an uneven thickness. While an uneven thickness of the material bond is of less relevance to the mechanical properties (as no direct correlation between thickness and mechanical strength was found in this study), other properties (e.g. electrical and thermal properties; see Fourier's law) may be affected.

A number of measures to counter these disadvantages have been briefly discussed in sections 6.2-6.6. While certain aspects (solidification-related shrinkage, voids and brittleness of the material bond) could be improved, it is unlikely that implementing these measures will significantly improve the overall soundness and mechanical strength of the castings. The addition of silicon, for example, counters the

volume contraction during solidification, but it also leads to an embrittlement of the interface through the formation of  $Mg_2Si$ . Similarly, the manipulation of the grain size, or the addition of erbium, promotes growth of the  $\gamma$  phase but does not prevent formation of the  $\beta$  phase, and thus there is no improvement in the overall stability of the bond.

Alternative processing methods to those used in this study are available, and could alter the findings. The high cooling rates associated with HPDC are thought to inhibit the formation of material bonds, as the resulting low reaction time between the aluminium and magnesium prevents the formation of a material bond. The application of a zinc-based coating on the aluminium alloy might facilitate the formation of a bond. But as the coating would involve an additional process step and thus costs, it is undesirable in economic terms. Moreover, the turbulent flow and high velocities of the melt during HPD casting make precise control over the solidification difficult. The use of Low Pressure Die Casting (LPDC) could be a promising approach, as this casting process would allow for a more precise control of the filling (Campbell, 1991). With this process the length of contact between the magnesium melt and the aluminium insert can be more precisely set, and thus solidification and thickness of the material bond can be optimised. Nevertheless, the problematic intermetallic  $\beta$  phase would still be present.

Overall, the demanding requirements with regard to process control and the listed disadvantages elaborated in this chapter, inherent to the materials, make it doubtful if Al/Mg compound castings will offer any advantages when used in actual industrial applications. The process of compound casting itself might still be of interest, for applications such as heat exchangers, where the mechanical strength of the bond between two metals plays a minor role. However, for components where heat transfer or electrical conductivity is important, castings with copper, such as Al/Cu compound castings, might be better suited than Al/Mg (Bakke et al., 2018).

## 7.9: References

- AGARWAL, R. and SOMMER, F. (1991) Calorimetric measurements of liquid Al-Mg alloys. *Zeitschrift fuer Metallkunde*, **82**, pp. 118.
- ALOKE, P. (2004) *The Kirkendall Effect in Solid State Diffusion*. PhD Thesis. Laboratory of Materials and Interface Chemistry, Eindhoven University of Technology.
- ALTENPOHL, D. (1965) *Aluminium und Aluminiumlegierungen*. 19<sup>th</sup> edn. Berlin/Heidelberg: Springer Verlag Berlin/Heidelberg GmbH.
- ASHBY, M. F., SHERCLIFF, H., and CEBON, D. (2014) *Materials: Engineering, Science, Processing and Design*. 3<sup>rd</sup> edn. Amsterdam: Butterworth-Heinemann.
- ASM INTERNATIONAL (1990) *ASM Handbook Volume 2: Properties and Selection: Nonferrous Alloys and Special-Purpose Materials*. 2<sup>nd</sup> edn. Materials Park, OH: ASM International.
- BAKKE, A., LI, Y., LOLAND, J., JORGENSEN, S., and KVINDE, J. (2018) Effect of Flux coating on Interfacial Microstructure in Bimetallic AlSi7Mg/Cu Compound castings. *Proceedings of the 16th International Aluminum Alloys Conference*. The Canadian Institute of Mining, Metallurgy and Petroleum.
- BAUCCIO, M. L. (1993) *ASM Metal Reference Book*. 3<sup>rd</sup> edn. Materials Park, OH: ASM International.
- BIRCUMSHAW, L. and RIDDIFORD, A. (1952) Transport Control in Heterogeneous Reactions. *Quarterly Reviews, Chemical Society*, (2), pp. 157-185.
- BRENNAN, S., BERMUDEZ, K., KULKARNI, N. S., and SOHN, Y. (2012) Interdiffusion in the Mg-Al System and Intrinsic Diffusion in  $[\beta]$ -Al<sub>3</sub>Mg<sub>2</sub>. *Metallurgical and Materials Transactions*, **43**(11), pp. 4043.
- BÜHRIG-POLACZEK, A., RÖTH, T., BAUMEISTER, E., NOWACK, N., and SUSSMANN, T. (2006) Hybride Leichtbaustrukturen in Stahlblech-Leichtmetall Verbundguss. *Internationaler Expertenkreis Automobil-Leichtbau 15. Europäische Automobil-Leichtbaukonferenz*. 9-10 May, 2006.
- CAMPBELL, J. (1991) *Castings*. Oxford: Butterworth-Heinemann.
- CAMPBELL, T., KALIA, R. K., NAKANO, A., VASHISHTA, P., OGATA, S., and RODGERS, S. (1999) Dynamics of Oxidation of Aluminum Nanoclusters using Variable Charge Molecular-Dynamics Simulations on Parallel Computers. *Physical Review Letters*, **82**(24), pp. 4866-4869.
- CHOI, D., AHN, B., LEE, C., YEON, Y., SONG, K., and JUNG, S. (2011) Formation of Intermetallic Compounds in Al and Mg Alloy Interface during Friction Stir Spot Welding. *Intermetallics*, **19**(2), pp. 125-130.
- CUI, Y. W., OIKAWA, K., KAINUMA, R., and ISHIDA, K. (2006) Study of Diffusion Mobility of Al-Zn Solid Solution. *Journal of Phase Equilibria & Diffusion*, **27**(4), pp. 333-342.
- DEGARMO, E. P. BLACK, J. T., and KOHSER, R. A. (2008) *DeGarmo's Materials and Processes in Manufacturing*. 10<sup>th</sup> edn. Chichester: Wiley.



- DIETRICH, D., NICKEL, D., KRAUSE, M., LAMPKE, T., COLEMAN, M.P., and RANDLE, V. (2011) Formation of Intermetallic Phases in Diffusion-Welded Joints of Aluminium and Magnesium alloys. *Journal of Materials Science*, **46**(2), pp. 357-364.
- DJURDJEVIĆ, M. B., MANASIJEVIĆ, S., ODANOVIĆ, Z., and DOLIĆ, N. (2013) Calculation of Liquidus Temperature for Aluminum and Magnesium Alloys Applying Method of Equivalency. *Advances in Materials Science and Engineering*, **2013**, pp. 1-8.
- DYBKOV, O. and DYBKOV, V. (2004) Analytical Treatment of Diffusional Growth kinetics of two Intermetallic-Compound Layers. *Journal of Materials Science*, **39**(21), pp. 6615-6617.
- DYBKOV, V. (1990) Interaction of 18Cr-10Ni stainless steel with liquid aluminium. *Journal of Materials Science*, **25**(8), pp. 3615-3633.
- DYBKOV, V. (2002) *Reaction diffusion and solid state chemical kinetics*. Kiev: The IPMS Publications.
- DYBKOV, V. (2007) Interfacial Interaction and Diffusion in Binary Systems. *Defect and Diffusion Forum*, **263**, pp. 75-80.
- EMAMI, S. M., DIVANDARI, M., ARABI, H., and HAJJARI, E. (2013a) Effect of Melt-to-Solid Insert Volume Ratio on Mg/Al Dissimilar Metals Bonding. *Journal of Materials Engineering and Performance*, **22**(1), pp. 123-130.
- EMAMI, S. M., DIVANDARI, M., HAJJARI, E., and ARABI, H. (2013b) Comparison between Conventional and Lost Foam Compound Casting of Al/Mg Light Metals. *International Journal of Cast Metals Research*, **26**(1), pp. 43-50.
- ERDÉLYI, G., BEKE, D. L., KEDVES, F. J., and GÖDÉNY, I. (1978) Determination of Diffusion Coefficients of Zn, Co and Ni in Aluminium by a Resistometric Method. *Philosophical Magazine B*, **38**(5), pp. 445-462.
- EREMENKO, V. and NATANZON, Y. (1970) Kinetics of External Dissolution of Metals in Metallic Melts. *Soviet Powder Metallurgy and Metal Ceramics*, **9**(8), pp. 645.
- EUSTATHOPOULOS, N. and DREVET, B. (1994) Relationship between reactivity and wettability in metal/oxide systems. *Composite Interfaces*, **2**(1), pp. 29-42.
- EUSTATHOPOULOS, N. (2015) Wetting by Liquid Metals—Application in Materials Processing: The Contribution of the Grenoble Group. *Metals*, **5**(1), pp. 350-370.
- FEUFEL, H., GÖDECKE, T., LUKAS, H. L., and SOMMER, F. (1997) Investigation of the Al-Mg-Si system by experiments and thermodynamic calculations. *Journal of Alloys and Compounds*, **247**(1), pp. 31-42.
- FRIEDRICH, B. (2015) *Understanding of Inclusions - Characterization, Interactions and Boundaries of Removability with Special Focus on Aluminium melts*.  
[https://www.researchgate.net/publication/299490901\\_Understanding\\_of\\_Inclusions\\_-\\_Characterization\\_Interactions\\_and\\_Boundaries\\_of\\_Removability\\_with\\_Special\\_Focus\\_on\\_Aluminium\\_melts](https://www.researchgate.net/publication/299490901_Understanding_of_Inclusions_-_Characterization_Interactions_and_Boundaries_of_Removability_with_Special_Focus_on_Aluminium_melts)

- FUKUI, K. and MAEDA, K. (1998) Distribution of solute at solid–liquid interface during solidification of melt. *The Journal of chemical physics*, **109**(17), pp. 7468-7473.
- GILLE, P. and GRIN, Y. (2018) *Crystal Growth of Intermetallics*. Berlin/Boston: Walter de Gruyter GmbH.
- GLATZEL, U. (2012) *Werkstofftechnologie und Halbzeuge*. Bayreuth: Lehrstuhl Metallische Werkstoffe, Bayreuth University.
- GUO, J. T., HUAI, K. W., GAO, Q., REN, W. L., and LI, G. S. (2007) Effects of rare earth elements on the microstructure and mechanical properties of NiAl-based eutectic alloy. *Intermetallics*, **15**(5), pp. 727-733.
- HAJJARI, E., DIVANDARI, M., RAZAVI, S. H., EMAMI, S. M., HOMMA, T., and KAMADO, S. (2011) Dissimilar Joining of Al/Mg Light Metals by Compound Casting Process. *Journal of Materials Science*, **46**(20), pp. 6491-6499.
- HUGHES, S. E. (2009) *A quick guide to welding and weld inspection*. Oxford: Woodhead Publishing.
- JYNGE, H. and MOTZFELDT, K. (1980) Reactions between molten Magnesium and refractory oxides. **25**(2), pp. 139.
- KAMMERER, C., KULKARNI, N., WARMACK, R., and SOHN, Y. (2016) Interdiffusion in Ternary Magnesium Solid Solutions of Aluminum and Zinc. *Journal of Phase Equilibria and Diffusion*, **37**(1), pp. 65-74.
- KAMMERER, C., KULKARNI, N., WARMACK, R., and SOHN, Y. (2014) Al and Zn impurity diffusion in binary and ternary magnesium solid-solutions, *Magnesium Technology 2014*, pp. 407-411. [https://doi.org/10.1007/978-3-319-48231-6\\_76](https://doi.org/10.1007/978-3-319-48231-6_76)
- KASSNER, M. E. and PÉREZ-PRADO, M. (2004) *Fundamentals of creep in metals and alloys*. Oxford: Elsevier.
- KOBAYASHI, T. (1998) Fracture Characteristics of Aluminum Casting alloys, *Proceedings of ICAA-6*, 1998 1998, pp. 127.
- KULKARNI, K. and LUO, A. (2013) Interdiffusion and Phase Growth Kinetics in Magnesium-Aluminum Binary System. *Journal of Phase Equilibria and Diffusion*, **34**(2), pp. 104-115.
- KUMAR, H., CHAKRABORTI, N., LUKAS, H., BODAK, O., and ROKHLIN, L. (2005) Aluminium-Magnesium-Silicon. In: G. EFFENBERG and S. ILYENKO, eds, *Ternary Alloy Systems - Phase Diagrams, Crystallographic and Thermodynamic Data: Light Metal Systems, Part 3: Selected Systems from Al-Fe-V to Al-Ni-Zr*. Berlin: Springer.
- LANGE, G. (2001) *Systematische Beurteilung technischer Schadensfälle*. 5<sup>th</sup> edn. New York: John Wiley & Sons.
- LI, C., CHI, C., LIN, P., ZHANG, H., and LIAN, W. (2015) Deformation behavior and interface microstructure evolution of Al/Mg/Al multilayer composite sheets during deep drawing. *Materials and Design*, **77**, pp. 15.
- LI, Y., WEI, Y., HUO, L., GUO, C., and HAN, P. (2014) Effect of Erbium on microstructures and properties of Mg-Al intermetallic. *中国稀土学报: 英文版*, **32**(11), pp. 1064-1072.

- LIANG, H., CHEN, S. L., and CHANG, Y. A. (1997) A thermodynamic description of the Al-Mg-Zn system. *Metallurgical and Materials Transactions A*, **28**(9), pp. 1725-1734.
- LIANG, P., TARFA, T., ROBINSON, J. A., WAGNER, S., OCHIN, P., HARMELIN, M. G., SEIFERT, H. J., LUKAS, H. L., and ALDINGER, F. (1998) Experimental investigation and thermodynamic calculation of the Al-Mg-Zn system. *Thermochimica Acta*, **314**(1), pp. 87-110.
- LIU, J. and KOU, S. (2015) Effect of diffusion on susceptibility to cracking during solidification. *Acta Materialia*, **100**, pp. 359-368.
- LIU, J. and KOU, S. (2017) Susceptibility of ternary aluminum alloys to cracking during solidification. *Acta Materialia*, **125**, pp. 513-523.
- LIU, X., ADAMS, J. B., ERCOLESSI, F., and MORIARTY, J. A. (1996) EAM potential for magnesium from quantum mechanical forces. *Modelling and Simulation in Materials Science and Engineering*, **4**(3), pp. 293-303.
- LIU, Y., CHEN, Y., and YANG, C. (2015) A study on atomic diffusion behaviours in an Al-Mg compound casting process. *AIP ADVANCES*, **5**(8), pp. 087147-087147-13.
- MATHUR, H. N., MAIER-KIENER, V., and KORTE-KERZEL, S. (2016) Deformation in the  $\gamma$ -Mg<sub>17</sub>Al<sub>12</sub> phase at 25–278 °C. *Acta Materialia*, **113**, pp. 221-229.
- MCLEOD, A. D. and GABRYEL, C. M. (1992) Kinetics of the growth of spinel, MgAl<sub>2</sub>O<sub>4</sub>, on Alumina particulate in Aluminum alloys containing Magnesium. *Metallurgical Transactions A*, **23**(4), pp. 1279.
- MERCURY CASTINGS (2019) Available: <https://www.mercalloy.com/aluminum-alloys-101/> [23 July 2019].
- MEZBAHUL-ISLAM, M., MOSTAFA, A. O., and MEDRAJ, M. (2014) Essential Magnesium Alloys Binary Phase Diagrams and Their Thermochemical Data. *Journal of Materials*, **2014**.
- MOLA, R. and DZIADON, A. (2008) Formation of magnesium-eutectic mixture layered composite. *Archives of Foundry Engineering*, **8**(4), pp. 127-132.
- MORISHIGE, T., KAWAGUCHI, A., TSUJIKAWA, M., HINO, M., HIRATA, T., and HIGASHI, K. (2008) Dissimilar welding of Al and Mg alloys by FSW. *Materials Transactions*, **49**(5), pp. 1129-1131.
- MOSER, Z., ZAKULSKI, W., RZYMAN, K., GASIOR, W., PANEK, Z., KATAYAMA, I., MATSUDA, T., FUKUDA, Y., LIDA, T., ZAJACZKOWSKI, Z., and BOTOR, J. (1998) New Thermodynamic Data for Liquid Aluminum-Magnesium Alloys from emf, Vapor Pressures, and Calorimetric Studies. *Journal of Phase Equilibria and Diffusion*, **19**(1), pp. 38.
- MOUNIB, M., PAVESE, M., BADINI, C., LEFEBVRE, W., and DIERINGA, H. (2014) Reactivity and Microstructure of Al<sub>2</sub>O<sub>3</sub>-Reinforced Magnesium-Matrix Composites. *Advances in Materials Science and Engineering*, **2014**, pp. 1-6.
- NAKAHARA, S. and MCCOY, R.J. (1980) Kirkendall void formation in thin-film diffusion couples. *Applied Physics Letters*, **37**(1), pp. 42-44.

- PANTELI, A., ROBSON, J. D., CHEN, Y. and PRANGNELL, P. B. (2013) The Effectiveness of Surface Coatings on Preventing Interfacial Reaction During Ultrasonic Welding of Aluminum to Magnesium. *Metallurgical and Materials Transactions A*, **44**(13), pp. 5773-5781.
- PATEL, V. K., BHOLE, S. D., and CHEN, D. L. (2012) Improving weld strength of magnesium to aluminium dissimilar joints via tin interlayer during ultrasonic spot welding. *Science and Technology of Welding and Joining*, **17**(5), pp. 342-347.
- PECHARSKY, V. and ZAVALIJ, P. (2009) *Fundamentals of powder diffraction and structural characterization of materials*. 2<sup>nd</sup> edn. Boston: Springer US.
- PEQUET, C., RAPPAZ, M., and GREMAUD, M. (2002) Modelling of microporosity, macroporosity, and pipe-shrinkage formation during the solidification of alloys using a mushy-zone refinement method: Applications to aluminum alloys. *Metallurgical and Materials Transactions A*, **33**(7), pp. 2095-2106.
- RADI, Z., BARNA, P.B., and LÁBÁR, J. (1996) Kirkendall voids and the formation of amorphous phase in the Al-Pt thin-film system prepared by high-temperature successive deposition. *Journal of Applied Physics*, **79**(8), pp. 4096-4100.
- RAGHAVAN, V. (2007) Al-Er-Mg (Aluminum-Erbium-Magnesium). *Journal of Phase Equilibria and Diffusion*, **28**(5), pp. 461-463.
- ROBSON, J., PANTELI, A., and PRANGNELL, P. B. (2012) Modelling intermetallic phase formation in dissimilar metal ultrasonic welding of aluminium and magnesium alloys. *Science and Technology of Welding and Joining*, **17**(6), pp. 447-453.
- RÜBNER, M., GÜNZL, M., KÖRNER, C., and SINGER, R. F. (2011) Aluminium–aluminium compound fabrication by high pressure die casting. *Materials Science & Engineering A*, **528**(22), pp. 7024-7029.
- SANGGHALEH, A. and HALALI, M. (2009) Effect of magnesium addition on the wetting of alumina by aluminium. *Applied Surface Science*, **255**(19), pp. 8202-8206.
- SCHRAMM, A., BOCK, B., SCHMIDT, A., ZIENERT, T., DITZE, A., SCHARF, C., and ANEZIRIS, C. G. (2018) Interface reactions of differently coated carbon-bonded alumina filters with an AZ91 magnesium alloy melt. *Ceramics International*, **44**(14), pp. 17415-17424.
- SU, H. L., HARMELIN, M., DONNADIEU, P., BAETZNER, C., SEIFERT, H. J., LUKAS, H. L., EFFENBERG, G., and ALDINGER, F. (1997) Experimental investigation of the Mg-Al phase diagram from 47 to 63 at.% Al. *Journal of Alloys and Compounds*, **247**(1), pp. 57-65.
- TANGUEP NJIOKEP, E. M., SALAMON, M., and MEHRER, H. (2001) Growth of intermetallic phases in the Al-Mg system. *Defect and Diffusion Forum*, (194-199), pp. 1581-1586.
- TAYAL, R., SINGH, V., KUMAR, S., and GARG, R. (2012) Compound Casting- A literature Review , *National Conference on Trends and Advances in Mechanical Engineering*, Oct 19-20, 2012 2012.
- VIALA, J. C., PERONNET, M., BARBEAU, F., BOSSELET, F., and BOUIX, J. (2002) Interface chemistry in aluminium alloy castings reinforced with iron base inserts. *Composites Part A*, **33**(10), pp. 1417-1420.

- WANG, L., WANG, Y., PRANGNELL, P., and ROBSON, J. (2015) Modelling of Intermetallic Compounds Growth Between Dissimilar Metals. *Metallurgical and Materials Transactions A*, **46**(9), pp. 4106-4114.
- WANG, N., YU, W., TANG, B., PENG, L., and DING, W. (2008) Structural and mechanical properties of Mg<sub>17</sub>Al<sub>12</sub> and Mg<sub>24</sub>Y<sub>5</sub> from first-principles calculations. *Journal of Physics D: Applied Physics*, **41**(19), pp. 195408.
- XIAO, L. and WANG, N. (2015) Growth behavior of intermetallic compounds during reactive diffusion between aluminum alloy 1060 and magnesium at 573-673 K. *Journal of Nuclear Materials*, **456**, pp. 389-397.
- XU, G., LUO, A., CHEN, Y., and SACHDEV, A. (2014) Interfacial phenomena in magnesium/aluminum bi-metallic castings. *MATERIALS SCIENCE AND ENGINEERING A-STRUCTURAL MATERIALS PROPERTIES MICROSTRUCTURE AND PROCESSING*, **595**, pp. 154-158.
- YAN, F., MCKAY, B., FAN, Z., and CHEN, M. (2012) Preliminary study of the characteristics of a high Mg containing Al-Mg-Si alloy, 2012, IOP Publishing.
- YAN, M. and FAN, Z. (2001) Review Durability of materials in molten aluminum alloys. *Journal of Materials Science*, **36**(2), pp. 285-295.
- ZAINON, F., AHMAD, K., and DAUD, R. (2016) The effects of Mg<sub>2</sub>Si<sub>(p)</sub> on microstructure and mechanical properties of AA332 composite. *Advances in Materials Research*, **5**(1), pp. 55.
- ZHANG, H., CHEN, Y., and LUO, A. A. (2014a) A novel aluminum surface treatment for improved bonding in magnesium/aluminum bimetallic castings. *Scripta Materialia*, **86**, pp. 52-55.
- ZHANG, H., CHEN, Y., and LUO, A. A. (2014b) Improved Interfacial Bonding in Magnesium/Aluminum Overcasting Systems by Aluminum Surface Treatments. *Metallurgical and Materials Transactions B*, **45**(6), pp. 2495-2503.
- ZHAO, D., KONG, Y., WANG, A., ZHOU, L., CUI, S., YUAN, X., ZHANG, L., and DU, Y. (2011) Self-Diffusion Coefficient of fcc Mg: First-Principles Calculations and Semi-Empirical Predictions. *Journal of Phase Equilibria and Diffusion*, **32**(2), pp. 128-137.
- ZHE, M., DEZELLUS, O., GARDIOLA, B., BRACCINI, M., and VIALA, J.C. (2011) Chemical Changes at the Interface Between Low Carbon Steel and an Al-Si Alloy During Solution Heat Treatment. *Journal of Phase Equilibria and Diffusion*, **32**(6), pp. 486-497.
- ZHOU, J., REN, L., GENG, X., FANG, L., and HU, H. (2019) As-cast magnesium AM60-based hybrid nanocomposite containing alumina fibres and nanoparticles: Microstructure and tensile behavior. *Materials Science & Engineering A*, **740-741**, pp. 305-314.
- ZHU, H. (2014) *Dissolution Rate And Mechanism Of Metals In Molten Aluminum Alloy A380*, Purdue University.

## Chapter 8: Conclusion and Future Work

Al/Mg compound castings were identified as offering several advantages compared to single-material components. Low specific weight and high strength, as well as cost efficiency, were cited as the main advantages. Unlike Al/Al or Al/Fe compound castings, aluminium's intrinsic oxide layer was not found to impede the formation of a material bond in Al/Mg compound castings. While not directly observed, it was deduced that the alumina was chemically reduced to form magnesium oxide and elementary aluminium, which are then dispersed within the castings and not thought to have a negative effect on the strength of the material bond.

The resulting material bond between the two metals was formed due to a combination of crystallisation from the liquid phase and diffusion in the solid state after solidification; this finding was in good agreement with existing research into compound castings. The total thickness of the material bond after casting was dependent on temperature, cooling rate, holding time and the chemical composition of the alloys used. The observed thicknesses of the material bond ranged between 0 and 8000 $\mu\text{m}$ , depending on casting parameters and alloys used. In fact, it was found that the ability of the magnesium melt to dissolve solid aluminium was the main contributing factor in determining the total thickness of the material bond. The material bond precipitates directly from the Mg melt, enriched with aluminium, at the solid/liquid interface, and is thus more distinct with higher amounts of aluminium dissolved. The main constituents of the material bond, in accordance with the corresponding phase diagrams, were the AlMg intermetallic phases  $\beta$  and  $\gamma$ . Adding silicon or zinc as a ternary element to the compound casting resulted in the formation of Si- and Zn-rich phases. The exact mechanisms of the formations of the Si- and Zinc-rich phases was different for the two elements.

- Silicon, regardless of amount, was found exclusively in the form of  $\text{Mg}_2\text{Si}$  particles. Due to the high liquidus temperature of the  $\text{Mg}_2\text{Si}$  particles, it is thought that bulk of the  $\text{Mg}_2\text{Si}$  in the material bond does not precipitate directly from the liquid phase (unlike the  $\beta$  and  $\gamma$  phases). Rather, it is the result of diffusion and the subsequent reaction with magnesium in the solid state. Under the conditions used in this study, the addition of silicon resulted in a thickness of the material bond of  $\sim 1150$  to  $\sim 1300\mu\text{m}$ .
- Zinc was dissolved by the magnesium melt and formed the zinc-rich phases  $\tau_1$  and  $\phi$  upon solidification of the melt. Both phases were only observed at zinc concentrations greater than 15wt%. In this study, the addition of zinc resulted in a material bond thickness of  $\sim 4000$  to  $\sim 8000\mu\text{m}$ .

High zinc concentrations of 30wt% led to the complete transformation of the microstructure of the aluminium and magnesium, and the formation of evenly shaped holes. This behaviour was attributed to zinc's high diffusivity and the low liquidus temperature of some parts of the AlMgZn system.

The strength of the material bond was assessed by means of push-out testing, and the material bond failed at relatively low loads, between 4 and 25MPa, confirming its brittle nature. The bond always failed inside the aluminium-rich intermetallic phase  $\beta$ , indicating that the magnesium-rich phases exhibited favourable properties. No correlation, between the magnesium and aluminium alloys used, the thickness of the material and the mechanical strength of the interface, was detected. Rather, defects such as voids and fractures were found to be detrimental to the mechanical strength of the material bond. The voids were commonly found in AlZn/AZ31 compound castings and are linked to an imbalanced diffusion process (Kirkendall effect). Fractures were either the result of mechanical stress (in AlSi/AZ31 and AlZn/AZ31 compound castings) or hot cracking (only in AlSi/AZ31 compound castings).

The AlMg and AlMgZn intermetallic phases displayed significantly lower liquidus and solidus temperatures than the Al and Mg alloys. As a consequence, the material bond solidifies after the bulk of the magnesium melt. The liquid to solid volume contraction then cannot be compensated, leading to the aforementioned voids.

## Future work

While the results from this study identified the key problems associated with Al/Mg compound castings, there is still potential for future research. Future work should thus focus on improving the following aspects of Al/Mg compound castings.

1. **Mechanical strength and soundness of the material bond.** The material bond was identified to be very brittle, and was thus the weakness of Al/Mg compound castings in terms of mechanical strength. The results of this work indicate that the magnesium-rich phases possess higher ductility compared to the aluminium-rich ones. Moreover, it was indicated that while the presence of the aluminium-rich  $\beta$  phase cannot be avoided, precise control of the temperature at the solid/liquid interface allows for the  $\gamma$  phase to grow at the expense of the  $\beta$  phase. Future work should focus on further understanding of how to affect the growth rates of, or modify, both intermetallic compounds. It should be investigated if formation and growth of the  $\beta$  phase can be completely suppressed at elevated temperatures. The effect of additional common elements, such as copper or nickel, or exotic elements, such as rare earths like erbium, on the formation of the material bond and its properties would also be worth investigating.
2. **Casting process of Al/Mg compound castings.** It has been established in this study that formation of the material bond is temperature- and time-dependent. At the temperatures needed to ensure removal of aluminium's oxide layer (400-450°C), the intermetallic  $\beta$  phase forms. Rapid cooling after removal of the alumina layer would possibly allow minimising the growth of the  $\beta$  phase and promote growth of the  $\gamma$  phase. However, if the cooling rates are too high, no material bond will form, as there is not enough thermal energy for dissolution and diffusion.

Thus, future research should focus on identifying the optimal cooling rate in Al/Mg compound castings, and the means to achieve it. Low Pressure Die Casting appears to be a promising approach, as mentioned in section 7.8.

3. **Electrochemical properties of Al/Mg compound castings.** Corrosion of the Al/Mg compound castings could be observed with the naked eye on sectioned samples. This is caused by the difference in the electrochemical potentials of the two metals. In the presence of water, or even humidity, an electrochemical reaction starts, akin to that in a galvanic cell, leading to the galvanic corrosion of the castings. If used in a humid environment, the susceptibility to corrosion is a concern for the commercial use of such a casting. Thus, upcoming research should address this issue by identifying the means to increase the casting's corrosion resistance (e.g. by alloying or passivation).

While there is still potential to optimise Al/Mg compound castings, it is doubtful if such castings will ever meet the requirements of the transportation industry in terms of mechanical strength and corrosion resistance, due to the drawbacks mentioned in section 7.1.